IntechOpen

Sustainable Energy
Technological Issues, Applications and Case Studies

Edited by Ahmed F. Zobaa,
Sara N. Afifi and Ioana Pisica

SUSTAINABLE ENERGY - TECHNOLOGICAL ISSUES, APPLICATIONS AND CASE STUDIES

Edited by **Ahmed F. Zobaa, Sara N. Afifi**
and **Ioana Pisica**

Sustainable Energy - Technological Issues, Applications and Case Studies
http://dx.doi.org/10.5772/62655
Edited by Ahmed F. Zobaa, Sara N. Afifi and Ioana Pisica

Contributors

Fanhua Ma, Kumar Mehra Roopesh, Wei-Ming Chen, Priyanko Guha Thakurta, Rudy Calif, François Schmitt, Olmo Duran Medina, Yuri Vorobiev, Iker Chavez Urbiola, Rafael Ramirez Bon, Liliana Licea Jiménez, Sergio Alfonso Pérez García, Pavel Vorobiev, Paul Horley, David Walwyn, Mahmoud Ghofrani, Negar Niromand Hosseini, Juan M. Ortiz, Helfrid Schulte-Herbruggen, Payam Malek, Guido Carpinelli, Pasquale De Falco, Antonio Bracale

© The Editor(s) and the Author(s) 2016
The moral rights of the and the author(s) have been asserted.
All rights to the book as a whole are reserved by INTECH. The book as a whole (compilation) cannot be reproduced, distributed or used for commercial or non-commercial purposes without INTECH's written permission.
Enquiries concerning the use of the book should be directed to INTECH rights and permissions department (permissions@intechopen.com).
Violations are liable to prosecution under the governing Copyright Law.

Individual chapters of this publication are distributed under the terms of the Creative Commons Attribution 3.0 Unported License which permits commercial use, distribution and reproduction of the individual chapters, provided the original author(s) and source publication are appropriately acknowledged. If so indicated, certain images may not be included under the Creative Commons license. In such cases users will need to obtain permission from the license holder to reproduce the material. More details and guidelines concerning content reuse and adaptation can be foundat http://www.intechopen.com/copyright-policy.html.

Notice

Statements and opinions expressed in the chapters are these of the individual contributors and not necessarily those of the editors or publisher. No responsibility is accepted for the accuracy of information contained in the published chapters. The publisher assumes no responsibility for any damage or injury to persons or property arising out of the use of any materials, instructions, methods or ideas contained in the book.

First published in Croatia, 2016 by INTECH d.o.o.
eBook (PDF) Published by IN TECH d.o.o.
Place and year of publication of eBook (PDF): Rijeka, 2019.
IntechOpen is the global imprint of IN TECH d.o.o.
Printed in Croatia

Legal deposit, Croatia: National and University Library in Zagreb

Additional hard and PDF copies can be obtained from orders@intechopen.com

Sustainable Energy - Technological Issues, Applications and Case Studies
Edited by Ahmed F. Zobaa, Sara N. Afifi and Ioana Pisica
p. cm.
Print ISBN 978-953-51-2839-7
Online ISBN 978-953-51-2840-3
eBook (PDF) ISBN 978-953-51-6689-4

Meet the editors

Ahmed F. Zobaa received his BSc (Hons), MSc, and PhD degrees in electrical power and machines from Cairo University, Egypt, in 1992, 1997, and 2002, respectively. From 2007 to 2010, he was a senior lecturer in renewable energy at the University of Exeter, UK. He was also an instructor from 1992 to 1997, a teaching assistant from 1997 to 2002, an assistant professor from 2003 to 2008, and an associate professor from 2008 to 2013 at Cairo University where he has also been a professor (on leave) since December 2013. Currently, he is a senior lecturer in power systems, an MSc Course Director, and a full member of the Institute of Energy Futures at the Brunel University London, UK. His main areas of expertise are power quality, (marine) renewable energy, smart grids, energy efficiency, and lighting applications.

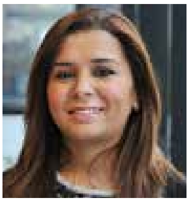

Sara N. Afifi received her BSc (Hons) degree in electrical power and machines from the Faculty of Engineering, Cairo University, Egypt, in 2005. Also, she received her MSc degree in energy policy and sustainability from the University of Exeter, UK, in 2009. Currently, she is a PhD student at the Brunel Institute of Power Systems, Brunel University London, UK. She is a member of the Institution of Engineering and Technology and the Energy Institute of the UK. Her areas of expertise include distributed generation, energy policy, and sustainability.

Ioana Pisica is a lecturer in Power Systems at the Brunel University London, Department of Electronic and Computer Engineering. She received her MSc in information systems from the Academy of Economic Studies from Bucharest and her PhD from the University Politehnica of Bucharest. Her research interests include modern optimization techniques for power systems with distributed generation and FACTS devices, machine learning for power systems control, power quality, smart metering, and ICT infrastructures for future power networks.

Contents

Preface

The climate change mitigation and sustainable energy development are currently vital priorities on governments' energy policies. The global target of reducing greenhouse gas emissions has emerged the critical transition from highly fossil fueled generation sources to renewable energy (nonfossil fuels) generation sources. The renewable power generation is considered one of the major solutions to mitigating climate change and in ensuring energy security. There are several renewable energy sources including the sun, wind, oceans, tidal waves, rivers, and earth temperature. All these sources are capable of generating electrical power on different scales. The global outlook has developed new opportunities and inventions in the research area of renewable energy technologies.

The implementation of hybrid renewable energy systems ensures overall system efficiency, reliability, and flexibility. However, there are several random variables and parameters that need to be optimized to identify accurate rating of the hybrid system components.

The fluctuated nature of energy sources such as wind speed (not constant throughout the year) leads to variable output power which in turn affects the system integration characteristics and operation. The transmission system operators (TSOs) struggle to control such output power variability, especially with interconnected transmission systems. The inter-TSO coordination would be an affordable option for flexible transmission system operation and management.

Indeed, the knowledge of the scaling behavior of the renewable energy resource data should be recognized; such as atmospheric wind speed for the case of wind power and global solar radiation in the case of solar power. In this book, a scaling exponent function is developed to identify the multifractal and intermittent properties of sustainable resources and energy data. In addition, a new multimodel probabilistic ensemble is proposed that combines a Bayesian-based and a quantile regression-based probabilistic method as individual predictors for probabilistic forecasting of PV system power. Furthermore, research in solar energy technologies is undertaken to discover affordable alternative materials and deposition techniques that could replace the current materials used and methods applied in the solar energy converters. The approach of new multilayered solar energy converters with electrically independent sequence of p and n semiconductor films is presented.

The fast pace of research has been able to invent new sustainable technologies to ensure the power systems' reliability, in cases if the renewable energy sources are not abundant enough to generate electricity. The potential of producing energy with the capability of energy storage through fuel cells where the hydrogen is the source of fuel is a vast growing technology.

The sustainable energy sources are potentially employed to substitute petrol fuels in transport engines such as buses and small vehicles. Hydrogen-enriched compressed natural gas engines are forthcoming energy carriers for the internal combustion engine, with higher thermal efficiency and less pollutant emissions.

The different availability of renewables has allowed various countries to adopt the most appropriate type of renewable energy technology according to their energy source adequacy/ abundance.

In Taiwan, ocean energy is considered as an abundant source of renewables due to its geographical location as an island. The Taiwanese government has approved the investment to construct an MW-scale demonstration electricity plant. In this book, the Taiwanese ocean energy experience is comprehensively presented. The technical and legal analyses of ocean energy implementation are provided. The challenges that they had to overcome to optimize the utilization of the most available ocean energy potential are discussed.

The sustainable transition in South Africa would be a good example for implementing rooftop solar, especially in low-income communities. Apart from the environmental benefits, sustainable energy technologies can boost the socioeconomic level of developing countries. More other advantages may be the continuous supply of energy and creation of new job opportunities.

Moreover, sustainable renewable energy sources such as the wind could be employed for generating electricity to operate water purification systems in remote areas. This, in turn, would overcome the health problems associated with drinking water scarcity issues.

This book is an attempt to cover the sustainable energy issues from a technical perspective. Furthermore, the sustainable energy applications and existing case studies are helpful illustrations for the broad understanding of the importance of sustainable energy.

Ahmed F. Zobaa, Sara N. Afifi and Ioana Pisica
Brunel University London,
United Kingdom

Chapter 1

Study of Quasi-Dimensional Combustion Model of Hydrogen-Enriched Compressed Natural Gas (HCNG) Engines

Fanhua Ma and Roopesh Kumar Mehra

Additional information is available at the end of the chapter

http://dx.doi.org/10.5772/65753

Abstract

The reserves of the petroleum-based fuels are directly correlated with the increasing demand of human mankind for energy production. With the growing world populations, industries, vehicles, and equipment, energy demand leads to the search for the substitute of petroleum fuels, which can cater for the need of people today. Considering the current global economic crisis, the interest in alternative fuels is extremely high. It is known that there is a limited amount of fossil-based fuels as a sustainable energy source. The majority of the energy used today is obtained from the fossil fuels. Due to the continuing increase over the cost of fossil fuels, demands for clean energy have also been increasing. With this increasing demand for energy very soon the petroleum fuels will be depleted so researchers are focusing on to find the ways and means to generate cheap and abundant renewable and clean energy sources. Moving ahead with these plans, hydrogen-enriched compressed natural gas (HCNG) engines have emerged as a future energy carrier for an internal combustion engine. Several countries are striving hard to bring down the pollution level by promoting hydrogen-enriched compressed natural gas-fueled vehicles in general by powering heavy vehicles like transportation buses as well as passenger cars. In general, under certain conditions, the indicated thermal efficiency of the HCNG engine is much better than CNG engines without compromising the high level of pollutant emissions. Even so, the hydrogen addition to CNG increases the NO_x emission, due to high heat generated inside combustion chamber. This can be minimized by application of lean-burn combustion or with three-way catalyst.

Keywords: hydrogen enrichment, HCNG, lean-burn combustion, hydrogen generation, combustion

1. Introduction

Many activities had been performed not long ago on the operation of internal combustion engines on gaseous fuels including SI and CI systems. Such type of activities had induced the need to produce engines that can adhere with the latest demanding regulations for cleaner tail-pipe emissions. Natural gas is frequently thought of as the most auspicious alternative fuels for vehicles. Natural gas is a highly abundant fuel compared to petroleum and is usually regarded as the cleanest of the fossil fuels, producing significantly less harmful pollutant such as CO, CO_2, and nonmethane HC emissions than gasoline. On the other hand, by comparing natural gas to diesel, it roughly filters the very fine particles called as particulate matter. Natural gas contains high hydrogen carbon ratio and a high research octane number (RON) which prompts the exhaust to be cleansed and permits for high antiknocking properties. The availability of hydrogen as an element is ample on earth and is frequently considered as the standard optional fuel in future. However, the present available facility is not able to use hydrogen as a massive fuel efficiently. With regard to enhance the importance of hydrogen soon, hydrogen can be mixed with natural gas to be used in ICE engines. This new fuel is known as HCNG, or hythane, which can be used vigorously for transportation in the upcoming time.

Along with the experimental research of the HCNG engines, numerical simulations of the combustion process have been evaluated by many researchers in past three decade. This chapter mainly focuses on simulation of combustion mechanism of the HCNG and comparison with the experimental results, improvements on laminar burning velocity, and types of numerical model used for predicting the combustion behavior of the hydrogen-enriched compressed natural gas.

2. Background

The research on hydrogen-natural gas blends as IC engine fuel is not new. Natural gas-hydrogen mixtures have been used in test engines dating back to as early as 1983. The experiments performed with an AVL engine fueled by 100% CNG + 0% H_2, 80% CNG + 20% H_2, 50% CNG + 50% H_2, 0% CNG + 100% H_2 by Nagalingam et al. [1].

In the year 1989, at Colorado State University (Hythane Company, LLC, 2007), HCI (Hydrogen Components, Inc.) started testing different blending ratios of H_2 and natural gas. The patented blend of hydrogen and CNG was popularly given the name of ‘Hythane’ by Hydrogen Components, Inc., in Littleton, Colorado. With the reference of US Patient #5,139,002 (Lynch and Marmaro 1992), the invention of ‘Hythane$^{®}$’ was done by Frank Lynch and Roger Marmaro, and in 1992, it was given a US patient. Here, hythane contains a blend of 15% hydrogen and 85% CNG, and it was used as a fuel for IC engines without any major modifications in the engine. The first hythane station was commenced in 1992. After that, many engines were manufactured and tested for using this new fuel, in order to understand the more significant features of HCNG fuel. Still, the research is going on the areas related to spark timing, blend ratio, and excess air ratio.

3. Merits

Hydrogen addition to compressed natural gas (CNG) for use as a fuel in an internal combustion engine is an impressive way to improve the burning velocity, with a laminar burning velocity of 2.9 m/s for H_2 verses a laminar burning velocity of 0.38 m/s for CH_4, which is the constituent of the natural gas. It can increase the cycle-by-cycle variations (CCV) due to comparatively below par lean-burn capabilities of the natural gas engine. Hydrogen contains rapid combustion speed, a large combustion limit, and low ignition energy. All these unique properties of the hydrogen can lower the exhaust emissions of the fuel, especially the methane and CO emissions. The fuel economy and thermal efficiency of an engine can be improvised by hydrogen enrichment. The thermal efficiency of HCNG is covered in more detail in a research paper presented by Ma et al. [2].

Hydrogen-enriched compressed natural gas enables the use of hydrogen at an initial phase while utilizing support of the existing CNG system. Due to all these steps, the hydrogen infrastructure will be established, but meanwhile this process will take time till the generation and efficiency demands of the hydrogen can be met in an economical manner. The ideas and innovations involved in the research of the HCNG engines definitely are helpful for hydrogen engine research. The HCNG can allow to neglect bottlenecks coupled with evaporative emissions and cold-start enrichment, which is generally seen in gasoline engines.

4. Obstacles involved in HCNG as a fuel

Few new challenges are involved in the usage of the $H_2 + CH_4$ gas blend as a fuel. A major and vital challenge using HCNG as a fuel for internal combustion engines is to lessen the perfect H_2/CH_4 blend ratio. Whenever the percentage of hydrogen increases in the natural gas at a particular level, abnormal combustion such as pre-ignition, knocking, and back-fire, difficulty will take place until the ignition timing and A/F ratio are fully regulated. The reason behind this phenomenon is the exceptionally higher burning velocity of hydrogen and its low quench distance, which leads to the combustion cylinder walls to be hotter. The higher heat loss from the cooling water is also observed. As the hydrogen fraction increases into CNG, the lean operation limit shifted positive side, and the maximum brake torque (MBT) degrades, which leads to the meaningful fact that there exits relationship between hydrogen fraction, ignition timing, and excess air ratio. Hence, searching the optimum set of hydrogen fraction, ignition timing, and excess air ratio along with the other parameters that can be optimized is a typical challenge.

The addition of H_2 has the opposite effect on the hydrocarbon emissions, so it is necessary to compromise at a hydrogen ratio for which the NO_x and hydrocarbon emissions are equally low. The emissions values of any fuels are probably the most important factor in determining whether or not the fuel is suitable as an alternative. However, the NO_x emissions for CNG are already extremely low compared to other traditional fuels like gasoline and diesel, but the addition of hydrogen causes increased NO_x emissions, which is not tolerable. Nowadays, emission control agencies of various countries are presenting more and more strict policies, so this is a challenge for all automobile manufacturing industries that they should more focus toward clean fuel like HCNG.

5. Hydrogen generation essential for HCNG adoption

Hydrogen production at low cost is the challenging task for present researchers. However, there are various advancements in existent technologies, and some new technologies are also on the platform for the production of hydrogen. Here, we sort out the hydrogen production methods into three subcategory, that is, hydrogen generation from fossil fuels, renewable sources of energy, and from biomass gasification. For future perspective, if existent CNG infrastructure will be replaced by HCNG ones, we need to generate more hydrogen at a reduced cost.

Technology	Merits	Demerits
Partial oxidation	Diminished desulfurization requirement, no catalyst requirement, high operating temperatures, low methane slip	Low H_2/CO ratio obtained Higher operation temperatures Complex handling process
Autothermal reforming	Lower process temperature than partial oxidation, low methane slip	Limited commercial experience Air/O_2 requirement
Steam reforming	Most developed industrial process, No O_2 requirement, lowest operating temperature, best H_2/CO ratio obtained	Highest air emissions

Table 1. A Comparison of fossil fuel reforming technology (modified from Ref. [3]).

The benefits and challenges to yield hydrogen and the methods are described in **Table 1**. At the end of the reforming process H_2, CO and CO_2 are protruded. For the smooth completion of the steam reforming process, it requires an external heat source but does not any demand of oxygen for the process. It has a less operating temperature and greater H_2/CO ratio than partial oxidation and autothermal reforming. Hydrocarbons are partially oxidized with O_2 to generate hydrogen. Partial oxidation (combustion) reaction is considered as the supreme source of energy to run this entire process. There is no catalyst required for this process, and it is more sulfur patient as compared to steam and autothermal reforming. The pressure requirement for the autothermal reforming is less than partial oxidation. There is no external energy required for partial oxidation and autothermal reforming. The complexity and expense of the system increase each of above processes, which require pure oxygen. As compared to the other reforming process technologies for fossil fuels, steam reforming is less costly and most common method to generate oxygen [3].

The characteristic of coal by gasification was examined under the experimental condition limit, which is the temperature at 650–800°C, pressure at 23–27 MPa, and rate of flow 3–7 kg/h. As a catalyst, K_2CO_3 and Raney-Ni and H_2O_2 as oxidant were used. The important effects of key operation parameters like temperature, pressure, flow rate, oxidant, catalyst, and concentration of coal slurry upon gasification were investigated. They found from their experiments that the high temperature condition is favorable for the gasification of coal in supercritical water, but the pressure has no meaningful effect on the result of gasification, and flow rate influences some gasification results, in pursuance of the experimental condition optimal rate of flow should be selected. Also, they included that K_2CO_3 gives good catalytic effect as compared to Raney-Ni. The gasification efficiency and hydrogen gasification efficiency increase with the advancement of concentration of coal slurry, whereas carbon gasification efficiency decreases. Freni et al. [4] have carried out experiments and have described that the syn-gas production from natural gas, by both partial oxidation and autothermal processes, has been reviewed. The steam reforming reaction process produces hydrogen from methane (CH_4) that gives higher hydrogen to carbon monoxide ratio close to 3. Continuous heat supply is required for these reactions because of its strong endothermicity. Without using great amount of energy, partial oxidation and autothermal process are good option for producing hydrogen also if less ratio of H_2/CO (2–3) is achieved. Moreover, smaller reactors or high continuity is present and possible, because the partial oxidation is faster than catalytic methane reaction with steam (SRM). Steam reforming reactors sharply work at contact time ≈1 s, whereas partial oxidation can be lower than 10^{-2} [5].

There are various types of renewable energy sources, such as geothermal, solar, wind, from which we can produce hydrogen. Tolga Balta et al. [6] discussed hydrogen generation methods powered by geothermal sources. In this case study, a high temperature electrolysis (HTE) process compound with and based on geothermal source is considered. They found that HTE system consumes 3.34 kWh_e at 230°C and produces 573 mol/s H_2. The overall system is obtained to be 87 and 86% efficiencies of energetic and exergetic, respectively. Kanoglu et al. [7] developed four models for the use of geothermal energy source for hydrogen yielding; they used geothermal output as input for the electrolysis process (EP): in Case 1, part of heat from geothermal for producing work for EP; in Case 2, part of heat from geothermal in an EP to preheat H_2O; in Case 3, heat from geothermal to preheat water in a high temperature EP and using a portion of geothermal work for electrolysis; and the left portion for liquefaction in Case 4. The results explain that when the geothermal water temperature increases, the percentage of hydrogen generation increases. Moreover, 1.34 g of H_2 may be generated by 1 kg of geothermal water at 200°C in a reversible operation for Case 1, and 1.42, 1.91 and 1.22 are corresponding values for Cases 2, 3, and 4. They compared also in the reversible and irreversible situations display that the second-law efficiencies of models are 28.5, 29.9, 37.2, and 16.1% in Case 1, Case 2, Case 3, and Case 4, respectively.

The gasification means the conversion of the biomass into a highly inflammable gas mixture by the partial oxidation of biomass at very high temperatures rages of 800–900°C. The whole process effectuates partial oxidation to transform carbonaceous feed stock gaseous energy conveyer take part of permanent, noncondensable gas mixture (CO, CO_2, CH_4, H_2, and H_2O). Basically in ideal gasification process, biomass transforms well enough to CO and hydrogen [8]. A most general known biomass resource is palm shell oil, and Cohce et al. [9] during his experimental investigations had studied the thermodynamic properties of the gasification process, which was followed by the SMR (steam methane reforming) and the various reactions involved in the process. During his experimental investigation made by a simulation tool, observations revealed regarding H_2 production using thermochemical biomass gasification using energy and exergy methods. Focus was also laid on evaluating the efficiency of H_2 generation from biomass. The moderateness of the H_2 generation from biomass and a crucial ability of biomass as a renewable energy source have been get through by considering two methods: (1) the heat expected for steam CH_4 reforming is supplied by fractioned syn-gas and (2) the steam methane reformer combustion reactor with externally supplied CH_4 gas. For the direct gasification process, a BCL-type low temperature indirectly heated steam gasifier is investigated. The simulation results show that on the basis of performance improvements, second case has higher energy and exergy efficiencies than first case.

The largest sources of organic waste are our houses, for example, food waste, lawn clippings, and also add the animal- and plant-based material and degradable carbon such as paper timber. Nielsen et al. [10] demonstrated pure hydrogen extraction from fermentation of waste from houses using anaerobic bacterial flora in a mixed form. The experiment was simulated in a bioreactor where 600 g waste from house was fermented. The bioreactor was continuously sprayed with gas N_2 at 3 ml/min and enters in from lower part. They found that throughout this study about 85–90% of the H_2 was separated by Pd/Ag membrane and also observed that ZnO did not expunction meaningful quantity of H_2.

Wu et al. [11] have done their experiments on waste wood gasification and were performed with scale gasification. They investigated the main factors on which hydrogen production depends in the noncatalytic process and catalytic process. The temperature influences the process involved; thus, it is indicated as most important factor of this experimental study and authors concluded that pure H_2 can be obtain from biomass of wood waste through high temperature gasification and reforming techniques. The synthesis gas (54% hydrogen yield by volume) obtains from feedstock at 950°C without a catalyst was reported. Use of catalyst like commercial steam reforming Ni catalyst improves the hydrogen yield at 750°C.

6. Fundamental properties of HCNG

There is a one impressive and very effective way to mix CNG with the fuel holds fast burning velocity. The high flame burning velocity and wide range of flammability limits in air make hydrogen the best gaseous option for CNG. The combination is anticipated to raise the lean-burn capability characteristic and lower the harmful engine's tail pipe emissions [12, 13]. **Table 2** lists few properties of hydrogen compared to CNG (methane) and gasoline. It is clearly observed that hydrogen and CNG have a similar combustion property. Hydrogen utilization in spark ignition engines as a charge gives significant improvements in the overall performance. The mixture of hydrogen and air has higher self-ignition temperature as compared to the different fuels; therefore, the presence of hydrogen creates an antiknock quality of fuel along with higher ignition temperature and lower flame luminosity, which makes it as a safe and clean fuel in comparison with the other conventional fuels [14]. A fusion of the little amount of hydrogen with air induced a flammable mixture, which can be fired in a combustion chamber of a conventional SI engine at below the lean combustion limit of gasoline/air mixture. The combustion of this highly lean mixture lowers the flame temperature and results directly to less heat transfer to the cylinder walls, higher the engine thermal efficiency, lower is the oxides of nitrogen exhaust emissions.

Fuel	**CNG**	**H_2**
Molecular weight	16.04	2.02
Equivalence ratio ignition lower limit in NTP air	0.1	0.53
Flammability limits	5~15	4~75
Minimum ignition energy (mJ)	0.29	0.02
Ignition temperature	918	858
Mass lower heating value (kJ/Kg)	119,930	50,000
Density of gas NTP (kg/m^3)	0.083764	0.65119
Quenching gap in NTP air (cm/s)	0.203	0.064
Percentage of thermal energy radiated	23–33	17–25
Diffusivity in air (cm^2/s)	0.2	0.63
Quality LHV	50.03	120
Volume LHV	35.37	10.805
Octane number	107.5	>130
Adiabatic index	1.315	1.142
Volumetric lower heating value at NTP (kJ/m^3)	10,046	32,573
Stoichiometric air-to-fuel ratio	34.20	17.19
Volumetric fraction of fuel in air, $\lambda = 1$	0.290	0.095
Volumetric lower heating value at NTP (KJ/m^3)	10,046	32,573
Stoichiometric air-to-fuel ratio	34.20	17.19
Volumetric fraction of fuel in air, $\lambda = 1$	0.290	0.095
Volumetric lower heating value in air, $\lambda = 1$	2913	3088
Burning speed in NTP air (cm/s)	265–325	37–45

Note: NTP denotes normal temperature (293.15 K) and pressure (1 atm).

Table 2. Properties of H_2 compared with methane (CH_4).

The laminar burning velocity of the hydrogen/air mixture is about six times as compared to the gasoline/air. This high laminar burning velocity of the hydrogen resulted that the actual indicator diagram shifted toward near to the ideal indicator diagram and produces the higher thermal efficiency of the engine [15]. Hydrogen has possessed wide variety of flammability limits with flammable mixtures from highly lean $\lambda = 10$ to highly rich $\lambda = 0.14$ ($\varphi = 0.1–7.1$). This provides a wide range of engine power output via changes in the blends excess air ratio. The flammability limits get more widen with improving temperature [16]. The minimum ignition energy of the H_2 + air blends at NTP condition is much lower than that of CH_4 + air and gasoline + air mixtures. Only 0.017 mJ, minimum energy, is required for the combustion of 20–26% hydrogen air mixture. As minimum ignition energy is generally calculated using an electric spark discharge, and it also depends on the gap between two electrodes. The spark gap for the above-quoted data is 0.5 mm. Using a spark electrode gap of 2 mm, the minimum ignition energy required is 0.05 mJ [17]. Methane gas (CH_4) is major part of the compressed natural gas (CNG) having less carbon atoms; therefore, the combustion of CNG is considered to be favorable clean fuel as gasoline and also produces less environmental effect. However, because of its lean-burn capacity and lazy burning velocity, CNG-powered spark ignition engines still have few demerits such as low thermal efficiency, low power output, large cycle by cycle variation, and these all increase specific fuel consumption [18].

Although hydrogen is an alternative fuel with very clean burning characteristics, in spite of having disadvantages like high flame propagation speed and wide flammability range. The weight of hydrogen storage, its complexity, the loss of power associated through the usage of pure hydrogen, and the backfire phenomenon are some of the factors to be thought over. The backfire problem can be solved by adding high percentage of hydrogen to CNG. Hythane is basically a blend of 15% hydrogen and 85% CNG and was patented by Frank Lynch of Hydrogen Components Inc., USA, by its energy content [19]. In many cases, backfire restricts the operating region of the air-fuel mixture on the 'rich' side. With the natural gas addition, stoichiometric mixtures can be run without any other precautions.

Coppens et al. [20] with an all-inclusive error of the laminar burning velocity was obtained to be less than ±0.8% cm/s when hydrogen fraction in the mixture was increased from 0 to 35%. The constant volume bomb with spherically expanding flames has very popular in an estimation of a laminar burning velocity along with the growing flame visualization technology in recent years, due to its enhanced accuracy and its ability of estimating few other flame-associated variables together with Markstein constant [21]. In the past years, laminar burning velocity of HCNG fuel was evaluated by many researchers at different hydrogen fractions (volume fraction $R_H = 0–100\%$) and equivalence ratio ($\varphi = 0.6–1.4$) [20, 22–24]. On the basis of experimental data, Huang et al. [22] proposed an empirical relation, which utilizes the conception of velocity increment. Equation (1) represents the formula of laminar burning velocity at NTP for CH_4 + air mixture

$$S_{l\_CH_4}(\phi) = -150.84\phi^3 + 287.6\phi^2 - 96.327\phi - 1.2924. \quad (1)$$

For hydrogen + air mixture, the following formula is used for calculating laminar burning velocity at NTP

$$S_{l\_H_2}(\phi) = 51.902\phi^3 - 394.46\phi^2 + 835.14\phi - 267.07. \tag{2}$$

And Eq. (3) is defined as the laminar burning velocity increment

$$\frac{\left[S_{L\_HCNG}(\phi) - S_{L\_CH_4}(\phi)\right]}{\left[S_{L\_H_2}(\phi) - S_{L\_CH_4}(\phi)\right]}, \tag{3}$$

where $S_{L\_H_2}(\phi)$ and $S_{L\_CH_4}(\phi)$ are laminar burning velocity of hydrogen and natural gas (methane). Laminar burning velocity of hydrogen and methane can be determined by the following empirical relation:

$$S_L = A(T^0)Y_{F,u}^m \frac{T_u}{T^0}\left(\frac{T_b - T^0}{T_b - T_u}\right)^n \tag{4}$$

$$T^0 = -E / \mathrm{In}\left(-\frac{p}{B}\right) \tag{5}$$

$$A(T^0) = F\exp\left(-\frac{G}{T^0}\right), \tag{6}$$

where $Y_{F,u}$ is a fuel fraction in unburned charge, p is the pressure, and T_u and T_b are temperature of unburned and burned zone. Other unknowns like constants B, E, F, G, m, and n can be calculated by properties of fuel used [25]. The increments of the laminar burning velocity on the basis of hydrogen fraction are shown in **Figure 1**. With the rise of hydrogen fraction, the increment of laminar burning velocity increases exponentially. It is observed by Ma et al. [26], and they proposed the correlation between these two parameters for HCNG (Eq. 7)

$$\frac{\left[S_{L\_HCNG}(\phi) - S_{L\_CH_4}(\phi)\right]}{\left[S_{L\_H_2}(\phi) - S_{L\_CH_4}(\phi)\right]} = 0.00737\exp\left(\frac{x}{20.38}\right) + 0.00334. \tag{7}$$

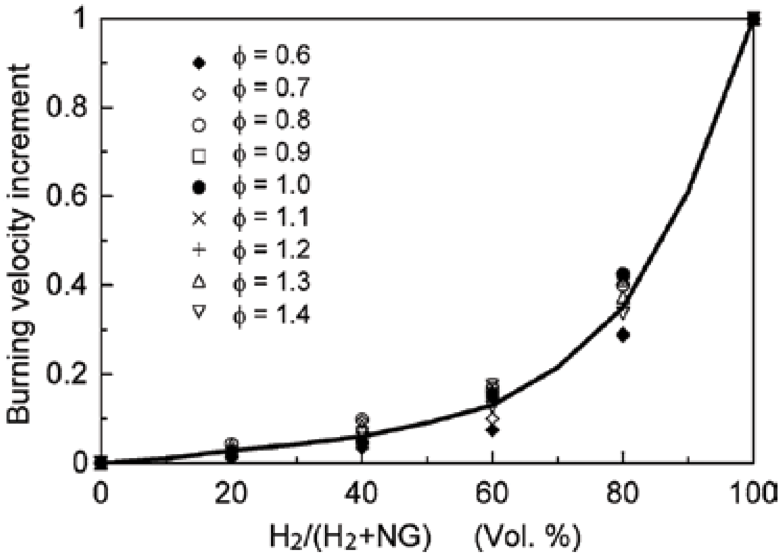

Figure 1. Burning velocity increment versus hydrogen fraction at different equivalence ratios [22].

Hence, the laminar burning velocity at various hydrogen volume percentage and equivalence ratios can be determined by using formula (2), and (7). After proposing Eq. (7), they checked its accuracy. The values determined by formula (Eq. 7) are compared with the experimental data, which are displayed in **Figure 2**, and the comparison is depicted in **Table 3**.

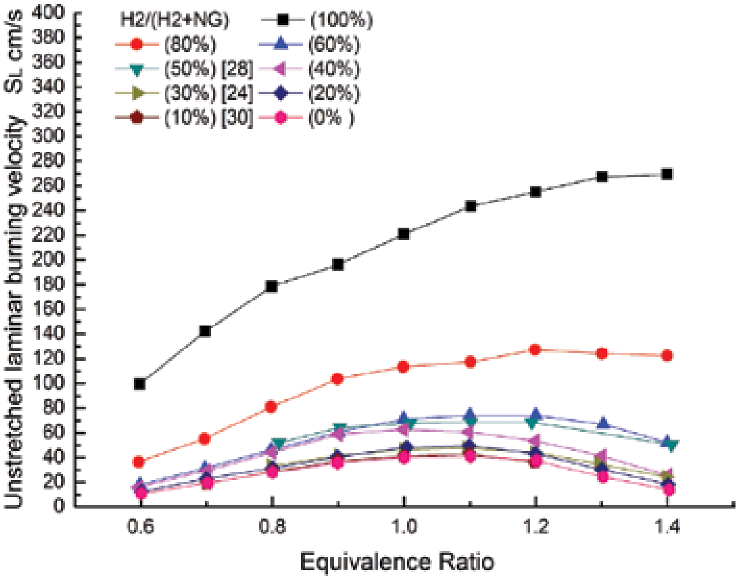

Figure 2. Laminar burning velocity of HCNG versus equivalence ratio [20, 22–24].

Φ	R_H						
	10	**20**	**30**	**40**	**50**	**60**	**80**
0.6		−2.6		2.6		−27.6	−13.7
0.7	11.6	2.6		12.2		−14.6	−12
0.8	−6.2	0.5	0.1	17.6	21.5	−5.1	0.8
0.9	−2.2	3.1	0.4	24.5	23.1	5.4	11.8
1	−4.2	8.5	0.4	20.7	18.4	9.4	9.5
1.1	−3	8.4	−0.1	14.5	15.4	8.1	5.4
1.2	−12.7	1.5	−2.5	8.15	18.4	9.8	11.2
1.3		2.3	6.5	9.2		14.8	12.7
1.4		−7.8	6.8	−6.6	29.8	7.5	16.3

Table 3. Comparison of the experimental value in **Figure 4** with calculated ones from Eq. (7).

From the **Table 3**, it is clearly observed that the experimental data of laminar burning velocity of HCNG are quite close to the determined values at low and high hydrogen fractions (0% < R_H < 60% and 60% < R_H < 100%). Nevertheless, for medium hydrogen fraction (30% < R_H < 60%) condition, it is found that the errors are quite high (>15%). According to procure, a correlation of the laminar burning velocity of HCNG is reasonable at medium and large hydrogen fractions and at various φ. The authors further examined the feasibility of a Le Chatelier's rule-like formula, which is depicted as follows:

$$S_{L\_HCNG}(\phi,x)=\frac{1}{x/S_{L\_H_2}(\phi)+(1-x)/S_{L\_CH_4}(\phi)}. \tag{8}$$

Φ	R_H					
	10	**20**	**30**	**40**	**50**	**80**
0.6		−5.3		−5		−2.9
0.7	−11.4	−3		−0.2		−13.5
0.8	−7.2	−6.8	−12.9	3.5	6.6	−6.7
0.9	−4.2	−5.2	−14.3	9.5	5.7	0.2
1	−6.2	0.8	−14.2	5	0.04	−2.3
1.1	−4.5	1.1	−14	−1.2	−2	−4.2
1.2	−13.2	−5.1	−14.9	−6.4	4.5	7
1.3		2.5	4.3	7.1		28.2
1.4		6	20.2	13.5	47.7	52.9

Table 4. Comparison of the experimental value in **Figure 4** with calculated ones from Eq. (8).

With the similar procedure, they compared the experimental and determined data through Le Chatelier's rule-like formula, and the results are tabulated in **Table 4**. It is observed that the values determined from Formula (8) are agreed with the experimental laminar burning velocity of HCNG at lean and stoichiometric conditions.

Miao et al. [27] studied flame propagation of assorted CNG/H_2/air mixtures in fixed volume combustion chamber under miscellaneous hydrogen volume percentage and equivalence ratios along with miscellaneous initial pressures. The flame stability and their impressing factors like Markstein length, density ratio, and flame thickness were acquired by analyzing flame image at various hydrogen volume percentage, initial pressure, and equivalence ratios. This experimental study concluded that at initial pressure, hydrogen volume percentage and equivalence ratio attempt a combined influence on unstretched laminar burning velocity and mass burning flux of CNG/H_2/air mixtures, and both abruptly increase along with the hydrogen enrichment in the natural gas.

7. Technical approach

Performance plays an important role in the choice of a fuel. HCNG has many advantages when it comes to performance because of the high octane number of hydrogen, and the engine performance generally increases with the addition of hydrogen. Generally, excess air ratio (λ), ignition timing, engine speed, and compression ration influence the performance of the engine greatly.

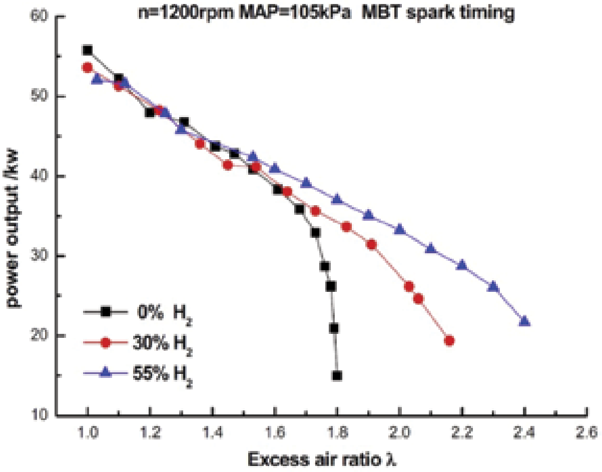

Figure 3. Engine's power performance versus excess air ratio [28].

Ma et al. [28] observed the influence of high volumetric ratio of hydrogen to CNG (55% H_2 + 45% CNG). The performance and emission characteristics were analyzed in a six-cylinder, single-point injection, turbocharged lean-burn natural gas engine. The experimental results revealed that using H_2 at a high volumetric ratio significantly increases in the lean-burn combustion limit and improves thermal efficiency. **Figure 3** shows that high H_2 enrichment to CNG gives high impression to slow down the decline in power. As excess air ratio increases, power output decreases, this is because of injected fuel quality degraded with the increasing λ, and outcome is the reduction in input energy of the engine, in addition. When $\lambda > 1.6$, HCNG gives more power output as CNG. It is shown in **Figure 4** that the mixing of H_2 at a high ratio in CNG significantly improves the lean-burn limit along with the higher thermal efficiency. The same effects have seen in another experimental study of the same the author [29].

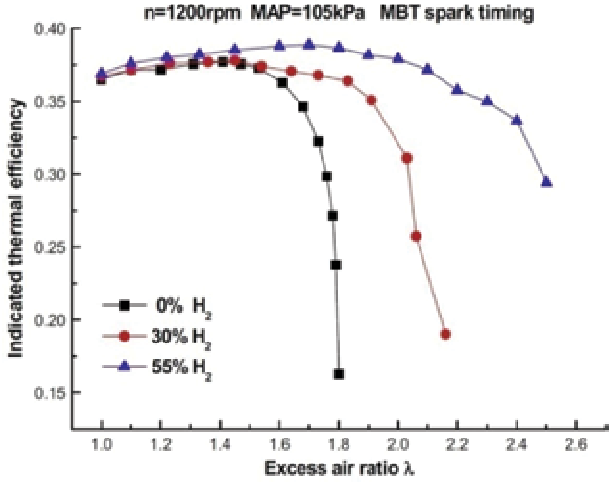

Figure 4. Indicated thermal efficiency versus excess air ratio [28].

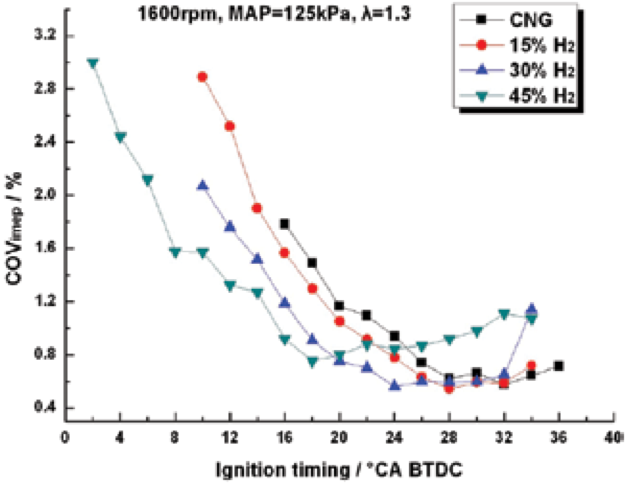

Figure 5. COV in IMEP versus ignition timing for fuel blends with various hydrogen fractions [30].

With respect to study the mechanism of the combustion of any fuel, the cycle-by-cycle variation (CCV) study of engine is very beneficial. It gives the clear picture of maximum pressure and mean effective pressure developed, which affects the power and efficiency of the engine. As discussed already that the COV_{imep} is an important factor to analyze combustion. Ma et al. [30] did experiments for investigating the consequences of addition of hydrogen on the combustion characteristic and CCV in a 6.2-liter, in-line six-cylinder turbocharged SING engine. The ITE and emissions were also analyzed through the series of experiments. They concluded that advancing the spark timing gives improved maximum pressure for used fuel blends. **Figure 5** shows the variation of the COV_{imep} versus ignition timing at different hydrogen fractions. With the increase in the spark advance, the COV_{imep} decreases significantly. Addition of H_2 into NG can lower the COV_{imep} at every spark timing, retarded from maximum brake torque spark timings.

Burning of fuel at lean condition ($\lambda > 1$) provides lower combustion temperature, and it is proved by many researchers that this is a meaningful and beneficial way to reduce NO_x emission, in the case of spark ignition engines only [31, 32]. Various authors have performed their research by adopting constant spark timing condition. But it is not enough information to predict the influence of ignition timing on combustion. Wang et al. [33] studied separately the influence of ignition timing on lean combustion limit through their series of experiments on the HCNG SI engine. The low and moderate engine load, various engine speeds and 0–40% by volume hydrogen fraction condition are adopted for experiments. **Figure 6** illustrates the consequence of ignition timing on lean combustion limit using three different conditions. The lean combustion limit improves with the advance of spark timing, and after reaching maximum value, it shows decreasing trend. This is because of the enough amount of fuel burned in the power stroke instead of near the completion of compression stroke. Moreover, they stated that over-retarded and over-advanced both ignition timings are not appropriate for smooth combustion at lean combustion limit at a particular operating condition.

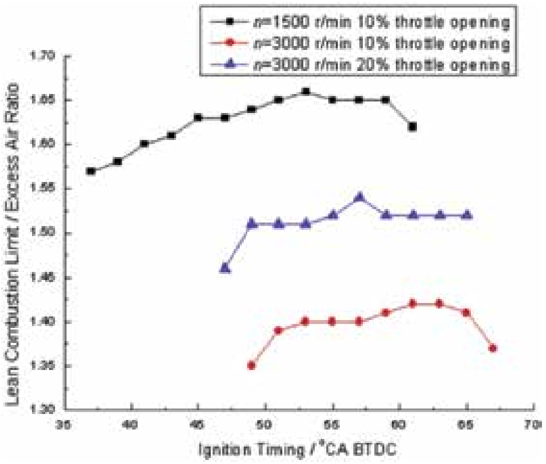

Figure 6. Effect of ignition timing on lean combustion limit [33].

An engines' behavior under idle conditions regarding fuel consumption and emissions is very important. A large part of driving cycle used in regulations like the New European Driving Cycle (NEDC) takes place at idle speed. Furthermore, real driving situations, especially in traffic jam haunted Asian megacities, may contain even more idling percentage. Ma et al. [34] experimentally investigated the effect of the equivalence ratio (φ) and spark advance angle (θ_i) on the idle behavior (engine speed 800 rpm) of the six-cylinder, single-point injection turbocharged hydrogen-fueled SING engine. They stated that with the increase in φ, the value of spark advance angle (θ_i) corresponding to the maximum ITE gradually decreases, whereas the ITE decreases along with an increasing φ. Under the condition of $\varphi \geq 0.6$, The NO_x emission increases with an increasing φ and θ_i. At lower φ and θ_i, COV_{imep} noticeably increases. The maximum cylinder pressure increases along with an increasing φ and θ_i. They reported that the optimum idle conditions (considering COV_{imep}, fuel consumption, emission performance) are $\varphi = 0.4$ and $\theta_i = 18°CA$. These conditions provide the 20% rise in ITE and 5 ppm lowered NO_x emission.

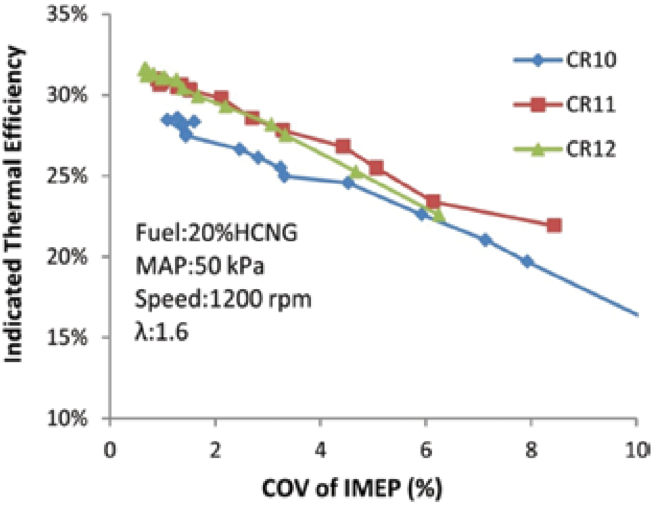

Figure 7. Variation in indicated thermal efficiency with COV of IMEP [35].

Many researchers studied the effects of compression ratio (CR) on the performance and emission characteristic of the hydrogen-enriched CNG engines. Ma et al. [35] investigated the effect of compression ratio (CR) and ignition timing on an in-line, six-cylinder, single-point injection, turbocharged SING engine. The experiments were performed under the condition of varying the ignition time with three different compression ratios of 10, 11, and 12. The engine speed was kept constant at 1200 rpm; excess air ratio was fixed at 1.6, and a constant manifold absolute pressure (MAP) of 50 kPa was selected for the tests. Based on their experimental data, they mentioned that with increasing compression ratio, it could be possible to achieve higher indicated thermal efficiency. The observations of the experimental study show that leading compression ratio gives improved brake torque and less brake-specific fuel consumption and increased peak pressure. It is found that at higher compression ratio, the heat release rate gets faster. As the indicated thermal efficiency increases, the COV of IMEP decreases and increasing CR can lower COV of IMEP as illustrated in **Figure 7**. Also, the rapid combustion period and early flame developments are reduced.

8. Quasi-dimensional combustion models

A quasi-dimensional model (QDM) is very popular to analyze the combustion process of the engine. Quasi-dimensional models have executed more precise results and also have the ability to describe a combustion process more accurately, due to two-zone consideration (unburned and burned) [36]. Ma et al. [26] presented a two-zone quasi-dimensional combustion model for HCNG SI engines with various hydrogen volumetric fractions. A two-zone (burned and unburned) thermodynamic model, turbulent entertainment combustion model, and important thermochemical equation were introduced. Simulation data were examined and compared by experimental data after getting the model constant by calibration for different hydrogen percentage, ignition timings, and equivalence ratios. It is observed that simulation results are quite near to the experimental results for lean conditions. **Figure 8** shows the two-zone combustion chamber for which the two-zone thermodynamic model was presented by assuming some assumptions. The following control equations are derived by the authors of this research paper based on mass and energy conservation law for two-zone thermodynamic models.

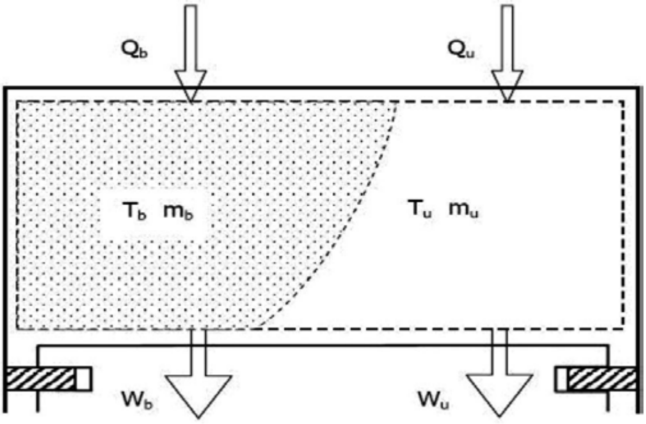

Figure 8. Two-zone combustion chamber [26].

$$\frac{dT_u}{d\theta} = \frac{1}{m_u c_{pu}} \left(V_u \frac{dP}{d\theta} + \frac{dQ_u}{d\theta} \right) \tag{9}$$

$$\begin{aligned}\frac{dT_b}{d\theta} = \frac{1}{m_u c_{pu}} \Bigg[& P\frac{dV}{d\theta} - \left(R_b T_b - R_u T_u\right)\frac{dm_b}{d\theta} \\ & - \frac{R_u}{c_{pu}}\left(V_u \frac{dP}{d\theta} + \frac{dQ_u}{d\theta}\right) + V\frac{dP}{d\theta}\Bigg]\end{aligned} \tag{10}$$

$$\begin{aligned}\frac{dP}{d\theta} = \frac{1}{\frac{c_{vu}}{c_{pu}}V_u - \frac{c_{vb}R_u}{R_b c_{pu}}V_u + \frac{c_{vb}}{R_b}V} & \left\{\left(1+\frac{c_{vb}}{R_b}\right)P\frac{dV}{d\theta}\right. \\ & - \frac{dQ}{d\theta} + \left[\left(u_b - u_u\right) - c_{vb}\left(T_b - \frac{R_u}{R_b}T_u\right)\right]\frac{dm_b}{d\theta} \\ & \left. + \left(\frac{c_{vu}}{c_{pu}} - \frac{c_{vb}}{R_b}\frac{R_u}{c_{pu}}\right)\frac{dQ_u}{d\theta}\right\},\end{aligned} \tag{11}$$

where u and b represent unburned zone and burned, respectively. The charge composition of the each zone is considered to be ideal gas means specific heats are only the function of temperature. The specific heat (molar) at constant pressure is expressed by the equation below

$$C_{p,m} = a_1 + \frac{a_2}{\theta} + \frac{a_3}{\theta^2} + \frac{a_4}{\theta^3} + \frac{a_5}{\theta^4}\left(1200K < T < 6000K\right) \tag{12}$$

$$C_{p,m} = a_6 + a_7\theta + a_6\theta^2 + a_6\theta^3 + a_6\theta^4 (200K < T < 1200K), \tag{13}$$

where θ represented by T/1000 and constants a_1–a_{10} can be determined by Ref. [37]. The specific heat (molar) of the various blend is determined by the following expression.

$$C_{p,m} = \sum C_{p,m,i} X_i, \tag{14}$$

where X_i represents molar fraction of species i. After comparing the simulation and experimental data, authors concluded that the presented two-zone quasi-dimensional model has the capability to conduct a performance simulation of a HCNG SI engine under different hydrogen enrichment ratios.

The fluid flow in the combustion chamber is largely turbulent. The turbulent structure of flame front regulates the combustion process notably. In compliance with the assumptions presented by Blizard, Keck, and various other researchers [38–40], large-scale turbulence is suppose to comprise highly dissipative regions of vortex sheets and the size corresponding to the Kolmogorov scale (η). Their spacing is proposed by the Taylor microscale (L_T) as shown in

Figure 9. L denotes the integral length scale and corresponds to the overall size of the turbulent eddy. Later, this structure was justified by Smith [41]. Daneshyar and Hill [42] conceived that for the spark ignition engine, Taylor microscale (L_T) is very important for the better understanding of the combustion behavior. Their study reveals that chemical reaction completed almost quickly with in the Kolmogorov scale.

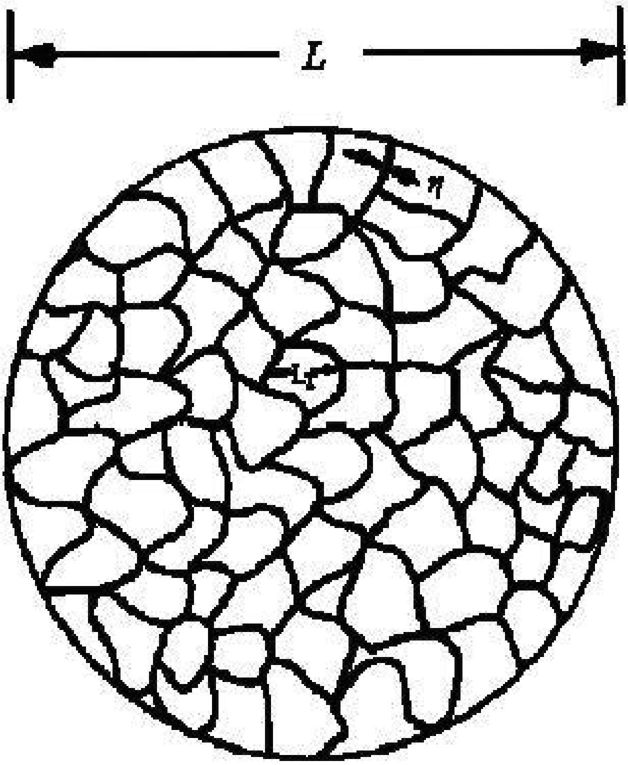

Figure 9. Schematic of the turbulence structure.

The model is presented by the authors of Ref. [26] and following this idea, it presumes as per Refs. [43, 44] that:

1. Ignition happens within the highly dissipative areas (vortex sheets) whose size is described by the Kolmogorov scale.
2. After spark, the ignition sites propagate along the vortex sheets with a velocity of $u' + S_L$ spherically, where u' is denoted by local turbulence intensity.
3. The flame front propagation is considered to be laminar process inside the spacing of the vortex sheets. Therefore, the combustion time span for a small eddy with the size of L_T is $\tau_c = L_T/S_L$.

The following governing equations could be derived by considering the above assumptions:

The rate of the entrainment of the unburned gas is as follows:

$$\frac{dm_e}{dt}=\rho_u A_f\left(S_L+u'\right) \tag{15}$$

In the above equation, m_e is denoted by mass entrained into the flame front; ϱ_u is the density of the gas in the unburned zone; and A_f is the area of the entrainment front.

Once entrained, the unburned gas will be burnt at a rate proportional to the mass of the unburned gas within the entrainment front, which is given by the following:

$$\frac{dm_b}{dt}=(m_e-m_b)/\tau_c \tag{16}$$

$$\tau_c = L_T / S_L, \tag{17}$$

where m_b is the mass burned, τ_c is the characteristic time, and L_T is the Taylor microscale.

By combining Eqs. (15) and (16), we can get the following:

$$\tau_c \frac{d^2 m_b}{dt^2}+\frac{dm_b}{dt}-\frac{dm_e}{dt}=0. \tag{18}$$

Equation (18) provides a burning law model that can be coupled to the thermodynamic, turbulent eddy structure, and the turbulent characteristics, which are correlated to the hydrogen blending ratios and the engine operating conditions. The method of calculating the three turbulence scales is briefly described here:

Integral length scale L:

$$L_0 = C_L \times H \tag{19}$$

$$L = L_0(\rho_{u0} / \rho_u)^{1/3}, \tag{20}$$

where ϱ_u is the density of the gas in the unburned zone, H is the chamber height, and the subscript 0 represents ignition timing. Taylor microscale L_T

$$L_T = 0.8L_{iv}(\rho_{in} / \rho_{u0})^{3/4}, \tag{21}$$

where ϱ_{in} is the density of gas in the intake stroke, and L_{iv} is the lift of the intake valve.

Turbulence intensity u′ is as follows:

$$u_0' = C_u \times C_m \tag{22}$$

$$u' = u'_0 (\rho_{u0} / \rho_u)^{1/3}, \tag{23}$$

where C_m is the mean velocity of piston movement, C_u is a constant, and 0 represents ignition timing. To justify the suggested quasi-dimensional combustion model, experiments below a broad range of functioning state are required. **Table 5** displays the nine operation conditions which are chosen for both experiments and simulation. The limit of nine operating conditions is slightly broad, in which speed (N), manifold absolute pressure (MAP), hydrogen mixture ratio (x), excess air ratio (λ), and spark timing (θ_{ig}) all are modified extensively.

Operational condition	Speed N (r/min)	MAP (kPa)	x (%)	λ	θ_{ig} (BTDC)
X1	1600	70	20	1.3	26
X2	1600	120	20	1.3	26
X3	1600	87	40	1.20	24
X4	1600	65	50	1.25	22
Y1	1200	105	10	1.33	30
Y2	1200	105	30	1.40	30
Y3	1200	105	0	1.63	30
Y4	1200	105	30	1.62	30
Z1	2400	80	0	1.30	32

Table 5. Operating conditions.

The experiments were evaluated on a six-cylinder, single-point injection, spark ignition gas engine. **Figure 10** illustrates the predicted and experimental pressure curves and mass fraction curves at each operating condition. For operating condition H, the predicted and experiment values are quite matched. The divergence in Case H is thought to be due to high cyclic variation and incomplete combustion, which are not considered in the quasi-dimensional model. With regard to make significant observations, more detailed combustion parameters are analyzed, including maximum pressure (P_{max}), the crank angle at which maximum pressure occurs (θp_{max}), rapid combustion duration (θ_{rd}) (10–90% MFB), crank angle of 50% MFB ($\theta_{50\%}$), indicated mean effective pressure (P_i), and P_i's relative error (εp_i), again considering Case H and the differences between the predicted and test outcomes are pretty close. **Table 6** displays the differences between the predicted and experimental results. It can be seen that the P_{maxs} shows error <0.15 MPa; (θp_{max})'s, θ_{rd}'s, and $\theta_{50\%}$'s value is <2°CA; P_i's <6%. The most evident difference appears at Case H, and the equivalence ratio is close to the lean limit.

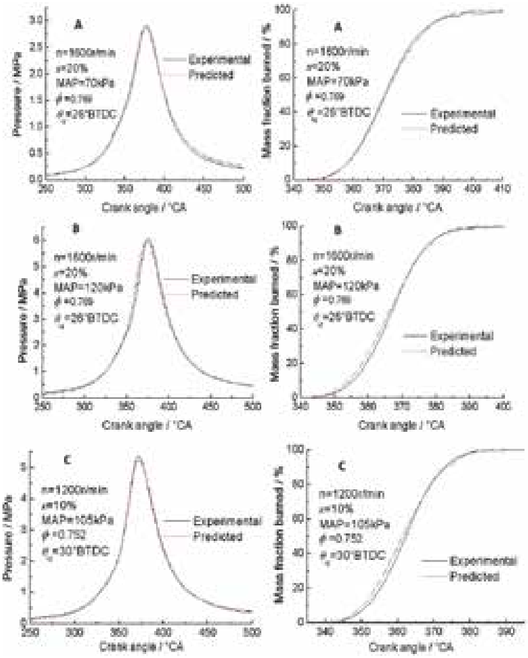

Figure 10. Comparison between experimental pressure, MFB, and predicted ones from the model under nine operating conditions.

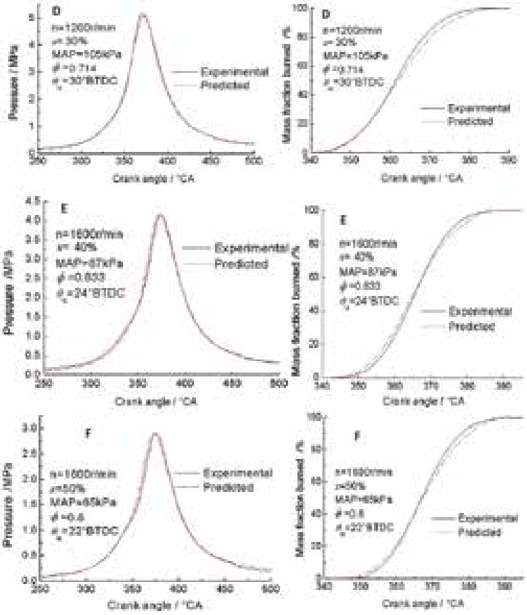

Figure 10. (continued)

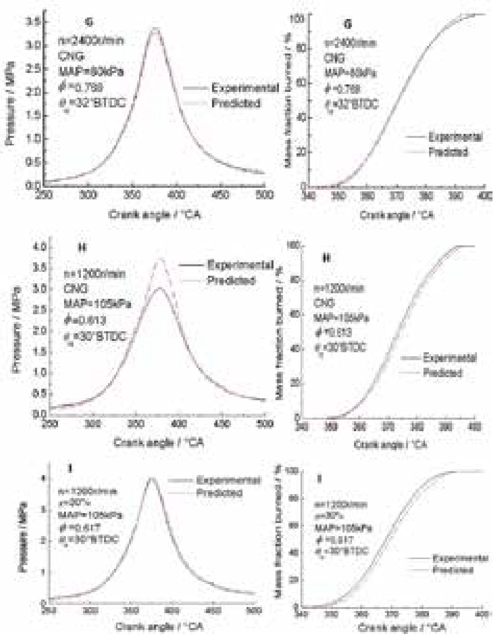

Figure 10. (continued)

Operation condition	P_{max} (MPa)	θp_{max} (°CA)	θ_{cd} (°CA)	$\theta_{50\%}$ (°CA)	P_i (MPa)	εp_i (MPa)
X1 Experimental	2.90	377	26.87	370.42	0.794	3.75
X1 Predicted	2.88	376	27.54	370.85	0.825	
X2 Experimental	6.05	376	22.59	366.84	1.572	2.21
X2 Predicted	6.01	374	24.53	366.19	1.526	
X3 Experimental	3.74	377	23.93	366.99	1.251	1.49
X3 Predicted	3.72	376	25.03	365.74	1.270	
X4 Experimental	5.18	371	21.61	361.41	1.187	2.94
X4 Predicted	5.07	372	23.01	361.97	1.223	
X5 Experimental	4.15	374	21.02	365.49	1.042	0.478
X5 Predicted	4.17	373	23.23	365.12	1.047	
X6 Experimental	2.91	375	20.98	366.90	0.725	3.46
X6 Predicted	2.91	373	24.50	367.29	0.751	
X7 Experimental	3.38	376	28.61	370.21	0.951	1.04
X7 Predicted	3.27	376	28.58	370.70	0.961	
X8 Experimental	3.02	378	26.62	373.21	1.067	6.23
X8 Predicted	3.73	378	27.50	374.38	1.138	
X9 Experimental	3.98	376	25.38	368.10	1.085	2.43
X9 Predicted	4.06	376	26.01	369.45	1.112	

Table 6. Difference between predicted and experimental results.

Basically, factors influencing the simulation accuracy contain two crucial basis: first, few assumption accuracies are not steady with real condition, like chemical reaction, no heat transfer between the burned and unburned zone; second, particular errors exit in the empirical relations determining specific heat, the adiabatic flame temperature, and the laminar burning velocity. These limitations do not get notable errors in this suggested model; furthermore, they should be scrutinized well when considering precision.

Ma et al. [45] developed a fractal-based quasi-dimensional combustion model for turbocharged SI engine works on pure NG and mixtures of NG/H_2. First, they analyzed the effect of MAP, φ, and hydrogen enrichment to NG on fractal dimension and then restructured the expressions of the fractal dimensions. The original and improved two-zone combustion models have compared with the experimental data under various loads, equivalence ratios, engine speeds, and hydrogen fractions. The improved model is very near to the experimental results at the premature combustion stage. In this fractal-based model, a multiplying factor connecting the burned mass density and unburned mass density has been used as follows:

$$\frac{A_T}{A_L} = \frac{S_b}{S_L} = \left(\frac{\rho_b}{\rho_u}\right)^{0.25} \left(\frac{L_{\max}}{L_{\min}}\right)^{D_3-2}, \tag{24}$$

where ϱ_b and ϱ_u are represented by the burned and unburned mass density, and the exponent is set to 0.25, while Matthews and Chin [46] presented the comparison between three assumptions about the ratio of the flame wrinkling scales. They suggested that the reasonable assumption for the correlation between the inner and outer cutoff of the wrinkling scales was the ratio of the integral length scale to the Kolmogorov scale: $L_{max}/L_{min} = l_i/\eta$. They also stated that the following model for D_3 predicted the measured fractal dimensions of flame in combustion engines with as error of <3.6% [47].

$$D_3 = D_{3\max}\frac{u'}{u'+S_L} + 2.0\frac{S_L}{u'+S_L}, D_{3\max} = 2.35, \tag{25}$$

where u′ is denoted by turbulence intensity and S_L is the laminar burning speed. The very similar equation is used by Perini et al. [48] for forecasting of D_3 from with distinct upper limit of D_3.

$$D_3 = D_{3\max}\frac{u'}{u'+S_L} + 2.0\frac{S_L}{u'+S_L}, D_{3\max} = C_{D_3} \times 2.35, \tag{26}$$

where C_{D_3} is the calibration coefficient and is set to 1.013. Equation (35) is proved to be reasonable and acceptable for the combustion simulation of HCNG fuel [48, 49]. As per the fractal analysis results of Ref. [50], the consequence of hydrogen portion in CNG on D_3 is added to Eq. (25) and the following equation is derived.

$$D_3 = D_{3\max} \frac{1}{1+\frac{1}{1+0.1x}\frac{S_L}{u'}} + 2.0\frac{1}{1+\frac{1}{1+0.1x}\frac{u'}{S_L}}, \tag{27}$$

where x is the hydrogen mole fraction in the HCNG. The operational condition for the tests is shown in **Table 7** for which the results of the simulation study were analyzed.

Operation condition	n (r/min)	MAP (kPa)	X	λ	θ_{ig} (BTDC
XA1	1600	70	0	1.3	28
XA2	1600	125	0	1.5	28
XA3	1600	1205	0	1.5	28
XA4	1600	70	0.15	1.3	24
XA5	1600	70	0.15	1.5	28
XA6	1600	125	0.15	1.3	20
XA7	1600	125	0.15	1.5	24
XA8	1600	70	0.3	1.3	28
XA9	1600	125	0.3	1.3	24
XA10	1600	125	0.3	1.1	20
XA11	1600	70	0.45	1.3	26
XA12	1600	70	0.45	1.5	24
XA13	1600	125	0.45	1.3	24
XA14	1600	125	0.45	1.5	22
XA15	1600	125	0.55	1.5	26
XA16	1600	125	0.55	1.3	24
XA17	1600	125	0.45	1.3	24
XB1	800	90	0.3	1.5	20
XC1	1200	110	0.3	1.5	22
XC2	1200	80	0.55	1.3	16
XD1	2000	90	0	1.4	32

Table 7. Difference between predicted and experimental result [45].

9. Demonstration projects

Because of harmful environmental consequences of the exhaust emission of the diesel/ gasoline-fuelled vehicles, several countries are committed to propose strict emission norms. Researchers are more and more focus to actualize the demands of the future's emission regulations. The HCNG engines have a promising technology for city transport system and medium duty vehicles. Last few years, various governments and vehicle manufacturers are providing funds for the HCNG demonstration projects to develop the zero emission vehicles (ZEV). Various HCNG demonstration projects have been performed all around the globe. Generally, the demonstration vehicles fuelled with HCNG blends have been experimented either on the laboratory or on the on road tests [51–58].

Munshi et al. [59] developed two 40-feet-long buses with modified CWI 5.9L B Gas Plus hydrogen-enriched CNG engines for the demonstration project. They compared these two HCNG buses with two CNG buses with similar engines. On road tests and comparison of these, four buses have been performed on the same routes of SunLine Transit Agency in California, Orange County Transit Authority Cycle, and City-Suburban Heavy Vehicle Route. All buses covered the planned 24,000 miles on road test trails on regular routes (see **Figure 11**). They found that after experiments in the laboratory and on road trails, the performance of the HCNG-equipped buses is much better than that of CNG buses with significant reduction in the emissions. **Figure 12** shows HCNG demonstration projects held successfully around the world.

Figure 11. A 40-feet-long transit bus at SunLine Transit Agency with HCNG dispenser [59].

Figure 12. Various demonstration projects all around the world.

10. Conclusion

The hydrogen-enriched compressed natural gas (HCNG) has noteworthy virtues as contrasted with natural gas in terms of performance. As the hydrogen fraction increases by the effect of brake, thermal efficiency also increases. The brake specific fuel consumption is directly proportional to the cycle by cycle variations. Hence, the former is reduced; the latter also reduces, but the thermal efficiency shows increment. There are numerous optimization parameters that can be altered to adjust to the HCNG fuel. The lean operational limit expands with the improvement in hydrogen fraction. This factor maximizes the thermal efficiency and marks down the NO_x pollutants. As the increased amount of intake air introduces in the cylinder at a high excess air ratio, the combustion turns up unstable resulting more unburned hydrocarbon emission from the tailpipe. Consequently, the excess air ratio should be determined by searching the finest feasible combination of NO_x and the HC emissions. One more process to decrease an emission is to shift ignition timing near to the top dead center; in spite of the fact that this is immensely dependent on the excess air ratio. To achieve an increment in the combustion, lean limit and decrement in the HC emission, the ratio of hydrogen can be raised. The greatest obstacle to implementing this promising alternative fuel is to build an infrastructure which can support this.

The future of the HCNG vehicles is bright, and this is shown by the demonstration project, which is presented all around the world in previous years. Nevertheless, hydrogen availability at a reduced cost, its delivery, and storage infrastructure is the challenge for implementing HCNG vehicles.

Author details

Fanhua Ma* and Roopesh Kumar Mehra

*Address all correspondence to: mafh@tsinghua.edu.cn

State Key Laboratory of Automotive Safety and Energy, Tsinghua University, China

References

[1] Nagalingam B, Duebel F, Schmillen K. Performance study using natural gas, hydrogen-supplemented natural gas and hydrogen in AVL research engine. International Journal of Hydrogen Energy. 1983;8(9):715–20.

[2] Ma F, Wang Y, Liu H, Li Y, Wang J, Zhao S. Experimental study on thermal efficiency and emission characteristics of a lean burn hydrogen enriched natural gas engine. International Journal of Hydrogen Energy. 2007;32(18):5067–75.

[3] Holladay JD, Hu J, King DL, Wang Y. An overview of hydrogen production technologies. Catalysis Today. 2009;139(4):244–60.

[4] Freni S, Calogero G, Cavallaro S. Hydrogen production from methane through catalytic partial oxidation reactions. Journal of Power Sources. 2000;87(1):28–38.

[5] Hickman D, Schmidt LD. Synthesis gas formation by direct oxidation of methane over Pt monoliths. Journal of Catalysis. 1992;138(1):267–82.

[6] Balta MT, Dincer I, Hepbasli A. Potential methods for geothermal-based hydrogen production. International Journal of Hydrogen Energy. 2010;35(10):4949–61.

[7] Kanoglu M, Bolatturk A, Yilmaz C. Thermodynamic analysis of models used in hydrogen production by geothermal energy. International Journal of Hydrogen Energy. 2010;35(16):8783–91.

[8] Saxena R, Seal D, Kumar S, Goyal H. Thermo-chemical routes for hydrogen rich gas from biomass: a review. Renewable and Sustainable Energy Reviews. 2008;12(7):1909–27.

[9] Cohce M, Dincer I, Rosen M. Thermodynamic analysis of hydrogen production from biomass gasification. International Journal of Hydrogen Energy. 2010;35(10): 4970–80.

[10] Nielsen AT, Amandusson H, Bjorklund R, Dannetun H, Ejlertsson J, Ekedahl L-G, et al. Hydrogen production from organic waste. International Journal of Hydrogen Energy. 2001;26(6):547–50.

[11] Wu W, Kawamoto K, Kuramochi H. Hydrogen-rich synthesis gas production from waste wood via gasification and reforming technology for fuel cell application. Journal of Material Cycles and Waste Management. 2006;8(1):70–7.

[12] Bell SR, Gupta M. Extension of the lean operating limit for natural gas fueling of a spark ignited engine using hydrogen blending. Combustion Science and Technology. 1997;123(1–6):23–48.

[13] Tunestål P, Christensen M, Einewall P, Johansson B, Jönsson O. Hydrogen addition for improved lean burn capability of slow and fast burning natural gas combustion chambers. SAE Special Publications. 2002;2002(1725):21–32.

[14] Sharma S, Ghoshal SK. Hydrogen the future transportation fuel: from production to applications. Renewable and Sustainable Energy Reviews. 2015;43:1151–8.

[15] Koroll G, Kumar R, Bowles E. Burning velocities of hydrogen-air mixtures. Combustion and Flame. 1993;94(3):330–40.

[16] Schröder V, Holtappels K, editors. Explosion characteristics of hydrogen-air and hydrogen-oxygen mixtures at elevated pressures. In: 2nd International Conference on Hydrogen Safety; 2005.

[17] Ono R, Nifuku M, Fujiwara S, Horiguchi S, Oda T. Minimum ignition energy of hydrogen–air mixture: effects of humidity and spark duration. Journal of Electrostatics. 2007;65(2):87–93.

[18] Khan MI, Yasmin T, Shakoor A. Technical overview of compressed natural gas (CNG) as a transportation fuel. Renewable and Sustainable Energy Reviews. 2015;51:785–97.

[19] Kavathekar K, Rairikar S, Thipse S. Development of a CNG Injection Engine Compliant to Euro-IV Norms and Development Strategy for HCNG Operation. SAE Technical Paper; 2007.

[20] Coppens F, De Ruyck J, Konnov A. Effects of hydrogen enrichment on adiabatic burning velocity and NO formation in methane + air flames. Experimental Thermal and Fluid Science. 2007;31(5):437–44.

[21] Verhelst S, Woolley R, Lawes M, Sierens R. Laminar and unstable burning velocities and Markstein lengths of hydrogen–air mixtures at engine-like conditions. Proceedings of the Combustion Institute. 2005;30(1):209–16.

[22] Huang Z, Zhang Y, Zeng K, Liu B, Wang Q, Jiang D. Measurements of laminar burning velocities for natural gas–hydrogen–air mixtures. Combustion and Flame. 2006;146(1):302–11.

[23] Ilbas M, Crayford A, Yılmaz I, Bowen P, Syred N. Laminar-burning velocities of hydrogen–air and hydrogen-methane-air mixtures: an experimental study. International Journal of Hydrogen Energy. 2006;31(12):1768–79.

[24] Halter F, Chauveau C, Djebaili-Chaumeix N, Gökalp I. Characterization of the effects of pressure and hydrogen concentration on laminar burning velocities of methane-hydrogen-air mixtures. Proceedings of the Combustion Institute. 2005;30(1):201–8.

[25] Ma F, Liu H, Wang Y, Wang J, Ding S, Zhao S. A Quasi-Dimensional Combustion Model for SI Engines Fuelled by Hydrogen Enriched Compressed Natural Gas. SAE Technical Paper; 2008.

[26] Ma F, Wang Y, Wang M, Liu H, Wang J, Ding S, et al. Development and validation of a quasi-dimensional combustion model for SI engines fuelled by HCNG with variable hydrogen fractions. International Journal of Hydrogen Energy. 2008;33(18):4863–75.

[27] Miao H, Jiao Q, Huang Z, Jiang D. Effect of initial pressure on laminar combustion characteristics of hydrogen enriched natural gas. International Journal of Hydrogen Energy. 2008;33(14):3876–85.

[28] Ma F, Wang M, Jiang L, Chen R, Deng J, Naeve N, et al. Performance and emission characteristics of a turbocharged CNG engine fueled by hydrogen-enriched compressed natural gas with high hydrogen ratio. International Journal of Hydrogen Energy. 2010;35(12):6438–47.

[29] Ma F, Wang M, Jiang L, Deng J, Chen R, Naeve N, et al. Performance and emission characteristics of a turbocharged spark-ignition hydrogen-enriched compressed natural gas engine under wide open throttle operating conditions. International Journal of Hydrogen Energy. 2010;35(22):12502–9.

[30] Ma F, Ding S, Wang Y, Wang Y, Wang J, Zhao S. Study on combustion behaviors and cycle-by-cycle variations in a turbocharged lean burn natural gas SI engine with hydrogen enrichment. International Journal of Hydrogen Energy. 2008;33(23):7245–55.

[31] Huang Z, Liu B, Zeng K, Huang Y, Jiang D, Wang X, et al. Experimental study on engine performance and emissions for an engine fueled with natural gas-hydrogen mixtures. Energy and Fuels. 2006;20(5):2131–6.

[32] Kornbluth K, Greenwood J, McCaffrey Z, Vernon D, Erickson P. Extension of the lean limit through hydrogen enrichment of a LFG-fueled spark-ignition engine and emissions reduction. International Journal of Hydrogen Energy. 2010;35(3):1412–9.

[33] Wang X, Zhang H, Yao B, Lei Y, Sun X, Wang D, et al. Experimental study on factors affecting lean combustion limit of SI engine fueled with compressed natural gas and hydrogen blends. Energy. 2012;38(1):58–65.

[34] Ma F, He Y, Deng J, Jiang L, Naeve N, Wang M, et al. Idle characteristics of a hydrogen fueled SI engine. International Journal of Hydrogen Energy. 2011;36(7):4454–60.

[35] Ma F, Li S, Zhao J, Qi Z, Deng J, Naeve N, et al. Effect of compression ratio and spark timing on the power performance and combustion characteristics of an HCNG engine. International Journal of Hydrogen Energy. 2012;37(23):18486–91.

[36] Heywood JB. Internal Combustion Engine Fundamentals. New York: McGraw-Hill; 1988.

[37] Sonntag RE, Van Wylen GJ. Introduction to Thermodynamics: Classical and Statistical. John Wiley & Sons; 1982.

[38] Blizard NC, Keck JC. Experimental and Theoretical Investigation of Turbulent Burning Model for Internal Combustion Engines. SAE Technical Paper; 1974.

[39] Lancaster DR. Effects of Engine Variables on Turbulence in a Spark-Ignition Engine. SAE Technical Paper; 1976.

[40] Tabaczynski RJ, Ferguson CR, Radhakrishnan K. A Turbulent Entrainment Model for Spark-Ignition Engine Combustion. SAE Technical Paper; 1977.

[41] Smith JR. Turbulent Flame Structure in a Homogeneous-Charge Engine. SAE Technical Paper; 1982.

[42] Daneshyar H, Hill P. The structure of small-scale turbulence and its effect on combustion in spark ignition engines. Progress in Energy and Combustion Science. 1987;13(1): 47–73.

[43] Tabaczynski RJ, Trinker FH, Shannon BA. Further refinement and validation of a turbulent flame propagation model for spark-ignition engines. Combustion and Flame. 1980;39(2):111–21.

[44] Wahiduzzaman S, Moral T, Sheard S. Comparison of Measured and Predicted Combustion Characteristics of a Four-Valve SI Engine. SAE Technical Paper; 1993.

[45] Ma F, Li S, Zhao J, Qi Z, Deng J, Naeve N, et al. A fractal-based quasi-dimensional combustion model for SI engines fuelled by hydrogen enriched compressed natural gas. International Journal of Hydrogen Energy. 2012;37(12):9892–901.

[46] Matthews RD, Chin Y-W. A Fractal-Based SI Engine Model: Comparisons of Predictions with Experimental Data. SAE Technical Paper; 1991.

[47] CHIN Y-W, Matthews RD, Nichols SP, Kiehne TM. Use of fractal geometry to model turbulent combustion in SI engines. Combustion Science and Technology. 1992;86(1–6):1–30.

[48] Perini F, Paltrinieri F, Mattarelli E. A quasi-dimensional combustion model for performance and emissions of SI engines running on hydrogen-methane blends. International Journal of Hydrogen Energy. 2010;35(10):4687–701.

[49] Verhelst S, Sierens R. A quasi-dimensional model for the power cycle of a hydrogen-fuelled ICE. International Journal of Hydrogen Energy. 2007;32(15):3545–54.

[50] Cohé C, Halter F, Chauveau C, Gökalp I, Gülder ÖL. Fractal characterisation of high-pressure and hydrogen-enriched CH 4–air turbulent premixed flames. Proceedings of the Combustion Institute. 2007;31(1):1345–52.

[51] Burke A, McCaffrey Z, Miller M, Collier K, Mulligan N. Hydrogen Bus Technology Validation Program. Institute of Transportation Studies; 2005.

[52] Dalhuijsen W, Bosma H, Merts M, Buning L. Internal Combustion Engine Vehicle: Emissions and Performance Using Blends of Natural Gas and Hydrogen. SAE Technical Paper; 2007.

[53] Munshi S, Gourley D, editors. HCNG engine powered transit buses operating on waste hydrogen. In: The NHA Annual Hydrogen Conference 2008; 2008.

[54] Eichlseder H, Klell M, Schaffer K, Leitner D, Sartory M. Potential of Synergies in a Vehicle for Variable Mixtures of CNG and Hydrogen. SAE Paper; 2009.

[55] Khatri D, Singh V, Pal N, Maheshwari M, Singh S, Chug S, et al. HCNG Evaluation Using a Sequential Gas Injection System for a Passenger Car. SAE Technical Paper; 2009.

[56] Unich A, Morrone B, Mariani A, Prati M. The Impact of Natural Gas-Hydrogen Blends on Internal Combustion Engines Performance and Emissions. SAE Technical Paper; 2009.

[57] Genovese A, Contrisciani N, Ortenzi F, Cazzola V. On road experimental tests of hydrogen/natural gas blends on transit buses. International Journal of Hydrogen Energy. 2011;36(2):1775–83.

[58] GRHYD Demonstration Project. www.engie.com. 2013.

[59] Munshi S, Nedelcu C, Harris J, Edwards T, Williams J, Lynch F, et al. Hydrogen Blended Natural Gas Operation of a Heavy Duty Turbocharged Lean Burn Spark Ignition Engine. SAE Technical Paper; 2004.

Chapter 2

Harvesting Green Energy from Blue Ocean in Taiwan: Patent Mapping and Regulation Analyzing

Jui-Chu Lin and Wei-Ming Chen

Additional information is available at the end of the chapter

http://dx.doi.org/10.5772/64889

Abstract

Taiwan is an island with abundant oceanic resources but devoid of resources to significantly utilize ocean power. In fact, the Taiwanese government has initiated several renewable energy policies to transform its energy supply structure from brown (fossil fuel-based) sources of energy to green (renewable-based) energy. In addition, in the 4th National Energy Conference held in 2015, ocean energy was identified as a key contributor to renewable energy source. Therefore, the Taiwanese government proposed the construction of a MW-scale demonstration electricity plant, powered by ocean energy, as promptly as possible. Compared with solar PV, wind, and biomass (waste) energy, the development of ocean energy in Taiwan has lagged behind. Therefore, the aim of this chapter is to boost ocean energy adaptation using analysis from technical and legal perspectives. This chapter first illustrates the ocean energy potential and develop blueprint in Taiwan. Next, through patent research from the Taiwan Patent Search System, this chapter identifies advantageous ocean power technologies innovated by Taiwanese companies, primarily wave and current technologies. Furthermore, through the examination of regulations and competent authorities, this chapter discusses the possible challenges for implementing ocean energy technologies in Taiwan.

Keywords: ocean energy, renewable energy policy, patent mapping, Taiwan

1. Introduction

The oceans cover two-thirds of the Earth's surface and contain abundant available energy sources. In addition to its huge potential as an energy source, ocean energy is also inexhaustible, less polluting, and does not occupy terrestrial space, making it a renewable energy source with great development value. Taiwan is entirely surrounded by seas, with an area of maritime territory approximately 4.72 times that of its land territory [1]. The seas contain a wealth of natural resources, one of which is renewable ocean energy. Taiwan lacks domestic fossil fuel sources and has long been dependent on energy imports. A proper understanding of renewable ocean energy and its advantages followed by effective development of this resource could lead the country to its first step towards energy independence, as well as reduce its reliance on imported fossil fuel [2].

During the concluding session of the 4th National Energy Conference (NEC) held in 2015, developmental conditions of the country's territorial waters were considered before an ultimate goal was set, with the premise of marine environmental protection. The goal was to establish a commercial grade power plant by 2030 and to have a kilowatt (kW) grade demonstration power plant up and running as soon as possible. Separately, Taiwan has created the Sustainable Energy Policy Convention to address both the energy and the environmental challenges that it faces and has implemented energy conservation and carbon emissions reduction plans to reach the policy objective of achieving success in its management of energy sources, environmental protection, and the economy.

At the same time, many projects on the research and development of energy technologies have been planned and implemented, including the Program for the Research, Development, and Promotion of Energy Saving and Carbon Reduction Technologies and the National Energy Program [3]. In addition, pilot demonstration projects have been used as a means to comprehend crucial technologies, so that domestic industries could improve the self-production ratio of power generator units. The success of these projects has also been used to attract operators to invest in and develop related technologies [4].

2. An island with abundant ocean energy potential

The seas surrounding Taiwan hold abundant amounts of ocean energy. In its *White Paper on Technologies for Energy Industries 2014*, the Bureau of Energy (BOE) assessed the country's ocean energy sources and concluded that there is great development potential for power generation using ocean thermal energy conversion (OTE), wave energy, and ocean currents. These are briefly described below [2].

2.1. Currents

Sites for power generation using tidal currents must have potential energy greater than 1 kW/m^2. These sites are distributed in the territorial waters of Penghu (Pescadores Islands) and Northern Taiwan, with an estimated development capacity of nearly 200 MW.

In addition to tidal currents, the Kuroshio Current (black tide) generates an abundant water flow near the south and east coast of Taiwan. Four potential sites were identified based on the condition of a flow velocity greater than 1.2 m/s. The estimated development capacity for each site could reach 1 GW.

2.2. Wave energy

Eight potential sites were selected based on the following criteria: (i) wave energy greater than 10 kW/m, (ii) water shallower than 50 m, (iii) slope of the terrain less than 10%, and (iv) nonrestricted areas. The sites were mainly distributed in the country's northeastern corner and territorial waters of the Yunchang underwater ridge. Wave energy at the ridge was approximately 13.60 kW/m, which ranks second after Cape Santiago/San Diego (15.93 kW/m). The development capacity of Taiwan's wave energy has been estimated at 2.4 GW.

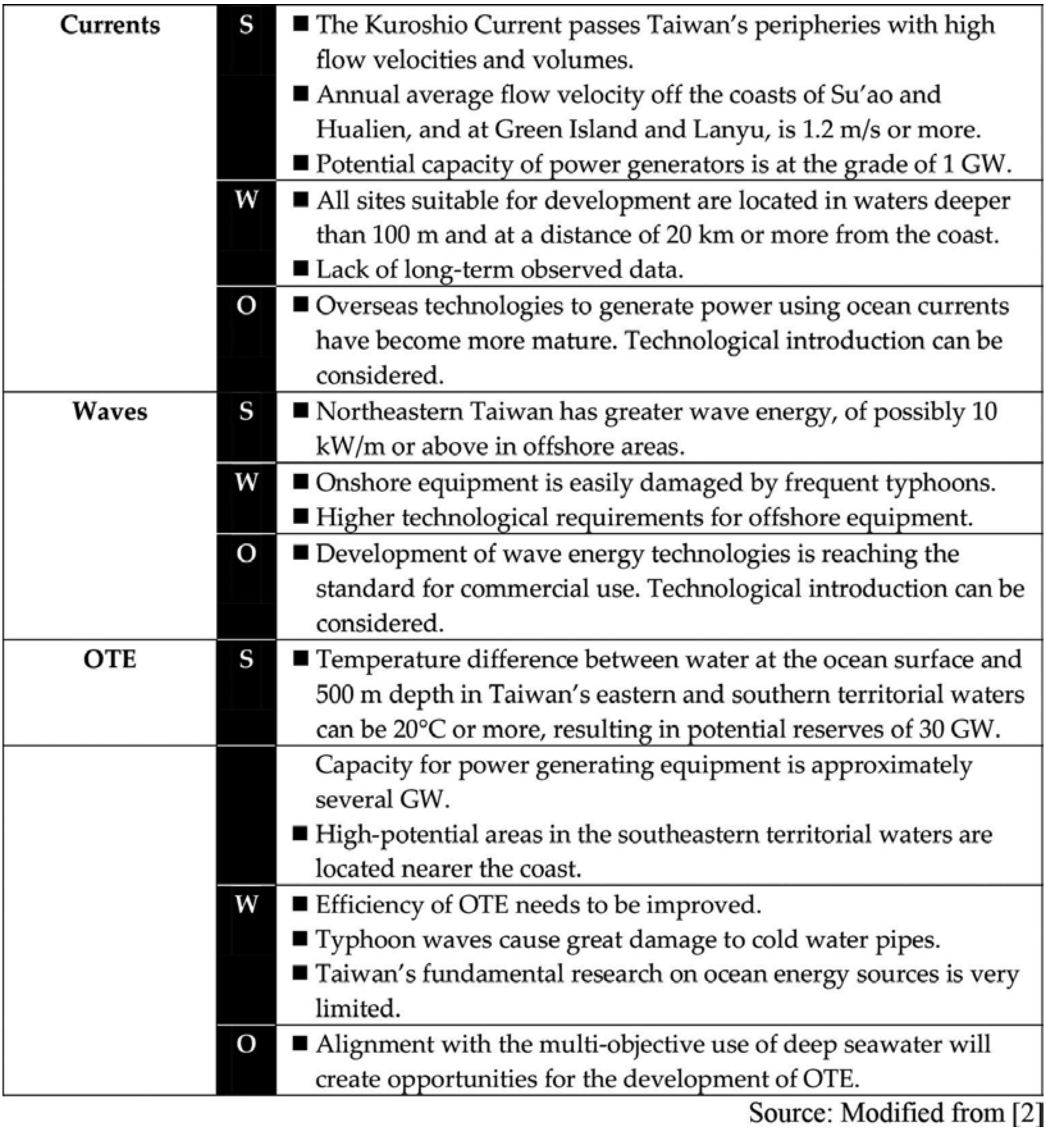

Currents	S	■ The Kuroshio Current passes Taiwan's peripheries with high flow velocities and volumes. ■ Annual average flow velocity off the coasts of Su'ao and Hualien, and at Green Island and Lanyu, is 1.2 m/s or more. ■ Potential capacity of power generators is at the grade of 1 GW.
	W	■ All sites suitable for development are located in waters deeper than 100 m and at a distance of 20 km or more from the coast. ■ Lack of long-term observed data.
	O	■ Overseas technologies to generate power using ocean currents have become more mature. Technological introduction can be considered.
Waves	S	■ Northeastern Taiwan has greater wave energy, of possibly 10 kW/m or above in offshore areas.
	W	■ Onshore equipment is easily damaged by frequent typhoons. ■ Higher technological requirements for offshore equipment.
	O	■ Development of wave energy technologies is reaching the standard for commercial use. Technological introduction can be considered.
OTE	S	■ Temperature difference between water at the ocean surface and 500 m depth in Taiwan's eastern and southern territorial waters can be 20°C or more, resulting in potential reserves of 30 GW.
		Capacity for power generating equipment is approximately several GW. ■ High-potential areas in the southeastern territorial waters are located nearer the coast.
	W	■ Efficiency of OTE needs to be improved. ■ Typhoon waves cause great damage to cold water pipes. ■ Taiwan's fundamental research on ocean energy sources is very limited.
	O	■ Alignment with the multi-objective use of deep seawater will create opportunities for the development of OTE.

Source: Modified from [2]

Table 1. Strengths, weaknesses, and opportunities for ocean energy development.

2.3. Ocean thermal energy (OTE) conversion

Nine potential OTE conversion sites are located in the east of Taiwan, based on the conditions of water shallower than 1000 m and a temperature difference larger than 20°C. Preliminary estimates have indicated that the development capacity of OTE power generation is 2.8 GW.

Table 1 lists the strengths, weaknesses, and opportunities of pursuing ocean energy in Taiwan. The common threats of different marine technologies are the natural limitations, including seafloor topography and climate. Especially, the stratum on the eastern side of Taiwan is slipping; the use of ocean energy faces severe challenges from the natural environment, including earthquakes and typhoons. In addition, the stage of global technology development is also a threat as well, countries that have been involved since the early stages of development have a better grasp of the crucial technologies for energy generation (including ocean currents, tides, waves, OTE, hydrated compounds, etc.). Therefore, it is necessary to in depth analyse Taiwan's advantaged ocean energy technologies, which will be illustrate in Section 4 of this chapter.

3. Blueprint for developing Taiwan's ocean energy

The Taiwanese BOE has not yet to include the ocean energy as a contribution of renewable energy source in the country's short- and medium-term (to 2030) promotion targets since the development of Taiwan's ocean energy technologies is still in the research and development stage (**Table 2**). It can be seen that the development of ocean energy occurs later compared to other renewable energy sources; however, the government drew an ocean energy development blueprint (**Table 3**) and intended to progressively develop ocean energy from the conceptual and verification stage to the development of small- to medium-scale systems, before proceeding to the development phase for large-scale systems and, eventually, commercial power plants [5].

Energy source	**2015**	**2020**	**2025**	**2030**
	Unit: MW			
Onshore wind energy	814	1200	1200	1200
Offshore wind energy	15	320	1520	3000
Hydraulic energy	2059	2100	2150	2200
Solar photovoltaic energy	842	2120	4100	6200
Geothermal energy	4	66	150	200
Biomass energy	745	768	813	950
Total	**4509**	**6574**	**9933**	**13,750**

Source: Ref. [2].

Table 2. Future promotion targets for renewable energy sources in Taiwan.

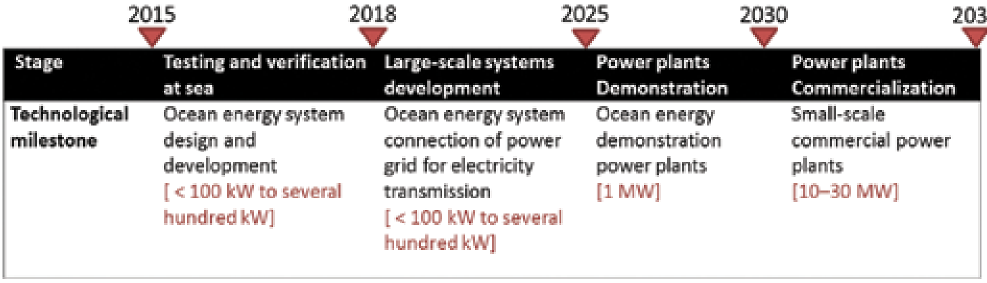

2015 2018 2025 2030 2035

Stage	Testing and verification at sea	Large-scale systems development	Power plants Demonstration	Power plants Commercialization
Technological milestone	Ocean energy system design and development [< 100 kW to several hundred kW]	Ocean energy system connection of power grid for electricity transmission [< 100 kW to several hundred kW]	Ocean energy demonstration power plants [1 MW]	Small-scale commercial power plants [10–30 MW]

Source: Modified from [5]

Table 3. Timeframe for ocean energy development in Taiwan.

In the ocean energy blueprint, the government plans to build a demonstrative wave generator for testing and verification purpose by 2018 and to connect the generator to the grid. Long-term testing and verification will provide the basis for rectifying and improving the design of the generator set, before the development of a commercial set is undertaken. The target is to complete the first 1 MW pilot demonstration plant in 2025 and to develop small-scale commercial power plants (30 MW) by 2030. There will be acceleration towards the full-scale development of commercial power plants by 2035, which will contribute to Taiwan's use of renewable energy sources to generate electricity [5]. However, as the beginning of 2016, the stage still stays on research and development. The plan of sea testing and verification, which was planned to implement by the end of 2015, was delayed because of typhoon.

Research is conducted, and development is fostered through technical cooperation undertaken jointly by academia and industry. The main undertakings are short-term testing at sea of power generators using tidal current. These include projects in the territorial waters of Keelung Sill by National Taiwan Ocean University and at the Penghu Bridge by Sun Yat-sen (Zhongshan) University, as well as the power generator system using ocean currents that was jointly researched and developed by Wanchi Steel Industrial Co., Ltd. and National Cheng Kung University.

4. Patent mapping and analysis

To understand the current development among Taiwan's industries regarding ocean energy technologies, so as to understand the current situation and characteristics of the relevant patents, a patents map is presented for an effective organizational analysis of patents information in this section.

4.1. Patent search and analysis procedures and methodology

The patent search and analysis procedures are as follows: first, to determine the subject; second, to collect and to review the relevant literature and public information; third, to develop patent search strategies and fourth, to draw patent map. The subject is to analyse marine technology development situation in Taiwan. Based on the review of the literature and relevant information, the ocean energy technologies were divided into two categories: (i) an analysis of types of ocean energy sources and (ii) a detailed study of the energy conversion methods used in each type.

As shown in **Table 4**, the types of ocean energy sources can be categorized as follows: (i) tidal energy, (ii) ocean currents, (iii) wave energy, (iv) ocean thermal energy (OTE), and (v) others (combined with wind energy or other sources). Among these categories, ocean currents and wave energy are currently mainstream develop in Taiwan [6–8][1] The energy conversion methods used by these two categories are shown in **Table 5** and can be preliminarily grouped into 15 methods. Thus, when performing the patent search and examining patents, both energy sources and conversion methods were considered so as to improve the degree of accuracy and rate of search returns.

Type	Description
Tidal energy	Potential energy difference between daily tidal fluctuations is used to generate electricity
Ocean currents	Ocean currents are used to drive hydraulic turbines for power generation
Wave energy	Potential energy difference, reciprocating force, or buoyancy difference caused by wave movements are used to generate electricity
OTE	Vaporized working fluid arising from temperature difference between deep and surface layers of seawater is used to drive turbines for power generation
Others	Various technologies are used, such as differences in salinity and auxiliary power from desalination equipment

Table 4. Types of energy sources used by ocean energy technologies.

Method	Description
(*i*) *Wave energy*	
Bellows	Buoys pushed by waves drive the bellows to pump air. The air is stored inside regulated storage barrels and is steadily released to drive the generators
Point absorber	Buoys are used to convert the potential energy difference, reciprocating force, or buoyancy difference caused by up-down movements of waves to mechanical energy. Depending on the installation method, the point absorber is either fixed or floating
Lever	Buoys are connected to a lever, which converts the potential energy difference, reciprocating force, or buoyancy difference caused by up-down movements of waves to mechanical energy

---

[1] The mainstream applications in Taiwan were not clearly stated in any single literature. However, most research papers and national policies were more frequent mentions of power generation using ocean currents and wave energy.

Method	Description
Oscillating wave surge converter	Dampers with reciprocating strokes are used to withstand the kinetic energy and impact of forward and backward movements, which are then converted to mechanical energy
Rotating mass	A mass is installed at an off-center location within the buoys. The up-down and left-right movements of waves cause the mass to rotate within the buoys, thereby generating mechanical energy
Attenuator	Buoys are aligned perpendicular to the waves. The up-down movements of waves cause the buoys to move along the axis. Mechanical energy is generated after applying selective and appropriate restrictions
Bulge wave	This is similar to the wave attenuator method
Oscillating water column	A device with a hollow structure is partially submerged in water with an opening beneath the water level. The hollow structure traps air that is above the water level. When the waves move, the surface of the water column within the device rises and falls, thereby compressing and expanding the internal air column. This drives the turbine and, in turn, the generator to produce electricity. The device is designed in such a way that regardless of air flow direction, the generator will rotate in a similar direction
Overtopping/ terminator device	Waves are used to capture the water reservoir stored between the surface and the depths of the sea. The water is then released with gravity, turning the turbine underneath to generate electricity. This type of device generally uses a collector to gather wave energy
(*ii*) *Ocean currents*	
Enclosed tips (Venturi)	A large conduit with openings is used to collect large amounts of ocean current energy. The highly efficient beam shrinkage effect is used to pass the collected ocean currents through a turbine generator installed within the conduit, which converts them to electrical energy
Horizontal axis turbine	Ocean currents cause underwater turbine blades to rotate, converting the fluid's kinetic energy to mechanical energy. Its unique characteristic is that the direction of the rotation axis is parallel with ocean currents
Vertical axis turbine	Ocean currents cause underwater turbine blades to rotate, converting the fluid's kinetic energy to mechanical energy. Its unique characteristic is that the direction of the rotation axis is perpendicular to ocean currents
Oscillating hydrofoil	This is comprised of a hydrofoil, oscillating boom, and hydraulic device. Tidal flows on both sides of the hydrofoil cause the boom to sway. The oscillating boom causes the high-pressure fluid to flow, driving the turbine inside the high-pressure flow system to generate electricity
Turbine	Large turbines are directly installed at the bottom of the ocean. Currently, this method is often combined with the conduit method
Tidal kite	A turbine is mounted on a submersible buoy, which is submerged below the water surface and installed in the direction of the ocean currents to capture the currents' kinetic energy

Table 5. Energy conversion methods used by ocean energy technologies.

To ensure comprehensiveness and completeness of patent search and analysis, a large-scale search of all relevant patents within the field was conducted using Taiwan's database on patent information.[2] Keywords with general meanings were used for searching, including the Chinese characters for "ocean/marine," "current," "wave," "tidal," "tide," "temperature," "thermal," "converter," "conversion," "salinity," "electricity," and "power generation". The returned results were checked for technical terminologies and natural language used in patents for power generation technologies using ocean energy. The keywords were then redefined for a subsequent search so as to exclude irrelevant patents and improve the rate of return for relevant patents. Other parameters used for the patents search are summarized in **Table 6**.

Parameter	Details
Company	Not specified
Region	Republic of China/Taiwan
Period	1990 to September 11, 2015
Fields	Summary of patent specifications
Browsing and filtering fields	Patent name, summary, diagrams
Language	Chinese
Database	Public database on Taiwan patents
Keywords	Ocean, marine, wave, tidal, tide, current, temperature, thermal, converter, conversion, salinity, electricity, power generation
Syntax	(Ocean OR marine OR wave OR tidal OR tide OR current OR temperature OR thermal OR salinity) @AB AND (power generation) @AB OR (wave AND energy) @AB OR (wave AND conversion) @AB

Table 6. Parameters in search for Taiwan's patents in marine power technologies.

4.2. Life cycle analysis of patented technologies

For the life cycle analysis, the development of patented technologies is divided into the following stages based on the number of patent applications: (i) emerging, (ii) growth, (iii) maturity, and (iv) decline [9]. The actual life cycle (**Figure 1**) is derived by plotting the number of patent applications or number of patentees under publication of application per year against the number of granted patents.

In **Figure 1**, the emerging stage is indicated by the portion of the curve that is gently rising. Willingness of companies to invest in the technology is low, while the number of patent applications and patentees are small. The curve rises sharply during the second stage, in which there is a technological breakthrough or companies have cognition of the technology's market value and compete to invest in its development. Consequently, the number of patent applications and patentees rapidly increase.

---

[2] Taiwan Patent Search System (http://twpat5.tipo.gov.tw/tipotwoc/tipotwkm). Agency: Intellectual Property Office, MOEA. Date of search: September 16, 2015. Scope: (i) granted patents (summary) for 1990 to September 11, 2015; and (ii) publication of applications (summary) for May 1, 2003, to September 11, 2015.

During the third stage, the curve rises upward almost vertically, indicating that companies are no longer investing resources in research and development of the technology. Only a minority continues to develop this type of technology, whereas other companies exhibit a low level of willingness to enter the market. The growth in the number of patent applications and patentees gradually declines. At the fourth stage, the curve bends backwards, indicating the industrial technology has reached a bottleneck that is difficult to break through. Another possibility is that the industry has become over mature; hence, there is negative growth in the number of patent applications and patentees.

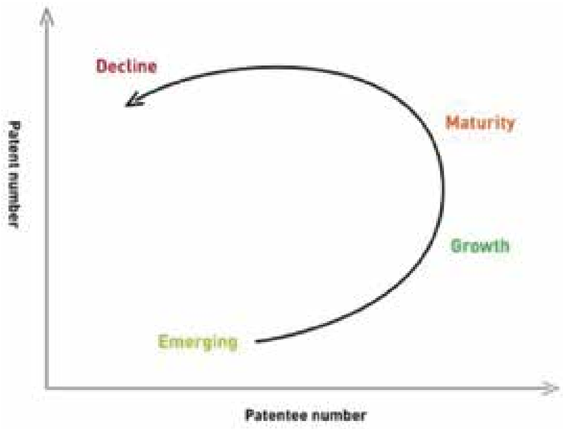

Figure 1. Life cycle of patented technologies [9].

The life cycle of Taiwan's patents in ocean energy technologies according to the year of the grant and the publication of the application are shown in **Figures 2** and **3**, respectively.

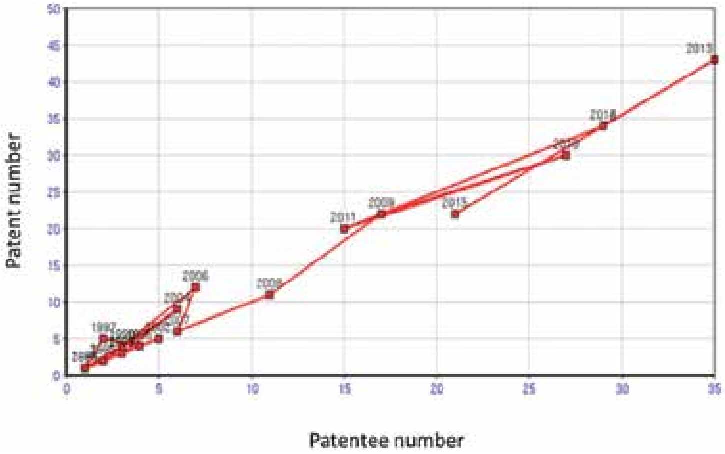

Figure 2. Life cycle of patented technologies for marine power generation according to year of grant.

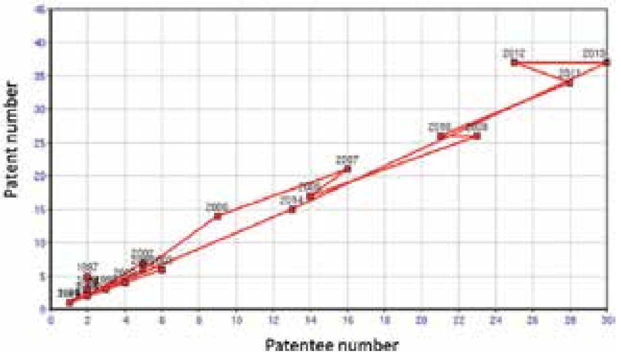

Figure 3. Life cycle of patented technologies for marine power generation according to year of publication of application.

The curves in **Figures 2** and **3** indicate that the development of Taiwan's patented technologies in marine power is moving from gradually to rapidly rising.[3] In other words, the development is between the emerging and the growth stages with considerable development potential.

4.3. Analysis of patented technologies based on annual number of applications

Taiwan's annual number of patent applications for ocean power generation is shown in **Figure 4**. **Figure 4** indicates the annual number of patent applications and granted patents, which have been increasing every year. With increasing awareness of green energy and guidance from government policies, the trends in relating inventions, researches, and development have correspondingly increased. This further proves that there is great development potential for marine power technology in Taiwan.

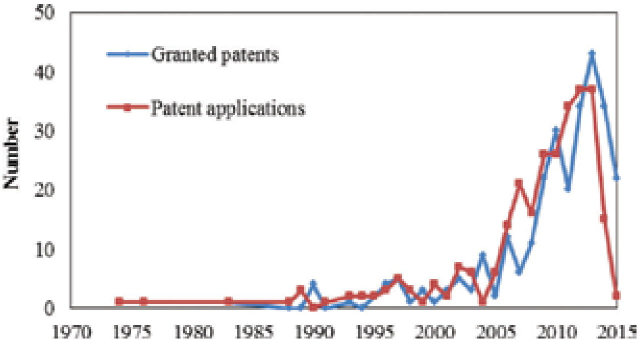

Figure 4. Annual number of patent applications for marine power generation (see Footnote 3).

---

[3] The patent search results showed in **Figures 2–4** include utility model patent and invention patent (not include design patent). Because utility model patent review requires 2–6 months and invention patent review takes 18 months from application to be openly revealed in the patent system, and this patent search was conducted in September 2015. Therefore, the numbers of 2014 and 2015 only include partial cases.

4.4. Nationality analysis of first applicants for patented technologies

The nationalities of the first applicants for Taiwan's patented technologies in marine power generation are shown in **Figure 5**. It can be seen that the relating patents were mostly Taiwanese research and development efforts. There are few foreigners applying for patents in Taiwan, which means they have not been actively applying for relating patents in the country. Such a patent distribution indicates that the Taiwanese have an opportunity to seek crucial technologies from patents in other countries and to adapt these technologies to Taiwan's oceanographic environment. Research and development in this area will facilitate the development of localized technologies for marine power generation.

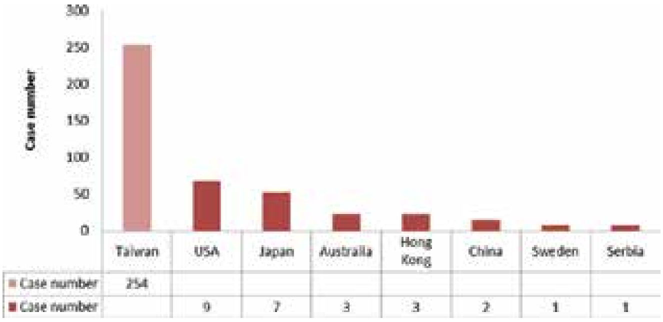

Figure 5. Nationality of first applicants for patents on marine power generation.

4.5. Analysis of patented technologies based on energy source

The patent distribution of different types of ocean energy is shown in **Figure 6**. The majority of patents made use of wave energy, followed by ocean currents. The Kuroshio Current along the east coast of Taiwan is stable while the waves at the territorial waters northwest of Penghu can generate power up to 15–20 kW/m. Thus, the development of relating technologies in Taiwan has capitalized on the unique characteristics of its geographical environment. In

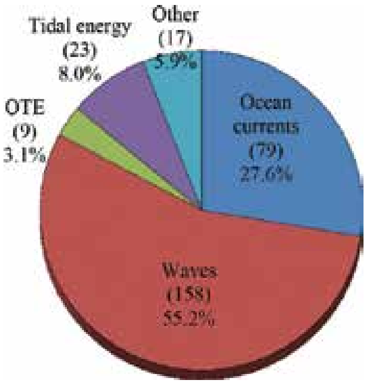

Figure 6. Distribution of patents on marine power generation based on energy source.

contrary, because of Taiwan's relatively short coastline and vast geographical disparities between its east and its west coasts, these features do not facilitate the development of power generation using differences in temperature or salinity [10].

4.6. Analysis of patented technologies based on energy conversion method

Since wave energy and ocean currents are the main types of ocean energy in Taiwan, the methods used for converting the energy supplied by the waves and currents to mechanical energy, which is then converted to electrical energy was identified. Subsequently, the patent distribution was analyzed. Patent summaries and diagrams that made use of wave energy were screened, and the distribution is shown in **Figure 7**.

The largest proportion (33.1%) of methods used the point absorber (both fixed and floating types), followed by the oscillating wave surge converter (18.4%). Other conversion methods accounted for 19.6% and included a combination of wind, tidal, and other forms of energy. There were also patents involving the use of various platforms (ship-like, load-bearing, and matrix) to stabilize the waves or enlarge the energy capture area.

Wave energy basically harnesses the up-down movement of waves. The kinetic energy of waves is converted to electrical energy through a steady-motion mechanism. Currently, the main developmental type used by most countries globally is the point absorber. Considering the conditions of the territorial waters and energy needed for construction, the Taiwanese BOE selected floating point absorber (FPA) as key technology for further development [11].

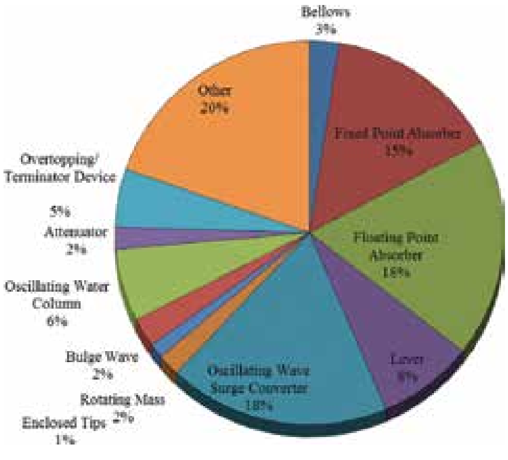

Figure 7. Distribution of patents based on energy conversion methods for wave energy.

The distribution of energy conversion methods for ocean currents is shown in **Figure 8**. The method with the largest proportion (41.8%) involved a spindle with blades, which rotate and drive the power generating device. This method was further separated into radial and axial types (26.6% and 15.2%, respectively). The next highest proportion was the underwater kite (including the addition of a mounted device suspended to face the direction of the ocean currents), which accounted for 15.2%. Although the "other" category totaled 35.4%, this in fact comprised multiple and dispersed types of patents, including the use of friction between ocean currents and metals for electrification, the combination of wind energy and sailboats, and a power generation system using a regulator rectifier module.

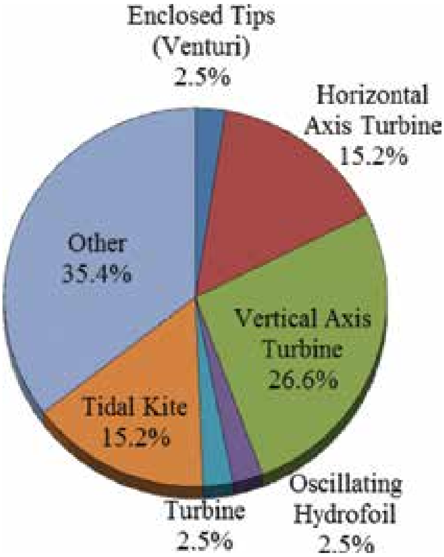

Figure 8. Distributon of patents based on energy conversion methods for ocean currents.

The Kuroshio Current passes the regional seabed off Taiwan's east coast. However, the waters there are very deep, making marine engineering far more difficult compared to power generation using wave energy. The construction and maintenance costs are also much higher. The lack of basic observed data on the Kuroshio Current also means that there is insufficient reliable information. In terms of Taiwanese patents for marine power technologies (**Figure 6**), although the number for power generation using ocean currents ranked second at 27.6%, it is still almost 30% fewer than those using wave energy. Hence, the BOE is studying and planning to build a to-scale ocean current model for Taiwan in order to evaluate the potential use of the Kuroshio Current [7]. The findings will serve as the basis for developing power generation technologies using ocean currents, which will contribute to the planning of a development blueprint.

5. Regulations and comptent authorities

Patent analysis result shows that Taiwan's ocean energy technologies are emerging and growing, especially wave and current technologies. To develop ocean energy technology, the government plays a crucial role in the early stages of development because ocean energy cannot be progressively developed from onshore to offshore, meaning that operators who invest in ocean energy have to bear much higher risks. In addition, legal and regulatory issues are continually cited as a major nontechnical barrier to the development of ocean energy [12]. Consenting is also generally regarded as a major nontechnological barrier to the progress of the marine renewable energy industry due to the complexity of the processes. Numerous licensing authorities, the lack of dedicated legal frameworks of the process, stakeholders for statutory consultation, mandatory EIA and the time scale that would possibly delay the privates entering the market in an early stage [13]. Therefore, to facilitate ocean energy development, this section identifies core issues, relating regulations, and competent authorities.

Figure 9. Core issues of deploying ocean energy based on four stages.

Core issues of ocean energy deployment are identified and listed according to four stages of deployment, i.e., preparation, construction, operation, and decommission (**Figure 9**). In the preparation stage, the operators have to select site, conduct environmental impact assessment, and prepare application documents. In the construction stage, the use of bases and artificial facilities, safety compliance of generator facilities, and grid connection are main issues. In the operation stage, the use of territorial waters and land has to be clarified. In addition, the stakeholders' rights adjustment is a crucial challenge. In fact, the rights issue (especially fishery right) has been raised in Taiwan for offshore wind energy development. In the decommission stage, the facilities decommissioning and electricity business transfer are key issues.

Once the core issues affecting the development of ocean energy industry are defined, the next step is to further examine relating legislation and competent authorities. Basically, legislation related to ocean energy development include Renewable Energy Development Act, Coastal Act, Electricity Act, Electricity Business Registration Rules, Fisheries Act, Environmental Impact Assessment Act, and so forth. Competent authorities of ocean energy are Ministry of

Economic Affairs (MOEA),[4] Ministry of the Interior (MOI), Council of Agriculture (COA), and Municipality or county (city) government. **Table 7** presents six issues and relating legislation and authority, as well as detailed questions for each issue.

Legislation	Competent authority	Issues
i. Application for power facilities construction		
• **Renewable Energy Development Act** • **Electricity Act** • **Electricity Business Registration Rules** • **Coastal Act**	• National: ○ MOEA • Local: ○ Municipality or county (city) government	• It is unclear whether local governments have jurisdiction over matters relating to territorial waters. Hence, it is doubtful that they should be appointed as the competent authority
ii. Use of territorial waters/land		
• **Renewable Energy Development Act** • **Law on the Territorial Sea and Contiguous Zone** • **Law on the Exclusive Economic Zone and Continental Shelf** • **Licensing measures for the construction, use, modification, & demolition of facilities/structures on artificial islands within the exclusive economic zone and continental shelf** • **National Property Act** • **Regional Planning Act** • **Coastal Act** • Ministry of the Interior (MOI) • Is the scope of usable territorial waters similar to that of off-shore wind power generation systems? • Does the central government have overall ownership rights of the territorial waters?		

---

[4] Bureau of Energy is under the Ministry of Economic Affairs

Legislation	Competent authority	Issues
What is the procedure for use of those waters? • Does the perspective of managing state-owned properties apply? Can leasing be arranged? • Are the bases for setting up power generators and equipment treated as facilities/structures on artificial islands?		
iii. Site selection		
• **No related statutes or provisions.** • **Need to consider the natural and social conditions, as well as make relevant changes to the rights holder.** • **Freedom of Government Information Act**	• Relevant authority for application and setting up procedures	• Relevant laws do not include the procedure to select sites for renewable energy power generators and equipment. Operators currently select sites on their own. However, public authorities should intervene, incorporate information disclosure and mechanisms for public participation • Local governments have to work with local self-governing bodies for the survey/assessment of sites
iv. Stakeholders' rights adjustment		
• **Renewable Energy Development Act** • **Fisheries Act** • **Shipping Act**	• Council of Agriculture (COA) • Ministry of Transportation and Communications (MOTC)	• Compensation under Article 29 of the Fisheries Act does not provide for development relating to renewable energy • Compensation is not stipulated under the Shipping Act • Local governments' obligation to assist in coordination between applicants and relevant rights holders is not clearly stipulated

Legislation	Competent authority	Issues
		• Need to compile case studies of successful agreements, with public disclosure of information
v. Safety compliance of offshore structures or generator sets		
• **Licensing measures for the construction, use, modification, and demolition of facilities or structures on artificial islands within the exclusive economic zone and continental shelf** • **Commodity Inspection Act** • **International certification standards**	• MOI • Bureau of Standards, Metrology, and Inspection	• Need to establish certification standards that comply with international technical standards
vi. Environmental impact assessment (EIA)		
• **EIA Act** • **Article 29, Item 1, No. 8 of "Details and scope identification criteria for development activities that shall conduct EIA" are to be implemented.**	• Competent authority for target business • Competent authority for EIAs (may be under the national or local authority, depending on target business)	• The competent authority for the target business of applying for/setting up of ocean energy power generators and equipment should be determined • Specifications for the review of ocean energy EIAs should be established

Table 7. Taiwan's legislation and competent authorities for the ocean energy industry.

6. Conclusion

Taiwan is an island with abundant ocean energy potential. Although ocean energy has not been identified as a contribution to energy supply component in the short- and medium-term (to 2030) promotion targets, the government has drawn a blueprint and set up timeline for ocean energy development.

Presently, Taiwan's patented technologies on ocean energy have passed the emerging and the growth phases. The number of patent applications made each year has been increasing, with the majority of applicants being Taiwanese. Most of the applications have involved the use of wave energy, with the predominant energy conversion method of fixed or floating point absorbers. The BOE has also selected the floating point absorber system as a major development project [11]. This indicates that the government's policies are in line with developments by private industries and that a unified, major investment direction has been established. Therefore, the development of ocean energy in Taiwan has substantial potential.

In addition to reviewing technology development status, identifying technologies with developing opportunities, examining regulations and the relevant competent authorities, the government must also looks to the future and promote the development of industries relating to ocean energy through demonstration projects, policy guidance, incentives, and other strategies (such as joint development with offshore wind energy). In doing so, the abundant ocean energy resources can be tapped, thereby enhancing Taiwan's degree of energy independence and promoting the localization of Taiwan's renewable energy industry.

Acknowledgements

This chapter is supported by the Ministry of Science and Technology (MOST), Taiwan, under National Energy Program Phase II (Grant no. MOST 105-3113-f-011-002). The authors like to acknowledge the enormous support from the members of the Law and Technology Innovation Center at the National Taiwan University of Science and Technology, especially thank Tsung-Ying Hsieh, Chia-Hung Liu, and Yu-Wen Peng.

Author details

Jui-Chu Lin[1] and Wei-Ming Chen[2*]

*Address all correspondence to: kattyouth@gmail.com

1 College of Intellectual Property Studies, National Taiwan University of Science and Technology, Taipei, Taiwan

2 Center for Applied Demography and Survey Research, University of Delaware, Newark, Delaware, USA

References

[1] Shyu CT. Geology of the Soils and Rocks of Taiwan's Mountains [Internet]. 2010. Available from: http://twgeoref.moeacgs.gov.tw/GipOpenWeb/imgAction?f=/2010/20102268/0001.pdf [Accessed: 2016-01-15]

[2] He WJ, editor. White Paper on Technologies for Energy Industry 2014. Taiwan: Ministry of Economic Affairs, Bureau of Energy; 2014. Available from: http://web3.moeaboe.gov.tw/ecw/populace/content/SubMenu.aspx?menu_id=2324 [Accessed: 2016-01-15]

[3] Ministry of Economic Affairs, Bureau of Energy. White Paper on Technologies for Energy Industry 2012. Taiwan: Ministry of Economic Affairs, Bureau of Energy; 2012.

Available from: http://web3.moeaboe.gov.tw/ECW/populace/content/SubMenu.aspx?menu_id=62 [Accessed: 2016-01-15]

[4] Ministry of Economic Affairs, Bureau of Energy. The Concluding Report. In: Proceedings of the 4th National Energy Conference; 26 January 2015; Taipei. Taiwan: Ministry of Economic Affairs, Bureau of Energy; 2015.

[5] Lin TC. Using the Oceans to Generate Power: A Sustainable and Flowing Energy Source that Remains Unexplored. Energy Monthly. 2015; December: 17–21. Available from: http://energymonthly.tier.org.tw/cnt.asp?issue=201512&page=17 [Accessed: 2016-01-15]

[6] Qiu RK. Energy and Sea: Introduction of Domestic Institutions for Marine Research. Energy Monthly. 2003; July: 27–29. Available from: http://energymonthly.tier.org.tw/outdatecontent.asp?ReportIssue=200307&Page=27 [Accessed: 2016-01-15]

[7] Zhang WQ, Yan ZW. Exploration of Domestic Marine Energy Development. Energy Monthly. 2010; August: 5–7. Available from: http://energymonthly.tier.org.tw/outdatecontent.asp?ReportIssue=201008&Page=5 [Accessed: 2016-01-15]

[8] Ministry of Economic Affairs, Bureau of Energy. Developing 20 KW Generating Unit: To Capitalize Marine Energy. Energy Monthly. 2014; October: 2–3. Available from: http://energymonthly.tier.org.tw/outdatecontent.asp?ReportIssue=201410&Page=2[Accessed: 2016-01-15]

[9] Hong YJ. Membrane Electrode Assembly (MEA) for Proton Exchange Membrane Fuel Cells: Patent Map and Patent Analysis. In: Proceedings of International Workshop of Fuel Cells; 22–23 September 2005; Taoyuan. Taoyuan: Yuan Ze University; 2005. Available from: http://goo.gl/BnMP19. [Accessed: 2016-01-15]

[10] Lu SM. Assessment of Developing Wave Energy in Taiwan. Science Development. 2015; 508: 56–59. Available from: http://ejournal.stpi.narl.org.tw/NSC_INDEX/Journal/EJ0001/10404/10404-09.pdf [Accessed: 2016-01-15]

[11] Ministry of Economic Affairs, Bureau of Energy. New Marine Energy: Technology of Floating Point Absorber. Energy Monthly. 2015; July: 8–10. Available from:http://energymonthly.tier.org.tw/outdatecontent.asp?ReportIssue=201507&Page=8 [Accessed: 2016-01-15]

[12] Wright G, O'Hagan AM, de Groot J, Leroy Y, Soininen N, Salcido R, Castelos MA, Jude S, Rochette J, Kerr S. Establishing a legal research agenda for ocean energy. Marine Policy. 2016; 63; 126–134. doi:10.1016/j.marpol.2015.09.030

[13] Simas T, O'Hagan AM, O'Callaghan J, Hamawi S, Magagna D, Bailey I, Greaves D, Saulnier JB, Marina D, Bald J, Huertas C, Sundberg J. Review of consenting processes for ocean energy in selected European Union Member States. International Journal of Marine Energy. 2015; 9: 41–59. doi:10.1016/j.ijome.2014.12.001

Chapter 3

The Use of the Technological Innovation Systems Framework to Identify the Critical Factors for a Successful Sustainability Transition to Rooftop Solar in Low-Income Communities within South Africa

David R. Walwyn

Additional information is available at the end of the chapter

http://dx.doi.org/10.5772/65293

Abstract

South Africa has a large unemployment rate with many households almost completely dependent on social grants for survival. Under such circumstances the potential of rooftop solar in developing vibrant and local energy micro-economies, which can generate and trade in electricity, is highly attractive. In this chapter, it is shown that such systems are uneconomic if considered from the perspective of a private investor. However a different conclusion emerges with respect to public funding. Even without considering the additional benefits of improved health and learning opportunities, lower levels of crime and lower levels of non-payment, rooftop solar becomes an attractive investment for the state, especially in areas of high solar irradiation. The 'electrification grant' could be delivered in several ways including the use of a subsidised feed-in-tariff. An initial analysis using the framework of technological innovation systems shows that much of the required structure for a rooftop solar system is already in place. However the state will need to boost efforts to train technicians to install and maintain the infrastructure, accelerate its initiatives to support local manufacture of photovoltaic modules, and strengthen the capability of the science and technology system to support the processes of technology diffusion and adoption.

Keywords: sustainability transition, technological innovation system, rooftop solar, photovoltaic, low-income community, South Africa

1. Introduction

Photovoltaics (PV) has evolved to be a significant source of electrical energy; by the end of 2014, cumulative PV capacity had reached 237 gigawatts (GW), equivalent to about 1.3% of the global electricity demand (see **Figure 1**). New capacity has been growing at an average of 40% per year since 2000 and it is predicted that by 2050 solar PV will be the largest source of electrical power, accounting for 16% of global demand [1].

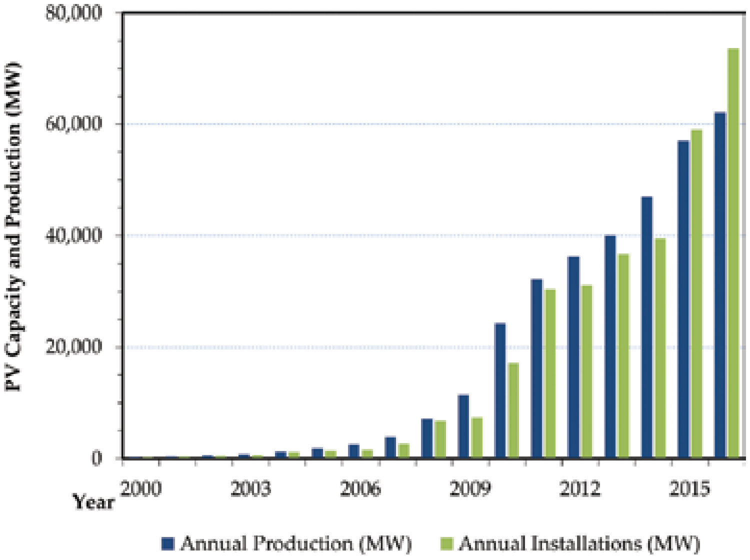

Figure 1. Annual PV production and installations. Source: updated with permission from REN21 [2], Masson and Brunisholz [3].

Surprisingly, this growth has been non-homogeneous with only five countries (China, Germany, Japan, United States and Italy) accounting for 62% of the total installed capacity. Although developing countries (excluding China) are becoming more visible as investors in PV capacity, driven largely by the increasing cost-competitiveness of the technology [2], their collective markets remain small compared to the developed countries.

The transformation of all countries to more sustainable energy systems, including both generation and demand, has become an active research area and forms part of a much broader set of studies on sustainability transitions, where the latter considers the means of promoting and governing a transition to sustainability. Although the studies do partly consider the technical challenges and possible technological solutions, the core of the research is focussed predominantly on how to change relationships, business models and behaviours, and hence achieve a fundamental transformation towards more sustainable modes of production and consumption [4]. The approach of technological innovation systems (TISs) has been proposed as one of several theoretical frameworks which can be used as a basis for such studies [5, 6].

In this chapter, the TIS framework has been applied to both understand and develop recommendations for how to change the relationships and conditions which presently shape the market for rooftop solar in South Africa. The framework is particularly applicable to analysing systems which display strong path dependencies and lock-ins, as is so evident generally for national energy systems. The chapter has four main sections. In the first section, the existing market structure and technological basics for PV are described. This is followed by a section on the principles of rooftop solar and particularly the application of the technology within low-income communities in South Africa, including a detailed techno-economic assessment. In the third section, the theory of technological innovation systems is introduced and then applied to the situation in South Africa. In the final section, the conclusions and recommendations of the study are presented.

2. The photovoltaics value chain and market structure

2.1. Manufacturing technology and cost

Although other materials are used, silicon wafer technology accounts for 93% of the total PV production [7]. The value chain begins mostly with the material polysilicon (also known as multi-crystalline silicon) which is cast into ingots, sliced into wafers, inlaid with a conductive grid to produce the silicon cells, then assembled into modules and finally installed onto rooftops (or other applications) in the form of complete PV systems. Other raw materials include monocrystalline silicon and thin films based on various combinations: cadmium, tellurium, selenium, gallium and arsenic.

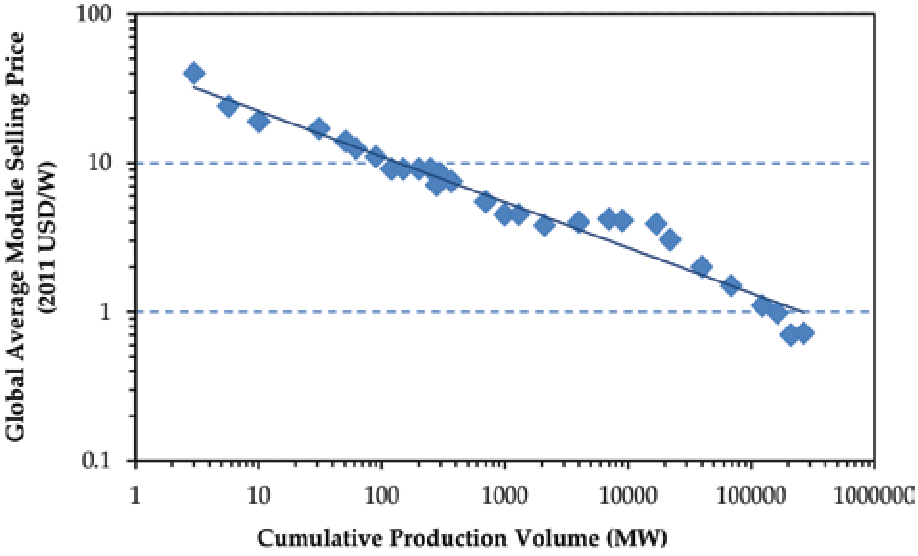

Figure 2. PV module selling price decreases as cumulative volumes increase.

The earlier stages of the manufacturing value chain are capital intensive, and the later stages labour intensive, with cost components (or value addition) being spread relatively evenly. The overall cost of PV has declined as manufacturing volumes have grown, as shown in **Figure 2**. The average module selling price is now about R10.1/W_p or \$0.72/W_p,[1] a decline of 15 times since 1992 when the price was R154/W_p or \$11/W_p. Using the equations of the learning curve [8], it is calculated that in the last 35 years, the average module price decreased by 35% for each doubling of cumulative production volume.

Much of the cost savings have been achieved as a result of the decreased usage of materials, which has been reduced significantly from about 16 g/W_p to less than 6 g/W_p due to increased efficiencies (17–22%) and thinner wafers [7]. In terms of energy payback (amount of time to produce the total energy required for manufacture), payback is reached in less than 1 year for southern Europe and countries with similar solar irradiation. The carbon dioxide avoidance factor of PV is reported to be 0.715 kg CO_2/kWh [7].

The cost of PV modules is only partly located in the modules themselves. Other components include the inverter, the wiring (electrical connectors) and the mounting frames. Relative costs by component are shown in **Figure 3**.

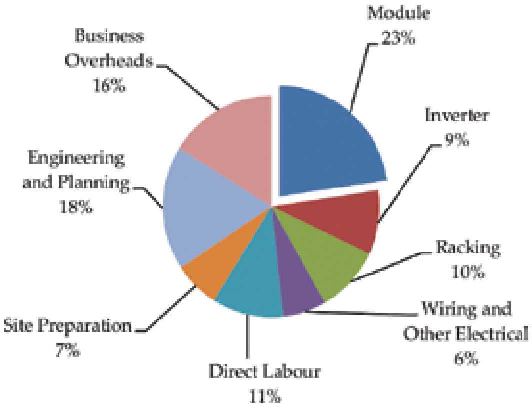

Figure 3. Breakdown of costs for PV systems. Source: Chung et al. [9] and IRENA Secretariat [10].

2.2. Job creation in the photovoltaics value chain

About 70% of the global manufacture of photovoltaic modules takes place in China, followed by the rest of Asia Pacific and Central Asia [7]. Of the 2.8 million global jobs in PV, 1.65 million are located in China, 377,000 in Japan and 194,000 in the United States [2]. The estimated number of jobs per segment of the value chain is shown in **Figure 4**; total jobs are 30 jobs per MW_p.

---

[1] Throughout this paper, two conventions have been used. All monetary values are quoted in US dollars, adjusted to 2011 values, and South African Rands, adjusted to 2015 values, with the approximate conversion rate being R14/\$. In addressing issues of power, these are quoted in watts (W) or kilowatts (kW) or megawatts (MW), with the suffix p referring to peak power (at a capacity factor of 100%) and the suffix c referring to actual output.

Currently, most of the local jobs are in the installation, operations and maintenance of the modules, with manufacture of the cells and modules taking place in other countries [12]. Although the REI4P includes criteria for value addition, these requirements have not been terribly successful in developing the value chain. Previous studies have suggested that sustainable jobs will most likely be created in countries with long-term policies and a holistic approach that addresses barriers all along the value chain [13].

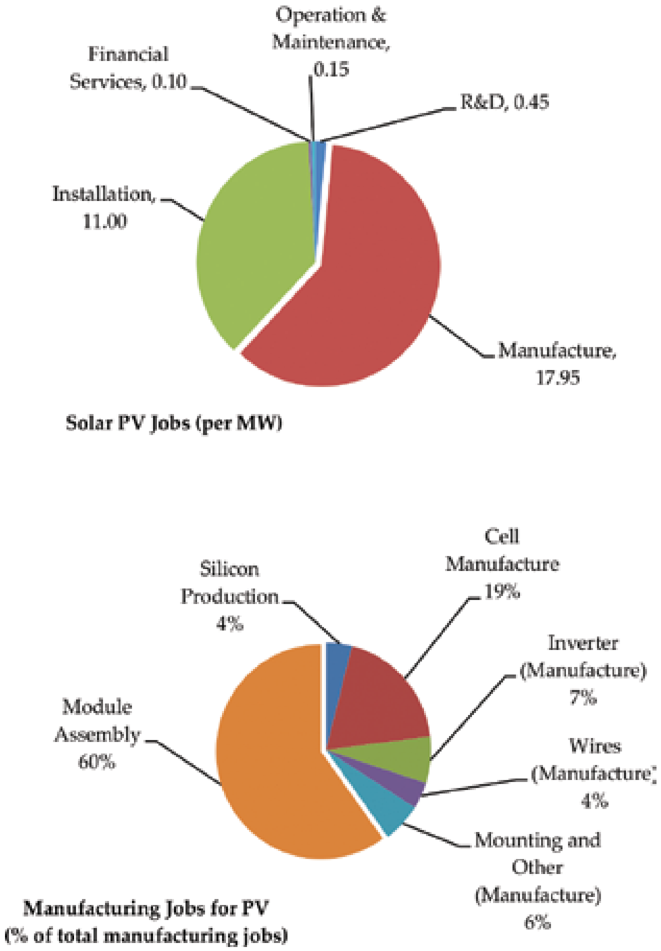

Figure 4. Solar jobs per MW_p in photovoltaics. Source: Walwyn [11].

2.3. Rooftop solar

Rooftop solar is already an appreciable component of power-generation systems in only a handful of countries, with the leading country being Australia, where the penetration of solar PV in residential consumption has reached 15% of the total electricity demand [14]. The use of PV as a means of both producing and consuming power has led to the definition of the term prosumer, which refers to the growing practice of rooftop systems supporting the energy needs of homeowners and also selling energy to the national grid.

Further growth of the residential market is constrained by the economics or payback periods associated with private purchase and ownership of such systems. For instance, although the cost of rooftop solar in Germany has fallen considerable from 5000 Euro/kW$_p$ in 2006 to 1270 Euro/kW$_p$ in 2015, consisting of 48% for the module and 52% for the balance of systems, the feed-in-tariff for PV has fallen to about 0.125 Euro/kWh [7], which is lower than the break-even production cost of about 0.148 Euro/kWh (the details of this costing are shown in Section 3.2). In other words, the tariff is generally too low to support investment in rooftop systems unless the bulk of the electricity generated is consumed within the household (i.e. consumption takes place during the hours of sunlight and the use of storage is avoided almost completely).

However, this analysis is not applicable to the case of low-income communities with high rates of unemployment and poverty, and significantly dependent on social grants as a means of survival. In such contexts, PV-derived energy offers the potential for the development of new economic activity. A regional innovation system built on rooftop solar could be an ideal application of an inclusive innovation leading to a high-impact sustainability transition and the long-term economic upliftment of these communities. This proposition is discussed in more detail in Section 3.2.

3. Photovoltaics in South Africa

3.1. Independent power producers

PV in South Africa has grown rapidly over the last 5 years and has now reached a total value of 1.2 MW$_p$ of installed capacity with another 1.1 MW$_p$ in progress, comprising at least 45 separate 'single-site' installations with an average capacity of 51 MW$_p$. This rapid expansion has been supported almost exclusively by the Renewable Energy Independent Power Producers Programme (REI4P). In the first four-bidding windows of the programme, it has successfully procured 6,300 MW of power from 92 independent power producers, involving an investment of $13.8 billion, including $3.8 billion in foreign investment [15]. The target for the programme is 17,800 MW of renewable power by 2030, with a mix between wind, PV, concentrated solar power, biogas, hydro and biomass. Wind and PV are presently the major technologies, accounting for 53 and 36%, respectively [15].

There has been some criticism of the programme, including that it has failed to deliver a new industrial base and new areas of technological capability [8, 16]. Instead, the local content provisions have only managed to encourage elaborate transfer-pricing practices which effectively bypass the requirement, and some short-term investment in local assemble [16]. It is not surprising that the REI4P should encounter criticism from various stakeholders. The public-policy environment is complex given the high rate of unemployment, the present low economic growth conditions, the severe legacy of an institutionalised inequality left by apartheid and the persistent poverty. Although social grants have been effective in dealing with the most severe forms of inequality and poverty, the country's political and economic spaces remain highly unequal and as a consequence the public-policy space is strongly contested.

This contest is evident in the energy sector, with the REI4P having to balance the needs for low-energy cost (and hence competitive tender processes) against social development, job creation in energy against job protection in mining and social development in outlying areas against social wages within urban areas. One important consideration is that the present energy policy is largely silent on the question of distributed generation. Although the REI4P has been successful in diversifying energy production, the independent power producers are still located as single sites. The programme and its overarching policy framework, the Integrated Resource Plan [17], has little provision for the incorporation of rooftop solar or other distributed technologies. The conditions for rooftop solar are now discussed in more detail.

3.2. Rooftop solar

Residential PV, or rooftop solar, is still in its infancy within South Africa. The existing regulatory process covers installations only above 100 kW, and there is presently a regulatory void in respect of smaller systems, referred to as small-scale-embedded generation. The country's energy regulator, the National Energy Regulator of South Africa (NERSA), is preparing the regulations governing net metering, or the process and rates by which rooftop solar systems or other forms of energy generation would be able to feed electricity into the national grid. A draft discussion paper was released in early 2016 for comment and is supposedly being finalised by the Department of Energy [18].

In the absence of the regulations, two municipalities (Cape Town and Nelson Mandela Bay Metropolitan Municipality) have already proceeded with schemes to allow larger scale producers to sell power back to the municipality. In the case of Cape Town, the allowable tariffs are unacceptably low (R0.57 per kWh relative to a purchase price in excess of R1.10 per kWh). The Nelson Mandela Bay Metropolitan Municipality, on the other hand, has agreed to purchase excess power from rooftop systems at the same value as the selling price from the municipality to the consumer. In other words, the consumer pays for the net usage only.

One reason often cited for the slow reform of energy regulations in South Africa for small-scale producers is that local authorities subsidise low-income consumers through a tiered-pricing system which allows the sale of energy to these consumers at lower prices. A shift to rooftop solar, particularly by the high-end consumers (>3000 kWh per month), may remove this flexibility and restrict the ability of municipalities to balance their revenue requirements with broader policy goals of economic development in low-income communities. In particular, the widespread adoption of rooftop solar and other means of local power generation could undermine revenue collection, and hamper other programmes on infrastructure development and redistribution [19].

However, this assertion does not survive closer evaluation. A separate study of municipal revenues for Cape Town has shown that the impact of rooftop solar will be minimal, especially if municipalities act proactively to reallocate their cost structured between distribution and supply [11]. As shown in **Figure 5**, although the high-end consumers pay on average 30% more per unit of energy than the low-end consumers, the former only account for 5% of the total revenue. More than 93% of users consume less than 500 kWh/month and provide 75% of the city's total revenue from electricity sales. In other words, the immediate impact on municipal revenues from the loss of electricity sales to high-end residential users, who are the most likely to invest privately in rooftop solar, will be negligible.

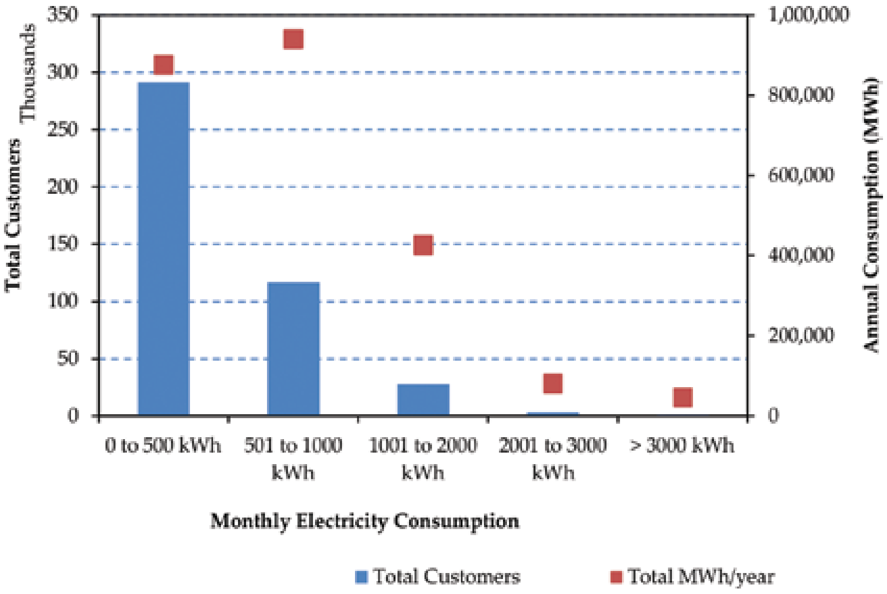

Figure 5. Profile of electricity consumers (Cape Town). Source: Walwyn [11].

At this point in the chapter, we are now ready to take an entirely new approach to the adoption of the technology. Rather than considering rooftop solar as a threat to revenues and redistributive programmes, it should be considered as precisely the opposite, namely as an effective means of achieving economic development within low-income communities. There are two critical factors in this discussion, namely the standalone rate of return or payback period for a newly installed grid-connected rooftop solar system without storage, and the overall level of support for low-income communities through the social grant system. Both aspects are now covered in more detail.

3.2.1. Techno-economic evaluation

In this chapter, the rate or return or payback period for rooftop solar has been estimated using a standard technique for obtaining a fully absorbed cost or single-year cost [20]. The technique requires the input of various parameters including capacity utilisation, the inverter efficiency, panel size, roof area and installed cost (see **Table 1**). The sizing of the system is based on the average rooftop size for a small house (detached or semi-detached, typically with a total rooftop area of about 45 m^2) and the average electrical energy demand for low-income households (about 500 kWh/month, as shown in **Figure 5**). It is also assumed that the project lifecycle is 20 years, capital is depreciated over 10 years, and that the only direct or indirect costs other than capital charges are a small amount of maintenance necessary to maintain high-capacity utilisation (4% of the installed capital cost per year). All labour costs are excluded since it is considered that the rooftop systems will be managed by the homeowners who will not charge for their labour.

Factor	Units	Value
Capacity utilisation	% of kW_p	25%
Inverter efficiency	% of input power	95%
Panel output	kW_p	0.25
Roof area	m^2	23
Installed system cost	R/kW_p	27,307
Selling price (to municipality)	R/kWh	1.40

Table 1. Input parameters.

The results show that the single year, fully absorbed cost is about R2.04 per kWh, this value being almost insensitive to the installed panel area, equivalent in effect to the number of panels. In other words, the break-even price is about R2.04/kWh or $0.15/kWh and the feed-in-tariff for rooftop solar should be at least this value for the system to generate a return on investment under standard assumptions. In the event that the excess power is sold at the present purchase price for power within a municipal area of South Africa (about R1.40), the project's internal rate of return will be 4%, which is below the cost of capital, and the net present value (NPV) of the estimated discounted cash flows will be negative (–R20,000 or –$1440), as shown in **Table 2**.

Number of panels		12
Rating	kW_p	3.0
Panel output	kWh/year	6,242
Capital cost	R	81,922
Fully absorbed single-year cost	R/kWh	2.04
Internal rate of return		0%
Net present value	2015 R	−20,000
	2011 $	−1440

Table 2. Economic model output values.

The techno-economics are sensitive to both module price and capacity utilisation, as shown in **Figure 6**. The latter is already high for most sites within South Africa, and the model has assumed a value of 25% and an inverter efficiency of 95%. However, the module prices have been declining over a long period, as discussed in Section 2.1. Further decreases are expected, which will make rooftop solar more competitive as a source of electrical energy.

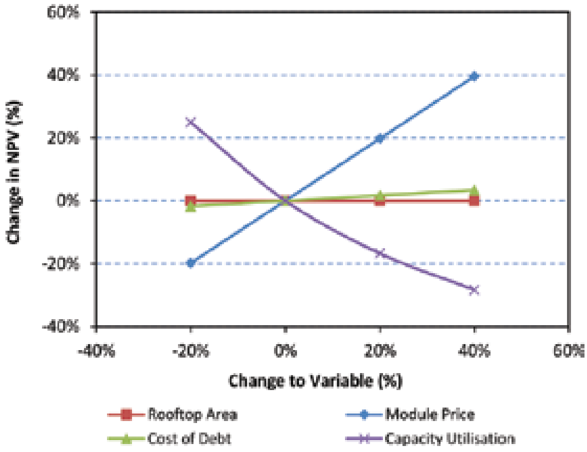

Figure 6. Sensitivity analysis for rooftop solar.

It is clear from this analysis that for the high-end consumers in South Africa rooftop solar is not presently competitive versus grid-delivered electrical energy, notwithstanding the recent price increases and the tiered system of electricity charges. However, this analysis must be nuanced when applied to low-income communities which are already recipients of extensive social grants, the latter aimed at addressing the high levels of unemployment and poverty in the country. In the following section, the extent of unemployment and the social-wage approach, which has been implemented by the Government post 1994, is discussed in more detail.

3.2.2. *Social grants through household electricity*

Social grants have been the most important means by which the government in South Africa has attempted to deal with unemployment and poverty. Although gross domestic product (GDP) and total employment have grown since 1994 (see **Figure 7** and **Table 3**) (expanded), unemployment rates have remained almost constant at about 35% of the total population. Government revenue has increased as shown in **Figure 7**, and a proportion of the increased revenue has been used to fund increases in the social wage, which now reach about 17 million citizens at an average wage of R6,870 per year (values in 2015 Rands) or $335/year, where these values have been adjusted to allow for the costs of distribution from Treasury to the recipients (10% of the total disbursements). The total cost of social grants in 2015/16 was R129 billion, and this figure is projected to grow further to R169 billion in 2018/19 [21] (see **Figure 8**).

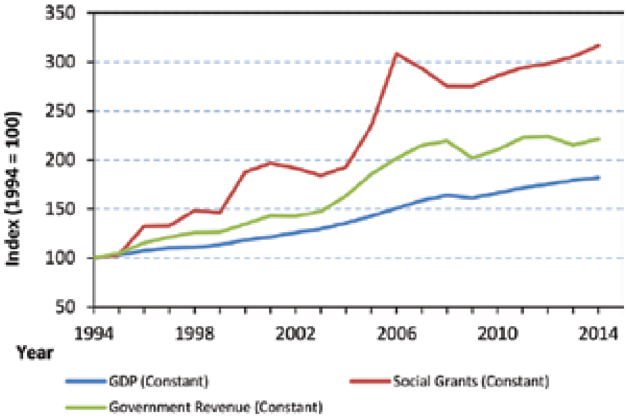

Figure 7. Relative values of GDP, total employment and government revenue. Source: Statistics South Africa [22].

	1994	2014	2015	% Change
Strict				
Employed	8896	15,055	15,830	69%
Unemployed	2489	5067	5400	104%
Unemployment rate	21.9%	25.2%		15.2%
Expanded				
Unemployed	4707	8157		73%
Labour force	13,603	23,212		71%
Unemployment rate	34.6%	35.1%		1.6%

Source: Statistics South Africa [23].

Table 3. Employment in South Africa, 1994–2015.

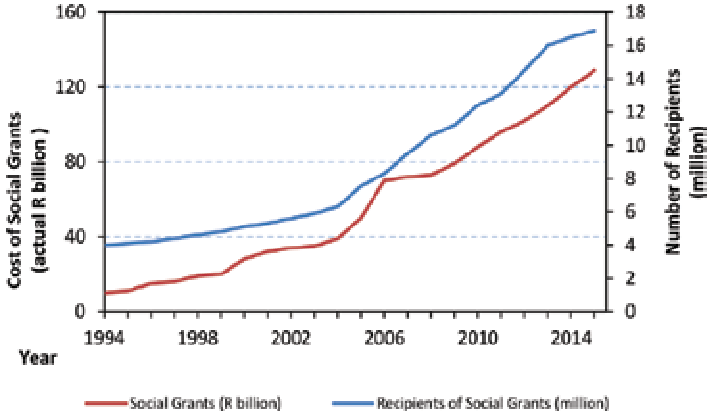

Figure 8. Value of social grants (actual R billion) and numbers of recipients (million). Source: updated with permission from National Treasury [24].

Assuming that there is at least one person per household on a social grant, and that the municipality already subsidises low-income household electricity purchases by about R360 per household per year [11], the net subsidy from central and local government is calculated at about R7230 per household per year. This calculation ignores a number of other factors which also contribute to the public cost including the high level of default on electricity payments within such communities, the opportunity cost as a consequence of inadequate lighting and heating in homes, the cost of crime and the public health burden.

In summary, it is apparent that rooftop solar is not presently viable for the private investor in South Africa. The break-even price is R2.04 per kWh, which is 50% higher than the average retail price at which electricity is available directly from the national grid for domestic consumers. However, there is a strong argument for the public sector to become more actively involved in the electrification of homes within low-income areas using rooftop solar. The state is already subsidising such homes at an average value of about R7,230 per year. If we assume that this subsidy is instead delivered in the form of a higher purchase price from all power delivered to the grid, or a net saving on energy purchases, the techno-economics of rooftop solar in low-income communities become more favourable with a neutral (as opposed to a negative) return on investment. Further discussion of this important result follows in Section 5.

4. Technological innovation systems

4.1. Theory and parameters

Discrete sub-sectors of a national system of innovation, such as the energy, machinery and transport, can be conceptualised as technological innovation systems. Such systems consist of actors, networks and institutions (rules and standards of the system), as well as material artefacts and knowledge, broadly classified as sociotechnical systems. Sociotechnical transitions, and by definition sustainability transitions, can be studied using a combination of the theory of TIS [25] and a three-phase model for technology development [26]. Such a framework is now applied in this chapter.

Sustainability transitions are long-term, multidimensional and fundamental transformation processes through which established sociotechnical systems shift to more sustainable modes of production and consumption. The objective in an analysis such as this study on South Africa is to identify which critical parameters need to be addressed in order to expedite a sustainability transition. In terms of TIS theory, there are seven key functions that need to be fulfilled in the maturation of emerging innovation systems [5], namely knowledge development and diffusion, resource mobilisation, market formation, influence on the direction of search, legitimation, entrepreneurial experimentation and development of positive externalities. For the purposes of this study, three indicators have been selected for each function as a means of defining the extent to which the necessary conditions for transition have been realised. The functions and their related indicators are shown in **Table 4**.

Item	Indicator	Level	Comment
Development of formal knowledge			
Volume of knowledge creation and development	Publications from South African universities; growth of research centres	Medium	Research on PV, rooftop solar and smart-grid technologies has increased in recent years but still in its infancy (about 50 publications on PV or smart grids per year relative to 650 in Germany).
Mode of knowledge creation and development	PhD studies and other	Medium	Limited relative to potential demand.
Process of knowledge creation and development	Linkages between universities/business	Poor	With the exception of Art Solar, the local market is dominated by international companies with limited links to local universities.
Resource mobilisation			
Developing human capital and specialised labour force	Graduates in PV	Medium to Poor	Growing output of university graduates with relevant qualifications but very limited numbers of technicians for installation and integration.
Mobilisation of financial resources	Funding for investment in production, innovation and R&D	Medium	Cost of capital generally higher in South Africa; R&D financial resources are available but not specific to the sector.
Existence of complementary assets	Formation and growth of centres for providing intellectual property services	High	South Africa has a strong intellectual property regimen including the patent office and the National Intellectual Property Management Office.
Market formation			
Market size and its growth	Market size; growth rate	High	PV market is growing strongly driven by the REI4P and the shortfall in energy generation within the national grid; high potential to expand to all areas including low-income communities in Northern Cape.
Incentives and inducement mechanisms for market growth	Scale of incentives	Medium	Present although not specific to PV; specific demand-side measures (supply contracts) and generalised supply-side incentives (R&D, human capital).
Customer groups and their purchasing behaviour	Differentiation of market	Low	Some interest from remote communities and households, but generally very limited awareness.
Influence on the direction of search			
Visions and expectations about the growth potential	Media interest	High	Strong media interest in renewables and carbon emissions.
Policy development and priority setting	Clear government policy	Medium	Government policy is clear for the development of independent power producers but uncertain for rooftop solar (IRP 2010–2030 and REI4P include detailed tender documents, quotas, price caps, requirements for local content, cap on foreign exchange exposure).
Current and complementary businesses	Development of new business areas within existing companies	Low	Local firms have been slow to diversify into renewable technologies with the exception of multinational and financial services firms.
Legitimation			
Developing necessary institutions and required regulations	Institutes for standardisation and	Low	Lack of clarity on the inclusion of rooftop solar systems within the national grid, including all

Item	Indicator	Level	Comment
	regulations for grid inclusion		aspects of integration, smart grids, metering and feed-in-tariffs.
Formation of advocacy coalitions and interest groups and their lobby power	Secretariat and lobby groups; releasing overall policies and strategies for promotion and development	Medium to High	Formation of the South African Photovoltaic Industry Association and Green Cape in order to support the development of local industry and lobby for policy support.
Promotional and extension activities	Newsletters and other	Poor	Infrequent newsletters and media coverage.
Entrepreneurial experimentation			
Mode of entrepreneurship	Entry of new 'diversified companies' from other sectors for exploiting the 'niche market'	Poor	This area of assessment is very unclear; although the market is apparent, there has been little innovation in terms of how firms can enter and prosper in the market given the existing regulatory context.
Experiences in using technology and its applications	Launch of new products	Medium	Some firms have developed unique products which incorporate PV such as lighting and home-cooking applications.
Knowledge diffusion and development of positive externalities			
Formation of division of labour and specialised value chain	Formation of networks and technology incubators	Poor	This area of the system is still weak; the value chain is largely undeveloped except for single-site installations and the provisions of the existing programme for local content are being avoided.
Information and knowledge flows and spillover	Formation and growth of the firms	Poor	Although the science and technology system in South Africa is strong by international standards relative to its peer group, knowledge spillovers have been minimal and local public research institutions have had limited impact.

Source: own data, [12, 16, 27, 28].

Table 4. Variables and levels of attainment.

It is noted that TIS is not the only analytical framework which can be used to study sustainability transitions. In a separate study of the renewable energy sector in South Africa, the frameworks of technological capabilities and global production networks have been applied in order to understand the embeddedness of PV as a technology within the national and international political economy [16]. The research highlighted the importance of finance and investment, the nature of global supply chains and the abuse of the more progressive elements of South Africa's renewable energy programme by international companies. In particular, Baker [16] concluded that a tension exists between the country's dependency on international companies and its desire to establish local manufacturing, and considered that the resolution of this tension is critical to the success of the programme. Similarly, an earlier study also argued that technology transfer on its own would not enable South Africa to reach its low carbon targets [27]. Noting that technological development was critical to achieving the targets, and that technology transfer in support of product sales did little to build internal or local capabilities, Rennkamp and Boyd [27] concluded that stronger policies were required to boost domestic technological capabilities.

Although both studies are relevant to our discussion, TIS has been used as the preferred framework since the focus of this work has been to understand the potential and constraints of rooftop solar in low-income communities. To a large extent, the roll-out of large-scale PV in this market will depend on the development of an innovation system which is quite distinct from the single-site architecture which has prevailed so far. In particular, the deployment as discussed in this chapter will require micro-economies of suppliers and service providers who will be able to install, integrate and maintain small-scale systems across a large number of sites. In this sense, TIS is a more appropriate analytical framework since it specifically covers the important aspects of entrepreneurial experimentation, knowledge diffusion and legitimation. The application of the framework to this micro-economy within the broader sector of PV is now discussed.

4.2. Evaluation of photovoltaics and rooftop solar systems in South Africa

Based on the results of this study, the PV and rooftop solar TIS within South Africa is at various stages of development, as shown in **Table 4**. Although there are strong demand factors including the net shortfall in generation capacity, several other factors remain weak including the availability of skilled human resources, the absence of a regulatory policy for feed-in systems within local authorities, limited progress in the establishment of local manufacture including PV modules and inverters, and a slow development of the necessary entrepreneurial skills within firms.

All of these factors will need to be addressed in the opening of the proposed micro-economy for rooftop solar within low-income communities. The issue of skilled human resources is an ongoing constraint to the economy and has been identified in several sectors, not only energy [29]. Furthermore, the weakness of entrepreneurial activity within the country has also been highlighted in several surveys and remains an issue for government policy [30].

However, the most important issue at present is the regulatory framework for rooftop solar and how the systems could be managed within the local authorities' distribution networks, including metering and feed-in-tariffs. As already mentioned, the national regulator is currently in a process of public consultation on this issue, but the decision has already passed its deadline and there seems little progress by the regulator. This tardiness reflects a general inability with respect to decision-making within government and has been ascribed to deeper political struggles over what is supported by the state and who benefits [28]. As a consequence, the government does not appear to move forward on important issues involving substantial realignment of public benefit, innovation and state support.

Although the government may seem intent on resolving the unemployment crisis, based on its policy documents such as the National Development Plan [31], at this stage it is failing to support the development of distributed energy generation due to a perceived disruption of the coal-mining sector and the stranglehold of Eskom, the latter being a parastatal that controls the national grid and most of the country's generation capacity. The transition from coal to PV will require more than the transfer of technology and support for a new cohort of homeowner entrepreneurs; it will require government to tackle the concerns of its partners in the trade unions and the parastatals over the diversification of the energy system. Such conflicts are not unusual in transitions and generally are only resolved under the pressure of widespread mobilisation or popular demand.

5. Discussion

The energy sector is evolving in several ways which have profound implications for policy makers. Firstly, energy generation is becoming increasingly distributed with energy sources being located closer to consumers [2]. Secondly, energy systems are becoming more complex with multiple sources, suppliers and distributors. Both aspects are particularly relevant to rooftop solar and stimulation of the latter requires careful consideration of the possible impacts including issues such as employment and grid stability. In South Africa, the technology has the potential to deal with three important public-policy objectives, namely equity, employment and economic growth. The development of vibrant local economies in rooftop solar systems could create much-needed jobs in low-income communities, improve access to electricity, provide new income sources to the unemployed and grow local economies.

However, this potential is being overlooked in favour of the continuation of a centralised power-generation system which is both exclusive and inefficient. It is argued that rooftop solar is uneconomic relative to the single-site systems, and that fluctuating outputs from PV systems require a duplication of generation sources. It has been shown in Section 3.2.2 that direct government support for rooftop solar in low-income communities can be justified on the basis of the high level of social grants which are already being delivered to these households. By switching from a system in which government provides cash grants to one in which it purchases power or power savings from poor households, it will simultaneously be meeting other important developmental priorities including those of increasing employment and economic growth. As noted in Section 2.2, 11 jobs per MW_p are created in the installation and maintenance of PV panels alone. These are generally less-skilled jobs which will not require long periods of retraining and investment in human resource development.

These arguments can be illustrated by considering a pilot scheme involving the installation of 3 kW_p rooftop solar systems across a single community of 1000 homes. The total installed cost for the systems will be about R80 million (about R80,000 per home), giving a total system capacity of 3 MW_p delivering 6,250 MWh per year into the homes with the surplus being direct to the national grid. The equivalent value of this energy to each home will be R8,740 per household per year, should the panels be connected directly to the national grid and the feed-in-tariff be set at the average selling price, as is presently the case in the Nelson Mandela Bay Metropolitan Municipality. The single-year cost to government for the installation has already been discussed and amounts to R12,730 per household year (R2.04 per kWh).

It has already been noted that the total value of government grants and subsidies amounts to approximately R7,230 per year for a single low-income household. If we now assume that the system of social grants is replaced by the installation of a rooftop solar system, the net additional cost to government will be R5,500 per household per year, for which it gains at least 33 jobs per 1000 households and the benefits of improved electrification. It makes sense that at least a portion of the initial capital investment is paid by the homeowner and that this loan should be handled in the same way as the present system for housing subsidies. If we assume that this proportion is at least as large as the extent to which the value of the electricity to each household exceeds the present value of social grants, then the net additional cost to government is R3,300 per household per year, or about R100,000 per job. The latter figure is reasonable for employment creation with values being reported by the existing government-sponsored scheme for employment creation (the Jobs Fund) being in the region of R50,000–150,000, depending on the sector and the quality of the job.

The details of this analysis provide a compelling argument. Replacing a system of social grants with a subsidised means of individual households becoming energy prosumers (consumers and producers) will have benefits at a number of levels. Firstly, it will improve access to and the affordability of electricity, which is recognised as a fundamental means of accessing other public goods, secondly, it will create local economic and employment growth at a competitive value, and thirdly, it will decrease levels of poverty in low-income communities without resorting to the use of a social grant. Finally, it will simultaneously address the need for the transition of South Africa's energy sector from non-renewable to renewable resources, as has been outlined in the Integrated Resource Plan [17].

6. Recommendations and conclusions

This study has shown that rooftop solar has real potential to deliver a viable and beneficial sustainability transition within South Africa. In particular, the development of a comprehensive technological innovation system will support the economic upliftment of low-income communities in addition to addressing the commitments by South Africa to the goals of the Paris Convention, creating employment and new economic activity.

However, the government has moved slowly to date in facilitating the development of rooftop solar. This transition will require it to take fundamental policy decisions relating to energy systems and economics; it will require the lead departments to coordinate and integrate the activities of multiple stakeholders; it will need the supporting departments to ensure that the appropriate regulations, infrastructure and resources are in place to support a country's energy vision.

There is little evidence that such decisions have been taken or even considered. The immediate priority for government if it wishes to develop a rooftop solar market in low-income areas as a sustainable alternative to social grants, the latter rapidly becoming unaffordable, is to finalise the regulations for feed-in-tariffs and the integration of rooftop systems with the national grid. In the medium term, it will also need to boost efforts to train technicians to install and maintain the infrastructure, accelerate its initiatives to support local manufacture of photovoltaic modules and smart metres, and strengthen the capability of the science and technology system to support the processes of technology diffusion and adoption within the sector.

Author details

David R. Walwyn

Address all correspondence to: david.walwyn@up.ac.za

Department of Engineering and Technology Management, University of Pretoria, Hatfield, Pretoria, South Africa

References

[1] Philibert C. Technology Roadmap: Solar Photovoltaic Energy. Paris: Renewable Energy Division (RED); 2014.

[2] REN21. Renewables 2016: Global Status Report. Paris: REN21; 2016. ISBN 978-3-9818107-0-7.

[3] Masson G, Brunisholz M. A Snapshot of Global PV (1992-2015). Paris: IEA-PVS, 2016. ISBN 978-3-906042-42-8.

[4] Markard J, Raven R, Truffer B. Sustainability transitions: an emerging field of research and its prospects. Research Policy. 2012;41(6):955–967.

[5] Bergek A, Jacobsson S, Carlsson B, Lindmark S, Rickne A. Analyzing the functional dynamics of technological innovation systems: a scheme of analysis. Research Policy. 2008;37(3):407–429.

[6] Bento N, Fontes M. The construction of a new technological innovation system in a follower country: wind energy in Portugal. Technological Forecasting and Social Change. 2015;99:197–210.

[7] Burger B, Kiefer K, Kost C, Nold S, Philipps S, Preu R, et al. Photovoltaics Report. Freiburg: Fraunhofer Institute for Solar Energy Systems; 2016.

[8] Walwyn DR, Brent AC. Renewable energy gathers steam in South Africa. Renewable and Sustainable Energy Reviews. 2015;41(1):390–401.

[9] Chung D, Davidson C, Fu R, Ardani K, Margolis R. U.S. Photovoltaic Prices and Cost Breakdowns: Q1 2015 Benchmarks for Residential, Commercial, and Utility-Scale Systems. Denver: National Renewable Energy Laboratory; 2015. Technical Report, NREL/TP-6A20-64746.

[10] IRENA Secretariat. Renewable Energy Technologies: Cost Analysis Series – Solar Photovoltaics. Bonn: International Renewable Energy Agency (IRENA); 2012.

[11] Walwyn DR. Local government resists the implementation of renewable technologies. In: Hostettler S, Gadgil A, Hazboun E, editors. Sustainable Access to Energy in the Global South: Essential Technologies and Implementation Approaches. Lausanne: Springer; 2015. p. 155-166.

[12] Mulcahy M. Review of the Competitive Bid for PV in South Africa; is SA Maximising Job Creation and Value for Money from Its Photovoltaic Industry? [Research paper presented in partial fulfilment of the requirements for the Masters of Development Finance]. Cape Town: University of Cape Town; 2012.

[13] IRENA. Renewable Energy Innovation Policy: Success Criteria and Strategies. Bonn: International Renewable Energy Agency (IRENA); 2013.

[14] Gifford J. Australia Leads World in Residential Solar Penetration Melbourne: PV Magazine; 2015. Available from: http://www.pv-magazine.com/news/details/beitrag/australia-leads-world-in-residential-solar-penetration_100021291/#axzz4DWCPU1hx [Accessed 03.07.2016].

[15] Department of Energy. Independent Power Producers Procurement Programme (IPPPP): An Overview. Pretoria: Department of Energy; 2015.

[16] Baker DL. Technology Development in South Africa: The Case of Wind and Solar PV. Sussex: Science Policy Research Unit, 2016. Working Paper Series SWPS 2016-05.

[17] Department of Energy. Integrated Resource Plan for Electricity 2010-2030, Revision 2, Final Report. Pretoria: Department of Energy; 2011.

[18] National Energy Regulator of South Africa. Small-Scale Embedded Generation: Regulatory Rules National Energy Regulator of South Africa. Pretoria: Government of South Africa; 2016. p. 1-31.

[19] Trollip H, Walsh V, Mahomed S, Jones B. Potential impact on municipal revenue of small scale own generation and energy efficiency. South African Economic Regulators Conference; Pretoria. Pretoria, 2012.

[20] Walwyn DR, Huddy SM, Rybicki EP. Techno-economic analysis of horseradish peroxidase production using a transient expression system in *Nicotiana benthamiana*. Applied Biochemistry and Biotechnology. 2015; 175(2):841–854.

[21] Ndenze B. Social grants to be increased by additional R11,5 billion Johannesburg: Times Live; 2016. Available from: http://www.timeslive.co.za/politics/2016/02/24/Social-grants-to-be-increased-by-additional-R115-billion [Accessed 06.07. 2016].

[22] Statistics South Africa. Gross Domestic Product First Quarter 2016. Africa SS. Pretoria: Statistics South Africa; 2016.

[23] Statistics South Africa. Employment, Unemployment, Skills and Economic Growth; An Exploration of Household Survey Evidence on Skills Development and Unemployment Between 1994 and 2014. Pretoria: Statistics South Africa; 2015.

[24] National Treasury. Budget Review. Treasury N. Pretoria: National Treasury; 2015.

[25] Carlsson B, Stankiewicz R. On the nature, function and composition of technological systems. Journal of Evolutionary Economics. 1991;1(2):93–118.

[26] Wilson C. Up-scaling, formative phases, and learning in the historical diffusion of energy technologies. Energy Policy. 2012;50:81–94.

[27] Rennkamp B, Boyd A. Technological capability and transfer for achieving South Africa's development goals. Climate Policy. 2015;15(1):12–29.

[28] Baker DL. Post-apartheid Electricity Policy and the Emergence of South Africa's Renewable Energy Sector. Helsinki: UNU-WIDER; 2016. WIDER Working Paper 2016/15.

[29] Faulkner D, Loewald C, Makrelov K. Achieving higher growth and employment: Policy options for South Africa. Pretoria: South African Reserve Bank; 2013. Working Paper WP/13/032013.

[30] Herrington M, Kew J, Kew P. 2014 GEM South Africa Report (South Africa: The Crossroads – a Goldmine or a Time Bomb?). Cape Town: University of Cape Town; 2014.

[31] National Planning Commission. National Development Plan 2030: Our Future – Make it Work. Pretoria: The Presidency, Republic of South Africa; 2011.

Chapter 4

Flexible Operation of Electric Power Transmission Grids

Priyanko Guha Thakurta

Additional information is available at the end of the chapter

http://dx.doi.org/10.5772/64611

Abstract

In order to reduce carbon emissions and increase sustainability many countries in the world are switching to renewable sources of energy for electricity production. European Commission has set targets for its Member States to reduce such emissions and proposed share of renewables of around 30% in gross final energy consumption by 2030. Moreover, the electricity market is decentralized in Europe. As a result of decentralization and increased renewable penetration into the system, Transmission System Operators (TSOs) are faced with new challenges to operate their system securely. Some of the means of congestion management by the TSOs have become costly after decentralization. Moreover, variability associated with renewables can create congestion in a distant grid location which belongs to another TSO. Hence, TSOs are forced to find alternatives to operate their systems securely and in a cost effective manner. Inter-TSO coordination is one such non-costly alternative which requires increasing attention when more renewables are integrated into the system. The coordination (preventively and/or curatively) will help to operate the existing transmission grids more flexibly when more renewables integration demands transmission expansion, which is severely limited in Europe.

Keywords: FACTS, HVDC, TSO, preventive control, corrective control, system security, renewable energy

1. Introduction

Before the mid-1990s, the operation of power system in Europe[1] was quite straightforward as a single entity was responsible for generation, transmission, and distribution of electric power. That single entity was responsible for the safe system operation for all timeframes at a

---

[1] The prime focus is laid on European power system.

minimum cost possible. In order to increase market competition, the power system was decentralized/unbundled/liberalized in the mid-1990s with different market players responsible for system operation. The entity responsible for power transmission is the so-called transmission system operator (TSO). This stakeholder is now responsible for the efficient and secure operation of the power system.

The TSOs are facing increasing challenges in planning and operation of their systems, especially after decentralization and increased penetration of renewables. Before unbundling, the TSOs have direct control over generation unit redispatch and managing power flows through their systems (line and busbar switchings, capacitor switching, etc.) in order to resolve system congestion. The investment decisions on both generation and grid expansion were rather coordinated, with the generation planned close to the load centers. After decentralization, the TSO still makes the investment decisions, but the decisions in investments regarding generation expansion are not coordinated with the decisions regarding grid expansion. As a result, the new generators are located closer to the energy source.

The European Commission (EC) has undertaken significant measures to reduce carbon footprint of Continental Europe, by setting targets such as 2020, 2030, and 2050 [1]. The electrical energy sector is seen as a significant contributor for reducing carbon emissions because of (in general) the concentrated emissions and the availability of potential alternatives. Solar and wind are such suitable alternatives amongst other nonconventional sources of energy. A significant amount of wind energy sources is installed in Continental Europe. **Figure 1** shows the installation trend of wind integration in Europe.

Annual wind power installations in the EU have increased steadily over the past 15 years from 3.2 GW in 2000 to 12.8 GW in 2015 (**Figure 1a**), with a compound annual growth rate of 9%. 141.6 GW of wind is installed in the EU in 2015. In this year, it has achieved a record growth rate of 9.7% (**Figure 1b**). Germany has the highest number of wind installations in the world. The other countries that follow Germany in terms of wind installed capacities are Spain, the United Kingdom, France, and Italy. Eleven other EU countries have over 1 GW of installed capacity [2].

These renewable energy sources are highly variable in nature. More installations of these generation sources and their integration with the existing transmission system lead to higher variability within the system, as the variable injections from these renewables lead to variable power flows in the system, and more balancing actions in the electricity market are required to cope with this variability of these generation sources. At the European level, the best locations for wind farms are mostly onshore and offshore, whereas the best locations for solar generation are southern Europe. As these generation sites are far away from load centers, a transmission network expansion is required, as the existing network is limited to cope with the variability of these power flows [3]. However, major investments in the transmission system expansion have been lacking due to heavy siting opposition [4].

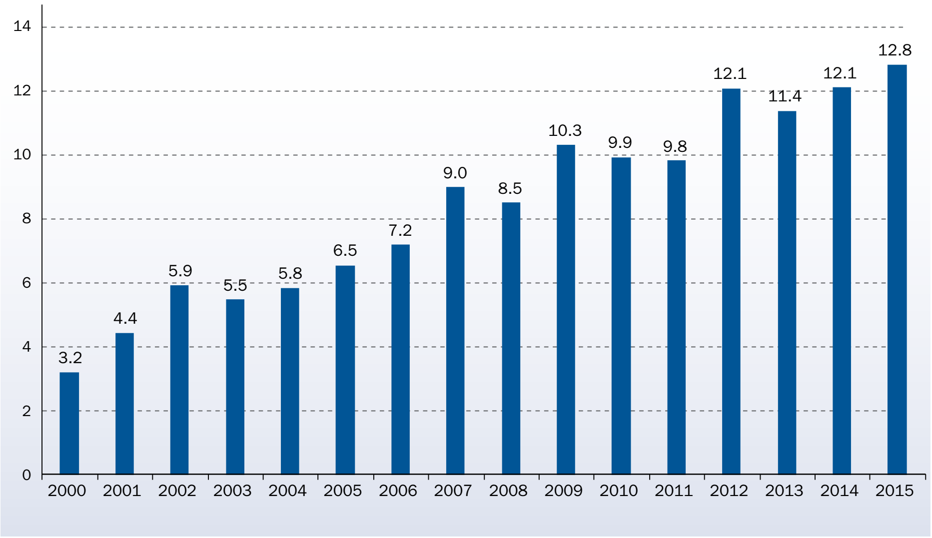

(a) Annual

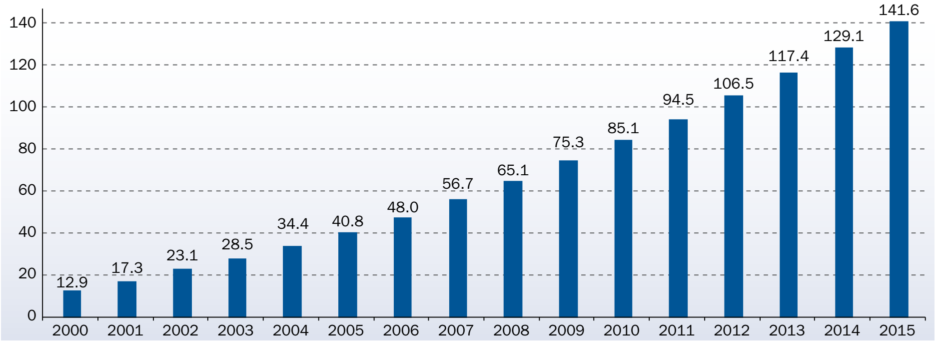

(b) Cumulative

Figure 1. Wind power installations in EU (GW) [2].

The changes, both in unbundling of the electricity sector and increased integration of renewables, have triggered a renewed interest in flexible alternating current transmission system (FACTS) devices, and especially in power flow controlling devices (PFCs) such as phase shifting transformers (PSTs) and High voltage direct current (HVDC). Several of these PFCs are installed in the European power system. FACTS devices, in general, are capable of controlling power flows [5–9], improving voltage stability [10–12] and small signal stability [13, 14], and damping power system oscillations [15–18].

Severe limitations for transmission expansion in Europe and the push towards integrating more renewables into the system lead to more stress on the existing grid. The only alternative that remains under those circumstances is to use the existing grid more flexibly and effectively with the help of already installed PFCs in the system. However, those devices need to be controlled in a coordinated manner among the TSOs in order to achieve a common objective, that is a system-based objective rather than individual-based.[2]

This chapter describes different activities that are involved in power system operation in Europe, especially in Central Western Europe (CWE[3]), starting from 2 days ahead of real-time operation and ending at real time. It also shows the effect of coordination among TSOs with respect to PFC operations that help to manage the system in an efficient way and increase more carbon-free generation sources into the system.

2. Power flow control and PFCs

For a lossless transmission line ($R_L = 0$) connected between buses "*s*" and "*r*", the active (P_L) and reactive (Q_L) power flows can be represented as [19]:

$$P_L = \frac{V_s V_r}{X_L} \sin(\theta_s - \theta_r) \tag{1a}$$

$$Q_L = \frac{V_s^2}{X_L} - \frac{V_s V_r}{X_L} \cos(\theta_s - \theta_r) \tag{1b}$$

where V_s and V_r are the bus voltage magnitudes of buses "*s*" and "*r*", respectively, θ_s and θ_r are the bus voltage angles of buses "*s*" and "*r*", respectively and X_L is the reactance of the transmission line. Both the active and reactive power are functions of four variables: line reactance, bus voltages at the two ends of the transmission line, and phase angle. In a meshed grid, line flows can be altered by changing any of those parameters. FACTS devices [6] are suitable means of altering those variables.

All PFCs are based on a switching technology in one way or the other. Based on different technologies used for switching, a classification can be made [20].

- The conventional devices use mechanical switching. Hence, these devices are not suitable for controlling system dynamics as they are relatively slow in operation. However, there are clear advantages of this technology, such as simplicity, relatively low cost, and high reliability [19].
- Thyristor-based devices can switch within a few periods of the mains frequency. However, they are line commutated devices, which limit their multiple switching operations within

---

[2] Controlling PFCs individually by a TSO can have a significant impact on its neighboring grid, as the European system is highly meshed and interconnected.

[3] A region consisting of Belgium, France, Luxembourg, Germany (Amprion, Tennet TSO GmbH and Transnet BW) and the Netherlands.

one half of the line voltage [21]. Classical high voltage direct current (HVDC) schemes employ such devices [19].

- Voltage source converters (VSCs) are relatively new type of converters that employ faster switching components. Pulse width modulation (PWM) schemes are used to control such devices. Such schemes are possible especially due to the latest advancements in solid-state components such as insulated gate bipolar transistors (IGBTs) [22]. VSCs are expensive, due to the high voltages used in the transmission system. The high switching frequency causes higher losses. However, new converter topologies, modulation techniques, and power electronic devices currently lowered the high switching frequency losses [19].

One such PFC is a so-called PST. The possibility of controlling the power flow by PSTs was already recognized long time ago, with the earliest applications more than 70 years before. PSTs are used to track slow load variations, in a timeframe of minutes to hours. Furthermore, they are used to redistribute line flows in systems with unequal loading on parallel paths. The PST inserts a voltage in the transmission line so that the phase angle between sending and receiving end voltages can be controlled. The basic operating principles for PSTs are ordinary transformer technology combined with on-load tap changers (OLTC). The phase angle shift is created by inserting a voltage in quadrature to the phase voltage. In ordinary three-phase systems, this quadrature voltage can be obtained as the line voltage between other phases. PSTs are also referred to as quadrature boosters. They are quite slow, but ideally suited to control power flow in the transmission system, e.g., to avoid overloading of critical lines or to counteract loop flows. Recently, a significant number of PSTs have been installed in continental Europe.

PSTs can be classified into direct/indirect and asymmetrical/symmetrical. A detailed description of these can be found in Ref. [19].

As stated in Section 1, the European TSOs are facing challenges to operate their systems securely. This is mainly due to the fact that increased penetration of renewable energy in one control area[4] of a TSO during real time can be significantly different than forecasted leading to congestion in the control area of another TSO, as the areas are highly meshed and interconnected. A typical example is shown in **Figure 2**. It is evident from the figure that approximately 7.4 GW of additional wind energy is injected into the system during real time at the 19th hour compared to that of the forecasted value. This extra injection created severe congestion in Dutch and Belgian transmission systems, which acted as an alternative path for the energy to reach the French system. This type of scenario will increase in the future with increased integration of renewables. There will be several such scenarios in the future in which a single TSO will not be able to solve problems in its own control area due to factors originating in another control area. In such cases, coordination will be a key aspect to address such problems.

---

[4] The area in which a TSO is solely responsible for power system security management. These areas are generally the geographic borders of the countries, exceptions being Germany and Luxembourg.

In order to understand the increased necessity of inter-TSO coordination in the future, it is necessary to understand the operation of European power system starting from 2 days ahead till close to real-time. The focus lies on the functioning of the system from a TSO perspective.

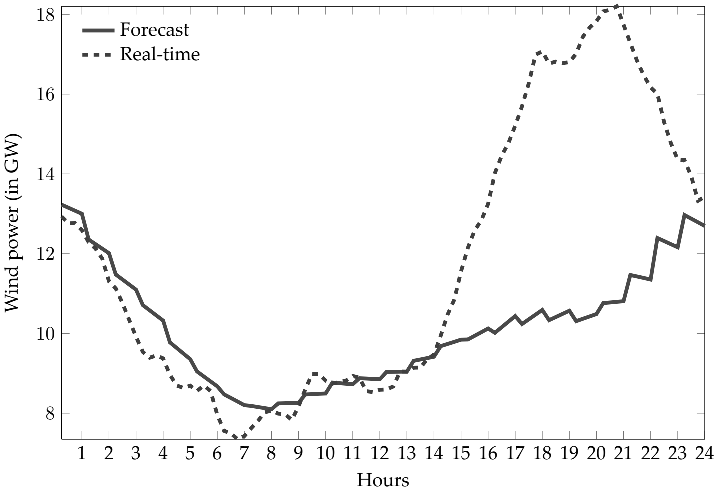

Figure 2. Wind power in Germany on January 19, 2012 [4].

3. Power system operation in Europe

The planning of power system in Europe during real time starts 2 days ahead of real time.

3.1. D-2

"D-2" represents 2 days ahead of real-time operation. The main activity that takes place at this timeframe is to assess cross-border capacities across the borders of interconnected countries. These cross-border capacities are then allocated to the day-ahead market. This process starts with defining an initial grid situation called basecase.[5] The physical margins available on the basecase situation are identified and additional exchanges are calculated and made available after the capacity calculation. The calculated results from the previous process are then validated by security engineers and involves:

- Taking into account the uncertainties that are not considered in the previous stage.
- Taking into account the operational limits, such as voltage limits. These limits are not taken into account in the calculation stage, due to the linearized problem.[6]

---

[5] It includes planned outages of network elements but does not include loss of network elements.

[6] DC approach is used for the calculation.

- Proposing corrections for the approximations made during the calculations.

The accuracy of this process depends on the availability of reliable information of the network of each TSO, including expected generation and load patterns and the corresponding buses at which they take place. Currently, flow-based capacity assessment is performed in the CWE region of Europe.

Detailed information about the activities at this timeframe can be found in Ref. [4].

3.2. D-1

"D-1" represents 1 day ahead of real-time operation. The electricity market is cleared at each power exchange (PE) of individual countries depending on the supply and demand bids and respecting the allocated cross-border capacities at each border assigned by the respective TSOs during D-2 system operation. The generation companies at each country optimize their generation portfolios that would meet the system demand with least possible cost (also termed as economic dispatch). The exact system bus injections are the outcome of it. These data are then provided to the TSOs to check the feasibility of the economic dispatch, as it does not consider the network topology. The TSOs perform security analyses of their respective control areas according to the contingency list. As part of standard operating practices, outages of all elements of the interconnected system at the level of 380/400 kV and above are considered as contingencies. Moreover, all outages of elements at the lower voltage levels of the interconnected system (220/150 kV) having significant influence on the security of the interconnected system operation are also considered as contingencies. Contingencies are of three types: normal, exceptional, and out-of-range. TSOs generally consider normal and exceptional contingencies in their contingency lists in order to check system security.

Each TSO prepares its contingency list consisting of all internal normal and exceptional contingencies considered relevant according to the risk management of the TSO. The risk management currently considered at the European level is "N[7]–k" criterion. The status of the control area of a TSO is reflected by it after an event defined in the contingency list. The N situation already includes L elements in outage. The N–k simulation considers those L elements as already out of operation and simulates the loss of k elements (these k elements are out of operation due to occurrence of an event defined in the contingency list) resulting in N–k state. Generally speaking, k is taken to be 1.

Any event in the contingency list must not endanger the security of the interconnected system operation. The operational condition within the control area of the TSO must not lead to triggering in an uncontrolled cascading outage propagating across the borders after an event. In order to prevent such cascading effects with impact outside the borders, each TSO launches N–1 security calculations, the aim of which is to become aware of the consequences of trips of network elements and to prepare adequate remedial actions (RAs) for managing such contingencies. The goal of RAs is to fully respect the N–1 principle taking inter-TSO coordi-

---

[7] It is also called basecase situation and is defined as the status of the control area of the TSO that includes outages but not contingencies. This situation takes into account all forecasted outages and known damages of network elements.

nation into account. The RAs must make sure that the principle of "no cascading with impact outside my borders" is respected at all times. The RAs are prepared at this timeframe by numerical simulations and to be duly applied in D timeframe. Mainly two types of RAs are considered by the TSOs: preventive and corrective.

3.2.1. *Preventive RAs*

Preventive RAs are a set of actions that are taken by the TSOs in anticipation to a need that may arise due to the lack of certainty to cope efficiently and in due time with the resulting constraints once they occur. With preventive RAs implemented, no immediate action is required when a contingency occurs, and the operator can slowly alter the grid parameters and topology to the next calculated optimal state including new security measures if the postcontingency state requires so. They are the first stage decisions, as grid security is the main objective [23].

3.2.2. *Corrective RAs*

Corrective actions are another set of measures that require immediate action of the operators to rapidly relieve the constraints with an implementation time delay for full effectiveness compatible with temporary admissible transmission loading (TATL[8]). These actions are implemented after the occurrence of the event. Before the event occurs, a screening of the possible contingencies and their required control actions is performed. Generally, outages of generators fall under this category. They are called second stage decisions [23].

When corrective actions are not sufficiently rapid, preventive RAs are implemented before the occurrence of the related contingency. The TSOs inform their neighboring TSOs if the corresponding RAs influence their neighbors in order to prevent countereffects on neighboring TSOs.

3.2.3. *Multistaged decisions*

The synchronous interconnection of the national grids of different countries in Europe in order to increase security of supply also has disadvantages with respect to managing the power system as the larger geographical regions need to be taken into account for security analyses. In such occasions, single contingency surveys seem inappropriate. The risk of cascading outages needs to be taken into account, which may lead to a partial or complete blackout. This may happen due to an unfortunate set of strategic outages and incidents, combined with unexpected injection patterns. In such cases, grid operators undertake multiple actions within a very short time. A series of decisions are undertaken to avoid the system to end up in a dangerous state [23].

In order to carry out load flow forecasts and to prepare RAs during this operational phase at D-1, it is necessary to exchange relevant data among the TSOs. This process of congestion forecasting is called day-ahead congestion forecast (DACF) procedure and is based on the most

---

[8] It is the loading in amperes, MVA or MW that can be accepted through a transmission line for a certain limited duration.

reliable network models exchanged by the TSOs. A total of 24 DACF files are prepared by each TSO in continental Europe, merged to form a single DACF file for each hour. Based on this merged file, contingency analyses are performed considering the designed contingency list of each TSO. Thus, a comprehensive 24-hour review of the security risks of the grid for the following day is generated. The RAs are then determined taking into account the severity of the constraints and the available time to relieve them.

3.3. Intraday and close to real-time (D)

At the day of actual operation, the basecase situation is determined by state estimation on the basis of measurements and topology. The scope of N–1 security calculations at this timeframe is:

1. Each TSO performs an automatic N–1 simulation systematically for all the contingencies inside the contingency list in order to detect potential constraints within the control area according to the risk policy of the TSO. Each of these simulations takes place with a periodicity of 15 minutes.

2. Each TSO performs an additional N–1 simulation to confirm the diagnosis of simulations performed in D–1, taking into account the new topology of the network. The efficiency of the remedies is mainly verified.

3. Each TSO also performs a new $\widetilde{\mathrm{N}} - 1$ security calculation in order to detect future constraints (a $\widetilde{\mathrm{N}}$ is a situation after tripping an element. In other words, $\widetilde{\mathrm{N}} = \mathrm{N} - 1$ + applied remedies). This analysis is carried out immediately after the RAs are implemented for the first N-1 event occurrence. Hence, a new set of RAs are prepared for the new constraints that may occur, including coordination among TSOs.

After the occurrence of the first contingency at this timeframe, the TSOs launch the already prepared RAs (prepared at D–1) without delay in order to keep the system secure, that is, new N (= $\widetilde{\mathrm{N}}$) is safe but new $\widetilde{\mathrm{N}} - 1$ may not be safe for the system. The impacted TSO, being then in a secure situation $\widetilde{\mathrm{N}}$ launches security calculation to detect the risk and prepare new remedies. The TSO implements remedies with the minimum delay. If the RAs for a $\widetilde{\mathrm{N}} - 1$ are available and efficient in a short while the system is safe. Otherwise, the neighboring TSOs are informed about the delay in finding appropriate remedies and seeks help from them in order to avoid or reduce the delay. The system is prone to risk at this particular state. The study of new remedies must be done quickly as the system can be jeopardized after the contingency if no remedies are identified. However, the delay cannot be estimated as it depends on the available remaining facilities of the power system. During such situation, the impacted TSO is in "Alert" state and provides the necessary information to its neighbors and searches convenient RAs with them.

Both at D-1 and D timeframes the regional coordination eases and enhances the search of (possible, but may or may not be optimized) coordinated solutions in case of a call for help. Coordination is done to decide on a convenient set of RAs in case best efforts by the impacted TSO to be implemented at first are not sufficient. Regional coordination enhances the chance to find optimized/nonoptimized remedies and to prepare procedures or agreements for coordinated remedies. The general principle that is followed to relieve constraints by applying RAs is:

- First, the impacted TSO monitoring a constraint violation checks the implementation of internal RAs by itself.
- If the internal RAs are not efficient,[9] appropriate RAs are decided in a coordinated manner with the neighboring TSOs.
- The prepared RAs are ready to be implemented in the control area where the contingency occurred or in the other control area(s) having significant impact.
- The RAs prepared with the help of regional coordination can involve other control area(s) having less impact.
- At this stage, specific analysis for costly measures taken by one or several TSOs to implement RAs is to be dealt within the framework of bilateral/multilateral TSO to TSO procedures.

4. Available means for RAs

The available means that are utilized by the TSOs for the RAs include costly and noncostly measures.

4.1. Noncostly measures

These remedial measures come at a zero cost to the TSOs. This is mainly due to the fact that these measures generally involve those assets which are owned and operated by them. Following measures are commonly undertaken by the TSOs:

1. Changing the topology of the system that includes some discrete actions on transmission devices. The most common practices within this action are transmission line switching [24–26] and substation busbar switching [24, 26].
2. Using FACTS devices.
3. Using HVDC that is owned and operated by the TSO.
4. Dynamic use of the existing transmission lines respecting their dynamic ratings rather than their static ratings. However, the prediction methods of the dynamic ratings must be reliable.
5. Inter-TSO coordination with respect to system operation.

---

[9] Efficient means that the RAs are prepared with respect to the compromise between their effectiveness and their costs.

4.2. Costly measures

These measures come at a significant cost to the TSOs in a decentralized environment.

1. Redispatching generation within the control area of the TSO or a cross-border redispatch [27].
2. Using HVDC that is not owned by the TSO.
3. By employing demand-side management (DSM) measure [28], that involves lowering the demand of electricity. This measure is treated as a dispatchable resource and is called upon when needed.
4. Curtailing load in the system. This is not done by the TSOs in Europe for congestion management, and is done manually or automatically for underfrequency cases when sufficient generation or managing congestion is not possible.

Considering the current scenario in Europe with respect to renewables integration more flexibility in system operation and increased inter-TSO coordination will be required in the future. The flexibility can be achieved by a coordinated control of PFCs. Several of the PFCs are already installed in continental Europe mainly for five reasons:

1. Give more control options to the TSOs after decentralization.
2. Help to manage variable energy flows caused by increased cross-border trade and higher intermittent generation.
3. Improve reliability by interconnecting different regions and even different synchronous zones.
4. Offer firm capacity to the market through control.
5. In some cases they are the only feasible investment options.

5. Mathematical modeling to take coordinated control of PFCs into account

This section briefly describes the mathematical approach to consider PFCs in a coordination process. DC approach is adopted, as it works very well for the transmission system of Europe [29].

5.1. Modeling of PSTs in power flows

The DC modeling of PSTs is derived in this section [19].

5.1.1. Bus angle difference approach

If a single PST with phase shift α_{kj} is connected in series with the line between buses k and j, the power through that line is:

$$P_{kj} = B_{kj}(\theta_{kj} + \alpha_{kj}) \tag{2}$$

The DC power flow equations in matrix form can be represented as:

$$\Delta\mathbf{P} = [\mathbf{B}^{\mathrm{T}}] \cdot [\Delta\theta] \tag{3}$$

Taking the phase shift into account, Eq. (3) becomes

$$\Delta\mathbf{P} = [\mathbf{B}^{\mathrm{T}}] \cdot [\Delta\theta] + [\mathbf{B}_{\alpha}^{\mathrm{T}}] \cdot \alpha_{kj} \tag{4}$$

where $\mathbf{B}_{\alpha}$ is a vector with value B_{kj} at position k, $-B_{kj}$ at position j, and zero elsewhere. Solving this matrix equation yields:

$$\Delta\theta = [\mathbf{B}^{\mathrm{T}}]^{-1} \cdot \left(\Delta\mathbf{P} - [\mathbf{B}_{\alpha}^{\mathrm{T}}] \cdot \alpha_{kj}\right) \tag{5}$$

Referring to the element (k,j) of the matrix $[\mathbf{B}^{\mathrm{T}}]^{-1}$ as c_{kj}; the angles θ_k and θ_j become:

$$\theta_k = c_{k1}\Delta P_1 + \cdots + c_{kk}(\Delta P_k - B_{kj}\alpha_{kj}) + \cdots + c_{kj}(\Delta P_j + B_{kj}\alpha_{kj}) + \cdots + c_{k(n-1)}\Delta P_{n-1} \tag{6}$$

$$\theta_j = c_{j1}\Delta P_1 + \cdots + c_{jk}(\Delta P_k - B_{kj}\alpha_{kj}) + \cdots + c_{jj}(\Delta P_j + B_{kj}\alpha_{kj}) + \cdots + c_{j(n-1)}\Delta P_{n-1} \tag{7}$$

Using the above two equations and considering $[\mathbf{B}^{\mathrm{T}}]^{-1}$ is symmetrical, the angle difference is:

$$\theta_{kj} = \theta_k - \theta_j = \sum_{i=1}^{n-1} \Delta P_i (c_{ki} - c_{ji}) + B_{kj}\alpha_{kj}(2c_{kj} - c_{kk} - c_{jj}) \tag{8}$$

Combining Eqs. (2) and (8), the active power through line kj considering PST in that line is

$$P_{kj} = B_{ij}\left(\sum_{i=1}^{n-1} \Delta P_i (c_{ki} - c_{ji}) + \alpha_{kj}(B_{kj}(2c_{kj} - c_{kk} - c_{jj}) + 1)\right) \tag{9}$$

Hence, the power flow through line kj with an installed PST is obtained by adding weighted sum of the system power injections ΔP_i and a linear term in the phase shift angle α_{kj}.

Similarly, the power flow through a line pq can be represented as a function of the installed PST setting in line kj.

$$P_{pq} = B_{pq}\left(\sum_{i=1}^{n-1} \Delta P_i (c_{pi} - c_{qi}) + \alpha_{kj} B_{kj} (c_{pj} - c_{pk} + c_{qk} - c_{qj})\right) \tag{10}$$

Though $\mathbf{B}^{\mathrm{T}}$ is a highly sparse matrix, $[\mathbf{B}^{\mathrm{T}}]^{-1}$ is very dense. Hence, the linear term in α_{kj} in Eq. (10) is nonzero for every line, except for the radial ones. This suggests that the PST has an influence over the entire network. However, the influence can be very small for distant lines.

5.1.2. PSDF approach

Phase shifter distribution factors (PSDF) can be defined as a change in the line real-power flow with respect to a change in the PST angle [30]:

$$\mathrm{PSDF} = \frac{\Delta P_{kj}}{\Delta \alpha_{pq}} \tag{11}$$

From Eqs. (9) and (10), PSDFs can be derived as:

$$v_{kj}^{kj} = \frac{\partial P_{kj}}{\partial \alpha_{kj}} = B_{kj}(1 + B_{kj}(2c_{kj} - c_{kk} - c_{jj})) \tag{12}$$

$$v_{kj}^{pq} = \frac{\partial P_{pq}}{\partial \alpha_{kj}} = B_{pq} B_{kj} (c_{pj} - c_{pk} + c_{qk} - c_{qj}) \tag{13}$$

From Eqs. (12) and (13), it is seen that these factors only depend on the network configuration and not on the bus power injections.

The power flows in the system with varying PST angle α_{kj} in terms of PSDFs are:

$$P_{kj} = P_{kj,0} + \alpha_{kj} v_{kj}^{kj} \tag{14}$$

$$P_{pq} = P_{pq,0} + \alpha_{kj} v_{kj}^{pq} \tag{15}$$

where $P_{kj,0}$ and $P_{pq,0}$ are the reference flows, i.e., the DC flow without considering any PSTs.

In presence of multiple PSTs in the system, the equations for the line power flows are adapted accordingly. If another PST is present in the line mn too, Eqs. (14) and (15) are modified as:

$$P_{kj} = P_{kj,0} + \alpha_{kj} v_{kj}^{kj} + \sum_{\substack{(m,n) \\ (m,n)\neq(k,j)}} \alpha_{mn} v_{mn}^{kj} \tag{16}$$

$$P_{pq} = P_{pq,0} + \sum_{(m,n)} \alpha_{mn} v_{mn}^{pq} \tag{17}$$

Hence, every PST contributes with an extra term to the power flow in the line.

It can be concluded that under the DC load flow assumptions, the active power flow in a line is a linear combination of the PST settings. The key element is the network configuration. Therefore, if the matrix of PSDFs is written as Ξ, a particular choice of PST angles leads to a constant term $\Delta\mathbf{P} = \Xi\alpha$ added to the line flows at zero phase shift.

5.2. Modeling of HVDC in power flows

The quadratic power flow equations are linearized for the DC grid [31]. The steady-state power flow in a HVDC line from bus k to m is represented by Eq. (18), where V_k is the voltage at bus k:

$$P_{km} = \frac{V_k(V_k - V_m)}{R_{km}} \tag{18}$$

R_{km} is the resistance of the HVDC line between the two buses. If it is assumed that the DC voltages are rather close to the nominal voltage, Eq. (18) can be approximated as:

$$P_{km} \approx \frac{V'_k - V'_m}{R_{km}} \tag{19}$$

The resulting voltages V'_k and V'_m give only the deviation from the nominal voltage at the reference bus. The ohmic losses in the DC grid are neglected.

6. Advantages of coordinated control of PFC operation

In order to address the challenges involved in achieving the environmental targets of the European Commission an FP7 project called Twenties was initiated in the year 2010 by the Commission. Work package 5 of the project addressed network enhanced flexibility (NET-

FLEX), which addresses how the existing transmission grid of Europe can be utilized with the help of PFCs and manage more renewables in the system.

6.1. Achieved flexibility in terms of daily system operation

The PFCs, especially the PSTs that are already installed in the power system of Europe, and especially in Western Europe, are used when the loop flows are over and above their prespecified values by the TSOs. These devices are also often used to manage system security by the TSO for its own control area or to manage problems originating in other control areas through coordination process. Within the scope of this work package, algorithms were developed to demonstrate that increased coordination among TSOs can resolve complex security problems which otherwise required costly measures.

Eight PSTs in CWE that were considered to show the coordination effect were Zandvliet, Van-Eyck (two of them), Diele (two of them), Meeden (two of them), and Gronau. They are shown in **Figure 3**.

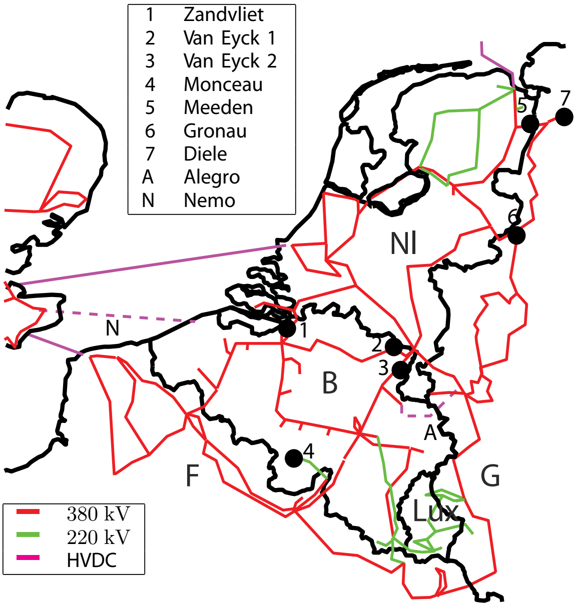

Figure 3. Existing controllable devices installed in CWE area [32].

Figure 4 shows a margin analysis graph. In the graphs, the loadings of the lines present in the critical branches (CB[10]) list are sorted from highest to lowest both for "N" and "N–1" situations and for all 24 hours, before and after optimization. The initial and optimized loadings present in the graphs can be defined as the ratios of initial to the maximum flows and ratios of the optimized to the maximum flows, respectively, for each line and for each contingency. On the

---

[10] It is defined as a transmission line that has a potential risk of being constrained due to network security reasons.

x-axis, the individual line loadings for all considered lines in every contingency situation are shown in a monotone diagram. A total of 45 CBs are taken into account in basecase, which considers all CBs in operation. Each CB is then taken out one at a time, and the flows on the remaining 44 CBs are calculated. Hence, each line occurs 45 times in each file and 24 files are generated for a day. The figure shows the results for all 24 hours and the number of data points along the horizontal axis is 48,600 [(45 CBs for basecase + 45 "N-1" cases × 44 CBs) × 24]. The x-axis shows lines (CBs) as a percentage, with each 25% representing 12,150 data points in **Figure 4(a)**. **Figure 4(b)** shows the zoomed-in part of the graph that is most relevant, consisting of first 500 data points. Hence, $\frac{500}{48,600} \times 100$ is the whole segment.

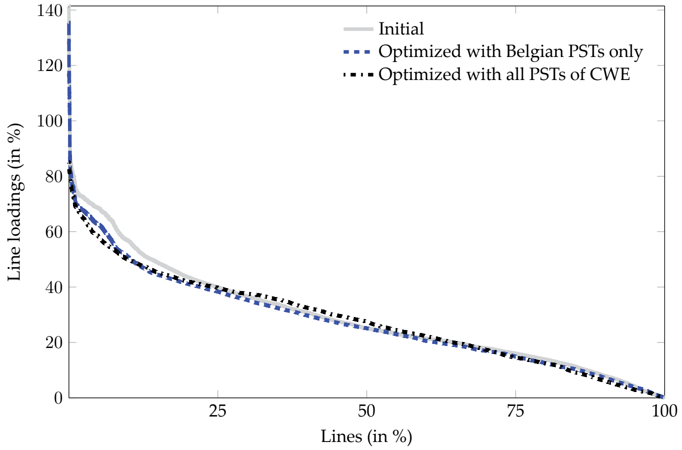

(a) Normal view

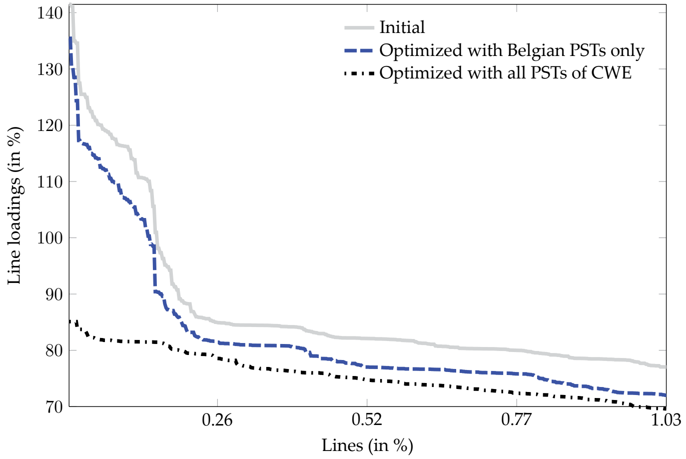

(b) Zoomed view

Figure 4. System loading.

It is evident from the figure that the system is already 41% loaded over the maximum allowable (represented by the solid line). This scenario is characterized with high wind in Northern Germany, creating congestion in the Belgian controlled area for a day in the past before the initiation of this project. The TSO of Belgium was not able to solve the problem with any noncostly means available and had to resolve the problem with costly measures (internal redispatch of generators). The problem still remains unsolved[11] with the help of Belgian PSTs only (Zandvliet and Van-Eyck's), as is evident from the dashed line in the figure. However, when all the considered PSTs are optimized simultaneously the overloading was eliminated and a margin of approximately 15% from the maximum allowable loading is achieved. This extra margin can be used to deal with uncertainties in the system, e.g., renewables. In Europe, this type of situation is increasing and will be going to increase in the future due to rapid integration of more renewables into the existing system. The coordination among TSOs is an essential noncostly means that TSOs must account for on a day-to-day basis in order to make the existing grid operation more flexible in terms of PFC operation so that both increased penetration of renewables and uncertainties inherent to them can be handled.

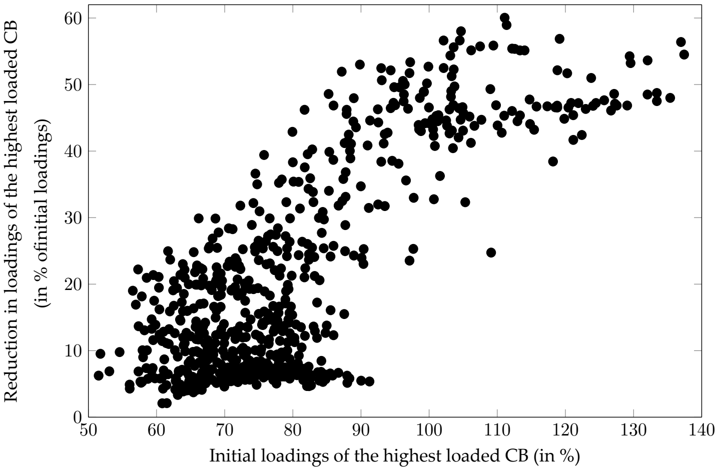

Figure 5. Reduction of highest loaded CB for every time-stamp for January 2013.

The developed algorithm was also validated for an entire month of January 2013 (it was a high wind period), the results of which are shown in **Figure 5**. The x-axis shows the initial loading of the system for each hour of the day of the entire month, whereas the y-axis represents the reduction in system loading from the initial. It is evident that in many cases the system was overloaded (all points on the x-axis beyond the 100% mark are overloaded situations). A careful investigation of the figure reveals that a significant reduction of overloading is achieved for the cases that are highly overloaded. For example, approximately 55% of loading is reduced for the case, which is initially loaded for 138%. In this particular

---

[11] Although the overloading is reduced a bit.

case additional 17% (100% − [138 – 55]%) of margin is achieved. Moreover, for all of the cases the system is relieved from overloading, and a significant amount of extra margin is attained for each of them. This clearly indicates coordination among TSOs indeed helps to avoid costly measures of removing system congestion, and will be often required in the future in Europe [33].

6.2. Achieved flexibility in terms of increased wind penetration

Increased intermittency demands increased balancing actions in a power grid. Severe congestion are frequent, demanding an expansion of the transmission grid. However, transmission grid expansion in Europe is severely limited. Hence, the existing grid must handle the increased penetration of uncertain generation sources. This can only be achieved by a flexible grid operation through inter-TSO coordination. The same work package addressed how much additional wind can be handled in the existing transmission grid in Europe.

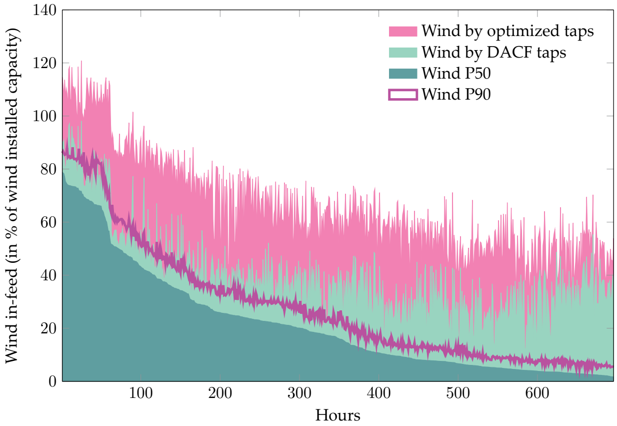

Figure 6. Additional wind that could be integrated during January 2013.

Figure 6 shows the results of 1 month validation of additional in-feed of wind. The forecasted wind or P50[12] values are represented by the cadet blue area for the entire month. The DACF files already integrate certain values of PST tap settings in order to keep loop flows through the transmission system of a TSO within certain limits decided by the TSOs themselves. The additional stress due to those already included tap positions is represented by the aquamarine area over and above the P50 values that can be handled with the help of all the PSTs in CWE, and for a given direction of stress (that is, for a certain GSK).[13] The wind P50 values are already integrated in the DACF files. The additional stress that can be han-

---

[12] Pxx represents an "xx" amount of probability that the wind in real time remains below the corresponding value (considering normal distribution).

[13] GSK, termed as generation shift keys defines the way of change in net position that is mapped to the generating units in a bidding area, representing in average the relation between the change in output of every generating unit inside the same market area. More information can be found in Ref. [33].

http://dx.doi.org/10.5772/64611

dled by optimizing all the PSTs in CWE area is represented by the carnation pink area. The fuchsia line represents the wind P90 values. The figure clearly shows that a significant amount of additional wind in-feed is possible in CWE with the help of PST coordination, which can even surpass P90 values in many cases. Hence, it is clear that an increased TSO coordination can help to handle more intermittency in the existing transmission grid by making the latter more flexible in operation [33].

Author details

Priyanko Guha Thakurta

Address all correspondence to: p.guhathakurta@skoltech.ru

Skoltech, Skolkovo Institute of Science and Technology, Moscow, Russia

References

[1] European Commission. *European Commission: Climate Action*. http://ec.europa.eu/clima/policies/ets/index_en.htm.

[2] EWEA. *Wind in Power 2015 European Statistics*. https://windeurope.org/wp-content/uploads/files/about-wind/statistics/EWEA-Annual-Statistics-2015.pdf. 2016

[3] P. Panciatici, G. Bareux, and L. Wehenkel. Operating in the fog: Security management under uncertainty. *IEEE Power Energy Mag.*, 10(5):40–49, 2012.

[4] P. G. Thakurta. *Increasing Transmission System Operation Flexibility using Power Flow Controlling Devices*. PhD thesis, Lueven: KULeuven, March 2015.

[5] D. J. Gotham and G. T. Heydt. Power flow control and power flow studies for systems with FACTS devices. *IEEE Trans. Power Syst.*, 13(1):60–65, Feb 1998.

[6] N. G. Hingorani and L. Gyugyi. *Understanding FACTS: Concepts and Technology of Flexible AC Transmission Systems*. New York: Wiley-IEEE Press, 1999.

[7] N. Li, Y. Xu, and H. Chen. FACTS-based power flow control in interconnected power system. *IEEE Trans. Power Syst.*, 15(1):257–262, Feb 2000.

[8] M. Noroozian, L. Angquist, M. Ghandhari, and G. Andersson. Use of UPFC for optimal power flow control. *IEEE Trans. Power Del.*, 12(4):1629–1634, Oct 1997.

[9] Y. Xiao, Y. Song, and Y. Sun. Power flow control approach to power systems with embedded FACTS devices. *IEEE Trans. Power Syst.*, 17(4):943–950, Nov 2002.

[10] H. Feng Wang, H. Li, and H. Chen. Coordinated secondary voltage control to eliminate voltage violations in power system contingencies. *IEEE Trans. Power Syst.*, 18(2):588–595, May 2003.

[11] W. Shao and V. Vittal. LP-based opf for corrective FACTS control to relieve overloads and voltage violations. *IEEE Trans. Power Syst.*, 21(4):1832–1839, Nov 2006.

[12] N. Yorino, E. El-Araby, H. Sasaki, and S. Harada. A new formulation for FACTS allocation for security enhancement against voltage collapse. *IEEE Trans. Power Syst.*, 18(1):3–10, Feb 2003.

[13] M. H. Haque. Improvement of first swing stability limit by utilizing full benefit of shunt FACTS devices. *IEEE Trans. Power Syst.*, 19(4):1894–1902, Nov 2004.

[14] Y. Tang and A. P. S. Meliopoulos. Power system small signal stability analysis with FACTS elements. *IEEE Trans. Power Del.*, 12(3):1352–1361, Jul 1997.

[15] B. K. Kumar, S. N. Singh, and S. C. Srivastava. Placement of FACTS controllers using modal controllability indices to damp out power system oscillations. *IET Gen. Transm. Distrib.*, 1(2):209–217, March 2007.

[16] Y. Li, C. Rehtanz, S. Ruberg, and L. Luo. Wide-area robust coordination approach of hvdc and facts controllers for damping multiple interarea oscillations. *IEEE Trans. Power Del.*, 27(3):1096–1105, July 2012.

[17] U. P. Mhaskar and A. M. Kulkarni. Power oscillation damping using FACTS devices: Modal controllability, observability in local signals, and location of transfer function zeros. *IEEE Trans. Power Syst.*, 21(1):285–294, Feb 2006.

[18] M. Zarghami, M. L. Crow, and S. Jagannathan. Nonlinear control of FACTS controllers for damping interarea oscillations in power systems. *IEEE Trans. Power Del.*, 25(4):3113–3121, Oct 2010.

[19] J. Verboomen. *Optimisation of Transmission Systems by use of Phase Shifting Transformers*. PhD thesis, Delft: TU Delft, 2008.

[20] D. Van Hertem, J. Verboomen, R. Belmans, and W. L. Kling. Power flow controlling devices: An overview of their working principles and their application range. In IEEE, editor, *Proceedings of the 2005 International Conference on Future Power Systems*, p. 6. IEEE, Nov 2005.

[21] R. M. Mathur and R. K. Varma. *Thyristor-Based FACTS Controllers for Electrical Transmission Systems*. New York: Wiley-IEEE Press, 2002.

[22] N. Mohan, T. M. Undeland, and W. P. Robbins. *Power Electronics: Converters, Applications, and Design*. New York: John Wiley & Sons, 2003.

[23] J. Rimez. *Optimal Operation of Hybrid AC/DC Meshed Grids*. PhD thesis, Leuven: KU-Leuven, March 2014.

[24] R. Bacher and H. Glavitsch. Network topology optimization with security constraints. *IEEE Trans. Power Syst.*, 1(4):103–111, 1986.

[25] E. B. Fisher, R. P. O'Neill, and M. Ferris. Optimal transmission switching. *IEEE Trans. Power Syst.*, 23(3):1346–1355, 2008.

[26] A. A. Mazi, B. F. Wollenberg, and M. H. Hesse. Corrective control of power system flows by line and bus-bar switching. *IEEE Trans. Power Syst.*, 1(3):258–264, 1986.

[27] ETSO. *Evaluation of Congestion Management Methods for Cross-border Transmission*. Technical report, Florence Regulators Meeting, 1999.

[28] E. Shayesteh, M. P. Moghaddam, A. Yousefi, M. R. Haghifam, and M. K. Sheik-El-Eslami. A demand side approach for congestion management in competitive environment. *Int. Trans. Electr. Energy Syst.*, 20(4):470–490, May 2010.

[29] D. Van Hertem, J. Verboomen, K. Purchala, and R. Belmans. Usefulness of DC power flow for active power flow analysis with flow controlling devices. In IET, editor, *Proceedings of the 8th IEE International Conference on AC and DC Power Transmission*, pp. 58–62. IET, Mar 2006.

[30] Z. X. Han. Phase shifter and power flow control. *IEEE Trans. Power Appt Syst.*, PAS-101(10):3790–3795, Oct 1982.

[31] R. Wiget and G. Andersson. Dc optimal power flow including HVDC grids. In IEEE, editor, *Proceedings of the IEEE Electrical Power & Energy Conference (EPEC)*, pp. 1–6. IEEE, Aug 2013.

[32] ENTSO-E. *Network Codes*. http://networkcodes.entsoe.eu/.

[33] P. G. Thakurta, J. Maeght, R. Belmans, and D. Van Hertem. Increasing transmission grid flexibility by TSO coordination to integrate more wind energy sources while maintaining system security. *IEEE Trans. Sust. Energy*, 6(3):1122–1130, Aug 2014.

Chapter 5

–5/3 Kolmogorov Turbulent Behaviour and Intermittent Sustainable Energies

Rudy Calif, François G. Schmitt and
O. Durán Medina

Additional information is available at the end of the chapter

http://dx.doi.org/10.5772/106341

Abstract

The massive integration of sustainable energies into electrical grids (non-interconnected or connected) is a major problem due to their stochastic character revealed by strong fluctuations at all scales. In this paper, the scaling behaviour or power law correlations and the nature of scaling behaviour of sustainable resource data such as flow velocity, atmospheric wind speed, solar global solar radiation and sustainable energy such as, wind power output, are highlighted. For the first time, Fourier power spectral densities are estimated for each dataset. We show that the power spectrum densities obtained are close to the 5/3 Kolmogorov spectrum. Furthermore, the multifractal and intermittent properties of sustainable resource and energy data have been revealed by the concavity of the scaling exponent function. The proposed analysis frame allows a full description of fluctuations of processes considered. A good knowledge of the dynamic of fluctuations is crucial to management of the integration of sustainable energies into a grid.

Keywords: turbulence, kolmogorov spectrum, intermittency, multifractality

1. Introduction

The installed capacity for energy from solar farms, wind farms and marine energy systems is constantly increasing in response to worldwide interest in low-emissions power sources and a desire to decrease the dependence on petroleum. The variability and unpredictability of this kind of resources over short time scales remains a major problem, as its penetration of this energy into the electric grid is limited. Hence, a good knowledge of renewable resource

INTECH
open science | open minds

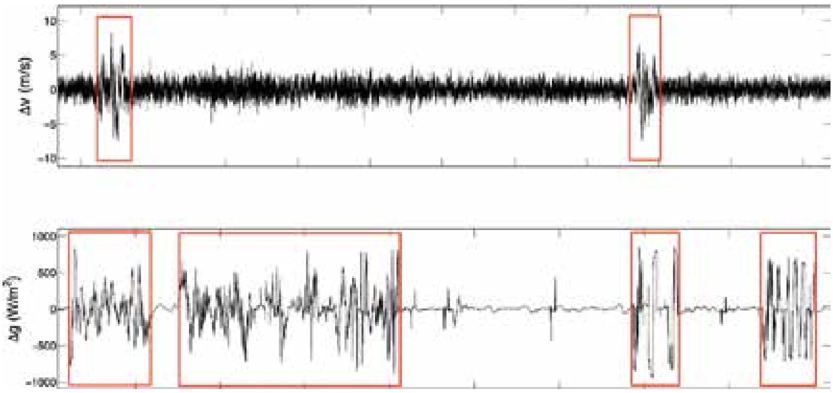

Figure 1. Examples of temporal increments of atmospheric wind speed Δv and the global solar radiation Δg. These sequences show intermittent bursts.

variations and intermittency is of real practical importance in managing the electrical network integrating this kind of energy.

Figure 1 illustrates examples of temporal increments of atmospheric wind speed and global solar radiation for a time scales $\Delta v = 5\,\mathrm{min}$. We can observe the existence of intermittent bursts. Following, the disciplinary field, the concept of intermittency can be defined differently [1, 2]. In the wind and solar energies fields, the concept of intermittency is often defined as the variability [2]. In turbulence field, Batchelor and Townsend have observed the intermittency experimentally for the first time in 1949 [3] and formalized in the multifractal framework after the seminal works of Kolmogorov [4]. The meaning of intermittency can change according to the authors. Frisch defines an intermittent signal if "it displays activity during only a fraction time, which decreases with the scale under consideration". According to Pope, a motion "sometimes turbulent and sometimes non-turbulent" characterizes an intermittent flow. In the engineering field, the intermittency is considered as a transition between a laminar and turbulent flows [1].

Here, the concept of intermittency in the fully developed turbulence framework is used, with with the help of multifractal analysis. This allows a better description of a stochastic signal at all scales and all intensities.

Multifractal analysis techniques have encountered an amount success through several disciplinary fields, such as, for instance, turbulence [5–8], finance [9–11], physiology [12], rainfall [13, 14] and geophysics [15, 16].

In this chapter, the intermittent properties of renewable resources data (wind speed, solar radiation and flow velocity data) and sustainable energy data (power output data from WECS and marine energy systems) are investigated using a classical multifractal analysis method, structure functions analysis.

The structure of this chapter is as follows. Section 2 describes briefly the fully developed turbulence framework. Section 3 presents the results analysis.

2. Fully developed turbulence framework

2.1. Richardson's cascade and Kolmogorov theory

The intuitive scheme of Richardson has largely inspired numerous authors in the turbulence field. Richardson provided a poetic form of energetic cascade [17] this is represented by a schematic illustration of Kolmogorov-Obhukov given in (**Figure 2**):

"Big whirls have little whirls that feed on their velocity,

And little whirls have lesser whirls

And so on to viscosity in the molecular sense"

The mathematical formalization of this scheme is given in 1940s by Kolmogorov who postulated the local-similarity hypothesis, i.e. small-scale turbulence is homogeneous and statistically isotropic in the inertial sub-range and hypothesized that velocity fluctuations Δv between two points separated by a distance r depend only on the average dissipation rate ε. This translates into the following expression for the squared fluctuations $S_2(r) = \left(\Delta v_r\right)^2 = \left(v_{x+r} - v_x\right)^2$ [4]:

$$S_2(r) \approx \varepsilon^{2/3} r^{2/3} \tag{1}$$

This has been generalized, considering the structure functions for moments of order $q > 0$ of the absolute spatial velocity increments as follows [18]:

$$S_q(r) \approx \varepsilon^{q/3} r^{q/3} \tag{2}$$

This leads to the famous K41 linear law (when there is no intermittency):

$$\zeta(q) = \frac{q}{3} \tag{3}$$

where $\zeta(q)$ is the scaling exponent of the structure functions:

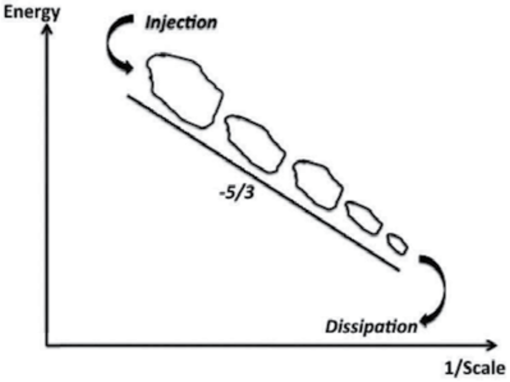

Figure 2. A schematic illustration of Kolmogorov-Obhukov spectrum that a −5/3 slope, based on Richardson's cascade concepts.

$$S_q(r) \approx r^{\zeta(q)} \tag{4}$$

This leads to the following expression for the power spectrum of velocity fluctuations in the Fourier space:

$$E(k) \approx k^{-5/3} \tag{5}$$

where k is the wave number.

In 1949, the experimental works of Batchelor and Townsend [3] highlighted the nonlinearity of the scaling exponent $\zeta(q)$ contrary to the K41 prediction. This nonlinearity indicates the intermittent character of the dissipation energy, caused by the inhomogeneity and anisotropy of the turbulent flow. To take intermittency into account, many theoretical formulations have been provided for a quantitative description of cascade processes and fitting the scaling exponent function $\zeta(q)$. The log-normal model was the first prediction describing the intermittency of the fully turbulence [18]:

$$\zeta(q) = \frac{q}{3} + \frac{\mu}{18}(3q - q^2) \tag{6}$$

where μ is the intermittency parameter. Thereafter, others models have been proposed. The most used are given in Section 2.3.

2.2. A description of scale invariance and multifractal framework

2.2.1. Self-similarity and scale invariance

The idea of describing natural phenomena by the study of statistical scaling laws is not recent [19]. Self-similarity has been widely observed in nature: self-similarity concept being the simplest form of scale invariance. A process $x(t)$ is self-similar if these statistical properties remains unchanged with the process $a^H x(t/a)$ obtained by simultaneously dilating the time axis by a factor $a > 0$, and the amplitude axis by a factor a^{-H}. H is called the self-similarity or Hurst parameter. This parameter provides information on the variability degree of process. A primitive model of self-similar signals is the fractional Brownian motion (fBm) $B_H(t)$ [20] for illustration, (**Figure 3**) shows a protion of flow velocity u dilated in the box, exibithing the statistical self-similarity features of flow velocity signal considered in this study.

The Fourier spectral density $E(f)$ of scale invariance or self-similar processes follows a power law obtained over a range of frequency f:

$$E(f) \sim f^{-\beta} \tag{7}$$

where β is the spectral exponent. According to some authors [19, 21, 22], it defines the degree of stationary of the signal:

- $\beta < 1$, the process is stationary
- $\beta > 1$, the process is no stationary
- $1 < \beta < 3$, the process is no stationary with increments stationary.

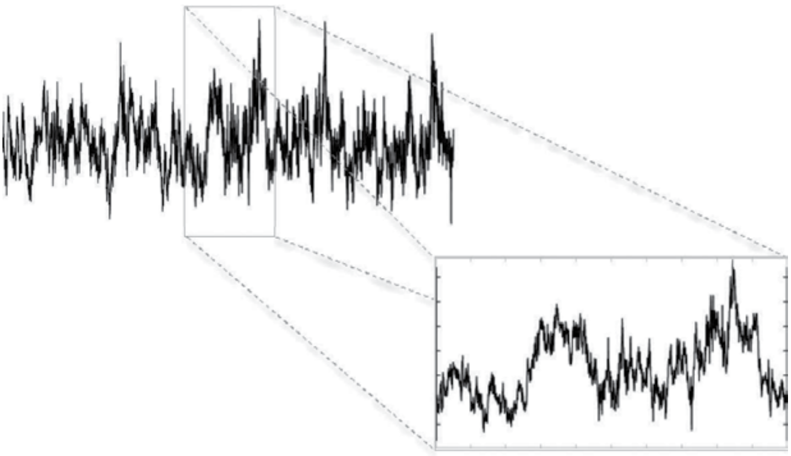

Figure 3. A portion of flow velocity u dilated in the box. This shows the statistical self-similarity features of flow velocity u.

2.2.2. Multifractal framework

The mathematical multifractal framework was appeared with the cascade multiplicative emergence in order to consider the intermittency of the energy dissipation in Turbulence.

Multiscaling concept allows the statistical description of stochastic signals for the modelling of physical systems, using multifractal technique analyses.

If $x(t)$ is a stochastic signal function of time, his scaling behaviour is highlighted when the time absolute time increments $|\Delta x| = |x(t+\tau) - x(t)|$, more precisely, the structure functions of order q respect the following relationship [5]:

$$S_q(\tau) = (|\Delta x|) \approx \tau^{\zeta(q)} \tag{8}$$

where τ is a time lag and ζ is the scaling exponent function. The full $(q, \zeta(q))$ curve for integer and non-integer q moments provides a full characterization of signal considered at all scales and at all intensities. The parameter $\zeta(2) = \beta - 1$ relates the second order moment to the β Fourier power spectrum scaling exponent. The parameter $H = \zeta(1)$ is the Hurst exponent with $0 < H < 1$. This parameter defines the degree of roughness or smoothness of a measured signal: more H is, the more the signal is smooth. The values of the $\zeta(q)$ function are estimated from the slope of the $S_q(\tau)$ versus τ in a log-log representation for all moments q. Concerning the scaling behaviour, the scaling exponent function is useful to characterize the statistics of a stochastic process. For a linear scaling function of the form qH, the signal is said to be monofractal; Brownian motion is described by $H = 1/2$, fractional Brownian motion is described by $0 < H < 1$, and homogeneous non-intermittent turbulence is described by $H = 1/3$. While for a nonlinear scaling exponent function, the signal is said to be multifractal. **Figure 4** illustrates the scaling behaviour of the $\zeta(q)$ function for instance a monofractal and multifractal processes. Furthermore, the concavity of $\zeta(q)$ function gives an indication on the intermittency degree of process considered: the more concave the curve is, the more intermittent the process [5, 22].

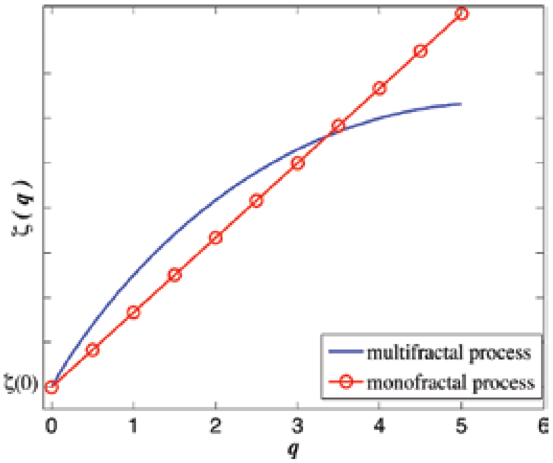

Figure 4. Examples of scaling exponent functions $\zeta(q)$ for a monofractal and a multifractal processes. The scaling exponent functions represented are linear and nonlinear (concave), respectively, for monofractal and multifractal processes.

2.3. Some multifractal models

Several models have been proposed to fit the scaling exponent function $\zeta(q)$ since in the literature, for instance, the "black and white" model [23], the log-normal model [18] and the log-stable model [22].

The "black and white" model proposed by Frisch et al. in 1978 is the simplest model [23]:

$$\zeta(q) = qH - \mu(q-1) \tag{9}$$

where H is the Hurst exponent and μ the intermittency parameter.

The classical lognormal model of the form:

$$\zeta(q) = qH - \frac{\mu}{2}(q^2 - q) \tag{10}$$

The log-stable or log-Lévy model proposed by Schertzer and Lovejoy in 1987 [22]:

$$\zeta(q) = qH - \frac{C_1}{(\alpha-1)}(q^\alpha - q) \tag{11}$$

where H is the Hurst exponent. The parameter C_1 is the fractal co-dimension measuring the mean intermittency: the larger C_1, the more the signal is intermittent. Furthermore, $0 < C_1 < d$ with d the dimension space (here $d = 1$). The multifractal Lévy parameter $0 < \alpha < 2$ inquires on the degree of multifractality i.e., how fast the inhomogeneity increases with the order of the moments. Furthermore, $\alpha = 0$ corresponds to the monofractal case and $\alpha = 2$ corresponds to the multifractal log-normal case.

In this chapter, we consider the log-normal model that provides a reasonable fit for the scaling exponent of data considered. In [24], the log-stable is considered for the global solar radiation data.

3. Results

In this chapter, we present analysis results from multiple time series sampled at different sampling rates and at different places. The atmospheric wind speed u was measured with a sampling frequency of 20 Hz during 40 h, on the wind energy site production of Petit-Canal in Guadeloupe an island located at 16°15′N latitude and 60°30′W longitude. The wind power output P was measured at the same place, with a sampling frequency of 1 Hz over a one-year period. A 10 MW wind farm delivers this wind power output. The global solar radiation measurements G was collected with a sampling frequency of 1 Hz over a one-year period, at the University site of Pointe-à-Pitre in Guadeloupe. The flow velocity measurements were generated from the facilities of the wave and current flume tank of IFREMER (French Research Institute for Exploitation of the Sea) in Boulogne-sur-mer (North of France). The data are collected with a sampling frequency of 100 Hz. **Figure 5** illustrates extract of signals considered. All the signals fluctuate over a large range scales showing the intermittent nature of sustainable resources and energy considered in this study.

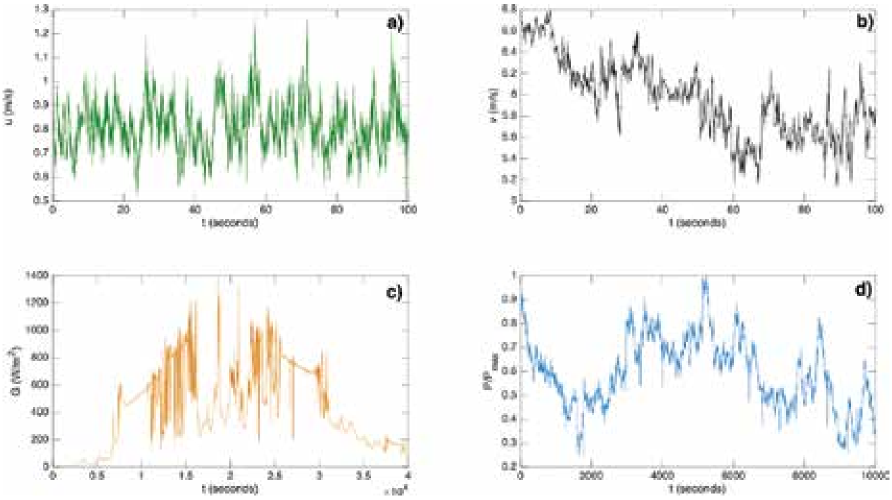

Figure 5. Examples of extract of signal considered: (a) flow velocity u, (b) atmospheric wind speed, (c) global solar radiation G, (d) normalized wind power output delivered by a wind farm. All the signals display strong fluctuations at all scales.

3.1. Fourier analysis of sustainable energy data and −5/3 Kolmogorov spectrum

The Fourier power spectral density separates and measures the amount of variability occurring in different frequency bands. In this section, the Fourier power spectral densities are estimated for our database in order to detect scale invariance. For a scale invariant signal, the following scaling power law is obtained over a range of frequency f:

$$E(f) \approx f^{-\beta} \tag{12}$$

where β is the exponent spectral.

Figure 6 shows the Fourier power spectral densities of databases described above, compared to the −5/3 Kolmogorov spectrum (red straight line), log-log representation. The spectra computed follow a power law of the $f^{-\beta}$ with β close to 5/3. As expected, the atmospheric wind and the flow velocity spectra demonstrate a scaling behaviour for the respective frequencies from about $f = 0.1–10$ Hz and $f = 0.1–50$ Hz with $\beta = 1.67$ close to the 5/3 Kolmogorov value [4, 25]. This is consistent with the values obtained for the inertial range in previous studies [26–28]. The wind power output spectrum displays a power law with $\beta = 1.68$ close to the 5/3 Kolmogorov value, for frequencies from about $f = 10^{-4}$ to 0.5 Hz. In 2007, Apt has shown that the wind power output from a wind turbine, follows a Kolmogorov spectrum over more than four orders of magnitude in frequency [29]. In [30], we show the wind power output spectrum with an exponent spectral close to the 5/3 value, which is observed for particular conditions.

The global solar radiation spectrum shows also a power law behaviour with $\beta = 1.66$ close to the 5/3 Kolmogorov value for frequencies from about $f = 0.7 \times 10^{-4}$ to 0.07 Hz. This scale invariance is indirectly linked to scale invariance of cloud field transported by atmospheric turbulence. In [31], a power law is also observed for the spectrum of cloud radiances obtained

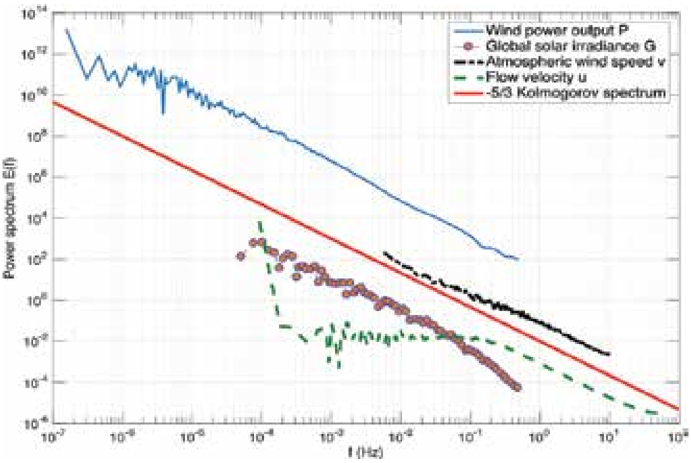

Figure 6. The Fourier power spectral densities for each dataset, compared with the −5/3 Kolmogorov spectrum.

from ground-based photography: the exponent spectral $\beta = 1.67$ is observed for clouds over ocean.

In summary, the spectra of sustainable data considered in this study, display power law behaviour with an exponent spectral close to the 5/3 Kolmogorov value. The slight difference with the exact 5/3 value is usually caused by intermittency effects [5, 22].

Furthermore, the Fourier power spectrum is a second order statistic providing information on medium level fluctuations, and consequently, its slope is not sufficient to fully describe a scaling process. Multifractal analysis is a natural generalization to fully study the scaling behaviour of a nonlinear phenomenon using, for example, the qth order structure functions.

3.2. Multifractal analysis of sustainable energy data

In order to qualify the nature of scaling behaviour (monofractal or multifractal), a multifractal analysis using qth order structure functions is applied to sustainable energy data to determine the scaling exponents $\zeta(q)$. For each dataset, the structure functions are computed on the temporal increments Δx as defined above. The details concerning the scale range of τ and q are given in the following references [24, 32–34]. As shown in [24, 32–34], the straight lines of structure functions indicate that the scaling of the relationship is well respected. Consequently, the scaling exponents $\zeta(q)$ are extracted from the slopes of the straight lines using a linear regression. **Figure 7** represents the scaling exponents $\zeta(q)$ corresponding to each dataset compared with a model proposed by Kolmogorov, the linear model K41, $\zeta(q) = q/3$. We can see that the scaling exponents $\zeta(q)$ obtained are nonlinear and concave. This highlights the

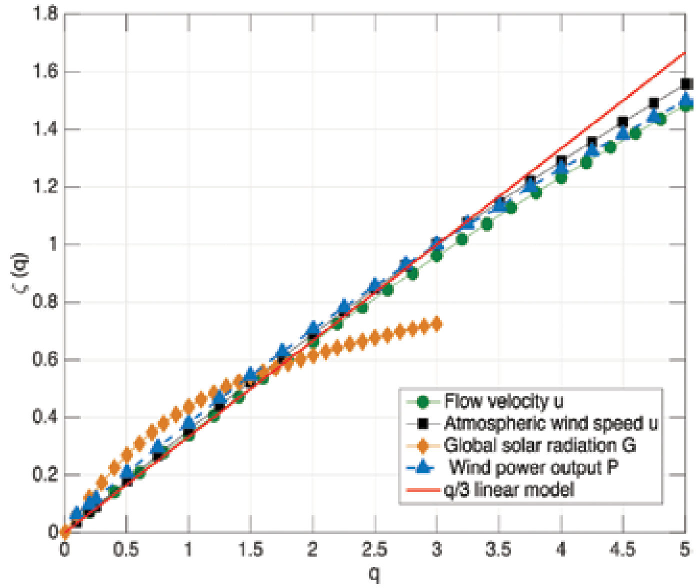

Figure 7. The scaling exponent functions $\zeta(q)$ for each dataset compared with the linear non-intermittent K41 model.

	H	$\zeta(2)$	μ
Flow velocity u	0.34	0.66	0.02
Atmospheric wind speed v	0.35	0.68	0.02
Wind power output P	0.38	0.70	0.06
Global solar radiation G	0.43	0.61	0.25

Table 1. Hurst exponent $H = \zeta(1)$, $\zeta(2)$ linked to the exponent spectral by $\zeta(2) = \beta$–1 and the intermittency parameter μ estimated for each dataset.

multifractal and intermittent character of considered sustainable data here. Furthermore, the degree of concavity gives an indication on the degree of intermittency: the more concave the scaling exponent curve is, the more intermittent the process. We recall that the intermittency parameter can be estimated by $\mu = 2\zeta(1)–\zeta(2)$ with $0 < \mu < 1$. **Table 1** draws up some parameters for each dataset: H the Hurst exponent, $\zeta(2)$, and the intermittency parameter μ.

As shown in **Figure 6** and indicated in **Table 1**, the global solar radiation G is the most intermittent.

4. Conclusion

This work highlights the intermittency and the scale invariance properties of flow velocity u, atmospheric wind speed v, wind power output P and global solar radiation G data, at all intensities and at all scales, in the fully developed turbulence framework.

We have shown for all datasets over the period encountered:

- The presence of a scaling regime or power law correlation of the form $f^{-\beta}$ over a broad range of time scales, in the Fourier space. The exponent spectral β is close to the exact 5/3 Kolmogorov value for all the datasets.
- The nature of the scaling behaviour for each dataset is determined using qth order structure functions analysis. The nonlinearity and the concavity of the scaling exponent functions $\zeta(q)$ obtained reveal the intermittent and the multifractal properties of datasets considered in this manuscript. This could result from the complex interaction of the turbulent atmospheric and the energy converter systems such as, for example, wind turbine.

With the increase in sustainable energies, a good knowledge of their nonstationary and intermittent properties is crucial. The fully developed turbulence framework is a relevant frame to analysis stochastic processes such as those considered in this manuscript. It allows providing a sharp description of fluctuations of processes at all scales and at intensities. The Hurst and the intermittency parameters can be used in stochastic simulations based on multifractal cascade model, as performed in [33]. Here, with a dynamical modelling of fluctuations sustainable energy considered, the interest could be, for instance, to test the stability evaluation of electricity grid.

Author details

Rudy Calif[1]*, François G. Schmitt[2] and O. Durán Medina[2]

*Address all correspondence to: rcalif@univ-ag.fr

1 Laboratory in Geosciences and Energies, University of Antilles, France

2 Laboratory in Geosciences and Oceanology, CNRS & University of Lille, Wimereux, France

References

[1] Seuront L and Schmitt FG: Intermittency. In Baumert H, Simpson J and Sündermann J editors. Marine Turbulences: Theories, Observations and Models. Cambridge, Royaume-Uni Press; 2005. pp. 66–78

[2] Tarroja B, Mueller F and Samuelsen S: Solar power variability and spatial diversification: implications from an electric grid load balancing perspective. International Journal of Energy Research. 2013; **37**: 1002–1016. doi:10.1002/er.2903

[3] Batchelor GK and Townsend AA: The nature of turbulent motion at large wave-numbers. Proceedings of the Royal Society of London A: Mathematical, Physical and Engineering Sciences. 1949; **199**: 238–255. doi:10.1098/rspa.1949.0136

[4] Kolmogorov AN: The local structure of turbulence in incompressible viscous fluid for very large Reynolds numbers. Doklady Akademii Nauk SSSR. 1941; **30**: 301–305

[5] Frisch U: Turbulence: the legacy of AN Kolmogorov. Cambridge, Royaume-Uni Press; 1995. 312 p. ISBN 978–0521457132

[6] Sreenivasan KR and Antonia RA: The phenomenology of small-scale turbulence. Annual Review of Fluid Mechanics. 1997; **29**: 435–472. doi:10.1146/annurev.fluid.29.1.435

[7] Bottcher F, Barth S, Peinke J: Small and large scale fluctuations in atmospheric wind speeds, Stochastic Environmental Research Risk, 2007; **21**: 299–308. doi:10.1007/s00477-006-0065-2

[8] Lohse D, Xia KQ: Small-scale properties of turbulent Rayleigh-Bénard convection. Annual Review of Fluid Mechanics 2010; **42**: 335–364. doi:10.1146/annurev.fluid.010908.165152

[9] Ghashghaie S, Breymann W, Peinke J, Talkner P, Dodge Y: Turbulent cascades in foreign exchange markets. Nature. 1996; **381**: 767–770. doi:10.1038/381767a0

[10] Schmitt FG, Schertzer D, Lovejoy S: Multifractal analysis of foreign exchange data. Applied Stochastic Models and Data Analysis. 1999; **15**: 29–53. doi:10.1002/(SICI)1099-0747(199903)15:1<29::AID-ASM357>3.0.CO;2-Z

[11] Calvet L, Fisher A: Multifractality in asset returns: theory and evidence. Review Economics and Statistics. 2002; **84**: 381–406. doi:10.1162/003465302320259420

[12] Ivanov P, Bunde A, Amaral L, Havlin S, Fritsch-Yelle L, Baevsky R, Stanley H, Goldberger A: Sleep-wake differences in scaling behavior of the human heartbeat: Analysis of terrestrial and long-term space flight data. Europhysics Letters. 1999; **48**: 594–600

[13] Schertzer D and Lovejoy S: Physical modeling and analysis of rain and clouds by anisotropic scaling multiplicative processes. Journal of Geophysical Research. 1987; **92**: 9693–9714. doi:10.1029/JD092iD08p09693

[14] Venugopal V, Roux SG, Foufoula-Georgiou E, Arnéodo A: Scaling behavior of high resolution temporal rainfall: new insights from a wavelet-based cumulant analysis. Physics Letters A. 2006; **348**: 335–345. doi:10.1016/j.physleta.2005.08.064

[15] Kantelhardt J, Koscielny-Bunde E, Rybski D, Braun P, Bunde A, Havlin S: Long-term persistence and multifractality of precipitation and river runoff. Journal of Geophysical Research. 2006; **111**: 1–13. doi:10.1029/2005JD005881

[16] Mauas PJD, Flamenco E, Buccino AP: Solar forcing of the stream flow of a continental scale South American river. Physical Review Letters. 2008; **101**: 168501. doi:10.1103/PhysRevLett.101.168501

[17] Richardson LF: Weather Prediction by Numerical Processes, 2nd ed. Cambridge, Royaume-Uni Press; 1922. 262 p. ISBN 978-0-521-68044-8

[18] Yaglom AM: The influence of fluctuations in energy dissipation on the shape of turbulence characteristics in the inertial interval. Soviet Physics Doklady. 1966; **11**: 26 p.

[19] Mandelbrot B: The Fractal Geometry of Nature. Macmillan; London, Royaume-Uni 1982.

[20] Manbelbrot BB and Van Ness JW: Fractional Brownian motions, fractional noises and applications. SIAM Review. 1968; **10(4)**: 422–437. doi:10.1137/1010093

[21] Marshak A, Davis A, Cahalan R and Wiscombe W: Bounded cascade models as nonstationary multifractals. Physical Review E. 1994; **49**: 55–69. doi:0.1103/PhysRevE.49.55

[22] Schertzer D, Lovejoy S, Schmitt F, Chigirinskaya Y and Marsan D: Multifractal cascade dynamics and turbulent intermittency. Fractals. 1997; **5(03)**: 427–471. doi:10.1142/S0218348X97000371

[23] Frisch U, Sulem PL, Nelkin M: A simple dynamical model of intermittent fully developed turbulence. Journal of Fluid Mechanics. 1968; **87**: 719–736. doi:10.1017/S0022112078001846

[24] Calif R, Schmit FG, Huang Y and Soubdhan T: Intermittency study of high frequency global solar radiation sequences under a tropical climate. Solar Energy. 2013; **98**: 349–365. doi:10.1016/j.solener.2013.09.018

[25] Obhukov AM: Energy distribution in the spectrum of turbulent flow. Izvestiya Akademii Nauk SSSR, Seriya Geologicheskaya. 1941; **5**: 453–466.

[26] Schmitt F, Schertzer D, Lovejoy S and Brunet Y: Estimation of universal multifractal indices for atmospheric turbulent velocity fields. Fractals. 1993; **1**: 568–575. doi:10.1142/S0218348X93000599

[27] Katul G and Chu CR: A theoretical and experimental investigation of energy-containing scales in the dynamic sublayer of boundary-layer flows. Boundary-Layer Meteorology, 1998; **86**: 279–312. doi:10.1023/A:1000657014845

[28] Lauren MK, Menabde M, Seed AW and Austin GL: Characterisation and simulation of the multiscaling properties of the energy-containing scales of horizontal surface-layer winds. Boundary-Layer Meteorology. 1999; **90**: 21–46. doi:10.1023/A:1001749126625

[29] Apt J: The spectrum of power from wind turbines. Journal of Power Sources. 2007; **169**: 369–374. doi:10.1016/j.jpowsour.2007.02.77

[30] Calif R, Schmitt FG, Huang Y and Medina O: Hurst exponent, multifractal spectrum and extreme events versus the installed capacity of wind farms, submitted.

[31] Sachs D, Lovejoy S and Schertzer D: The multifractal scaling of cloud radiances from 1m to 1km. Fractals. 2005; **10**: 253–264. doi:10.1016/j.jhydrol.2005.02.042

[32] Calif R and Schmitt FG: Modeling of atmospheric wind speed sequence using a lognormal continuous stochastic equation. Journal of Wind Engineering and Industrial Aerodynamics. 2012; **109**: 1–8. doi:10.1016/j.jweia.2012.06.002

[33] Calif R, Schmitt FG and Huang Y: Multifractal description of wind power fluctuations using arbitrary order Hilbert spectral analysis. Physica A: Statistical Mechanics and Its Applications, 2013; **392**: 4106–4120. doi:10.1016/j.phisa.2013.04.038

[34] Medina OD, Schmit FG and Calif R: Multiscale Analysis of Wind Velocity, Power Output and Rotation of a Windmill. Energy Procedia. 2015; **76**: 193–199. doi:10.1016/j.egypro.2015.07.897

Chapter 6

Multilayered Solar Energy Converters with Flexible Sequence of *p* and *n* Semiconductor Films

Yuri V. Vorobiev, Iker R. Chávez Urbiola,
Rafael Ramírez Bon, Liliana Licea Jiménez,
Sergio A. Pérez García, Pavel Vorobiev and
Paul Horley

Additional information is available at the end of the chapter

http://dx.doi.org/10.5772/65013

Abstract

Non-traditional design of multi-layered solar energy converters is proposed, with electrically independent *p-i-n* junctions. This new approach allows utilization of cheap and abundant II-VI, IV and IV-VI materials instead of III-V ones, using also cheap and economic deposition techniques like Chemical Bath Deposition (CBD) or Chemical Vapor Deposition (CVD) instead of expensive Molecular Beam Epitaxy (MBE). The CVD reactor with three atomic sources was built and used. II-VI and IV-VI semiconductor materials were prepared either in CVD reactor, or by CBD techniques. Besides, the original two-stage technology was employed: first the precursor oxide/hydroxide film of corresponding metal (like cadmium oxide/hydroxide) was prepared by some variety of CBD methods, and at the second stage, in CVD reactor the non-metallic component of precursor film was substituted by chalcogen, producing materials like CdS, CdSe, PbTe, etc. The semiconductor materials thus produced were of high quality, with basic parameters corresponding to those for the single crystals. Several experimental multilayered converters were constructed (in particular, with CdS/CdTe, CdS/PbS and Si/PbTe active bilayers). The preliminary results of their studying have shown that these and similar devices can be used in solar cells and photo sensors with satisfactory efficiency, and have great potential for improvement.

Keywords: multilayered solar cells, independent *p-n* junctions, II–VI and IV–VI semiconductor films, chemical bath deposition, chemical vapor deposition

1. Introduction

To utilize efficiently, a wide solar spectrum in conversion of solar radiation to electricity, several semiconductors with different band gaps must be used. This is usually realized in tandem solar energy converters with 2–4 *p-i-n* junctions of different semiconductors connected in series [1–3]. This design is applied to the solar cells made of different materials, including amorphous and organic ones. However, in the most efficient tandem converters (like those used in space applications), the expensive III–V materials are usually used, with molecular beam epitaxy (MBE) deposition technique that is also expensive. Besides, the serial connection of the elements means that the least effective junction defines the total photo current generated; the tunneling between adjacent *p-i-n* junctions causes additional losses.

Recently, we proposed a different construction of solar energy converters based on two of our patents [4–6], with electrically independent junctions that allow having a flexible sequence of *p* and *n* layers in them, and physically separate several junctions. This approach brings additional degrees of freedom to the converter's design, reduces the losses due to tunneling among the junctions and allows utilization of essentially cheaper II–VI, IV and IV-VI materials instead of III–V ones, with simple, cheap and ecologically pure technologies such as chemical bath deposition (CBD) with its variations (photo chemical bath deposition (PCBD) and successive ionic layer adsorption and reaction (SILAR)) or chemical vapor deposition (CVD), preserving high efficiency of solar energy conversion. This approach is explained in detail below, and the corresponding preliminary experimental results are presented.

2. Tandem solar cells—advantages and shortcomings: revision of the classical architecture

The first solar cell (1954) had the efficiency of 6%; today, after more than 60 years of research and development, the commercial solar modules reach efficiencies of 10–15%. This small value is a consequence of a wide solar spectrum, so that photons with maximum energy of 3–4 eV being absorbed in a semiconductor cell's material (Si, for example, with a band gap of around 1 eV) produce one electron-hole pair separated after thermalization in energy scale by this 1 eV, and the difference between the photon's energy and the band gap value is quickly (at approximately 10^{-12} s) transformed to heat by the process of emission of phonons. On the other hand, photons with energy smaller than the band gap are not absorbed and thus lost for energy conversion. Consequently, even in an ideal case when no other losses are present, the efficiency of one-semiconductor solar cell is not larger than approximately 30% (the so-called Schokley-Queisser limit [7]), and the corresponding practical limit is around 15%.

To achieve a higher efficiency of solar energy conversion, the abovementioned tandem photovoltaic converters are used, which actually are serially connected *p-i-n* junctions of different semiconductor materials with gradually decreasing band gap, such as GaAs-Ge, InGaP-GaAs-Ge [8] or InGaAsN-GaAs-InGaAlP [9], so that each junction absorbs a part of solar spectrum with photons larger than its band gap, transmitting the rest of the spectrum to the next junction. The record efficiency of such a tandem is around 40%, with the price higher than that of conventional solar modules by orders of magnitude: that is why they are used mainly in satellites, and their production [8] is closely related to satellite industry.

The high cost of production of the classic tandem cells is an evident consequence of the necessity of a very precise design of each of the constituent *p-i-n* junctions, in a sense that each one must generate the same photocurrent on absorbing of the corresponding part of solar spectrum, because of their serial connection. To fulfill this condition, a strict control of the deposition process is needed (expensive MBA equipment), together with expensive III–V semiconductor materials. We believe that following this route, it will be impossible to create efficient and economic solar energy converter for terrestrial applications.

2.1. Multi-junction solar energy converters with electrically independent *p-i-n* junctions

Our approach is based upon the elimination of serial connection of the *p-i-n* junctions in a tandem, making them electrically independent, with the idea that if the tandem is not working alone (reasonable assumption in case of mass application), it is always possible to find an optimum connection of constituents even if they do not generate the same current thus evading the main restriction of the classical tandem. At that, the device can be monolithic or have physically separated parts; we are not proposing stack of separate cells (see, for example, [10]).

Thus, we suggest [4–6] that each semiconductor *p-i-n* junction in the converter has electric contacts at both ends, and to make its parts electrically independent, an insulating layer can be introduced between the parts; we shall see that it will not always be necessary. The simplest case is a two-junction device, presented in **Figure 1** (left part—the device construction scheme; right part—scheme of energy bands). We stress that in this case, no tunnel junction exists in the device, which gives additional advantage over the classical tandem.

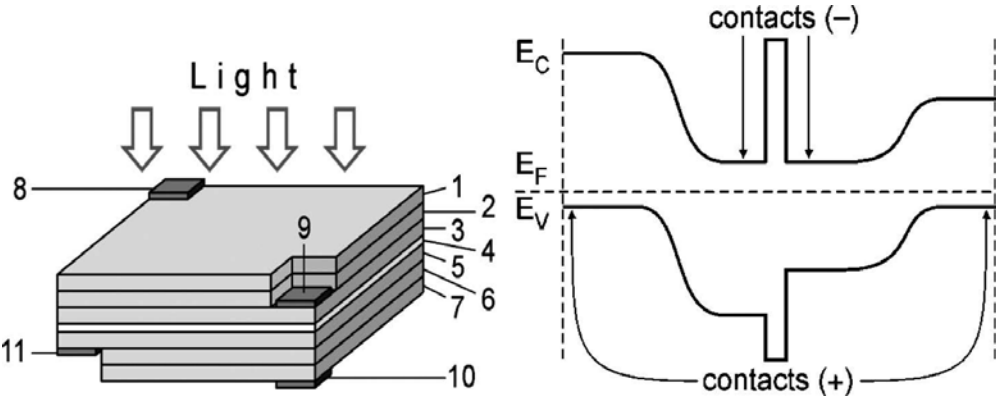

Figure 1. Construction scheme (left) and energy band diagram (right) of a two-junction device.

As illustrated in **Figure 1**, the two-junction version of our solar energy converter includes the two *p-i-n* junctions of the semiconductor materials having different band gap values. The top cell has a «*p-i-n*» sequence of layers; the bottom cell has a «*n-i-p*» sequence, with an insulating layer between the two active cells.

The top cell comprises the *p*-layer 1, the *i*-layer 2 and the *n*-layer 3. After the insulating layer 4 follows the *n*-layer of the bottom cell 5, then the *i*-layer 6 and the *p*-layer 7. The top contact 8 to the upper *p*-layer 1 of the top cell serves for electrical connections; the transparent conductive layer (or heavily doped one) can be introduced between the *p*-layer 1 and the contact 8 (not shown in the figure); 9 is the electric contact to the *n*-layer 3 of the top cell; 11 is the electric contact to the *n*-layer 5 of the bottom cell, and 10 is the electric contact to the p-layer 7 of the bottom cell. Again, the contacts 9–11 can be added with the transparent conductive layer on the surface of the corresponding semiconductor layer.

The possible ways of the electrical connections of the contacts are shown in **Figure 2**. **Figure 2A** refers to the case when there is only one working two-junction device of the present type. Since the two cells, as a rule, generate the different photo voltage (the larger is the band gap, the larger the potential barrier, and the larger voltage), the only possible way of connection is in series, which is illustrated by the **Figure 2A**: the negative contact of one cell is connected to the positive contact of the other one, and the other two contacts are used to connect the device into external circuit.

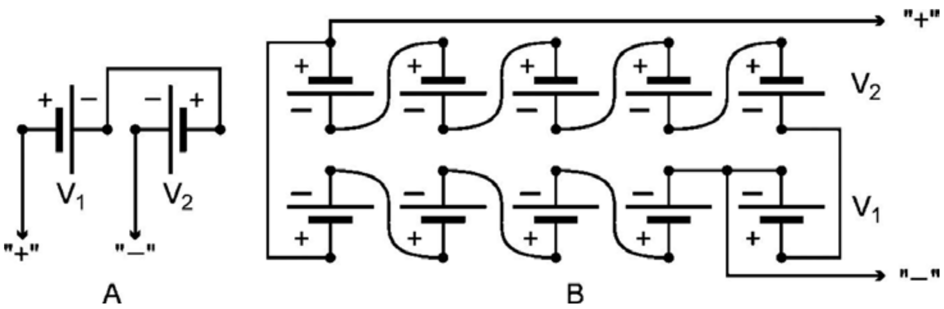

Figure 2. Electrical connections among device's elements (see text for the details).

When several devices of this type are working (in a solar module), there are many options of connection, which might be chosen to provide the necessary voltage of the module. **Figure 2B** gives an example of the cells' interconnection in a module consisting of five two-junction converters of the present type, corresponding to the case, when the photo voltage of the top cell is $V_1 = 1.55$ V and the photo voltage of the bottom cell is $V_2 = 0.93$ V. All five bottom cells and one of the top cells are connected in series producing the voltage $5 V_2 + V_1 = 6.2$ V; the other four top cells connected in series produce the same voltage: $4 V_1 = 6.2$ V. These two arrays must be connected in parallel, to double the photo current. For a larger amount of the devices in a module, there will be more options in electrical connections.

It is evident that the order of semiconductor layers can be reversed (i.e., the device of the type $(n\text{-}i\text{-}p)_1$-insulating layer-$(p\text{-}i\text{-}n)_2$ can be formed, with the same characteristics but the opposite charge on the contacts compared to the case described).

To reduce the solar light reflection at the surface, the antireflection layer might be added to the top cell. In this respect, the multi-junction device of our type is not different from the traditional multi-junction devices. To reduce the reflection losses at the interface between semiconductor and insulating layer, the latter layer's material should have relatively large refractive index N. For example, with the insulating layer of TiO_2 ($N = 2.5$) and semiconductor of GaAs type ($N = 3.5$), the interface reflection coefficient will be less than 3%. For this approximate estimation, we use the Fresnel formula for reflection coefficient at normal incidence

$$R = \left(\frac{\frac{N_2}{N_1} - 1}{\frac{N_2}{N_1} + 1} \right)^2 \tag{1}$$

where N_2 and N_1 are the refractive indices of the materials on two sides of an optical interface (as it is seen from the formula, the order of layers does not affect the reflection coefficient).

Having smaller losses than the traditional two-junction solar energy converter (no tunnel junctions), our device is capable to have higher efficiency and has more options for optimization.

For our version of the three-junction converter, we present the equilibrium energy band diagram in **Figure 3** (left, here the three cells are denoted by numbers I, II and III from left to right).

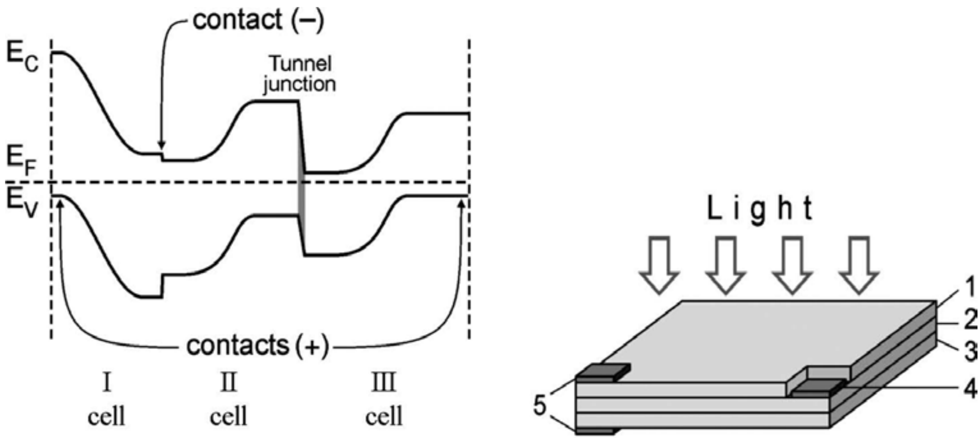

Figure 3. Energy band diagram (left) and construction scheme (right) of three-junction device.

This is a special case, when no insulating layer is needed: The two cells with the larger band gaps both have *n*-layers at the boundary where the electrode is needed and not the insulator; besides, there is only one tunnel junction instead of two in the traditional three-junction tandem. The device has only three contacts (less than in our two-junction device); the band gaps of the three semiconductor materials are again chosen to utilize in an optimal way the solar spectrum: Here, we must have approximately equal numbers of photons absorbed by the second and the third cells (counting from left to right) which are internally connected in series, but there is no need to have the same photon numbers (i.e., the same photo current) in the first cell.

The sequence of layers from the top to the bottom is as follows: $(p\text{-}i\text{-}n)_1$-$(n\text{-}i\text{-}p)_2$-$(n\text{-}i\text{-}p)_3$. One comment in relation to the choice of the type of material and the doping level of semiconductor layers: It has to make the photo voltage of the first cell approximately equal to the summary photo voltage of the II–III cells tandem. Electric contacts (indicated in **Figure 3** left by arrows) are made to the external layers and to the interface of the first and the second cell.

As in our two-junction device, the transparent conductive layer (or heavily doped one) can be introduced in the contact region, to improve the electrical quality of the contact. Right part of **Figure 3** gives a scheme of construction of the three-junction solar cell device of our type. Here, 1 is the top active cell (i.e., $(p\text{-}i\text{-}n)_1$), 2 is the second one ($(n\text{-}i\text{-}p)_2$) and 3—the third ($(n\text{-}i\text{-}p)_3$), 4 is the interface contact (to the "*n*" regions of the cells 1 and 2, charged negatively under illumination), and 5—the two external contacts (to the "*p*" region of the cells 1 and 3, charged positively under illumination). The two contacts 5 must be interconnected, thus the first cell and the tandem of the two other cells with approximately the same photo voltage are connected in parallel, approximately doubling the photo current.

As in the previous case, we can reverse the layer's sequence, just changing the sign of the voltage generated. Thus, the device of the type $(n\text{-}i\text{-}p)_1$-$(p\text{-}i\text{-}n)_2$-$(p\text{-}i\text{-}n)_3$ is equivalent to the one just described. Having only one tunnel junction instead of 2, our device is capable to have higher conversion efficiency than the traditional one.

For the four-junction solar cell device, we present the equilibrium energy band diagram in **Figure 4** (here, the four cells are denoted by numbers I, II, III and IV from left to right), and the construction scheme in **Figure 5** (left). The device has two insulating layers (4 and 7 in **Figure 5**); the part between them is a traditional two-junction tandem with one tunnel junction ($(n\text{-}i\text{-}p)_2$-$(n\text{-}i\text{-}p)_3$) whereas the two parts with an inside insulating layer comprise the two-junction converter of our design, the top one (with the larger band gaps) having the following sequence of layers: $(p\text{-}i\text{-}n)_1$—insulating layer—$(n\text{-}i\text{-}p)_2$, and another one has the reversed sequence: $(n\text{-}i\text{-}p)_3$—insulating layer—$(p\text{-}i\text{-}n)_4$. In **Figure 5** left, the number 3 corresponds to the top active cell I of the type $(p\text{-}i\text{-}n)_1$, number 5 shows the cell II with layer sequence $(n\text{-}i\text{-}p)_2$, 6 is cell III and 10 corresponds to cell IV. The contacts are made to the external layers of the device (1 and 12 in **Figure 5**, shown by arrows in **Figure 4**) and to the semiconductor layers adjacent to the insulating layers (another arrows in **Figure 4**, the two pairs 2 and 8, 9 and 11 in **Figure 5** left). As in the previous two cases, the transparent conductive layer (or heavily doped one) can be introduced in the contact regions, to improve the electrical quality of the contacts.

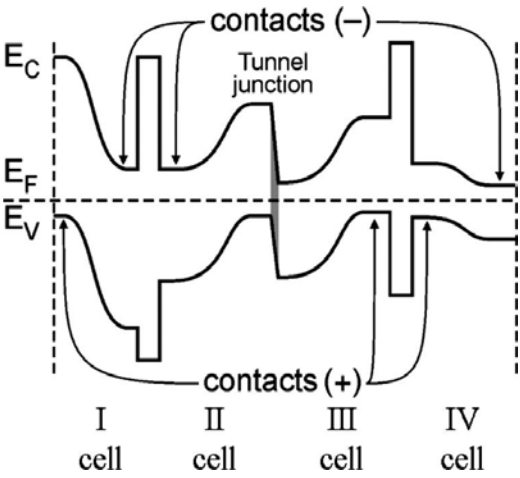

Figure 4. Energy band diagram of a four-junction device.

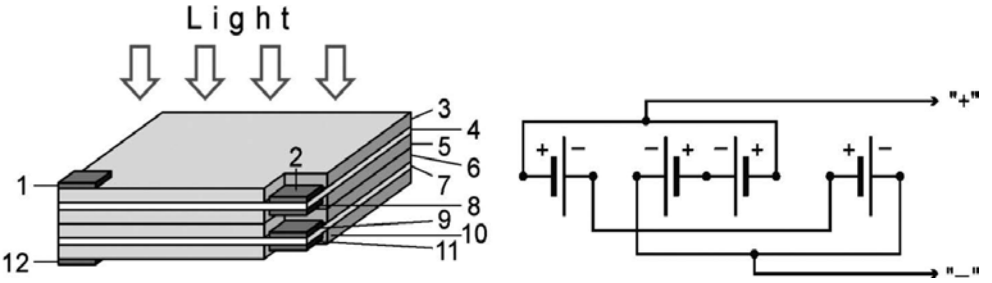

Figure 5. Construction scheme (left) and electrical connections (right) for a four-junction device.

Under illumination, the contacts to "*p*" layers are charged positively (1, 9 and 11 in **Figure 5**) whereas the contacts to "*n*" layers are negatively charged (2, 8 and 12 in **Figure 5**).

The photo voltage gradually decreases from cells I to IV; thus, it is natural to connect in series the top and the bottom cells (i.e., the cells I and IV) which gives approximately the same voltage as the tandem of the cells II and III; these two pairs (I—IV and II—III) must be connected in parallel. This cell connection is shown in **Figure 5** right. Here, the contacts 2 and 11 of **Figure 5** left are interconnected to provide the connection in series of the cells I and IV; the contacts 1 and 9 are connected making the "+" general output contact of the device, and the contacts 8 and 12 are connected making the "−" general output contact.

The cells' materials must be chosen in such a way that the cells II and III comprising a traditional tandem device absorb equal amount of photons of the solar spectrum and produce the same photocurrent; the cells I and IV are also connected in series, so they have to absorb equal amount of photons and give the equal photo current, but this photon amount (and the photo current) is not necessarily equal to the amount of photons absorbed by the cells II and III and their photo current. Thus in the present design, we have additional degree of freedom in division of solar spectrum among the active cells and more options for the efficiency optimization.

Again, the sequence of layers can be reversed without any principal changes (i.e., each of the semiconductor "*p*" layers might be substituted for the "*n*" layer, and vise versa). In relation to the antireflection coating, there is no difference from the traditional multi-junction device; again, the insulating layers with high refractive index must be recommended. Having only one tunnel junction instead of 3, our device is capable of having higher conversion efficiency than the traditional four-junction tandem solar energy converter.

2.2. Auto-concentrating multi-junction solar system

All the constructions above are assumed to be the monolithic devices similar in this sense to the traditional tandems; on the other hand, they can work either under normal or concentrated solar radiation, again as the traditional ones. Physical separation of the entrance solar cell (the one with *p-i-n* junction made of semiconductor material with the largest band gap) analyzed in this section presents additional degrees of freedom in total system's design and some new possibilities of application.

The following construction is anticipated. The converter includes several entrance cells that are working in non-concentrated sunlight (cells I in **Figure 6**) and form the concentrating reflector for the part of solar spectrum that is not absorbed in these entrance cells, i.e., composed of photons with energies below the value of their band gap. For that, each entrance cell is designed in such a way that it specularly reflects the part of solar radiation with the photon energies below its band gap that is not absorbed by the cell. In the focal plane of this concentrator, the two-junction tandem converter is positioned (II and III in **Figure 6**). As illustrated in **Figure 7**, the cell I with the largest band gap possesses the interference antireflection coating 2 adjusted to minimize reflection of the solar radiation (1) with photon energies above the band gap, i.e., in the cell's working spectral region, which is approximately 2–3 eV. The mean value

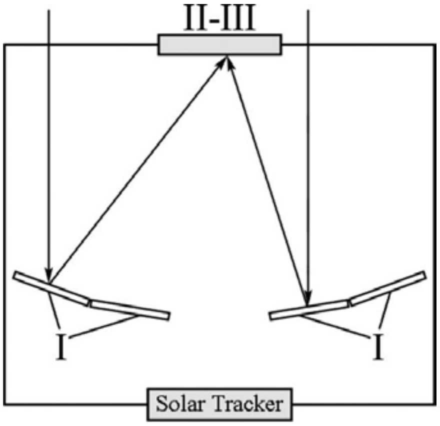

Figure 6. Auto-concentrating device.

for the wavelength in this region is $\lambda_1 \cong 500$ nm; from the condition of destructive interference of the light beams reflected from the two sides of the coating, we get the optimal thickness d = $\lambda_1/4N$ (N—refractive index of the coating material).

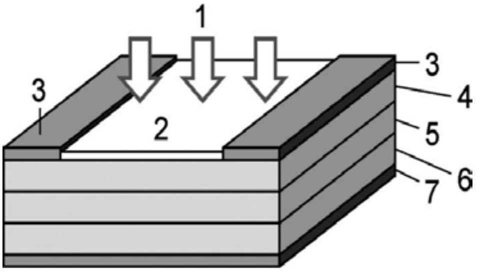

Figure 7. Construction of entrance cell I.

The other parts of the cell I are as follows: the top contacts 3, the semiconductor "*p*" layer 4, "*i*" layer 5, the "*n*" layer 6 and the back electrode 7. As in the previous cases, the sequence of layers can be reversed. The transparent conductive layer can be added at the top of the layer 4, to improve the contact electrical quality. The metal back electrode 7 has a mirror finish and, except for being a contact, serves as a mirror giving a specular reflection of the light passing the cell without absorption. This refers to the light with the photon energies smaller than the band gap E_{gI} (which is around 2 eV).

In relation to the photons with energies larger than E_{gI}, which are absorbed producing the photo voltage, cell I can be made with the active layers thickness half of that used in the traditional cell design, because in our cell, the light passes the active region twice. Except for the thickness reduction, this effect gives the more uniform photo excitation of the cell.

In the working region of the cells II and III (the mean photon energy is around 1.2 eV, the corresponding $\lambda_2 \cong 1000$ nm), the antireflection coating 2 of a cell I acts like a mirror: Here, the conditions for the constructive interference are held, d = $\lambda_2/2n$. This together with the mirror back electrode creates favorable condition for the specular reflection from the cell I of the major part of solar radiation not absorbed within the cell I. The reflected radiation is directed to the two-junction (cells II–III) device which scheme is not different from that shown in **Figure 1**.

Now, we add some details to the general scheme of the device discussed that is shown in **Figure 6**. Several cells I form concentrating reflector having the two-junction device with cells II–III in its focal plane. The area of each cell I is equal to the area of the two-junction device, and each cell I reflects its part of the incident solar radiation flux onto the II–III device; thus, the amount of light reflected by each cell I and falling onto the II–III device is multiplied by the number of these cells. All the cells of the device form a rigid construction; it is kept oriented to the Sun by the two-axis Sun tracking system (see [11, 12]).

The working region of the tandem II–III in the scheme of **Figure 6** corresponds to infra red radiation; some kind of heat engine can be used instead of this tandem (thermoelectric generator TEG, Stirling engine, etc.) that will convert a device into an efficient hybrid solar system. Several example of this construction were analyzed in papers [13, 14].

2.3. Summary

We have demonstrated that our original approach in construction of multi-junction solar energy converters allows wider choice of semiconductor materials and techniques of their production in comparison with the traditional design. As an immediate consequence, more economic converters can be developed and built. Our attempts of experimental realization of the possibilities thus arising are the subject of the following sections.

3. Technologies to realize all advantages of the new architecture

The total production cost of any device is determined by the cost of materials used and of the technology employed. We have already mentioned that the possibility of utilization of semiconductor materials of the groups II–VI, IV and IV–VI greatly widens the choice of economic and abundant raw materials for the energy converting devices. On the other hand, the corresponding technologies must be also economic, easily scalable, consuming small amount of energy and ecologically friendly: Devices for production of clean energy demand clean technologies. Below, we briefly describe the available technologies of this kind, in particular, their versions that we have employed and developed.

3.1. Eco-friendly chemical and photo chemical bath deposition; SILAR

Chemical bath deposition is a well-known and used more than 100 years technique (see review [15]), previously for production of photo detectors such as PbS and PbSe, and more recently, in thin film solar cells. Nowadays, it became much more popular because with it the nanocrystalline or nanoporous materials can be grown. It is easily scalable, low temperature and little energy consuming. It is not necessarily ecologically pure. For example, chemically deposited CdS window layers have been used in the last years in high efficiency CdTe/CdS and CIGS/CdS solar cells. However, the chemical deposition of CdS thin films by generally accepted CBD recipes at large scale could raise serious environmental problems because this process usually utilizes ammonia which is highly volatile, toxic and thus harmful to the environment. Furthermore, the volatility of ammonia changes the pH of reaction solution along the deposition process and hence results in irreproducible film properties [16]. Thus, the search for new chemical deposition processes to obtain chalcogenide semiconductor films with applications in large scale, which involve some solutions to the environmental issues, is now of great practical interest.

In the last few years, in our group, we have developed convenient alternative CBD processes for the growth of good quality CdS and CdSe thin films (see, for example, [16, 17]). We found that ammonia-free chemically deposited CdS layers perform quite well as window layers in CdTe/CdS solar cells and as semiconductor active layers in thin film transistors [18, 19]. Below, we give some examples of application of CBD and its derivatives (PCBD and SILAR) for production of material such as CdS, CdSe, CdTe, PbS, PbSe, PbTe and some devices based on them. In particular, we developed CdS/PbS solar cell with energetic efficiency of 1.6% and quantum efficiency of 25% (**Figures 8** and **9**) using only ammonia-free CBD process [20].

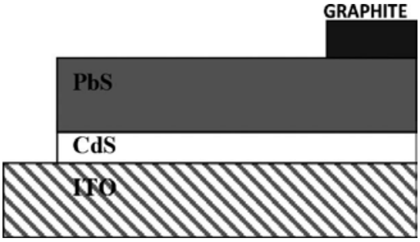

Figure 8. Construction of CBD CdS/PbS cell.

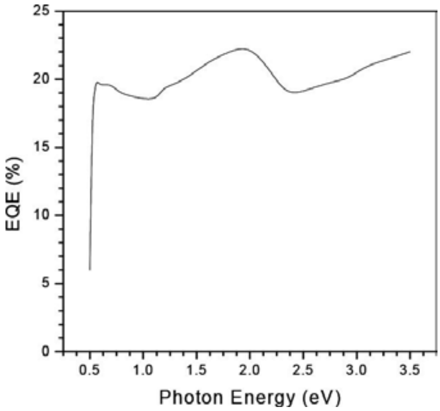

Figure 9. Cell's quantum efficiency.

The photo chemical bath deposition (PCBD) process basically repeats a traditional CBD, with addition of UV illumination. There are two types of UV lamps: the short wave ones (265 nm) and the long wave (365 nm); both were used. The UV illumination of the solution has a purpose to promote the reaction, which can be realized without this radiation, but will take much more time. For example, in the specific case of deposition of plumbonacrite $6(PbCO)_3{\cdot}3(Pb(OH)_2){\cdot}PbO$ that can be later used for production of PbS, PbTe, etc., the reaction duration with UV radiation shortens approximately 20 times.

The deposition process was carried out at room temperature (25°C) in a flat beaker with a total area of 20 cm^2; the deposition area is just limited by the size of the beaker and the irradiated area, so this process can be reproduced in large scale. The plumbonacrite film was deposited in a solution prepared in a flat beaker by the sequential addition of 20 ml at 0.2 M of $(CH_3COO)_2Pb{\cdot}3H_2O$, (lead acetate, trihydrate), 20 ml at 0.4 M of $C_6H_5Na_3O_7{\cdot}2H_2O$ (sodium citrate, dihydrate), at this point, the solution presents a white color; then, it should be quickly added with 20 ml at 0.5 M of KOH (potassium hydroxide) and deionized water to fill a total volume of 80 ml. Then, the solution was placed under UV radiation with a UV lamp (365-nm-long wave radiation, 22 W, see **Figure 10**) at room temperature to realize a PCBD process; a white dense thin film appears after 5 h. Without illumination, the deposition time necessary is almost 20 times larger. The dissociation of lead acetate gives the metal ions with the action of the complexing agent, also provides the basis for the formation of CO_3^{2-} ions, as well as the KOH provides OH^-, O^{2+} and K^- ions, which are employed in the main reaction.

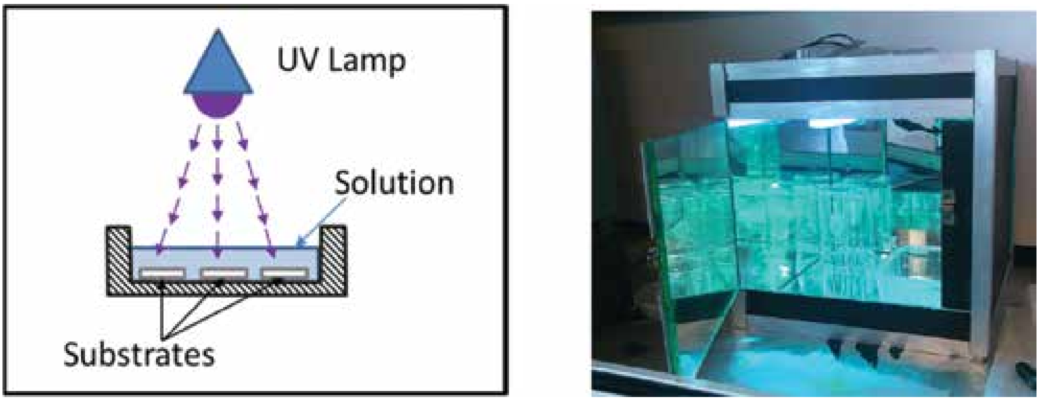

Figure 10. Photo chemical bath deposition scheme and photo of the actual bath.

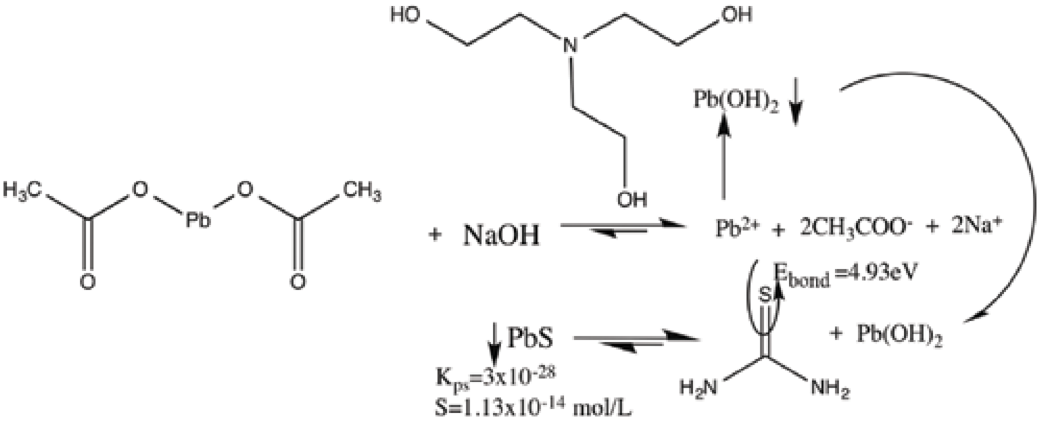

Figure 11. Simple cluster reaction mechanism.

The next example to illustrate the action of UV illumination in the CBD processes is the particular case of deposition of PbS film. The standard CBD reaction involves two steps, nucleation and particle growth. The film growth can take place either by ion-by-ion condensation of materials or by adsorption of colloidal particles from the solution on the substrate [21, 22].

The PCBD reactions, for this study, follow the same pathway that the CBD one, where the UV lamp provides energy to the reaction (see explanation below). The CBD reaction involves two reactions mechanism, the first one consists of simple cluster (hydroxide) mechanism, which occurs when the formation of the lead hydroxide takes place. Pb^{2+} ion results from $Pb(OH)_2$ at basic pH in aqueous solution; Trietanolamine(TEA) inhibits the precipitation of $Pb(OH)_2$ and allows the hydroxide to break the double bond C=S of thiourea yielding S^{2-} ion. Coupling of Pb^{2+} and S^{2-} ions renders PbS. The energy required to break C=S bond is 4.93 eV, this energy corresponds to photon within the UV region. When the PbS exceeds the solubility constant (K_s), the PbS starts to precipitate, see **Figure 11**.

The second reaction mechanism, ion-by-ion mechanism, involves the hydrolysis of the thiourea [23]. This reaction mechanism generally occurs at acid pH, but the amphoteric behavior of water triggers the spontaneous hydrolysis of thiourea. For this reaction to occur, it is also necessary to break the bond between atoms C and S (see **Figure 12**).

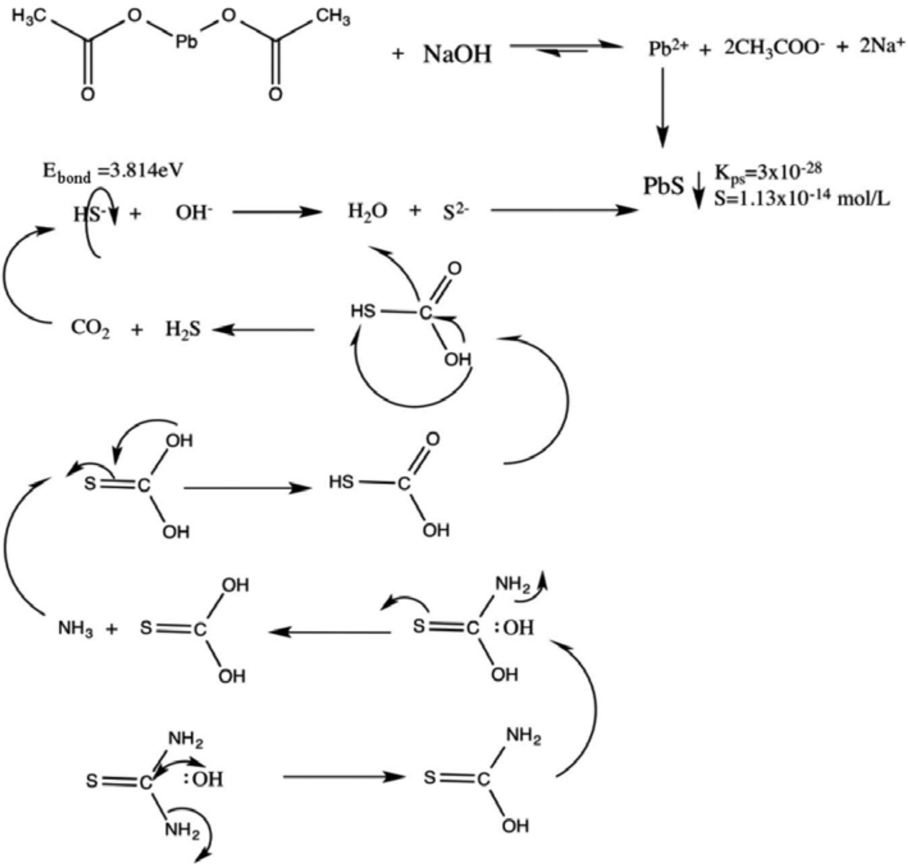

Figure 12. Ion-by-ion reaction mechanism.

It refers to the hydrolysis of the thiourea. The energy needed to break this bond is 3.81 eV. As in the simple cluster mechanism, the energy necessary to cleave bonds involved in the reaction is within the UV spectral region; in this way, UV lamp provides energy to the reaction thus further promoting the formation of the PbS.

3.1.1. Successive ionic layer adsorption and reaction technique (SILAR)

The SILAR method involves the immersion of the substrate separately into solutions, alternating cationic and anionic ones; besides, a process can involve an inter step between the cationic and anionic treatment, which usually is an immersion of the substrate into deionized water in order to remove a solution excess or badly adsorbed particles. For example, we describe how with SILAR, we obtained cadmium oxide hydroxide that by annealing can be easily converted to transparent conductive oxide (TCO) CdO for application in solar cells [24].

The process includes four following steps (highlighted with numbers in **Figure 13**): (1) immersing the substrate in the cadmium-rich solution for 20 s to create a thin liquid film containing a complex that includes cadmium ions onto the substrate; (2) immediately immersing the withdrawn substrates in hydrogen peroxide solution for 20 s to form a $Cd(O_2)_{0.88}(OH)_{0.24}$ layer; (3) drying the substrate in air for 60 s; and (4) rinsing the substrate in a separate beaker for 20 s to remove loosely bonded particles. Only three cycles are necessary to form a white transparent layer of $Cd(O_2)_{0.88}(OH)_{0.24}$ over the substrate. The thickness of the film is controlled by the number of cycles, thus for a thicker layer, several cycles are needed. Up to 50 cycles was done in order to study the kinetics of growth.

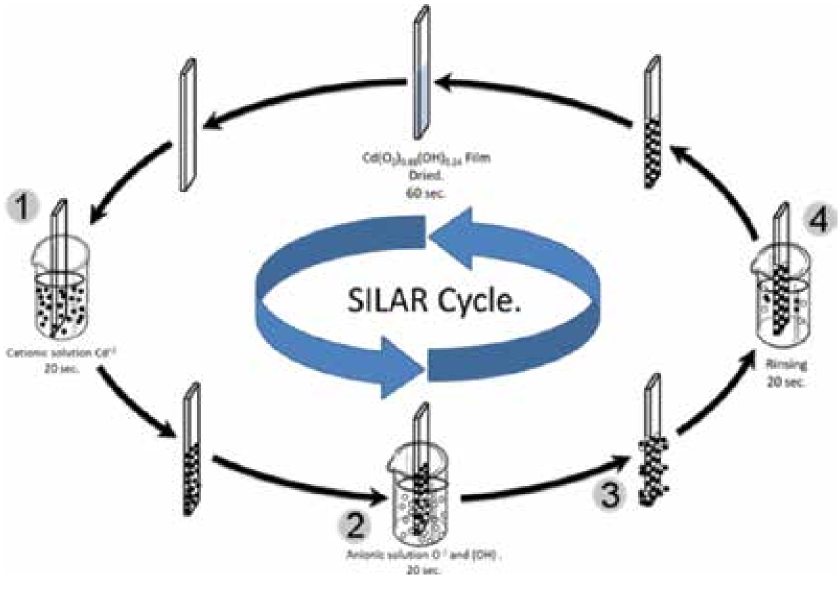

Figure 13. SILAR cycle.

An important issue for the development of semiconductor films is the thickness control. In this regard, SILAR-CBD is a technique that offers an effective and easy way to control the film thickness by a number of cycles. In particular, for this specific process, each cycle adds 21 nm of thickness.

The mechanism of $Cd(O_2)_{0.88}(OH)_{0.24}$ film formation by SILAR method can be illustrated as follows. We used two main solutions; the first one with cadmium ions is composed of cadmium acetate $Cd(CH_3CO_2)_2$ (0.1 M) as a source of Cd2+ ions. In order to produce a complexed Cd^{2+} ion, we add triethanolamine $C_6H_{15}NO_3$ (0.5M) as complexing agent (Ph = 9 of solution). Eq.(2) below describes the chemical reactions.

$$Cd(CH_3CO_2)_2 + \ C_6H_{15}NO_3\grave{a}2CH_3COOH \ + \ C_6H_{13}CdNO_3 \tag{2}$$

When the substrate is immersed in the above solution, these complexed cadmium ions are adsorbed onto the substrate due to attractive force between ions in the solution and surface of the substrate. These forces can be Van der Waals forces, cohesive forces or chemical attractive forces. The substrate is then immersed in dilute H_2O_2 solution to convert the cadmium complex into $Cd(O_2)_{0.88}(OH)_{0.24}$ by the following reactions

$$2H_2O_2 + H_2O \rightarrow 2H_2O + O_2 + (OH)^- + H^+ \tag{3}$$

$$Cd^{+2} + 0.88O + 2 + 0.24OH^- \rightarrow Cd(O_2)_{0.88}(OH)_{0.24} \tag{4}$$

3.2. Chemical vapor deposition with several evaporation sources

For CVD process, we have built Hot Wall CVD reactor with three sources of hot atomic gas transported to substrate with a neutral gas flow (nitrogen or argon). The scheme of the reactor is presented in **Figure 14** (here, we show only one Te source).

The actual reactor is a quartz cylinder (**Figure 15**) with the length of 120 mm and internal diameter of 74 mm, opened at the top and having four quartz tubes at the bottom with diameter of 12 mm and length of 335 mm. The tubes serve for transport gas input and exit and for positioning of the sources for material evaporation.

Thus, three sources could be used simultaneously, with separate regulation of gas flux for each of them, and with the possibility of using two or three different gases in the same experiment. The maximum dimensions of the films deposited are restricted by the cylinder's internal diameter. The substrate holder for material deposition is placed at the top of reactor. It consists of graphite ring with graphite plate having four windows of 10 × 10 mm^2 each that define dimensions of actual samples, and the upper vacuum-tight cover that prevents a gas escape from reactor.

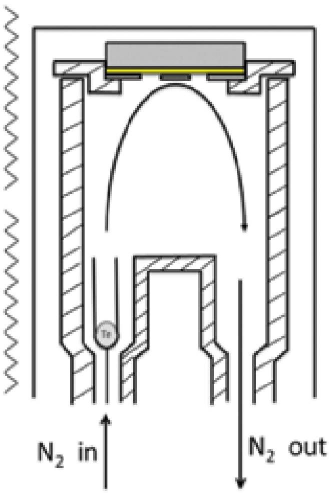

Figure 14. General scheme of CVD hot wall reactor.

Figure 15. Upper part of quartz reactor with sample holder and substrate.

The reactor is fixed on the metallic base (**Figure 16**) that contains the elements necessary for gas input, output and flow control as well as for measurements of the material source's temperatures; besides, it has double walls with water circulating between them, to keep the ambient temperature of the gas leaving the reactor through the water seal thus avoiding a possible leakage of toxic gases. The active part of the reactor containing sources and substrate is placed within an oven that is divided in two parts having separate regulation of electric current passing through their heating resistances, so that necessary temperatures of sources and of substrate can be chosen and maintained. According to the accepted classification, this reactor is a hot wall reactor which is surrounded by heating system that can reach a maximum temperature of 900°C in substrate and source part separately. A special computerized system was designed and made for programming and automatic monitoring of all stages of the deposition process. When two atomic sources were used (for example, to deposit CdTe or CdSe films), they were placed within Knudsen cells, and the evaporation rate was controlled by the cells opening diameters, and their temperature. The transporting gas flux was chosen to provide laminar flow in all parts of the reactor; the character of the flow was studied by simulation, using program COMSOL Multiphysics 4.4.

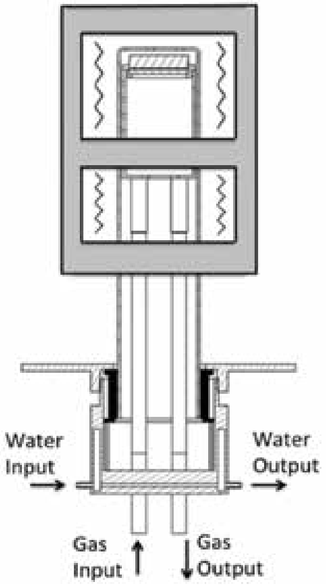

Figure 16. Quartz reactor fixed to the base.

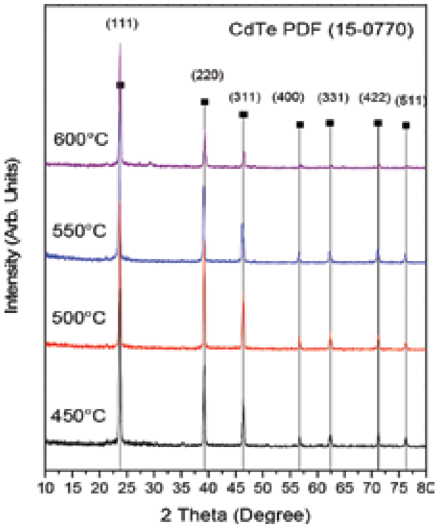

Figure 17. X-ray analysis of CdTe samples (see text).

Figure 17 presents X-ray diffraction pattern obtained on CdTe film deposited in our reactor at different temperature of both sources of Cd and Te (the temperature is given by the reactor's Hot Walls). The character of the pattern showed a polycrystalline nature for all films, which is consistent with the standard cubical structure of cadmium telluride (PDF 17-0750; the significant peaks observed at 2θ = 22.73°, 39.31°, 46.44°, 56.83°, 62.45°, 71.11° and 76.25° are indexed as (111), (220), (311), (400), (422) and (511), respectively).

3.3. Two-stage CBD/CVD technique

We also developed the two-stage process for deposition of II–VI and IV–VI semiconductor films, namely CdTe, CdSe, PbS, PbSe and PbTe. Here, we illustrate this two-stage process with an example of obtaining of PbTe films from precursor plumbonacrite deposited by some variety of chemical bath deposition. In the first stage, plumbonacrite $Pb_{10}(CO_3)_6O(OH)_6$ was deposited onto glass substrate by PCBD, using ammonia-free low-temperature process in alkaline aqueous solution. Then, in the second stage, the obtained film was placed in our CVD reactor described in the previous section, where it acted as substrate in a reaction of substitution of nonmetallic film component by Te, thus forming PbTe films. The nitrogen flux of 0.25 lt/min was used as transporting gas. The source temperature was adjusted between boiling (Tb) point and melting point (Tm) with the aim to control the flux gas of the source (Te source, Tm = 449.51°C, Tb = 988°C). The substrate temperature was adjusted to improve the quality of the film (see [25, 26] for details).

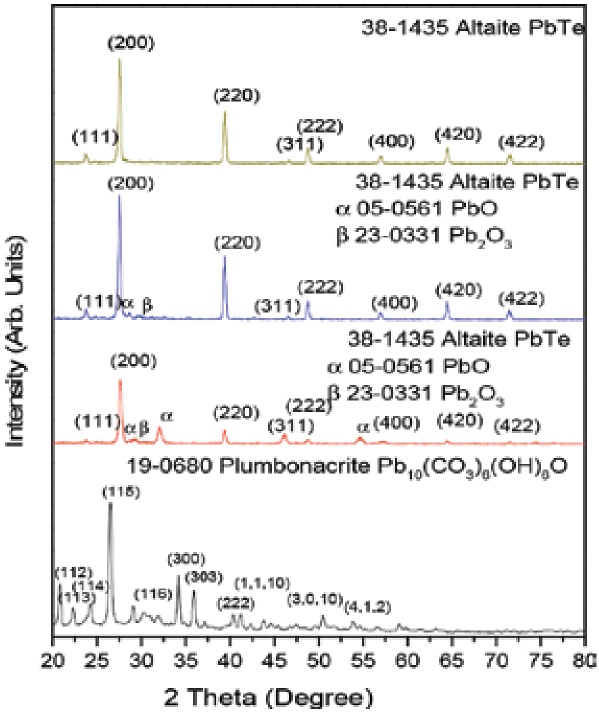

Figure 18. Illustration of development of PbTe in CVD reactor.

XRD patterns for plumbonacrite film and the film after tellurium gas treatment are shown in **Figure 18**. The character of the pattern and the peaks intensities show polycrystalline nature for all films. At the bottom of **Figure 18**, it is possible to see the plumbonacrite diffraction pattern which is consistent with the standard hexagonal structure of plumbonacrite (powder diffraction file 19-0680), and after telluride gas treatment (20, 40 and 60 min), the plumbonacrite structure suffers a change turning from hexagonal structure to cubical structure of lead telluride. The total conversion to lead telluride from plumbonacrite takes place at 60 min; the conversion time depends on the film thickness. For 20 and 40 min of treatment, it is possible to appreciate that the plumbonacrite film starts to decompose into lead oxides as PbO (PDF 05-0561) and PbO_2 (PDF 23-0331), and later these also turn into lead telluride. This fact is possible to confirm by observation that peaks appearing at 20 min decrease at 40 min and vanish at 60 min, where only the planes associated with the lead telluride (PDF 38-1435) remain.

In a similar manner, we obtained CdTe and CdSe films using as a substrate in CVD reactor, the cadmium oxide hydroxide $Cd(O_2)_{0.88}(OH)_{0.24}$ film produced by some of the CBD versions; the sources of Te and Se were used in a CVD process, correspondingly for CdTe and CdSe. Using Si as a substrate in the first (CBD) stage, we get rectifying structures as *n*-Si/*p*-PbTe acting as photodiode or a component of multi-junction solar cell.

The SEM images (**Figure 19**) show that the material precursor is composed of small spherical grains with an approximate size of 500 nm; after CVD, the resultant CdSe film has a grain size of 2–3 μm. The composition of the precursor film was studied with EDAX complement to SEM, and it has shown the composition of the CdSe film with a Se/Cd ratio of 0.915. The lateral micrograph gives an estimate for the film thickness: The precursor film has a thickness of 15 μm, and the CdSe film has the same thickness after 30 min of CVD. The investigated optical and structural properties of the films obtained do not differ from those of the bulk material, evidencing the good quality of the material made.

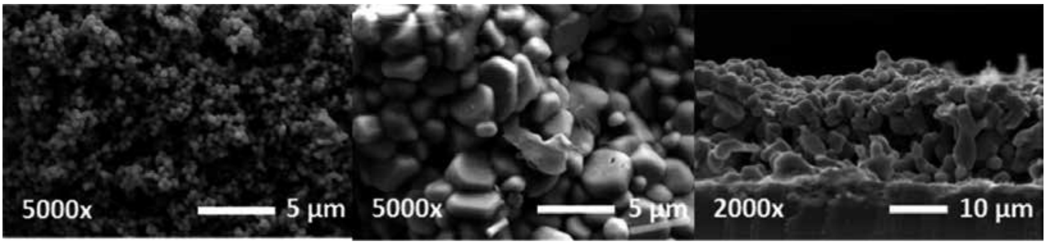

Figure 19. Left to right: frontal image of precursor film, frontal and lateral views of CdSe film.

3.4. Summary

We see that the techniques described can be successfully used for production of the multilayered (multi-junction) devices for solar energy conversion, providing simple, easily scalable, economic and ecologically friendly processes.

4. First results: multilayered photo diodes and solar energy converters based on II–VI and IV–VI semiconductor materials

In the sections above, we described a variety of semiconductor materials obtained with ecologically friendly and simple techniques. Application of these materials for design and construction of economic photo sensitive structures and solar energy converters is a great project in which we are engaged now. We already mentioned a solar cell based on CdS/PbS films developed by pure chemical route [20]. Below, we give two examples of the two-layered devices already developed—a light sensing photo diode based on Si/PbTe, and a CdS/CdTe-based solar cell.

4.1. Structure and parameters of *n*-Si/*p*-PbTe photo diode

The deposition of the main components of the device was described above (that of plumbonacrite on Si substrate by PCBD in 3.1, its transformation to PbTe in 3.3). Hall measurements show *p*-type conductivity of PbTe, the results are presented in **Figure 20**.

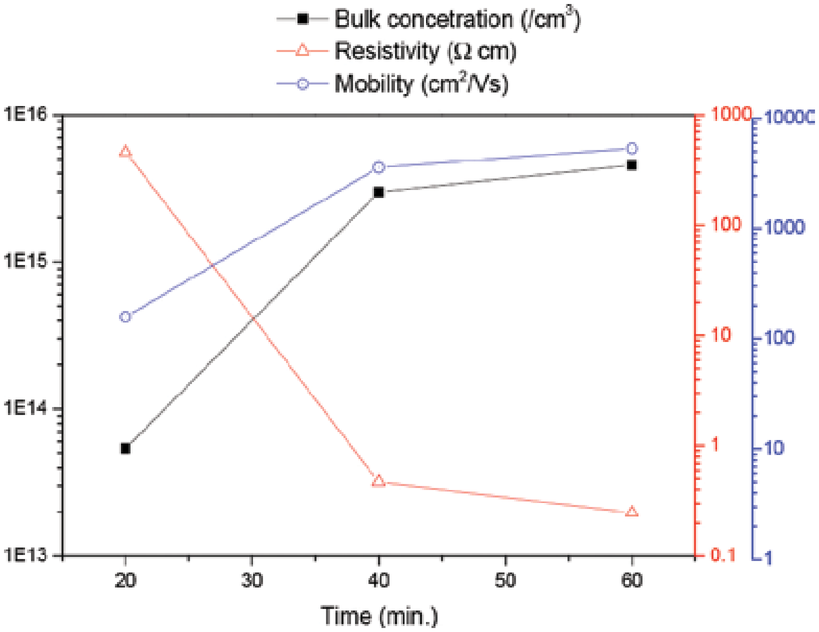

Figure 20. Electrical parameters of PbTe film.

Hole concentration in PbTe was increasing with an increase in the treatment time under tellurium hot gas up to 10^{16}/cm^3, with mobility changes from 150 to 700 cm^2/V s. The **Figure 21** gives the device structure (insert) and the I–V characteristics under illumination with tungsten lamp providing a total irradiation of 1500 W/m^2.

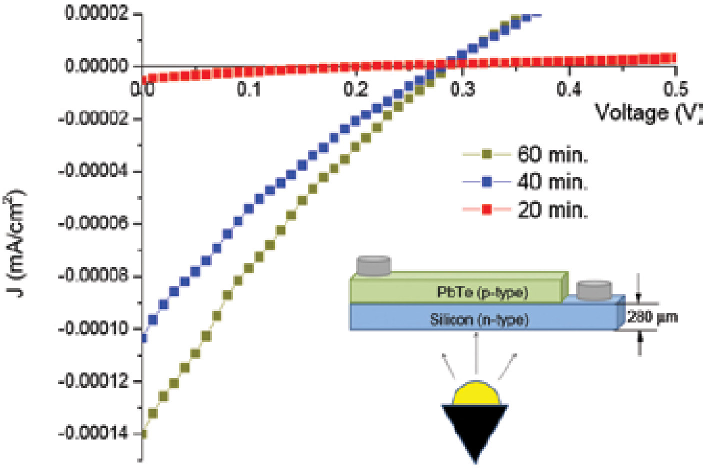

Figure 21. Current-voltage characteristics of a diode depending on Te gas treatment.

The device was illuminated from the silicon side which has a thickness of 280 µm. The characteristics observed are typical of a solar cell, but with very poor fill factor and efficiency, so there is an open field for the cell optimization.

However, if the structure is treated as a light sensor (photodiode), its main parameter is the photo responsivity (photo current per watt of light intensity); in our case, it is S = 0.1 A/W, quite comparable with responsivity of commercial photo diodes (for example, commercial GaP/Au photo diode has sensitivity S = 0.15 A/W [27]). Except for this photo diode, we elaborated two other bilayered photo diode structures: One with *n*-Si/*p*-CdTe active layers having the responsivity S = 1.4 A/W, and another of *n*-CdS/*p*-PbS, with S = 1.2 A/W. Thus, we demonstrate that our sensors photo diodes can be superior to some commercial ones.

4.2. Investigation of CdS/CdTe semiconductor structure for solar cell

The *n*-CdS/*p*-CdTe bilayered structure is a core of a special type of solar energy converters that are already in the market, with relatively large annual production (First Solar Company) and acceptable efficiency of around 14% [28, 29]. Our purpose was not the repetition of their construction scheme and techniques, but investigation of the properties of this active bilayered structure as a function of the deposition parameters which we can control using our technologies that are different from those employed in First Solar, with an idea that this (or similar) structure can serve as a part of our future multilayered converter. In particular, we investigated an effect of $CdCl_2$ treatment upon the structure parameters.

The 300-nm-thick CdS layer was prepared by CBD on glass substrate covered with a thin conducting layer of ITO (see [20]), and CdTe film was deposited over this layer in our CVD reactor with two atomic sources. For these sources, we employed Knudsen cell with Cd having an opening of 1.96×10^{-6} m², and for Te – 3.17×10^{-5} m² that gives approximately equal atomic flux of both components in the deposition region. A special attention was given to the uniformity of CdTe film thus obtained: The results of the simulation of the gas flow in the reactor were used to adjust the deposition parameters (the temperatures and the neutral gas flow). As seen in **Figure 17** above (Section 3.2), CdTe polycrystalline films with standard cubical structure were obtained at sources temperatures from 450 to 600°C (the substrate temperature at all cases was kept smaller by 50°C); average crystal size found from the diffraction peak width was around 30 nm, growing slightly as the temperature increases.

Figure 22 shows that deposition temperature had a marked effect on the grain size: It increases as the temperature increases, being 0.37 μm at 450, 1.67 μm at 500, 3.02 μm at 550 and 6.4 μm at 600°C. It is well-known that large grains are favorable for solar cell's materials. Optical data agree with X-ray diffraction giving 1.5 eV band gap that is normal for cubic crystals (see **Figure 23**, inset show position of the derivative of absorption coefficient with sharp peak at 1.5 eV).

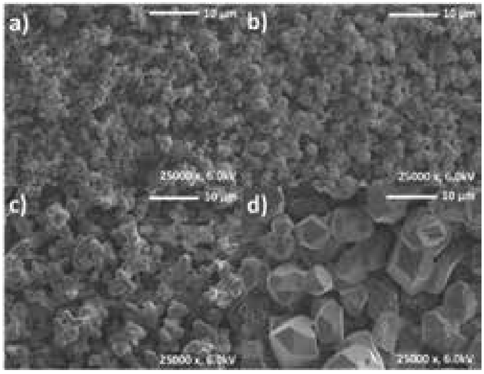

Figure 22. SEM images of CdTe films at different sources temperature: 450°C (a), 500°C (b), 550°C (c) and 600°C (d).

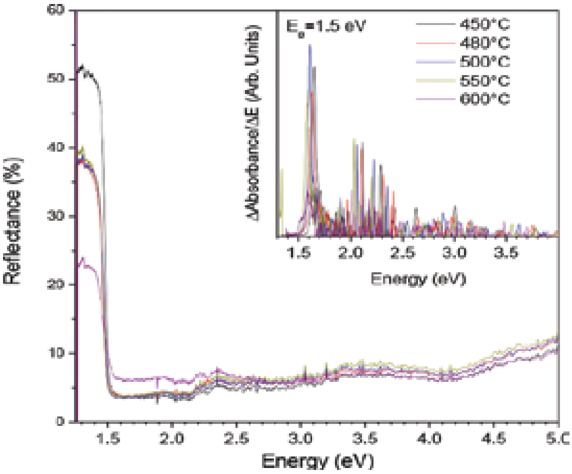

Figure 23. Reflection spectrum of CdTe film and its derivative (insert).

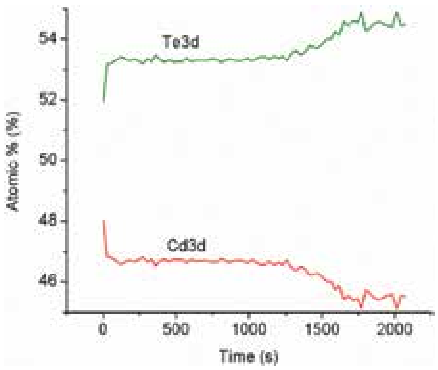

Figure 24. Atomic distribution in CdTe (see text). External boundary at the left.

XPS data (**Figure 24**) give the atomic distribution along the CdTe film. The abscissa shows the etching time (2000 s with etching rate of 0.66 nm/s gives the film thickness of 1.32 μm, etching rate was calibrated with Ta_2O_5 standard). We see a considerable excess of Te, especially in the internal part of the film (right edge, **Figure 24**).

The variation of the Te 3d signal binding energies (**Figure 25** for Te 3d level; for Cd, we have similar data) shows the oxidation effects (the presence of oxygen) at near-surface region, significant at about two thirds of the film's thickness.

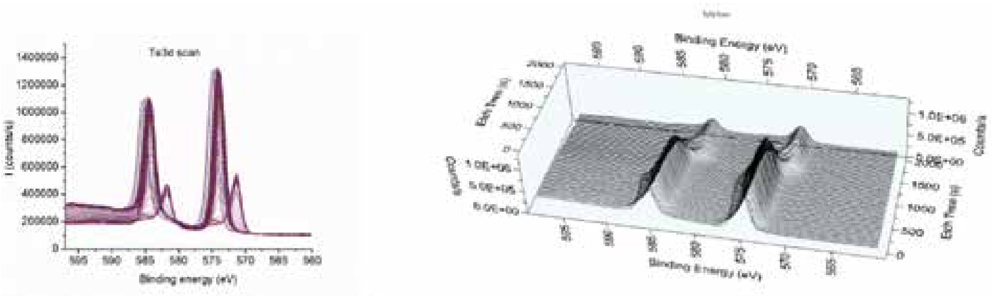

Figure 25. XPS binding energies for Te 3d level in CdTe (see text).

Binding energies for the Te 3d signal of the Te $3d^{5/2}$ 575 eV and Te $3d^{3/2}$ 585 eV at the outmost part of the cell, and shifting to Te $3d^{5/2}$ 572 eV and Te $3d^{3/2}$—582 deeper in the cell. According to NIST database [30], internal values are those characteristic for the bulk CdTe, external are shifted to higher energies due to oxidation.

It is known that an excess of Te (vacancies of Cd) produces acceptors in CdTe, but the oxygen (isovalent impurity) acts as a donor [31], so the resulting conductivity is unclear. Measuring the sample work function with Kelvin Probe equipment, we came to the conclusion that CdTe film in our CdS/CdTe system is of *n*-type, see the band diagram (**Figure 26**, solid lines).

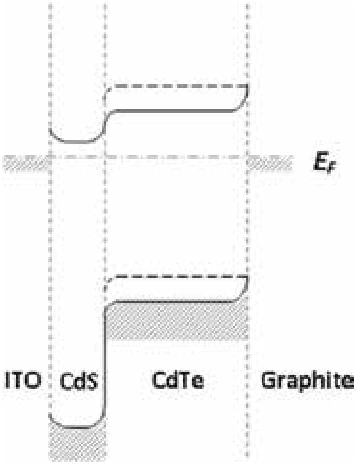

Figure 26. Band diagram of a CdS/CdTe structure.

In **Figure 26** we see, first of all, the barrier of around 0.25 eV between the c-bands of CdS and CdTe, and upper curving of both bands of CdTe at its surface near the graphite electrode by another 0.25 eV. Correspondingly, we observed photo voltage generation of approximately 0.25 V when illuminating the structure from each side.

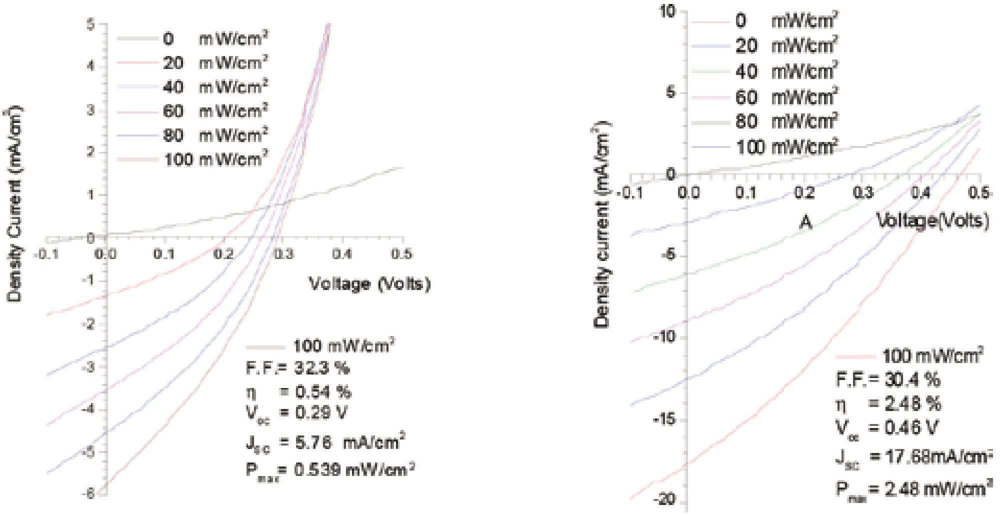

Figure 27. I–V curves of CdS/CdTe solar cell before (left) and after (right) the $CdCl_2$ treatment.

Slight upper band curving in CdS near contact with ITO is a consequence of higher work function of the ITO compared to CdS.

Solar cell based on this structure possesses modest characteristics (**Figure 27** left) with the efficiency of less than 1%, the open circuit voltage V_{oc} of 0.3 V and the short circuit current of

I_{sc} 6 mA/cm^2. A standard treatment with $CdCl_2$ (10 min in saturated solution, then rinsing and annealing at 300°C for 2 h) drastically changes all characteristics, as expected (**Figure 27** right, [32]): much larger values of I_{sc}, V_{oc} and efficiency. Since the mechanism of this treatment action is still not quite clear, we perform some study to find out just what parameters are affected by the treatment. It is already known that the treatment enhances grain growth. Our SEM images show that, indeed, after the treatment much larger grains appear.

Besides, these images show (**Figure 28**) that before the treatment (left image), the definite boundaries separating individual grains are observed, but after treatment (right image) the grain separation practically disappear, as if the grains were melted. The other factors that we found are an increase in the photoconductivity of the CdTe film (i.e., increase the lifetime of nonequilibrium charge carriers) and improvement of the stoichiometry: According to the EDAX data, the atomic ratio of Cd and Te was 0.953 before treatment, and became 0.977 after it. The CdTe film remained of *n*-type, but the barrier between the c-bands of CdS and CdTe increased to 0.5 eV as shown in **Figure 26** by the dashed lines, giving the corresponding increase in the cell's open circuit voltage. The fact that the Fermi level in CdTe lies above the middle of the band gap agrees with observation made in Ref. [33].

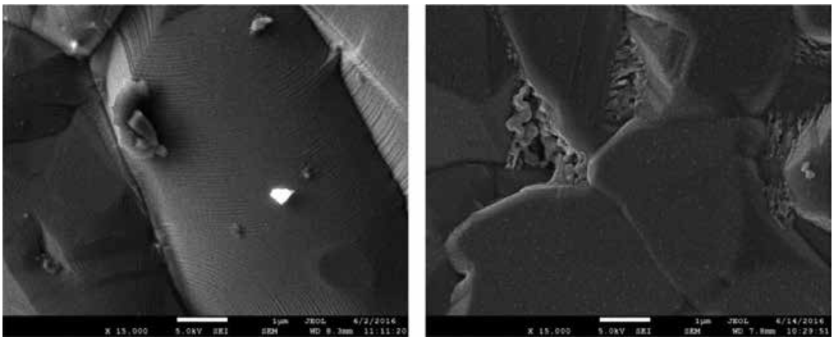

Figure 28. Effect of $CdCl_2$ treatment upon morphology of CdTe.

We see that the standard construction of CdS/CdTe cell made with standard treatment is not ideal for solar energy conversion, giving the incorrect conductivity type of the main absorber material, and having additional serial resistivity at the ITO/CdS contact. Therefore, we plan to study the different constructions with the different treatment for application in the multilayered solar energy converter.

4.3. Summary

It is shown that with technologies utilized, efficient photo sensors can be made based on semiconductors II–VI and IV–VI, with better parameters than devices present in the market made of III–V semiconductor GaP. It is also evident that these techniques have a great potential in development of efficient and economic solar energy converters.

5. Conclusions

We demonstrated that following our original approach in construction of multilayered semiconductor photovoltaic devices and using ecologically friendly and small energy consuming technologies, particularly the ammonia-free chemical routes and photo chemical bath deposition technique developed in our group, economic and efficient devices can be made. We believe that this is the way towards the economic and efficient solar energy converters for terrestrial applications.

Acknowledgements

I.R. Chávez-Urbiola wishes to thank CONACYT for his scholarship. Y.V. Vorobiev thanks CONACYT (project #259982) for financial support of his sabbatical leave to CIMAV Campus Monterrey. We acknowledge the technical assistance of Luis Gerardo Silva Vidaurri, C.A. Avila Herrera, J.E. Urbina Alvárez and A. Jiménez Nieto.

Author details

Yuri V. Vorobiev[1*], Iker R. Chávez Urbiola[1], Rafael Ramírez Bon[1], Liliana Licea Jiménez[2], Sergio A. Pérez García[2], Pavel Vorobiev[2] and Paul Horley[2]

*Address all correspondence to: vorobiev@cinvestav.mx

1 CINVESTAV-Querétaro, Libramiento Norponiente 2000, Querétaro, QRO, México

2 CIMAV/Monterrey, Parque de Investigación e Innovación Tecnológica, Apodaca, NL, México

References

[1] H. Cotal, C. Fetzer, J. Boisvert *et al.*, III–V multijunction solar cells for concentrating photovoltaics, *Review Energy and Environmental Science*, vol. 2, pp. 174–192, 2009.

[2] A. Hoffmann, U. W. Paetzold, C. Zhang *et al.*, Advancing tandem solar cells by spectrally selective multilayer intermediate reflectors, *Optics Express*, vol. 22, pp. 1270–1277, 2014.

[3] O. Isabella, A. Hendrikus *et al.*, Thin-film silicon-based quadruple junction solar cells approaching 20% conversion efficiency, *Solar Energy Materials and Solar Cells*, vol. 129, pp. 82–89, 2014.

[4] Y. Vorobiev, J. González-Hernández, H. Esparza-Ponce, and P. Gorley, Mexican Patent No. 274256, 2010.

[5] Y. Vorobiev, J. González-Hernández, H. Esparza-Ponce, and P. Vorobiev, Mexican Patent No. 312841, 2013.

[6] I. R. Chávez-Urbiola, Y. V. Vorobiev, and R. Ramírez Bon, New principles in design and technology of multi-junction solar energy converters, *International Journal of Materials, Mechanics and Manufacturing*, vol. 4, no. 1, pp. 80–84, 2016.

[7] W. Shockley, and H. J. Queisser, Detailed Balance Limit of Efficiency of *p-n* Junction Solar Cells, *Journal of Applied Physics*, vol. 32, pp. 510–519, 1961.

[8] Spectrolab website http://www.spectrolab.com/solarcells.htm

[9] D. Kanama, and H. Kawamoto, Science and technology trends, *Quarterly Review*, vol. 28, 2008, pp. 57–74.

[10] S. Yoshidomi, J. Furukawa, M. Hasumi, and T. Sameshima, Mechanical stacking multi junction solar cells using transparent conductive adhesive, *Energy Procedia*, vol. 60, pp. 116–122, 2014.

[11] Y. Vorobiev, P. Vorobiev, P. Horley, and J. González-Hernández, Experimental and theoretical evaluation of the solar energy collection by tracking and non-tracking photovoltaic panel, Proceedings of 2005 Solar World Congress (ISBN-0-89553-177-1), Orlando, FL, USA, August 6–12, 2005.

[12] P. Vorobiev, and Y. Vorobiev, Automatic Sun tracking solar electric systems for applications on transport, Proceedings of 7th International Conference CCE 2010, Chiapas, Mexico, Septrember 8–10 2010, pp. 66–70.

[13] Y. Vorobiev, J. González-Hernández, P. Vorobiev, and L. Bulat, Thermal-photovoltaic solar hybrid system for efficient solar energy conversion, *Solar Energy*, vol. 80, pp. 170–176, 2006.

[14] E. A. Chávez-Urbiola, Y. V. Vorobiev, and L. P. Bulat, Solar hybrid systems with thermoelectric generators, *Solar Energy*, vol. 86, pp. 369–378, 2012.

[15] G. Hodes, Semiconductor and ceramic nanoparticle films deposited by chemical bath deposition. A review, *Physical Chemistry Chemical Physics*, vol. 9, pp. 2181–2196, 2007.

[16] M. G. Sandoval-Paz, and R. Ramírez-Bon, Analysis of the early growth mechanisms during the chemical deposition of CdS thin films by spectroscopic ellipsometry, *Thin Solid Films*, vol. 517, pp. 6747–6752, 2009.

[17] H. E. Esparza-Ponce, J. Hernández-Borja, A. Reyes-Rojas, M. Cervantes-Sánchez, Y. V. Vorobiev, R. Ramírez-Bon, J. F. Pérez-Robles, and J. González-Hernández, Growth technology, X-ray and optical properties of CdSe thin films, *Materials Chemistry and Physics*, vol. 113, pp. 824–828, 2009.

[18] R. Ochoa-Landín, J. Sastre-Hernández, O. Vigil-Galán, and R. Ramírez-Bon, Chemically deposited CdS by an ammonia-free process for solar cells window layers, *Solar Energy*, vol. 84, pp. 208–214, 2010.

[19] A. L. Salas-Villaseñor, I. Mejía, J. Hovarth *et.al.*, Impact of gate dielectric in carrier mobility in low temperature chalcogenide thin film transistors for flexible electronics, *Electrochemical and Solid State Letters*, vol. 13, pp. H313–H316, 2010.

[20] J. Hernandez Borja, Y. V. Vorobiev, and R. Ramirez Bon, Thin film solar cells of CdS/PbS chemically deposited by an ammonia-free process, *Solar Energy Materials and Solar Cells*, vol. 95, pp. 1882–1888, 2011.

[21] R. S. Mane, and C. D. Lokhande, Chemical deposition method for metal chalcogenide thin films, *Materials Chemistry and Physics*, vol. 65, p. 1, 2000.

[22] C. E. Pérez-García, R. Ramírez-Bon, and Y. V. Vorobiev, PbS thin films growth with CBD and PCBD techniques: a comparative study, *Chalcogenide Letters*, vol. 12, pp. 579–588, 2015.

[23] H. Lima-Lima, and O. Portillo-Moreno, Análisis de reacciones en la transición de CdS (semiconductor) a CdCO3 (aislante) enformato de películas delgadas obtenidas mediante DBQ, *Superficies Y Vacio*, vol. 21, p. 21, 2008.

[24] I. R. Chávez-Urbiola, R. Ramírez Bon, and Y. V. Vorobiev, The transformation to cadmium oxide through annealing of cadmium oxide hydroxide deposited by ammonia-free SILAR method and the photocatalytic properties, *Thin Solid Films*, vol. 592, pp. 110–117, 2015.

[25] I. R. Chávez-Urbiola, J. A. Bernal Martínez, J. Hernandez Borja, C.E. Perez Garcia, R. Ramírez Bon, and Y. V. Vorobiev, Combined CBD-CVD technique for preparation of II–VI semiconductor films for solar cells, *Energy Procedia*, vol. 57, pp. 24–31, 2014.

[26] I. R. Chávez-Urbiola, J. A. Bernal Martínez, V. P. Makhniy, R. Ramírez Bon, and Y. V. Vorobiev, Preparation of II–VI and IV–VI semiconductor films for solar cells by the isovalent substitution technique with a CBD-made substrate, *Inorganic Materials,* vol. 50, pp. 546–550, 2014.

[27] DatasheetsforGaPphotodiodesG1961,G1962andG1963producedbyHamamatsu, product catalog. http://www.hamamatsu.com/us/en/pro ducts/category

[28] R. G. Dhere *et al.*, Development of substrate structure CdTe photovoltaic devices with performance exceeding 10%, Proceedings of 38th IEEE PVSC, pp. 3208–3211, 2012.

[29] Internet data. http://energy.gov/eere/sunshot/cadmium-telluride

[30] G. C. Rodrigues, P. Indelicato, J. P. Santos, P. Patté, and F. Parente, Systematic calculation of total atomic energies of ground state configurations, *Atomic Data and Nuclear Data and Tables*, vol. 86, pp. 117–233, 2004.

[31] J. Li, and S.-H. Wei, Alignment of isovalent impurity levels: oxygen impurity in II–VI semiconductors, *Physical Review B*, vol. 73, 041201-1-4, 2006.

[32] I. M. Dharmadasa, Review of the CdCl2 treatment used in CdS/CdTe thin film solar cell development and new evidence towards improved understanding, *Coatings*, vol. 4, pp. 282–307, 2014.

[33] T. Schmeyer, J. Fritsche, A. Thiben *et al.*, Effect of in situ UHV CdCl2-activation on the electronic properties of CdTe thin film solar cells, *Thin Solid Films*, vol. 431–432, 84–89, 2003.

Chapter 7

A New Ensemble Probabilistic Method for Short-Term Photovoltaic Power Forecasting

Antonio Bracale , Guido Carpinelli and
Pasquale De Falco

Additional information is available at the end of the chapter

http://dx.doi.org/10.5772/65993

Abstract

The high penetration of photovoltaic (PV) systems led to their growing impact on the planning and operation of actual distribution systems. However, the uncertainties due to the intermittent nature of solar energy complicate these tasks. Therefore, high-quality methods for forecasting the PV power are now essential, and many tools have been developed in order to provide useful and consistent forecasts. This chapter deals with probabilistic forecasting methods of PV system power, since they have recently drawn the attention of researchers as appropriate tools to cope with the unavoidable uncertainties of solar source. A new multi-model probabilistic ensemble is proposed; it properly combines a Bayesian-based and a quantile regression-based probabilistic method as individual predictors. Numerical applications based on actual irradiance data give evidence of the probabilistic performances of the proposed method in terms of both sharpness and calibration.

Keywords: smart grids, distributed power generation, forecasting methods, forecast uncertainty, photovoltaic systems

1. Introduction

Several kinds of distributed energy resources currently are involved in modern electrical distribution system development, allowing to enhance the overall system efficiency and to reduce overall greenhouse gas emissions. However, the integration of distributed energy resources into power networks is a challenging task in the view of their planning, management, and operation; thus, new research contributions are strongly encouraged in this area [1–3].

Photovoltaic (PV) and wind power plants are acknowledged to bring technical, environmental, and economic benefits to power systems, and their diffusion has straightforwardly grown during past years. Unfortunately, the intermittent and random nature of both solar and wind energy negatively affects the efficient, reliable and secure operation of electrical power systems. Then, accurate methods for forecasting wind and PV power generation, as well as appropriate measures to quantify the goodness of the previsions in both technical and economic terms, are mandatory. In particular, forecasting methods should be fitted to operate on different time horizons, as they are involved in several real-time, scheduling, and planning power system tasks; also, since electrical power has become a necessity with a specific and strongly variable value, the economic impact of forecasts cannot be neglected.

More in detail, with the deregulation of energy market in the 1990s and the widespread dissemination of renewable generation at the beginning of the twenty-first century, the use of performing tools for load and generation power forecasting is becoming more and more important from System Operators to Electric Utilities and Energy Traders, Independent Power Producers and Consumers [4–8]. Accurate forecasting of renewable generation also helps industrial customers/prosumers to better control their operational processes, thanks to demand response activities and electrical storage system use, and schedule and plan appropriate energy market bidding and maintenance strategies.

Forecasts are also needed when the solar/wind power producers do not participate directly in the markets, as is the case in some countries. For example, Italian wind/solar producers are not yet allowed to participate directly in the shorter time-period markets for deviations and adjustments (*short-term balancing markets*) and deliver instead their powers to the "Gestore dei Servizi Energetici" (GSE), the Italian state-owned company that promotes and supports renewable energy sources. GSE, in turn, sells the wind/solar power at the *day-ahead market* and, then, needs accurate forecasting tools for optimizing offers [9]. However, Italian Authority started a test program in June 2016 in order to allow renewable producers to participate also to *dispatching markets* [10] within the end of 2018. Thus, the requirements in terms of forecast performances will surely increase during this period.

Many deterministic and probabilistic methods for forecasting wind and PV power have been proposed in the relevant literature [11–15]. The outputs of deterministic methods are single values of power, and no further information on the uncertainty of the prediction is provided. Nowadays, the development of probabilistic tools is strongly encouraged, since they completely address the unavoidable uncertainties related to wind and solar source; this facilitate the operators' decisions, especially in risk-related tasks such as electrical market bidding [16, 17]. Two subcategories of probabilistic methods can be distinguished: the first is based on an underlying deterministic model and provides the uncertainty of the error usually expressed in terms of prediction intervals or quantiles, while the second is based on a direct approach that directly provides the predictive probabilistic representation of the wind or PV power (i.e. through a predictive probability density function or cumulative distribution function).

Probabilistic forecasts can be provided by either a single predictor or through a convenient combination of multiple deterministic or probabilistic predictors. The latters are known in the relevant literature as "ensemble forecasts" and are expected to perform better than each of the single predictors [13].

This chapter deals with the problem of direct probabilistic forecasting of PV power. A new multi-model ensemble forecasting method (MEM) is proposed and is used to properly combine two probabilistic base predictors. The base predictors are a Bayesian-based method (BM) and a quantile regression-based method (QM); both were successfully used for the forecasting of PV power in the relevant literature [18–21]. Numerical applications were performed to validate the method on the basis of actual solar measurements; the performances of the proposed method are quantified numerically in terms of a proper score [i.e. the pinball loss function (PLF)] and graphically through diagrams (PIT histograms and reliability diagrams), accounting for probabilistic reliability and probabilistic sharpness of forecasts.

The key result of this chapter is, then, the proposal of a new ensemble probabilistic method for PV power forecasting, based on the aggregation of two probabilistic methods. Outputs of the single base predictors were processed and combined through the application of a linear pool technique [22–24] based on the minimization of the PLF. The proposed method seems particularly useful for both forecasters and forecast users being the method characterized by good reliability and sharpness, for a wide range of short-term forecasting intervals.

The remainder of the chapter is organized as follows. Base predictors are briefly recalled in Section 2, and also the proposed MEM for PV power forecasting is shown in Section 2. Numerical applications are shown in Section 3, Section 4 provides our conclusions, and some definitions about the forecast properties are explained in Appendix.

2. Probabilistic forecasting methods

Various methods were proposed for the forecasting of PV power, and the relevant literature shows a wide range of papers dealing with this subject. The majority of the proposed methods are deterministic in nature even though recently a great attention was paid to the probabilistic forecast that is object of interest in this chapter.

Probabilistic forecast usually takes the form of a predictive probability density function and has the general goal of maximizing the sharpness of the predictive distribution, subject to calibration (also addressed as reliability) [25, 26]. Sharpness is related to the concentration of the predictive probabilities and is an intrinsic property of the forecast alone, while calibration corresponds to the probabilistic correctness of the forecasts, i.e. refers to the statistical consistency between probabilistic forecasts and observations. Reliability can be assessed via reliability diagrams or probability integral transform (PIT) histograms. Sharpness, in the case of density forecasts for a real-value variable, can be assessed in terms of the associated prediction intervals (see Appendix). Proper scoring rules,[1] such as the continuous ranked probability

---

[1] Given an observation of a random variable extracted from a distribution *F*, a score for this observation is defined "proper" if its maximum (or minimum depending on the nature of the score) value is obtained when the probabilistic forecast is the distribution *F*. The score is defined "strictly proper" if all of its values are lower (or higher) than its maximum (or minimum) when the probabilistic forecast is a distribution *G≠F* [27].

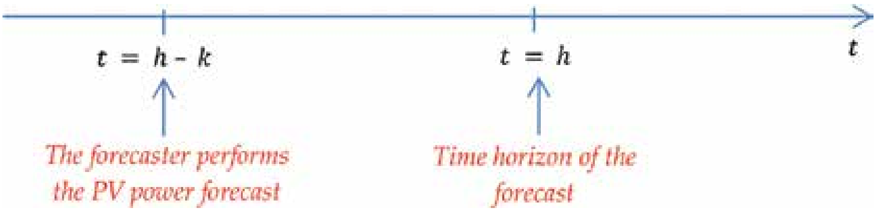

Figure 1. Forecast time scale.

score (CRPS) and the PLF (Appendix), can be used for assessing both sharpness and calibration simultaneously.

In this section, we first briefly recall the BM and QM, as we use them as probabilistic base predictors in the new MEM; then, we present the MEM with extensive details.

In the following, we suppose that the forecaster performs the PV power forecast at time $t = h{-}k$ for the time horizon $t = h$, with k being the lead time (1, 2, …, 24, … h) (**Figure 1**).

2.1. The Bayesian forecasting method

The BM provides a predictive PDF of the PV power applying the Bayesian inference of a data set of past observations [18, 19].

This method is based on a two-step procedure:

Step 1—An analytic PDF is selected to model the randomness of PV power.

Step 2—The parameters of the PDF selected at Step 1 are predicted.

In the relevant literature [28], the normalized Beta distribution was suggested as an adequate PDF to characterize the solar irradiance random variable. When the PV generation system is equipped with a maximum power point tracker (MPPT), the output active power of the PV system at hour, P_{PV_t}, is a linear function of the total irradiance I_{β_t} (in kW/m^2) at hour t on a surface with an inclination β to the horizontal plane [28, 29]:

$$P_{PV_t} = S_C \eta I_{\beta_t} \tag{1}$$

where S_C is the surface area of the panel array (in m^2), and η is the total efficiency of the PV system. As the relationship (Eq. 1) is linear, also the PV power can be modelled through a Beta distribution; consequently, the normalized Beta distribution for the PV power at the time horizon $t = h$ is:

$$f_{BM_h}(P_h | \sigma_h, \varphi_h, P_r) = \frac{\left(\frac{P_h}{P_r}\right)^{\sigma_h - 1} \cdot \left(1 - \frac{P_h}{P_r}\right)^{\varphi_h - 1}}{P_r \cdot \mathrm{B}(\sigma_h, \varphi_h)} \tag{2}$$

where σ_h, φ_h are the shape parameters, P_r is the maximum value of power produced by the PV installation (P_h is therefore defined over the range [0, P_r]), and $\mathrm{B}(\cdot, \cdot)$ is the Beta function (see

Appendix for its mathematical explanation). The maximum value of power P_r produced by the PV installation is assumed known. The shape parameter $\varphi_h$in Eq. (2) can be expressed as a function of the mean value μ_{BM_h} and of the shape parameter σ_h of the Beta PDF, i.e.:

$$\varphi_h = \frac{\sigma_h \cdot (P_r - \mu_{BM_h})}{\mu_{BM_h}}. \tag{3}$$

Then, a re-parameterization of the PDF (Eq. 2) in terms of μ_{BM_h}, σ_h leads to the knowledge of the predictive PDF if the mean value μ_{BM_h} and the shape parameter σ_h are known for each time horizon of interest.

The mean value μ_{BM_h} can be estimated through a time series model, which links the mean value μ_{BM_h} of PV power at hour h to the measurements of, respectively, the last U known values of PV power and of other exogenous inputs; for example, assuming the cloud cover cc and air temperature at, which are collected until the hour $t = h–k$, as exogenous inputs, it is:

$$\begin{aligned} \mu_{BM_h} &= \gamma_1 P_{h-k} + \cdots + \gamma_U P_{h-k-U+1} + \delta_1 cc_{h-k} + \cdots + \delta_U cc_{h-k-U+1} \\ &+ \delta_{U+1} at_{h-k} + \cdots + \delta_{2U} at_{h-k-U+1} + \gamma_0 \end{aligned} \tag{4}$$

where $\gamma_0, \ldots, \gamma_U, \delta_1, \ldots, \delta_{2U}$ are the $3U + 1$ coefficients of model. These coefficients can be estimated by solving a least square minimization problem in the forecasting training period, assuming the realizations of the random variable to be known.

Then, the remaining unknown shape parameter σ_h in the PDF of PV power given by Eq. (2) is estimated in the Bayesian inference framework.

Let:

i. $\boldsymbol{P}^M_{h,k}$ be the vector the elements of which are the G measurements of PV power observed until the time, $t = h–k$, i.e. $\boldsymbol{P}^M_{h,k} = \{P^M_{h-k-G+1}, \ldots, P^M_{h-k}\}$;

ii. $p(\sigma_h|\overline{z}_\sigma)$ be the assigned prior distribution of the unknown shape parameter σ_h with $\overline{z}_\sigma = \{\overline{z}_{1_\sigma}, \ldots, \overline{z}_{HP_\sigma}\}$, i.e. the vector of its hyper-parameters[2]; and

iii. $p(P_h|\sigma_h)$ be the PDF (Eq. 2) in which the mean value μ_{BM_h} is assigned and given by Eq. (4).

The posterior predictive distribution $p(P_h|\boldsymbol{P}^M_{h,k}, \overline{z}_\sigma)$ of PV power, i.e. the desired forecasted probability density function, can be calculated through the total probability theorem as:

---

[2] Prior parameter knowledge is expressed through corresponding prior distributions, whose parameters are usually called hyper-parameters, and they are denoted by an upper hyphen. The choice of prior distributions depends on the degree of prior confidence the forecaster puts into each parameter. Uninformative prior distributions are selected when no or few prior knowledge is available on the specific parameters; Jeffreys distribution was specifically proposed for such kind of Bayesian applications, but also uniform distributions or Normal distributions with large variance have been used. Instead, when a significant prior knowledge is available, informative prior distributions can be selected (e.g., Normal distribution with small variance) [30, 31].

$$p(P_h|\boldsymbol{P}_{h,k}^{M},\overline{z}_{\sigma}) = \int p(P_h|\sigma_h)p(\sigma_h|\boldsymbol{P}_{h,k}^{M},\overline{z}_{\sigma})d\sigma_h \tag{5}$$

The Bayesian inference of PV power measurements $\boldsymbol{P}_{h,k}^{M}$ on the prior distribution $p(\sigma_h|\overline{z}_{\sigma})$ allows the computation of the posterior distribution $p(\sigma_h|\boldsymbol{P}_{h,k}^{M},\overline{z}_{\sigma})$ of the shape parameter σ_h in Eq. (5), as follows:

$$p(\sigma_h|\boldsymbol{P}_{h,k}^{M},\overline{z}_{\sigma}) = \frac{p(\boldsymbol{P}_{h,k}^{M}|\sigma_h)\cdot p(\sigma_h|\overline{z}_{\sigma})}{\int p(\boldsymbol{P}_{h,k}^{M}|\sigma_h)\cdot p(\sigma_h|\overline{z}_{\sigma})\cdot d\sigma_h} \tag{6}$$

where $p(\boldsymbol{P}_{h,k}^{M}|\sigma_h)$ is the likelihood function of the samples in $\boldsymbol{P}_{h,k}^{M}$, given the shape parameter σ_h, as follows:

$$p(\boldsymbol{P}_{h,k}^{M}|\sigma_h) = \prod_{m=1}^{G} p(\boldsymbol{P}_{m}^{M}|\sigma_h) \tag{7}$$

Unfortunately, since $p(P_h|\sigma_h)$ is a Beta distribution, no conjugate prior distribution for σ_h can be found analytically; then, Eq. (6) and therefore Eq. (5) cannot be calculated in closed form. However, the un-normalized posterior distribution $q(\sigma_h|\boldsymbol{P}_{h,k}^{M},\overline{z}_{\sigma})$ of the scale parameter σ_h can always be provided; it is given by:

$$q(\sigma_h|\boldsymbol{P}_{h,k}^{M},\overline{z}_{\sigma}) = p(\boldsymbol{P}_{h,k}^{M}|\sigma_h)\cdot p(\sigma_h|\overline{z}_{\sigma}) \tag{8}$$

Once known the un-normalized posterior distribution $q(\sigma_h|\boldsymbol{P}_{h,k}^{M},\overline{z}_{\sigma})$ given by Eq. (8), two sampling methods (i.e. the Metropolis-Hastings (MH) algorithm and the Gibbs algorithm [30, 31]) are commonly used in the literature to obtain samples of the posterior distribution $p(\sigma_h|\boldsymbol{P}_{h,k}^{M},\overline{z}_{\sigma})$. The MH algorithm was used in the numerical applications of this chapter. Eventually, once samples from the posterior distribution are obtained, straightforwardly the samples of the searched posterior PDF $p(P_h|\boldsymbol{P}_{h,k}^{M},\overline{z}_{\sigma})$ of PV power can be drawn.

2.2. The quantile regression forecasting method

The BM shown in the preceding subsection requires that an analytic PDF of PV power is selected in order to estimate the parameters of the selected PDF for the desired time horizon. To avoid any assumptions on the density functions, one might restrict attention to estimating only a finite number of quantiles of the distribution [20, 21, 32]. These quantiles can be estimated using historical data in the QM framework. Indeed, the input of the model is the column vector of V explanatory variables $\boldsymbol{y}_h = \{y_{h_1}, \ldots, y_{h_V}\}$ linked to the measurements of PV power and other meteorological quantities.[3] In the most general form, the α-quantile $P_h^{(\alpha)}$ of PV power at the time horizon of the forecast $t = h$ can be estimated through a linear regression as:

---

[3] In a regression model, the inputs are usually called "independent variables" and the output is usually called "dependent variable". However, the term "explanatory variables" is here preferred to the term "independent variables" in order to avoid confusion, as it is possible to have two (or more) input variables that are not independent on each other (e.g., some regression models use measurements of both temperature and squared temperature).

$$P_h^{(\alpha)} = \boldsymbol{\beta}^{(\alpha)} \cdot \boldsymbol{y}_h + r_h^{(\alpha)} \tag{9}$$

where $\boldsymbol{\beta}^{(\alpha)}$ is a row vector of V coefficients to be estimated, and $r_h^{(\alpha)}$ is a residual white noise at time $t = h$. Starting from Eq. (9), the expected value $\hat{P}_h^{(\alpha)}$ of $P_h^{(\alpha)}$ is given by:

$$\hat{P}_h^{(\alpha)} = \hat{\boldsymbol{\beta}}^{(\alpha)} \cdot \boldsymbol{y}_h \tag{10}$$

and, then, the problem of quantile estimation reduces to find an estimation $\hat{\beta}^{(\alpha)}$ of the row vector $\boldsymbol{\beta}^{(\alpha)}$.

If the data set $\{P_1, \ldots, P_D\}$ of D past hourly measurements of PV power and the corresponding D vectors of explanatory variables $\boldsymbol{y}_1, \ldots, \boldsymbol{y}_D$ are available for the given forecasting training period, $\hat{\boldsymbol{\beta}}^{(\alpha)}$ can be obtained by solving the following minimization problem:

$$\hat{\boldsymbol{\beta}}^{(\alpha)} = \arg\min_{\beta^{(\alpha)}} \sum_{d=1}^{D} I_d \tag{11}$$

where each value I_d is calculated as:

$$I_d = \begin{cases} \left(P_d - \boldsymbol{\beta}^{(\alpha)} \cdot \boldsymbol{y}_d\right) \cdot (\alpha - 1), & \text{if} \quad P_d < \boldsymbol{\beta}^{(\alpha)} \cdot \boldsymbol{y}_d \\ \left(P_d - \boldsymbol{\beta}^{(\alpha)} \cdot \boldsymbol{y}_d\right) \cdot \alpha, & \text{if} \quad P_d \geq \boldsymbol{\beta}^{(\alpha)} \cdot \boldsymbol{y}_d \end{cases}. \tag{12}$$

The solution of Eq. (11) can be found in the least square framework; also, an effective solution to problem (Eq. 11) was proposed in Ref. [20]. Once the selected Q quantiles of PV power are estimated, the predictive CDF can be obtained through linear interpolation.

2.3. The multi-model ensemble method

Pierre-Simon Laplace came up in 1818 with the idea of merging different forecasts into a new, combined forecast; obviously, the combined forecast should provide a mean error that is lower than the error of each constituent individual forecast. This is possible since individual forecasts usually contain some independent information that can be exploited in a convenient combination. Bates and Granger then followed up in 1969 with a paper that set standards for the combination of forecasts. After that, hundreds of relevant studies have been carried out and applied to a variety of fields of research, including economics, management, systematics, biomedicine, meteorology, and climatology [13, 33, 34].

Among the large number of possible ensemble methods, in this subsection, we propose a new multi-model competitive ensemble forecast method that consists in training the two probabilistic predictors shown in the previous subsections, and in processing their outputs in such a way to guarantee adequate sharpness and calibration of the final forecast.

The proposed method consists in three steps (**Figure 2**):

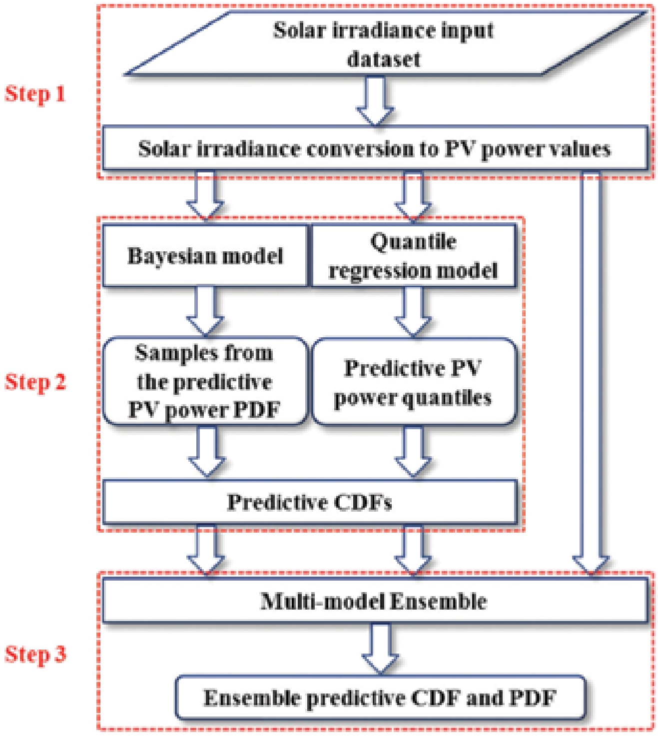

Figure 2. Two-model ensemble forecast.

Step 1—Collection of the input data: available measurements must be collected and, if necessary, processed in order to form the data that are used as inputs.

Step 2—Selection and running of base predictors: the base probabilistic models are chosen on the basis of the forecaster's experience and the available input data sets; then, the models are utilized for a training period.

Step 3—Processing of the outputs of the single base predictors: the outputs of all of the base predictors are aggregated by applying adequate and robust criteria to obtain an ensemble forecast that operates better than any of the base predictors guaranteeing adequate levels of reliability and sharpness of forecasts.

The selection of the base predictors (Step 2) and the processing of the outputs of the single base predictors to obtain a good performing ensemble (Step 3) are obviously particularly critical.

In the proposed MEM, the chosen base predictors are the BM and QM of Sections 2.1 and 2.2. Indeed, since diversity is a key feature in competitive ensemble forecasting, it was experimented that these two predictors return usually different decisions, and then they could provide a good improvement in terms of their ensemble.

With reference to Step 3, as shown in Ref. [22, 24], the linear pooling of base probabilistic predictors can be suitable for the aggregation. Other approaches (e.g. in the Bayesian framework or through the logarithmic pooling [13, 22, 35]) were also considered in the relevant literature.

The linear pooling is performed on the cumulative distribution functions (CDFs) obtained through the base predictors, since they are easier to manage when different kinds of predictors have to be aggregated. The output of the MEM is the predictive CDF $F_{MEM_{h,k}}(P_h)$, i.e. the linear combination of two predictive CDFs $F_{BM_{h,k}}(P_h)$, $F_{QM_{h,k}}(P_h)$ of the PV power for the horizon time h. It results in the following weighted sum:

$$F_{MEM_{h,k}}(P_h) = w_1 \cdot F_{BM_{h,k}}(P_h) + w_2 \cdot F_{QM_{h,k}}(P_h) \tag{13}$$

where the weights are conveniently selected in order to guarantee that the output function is indeed a CDF defined in the interval $[0, P_r]$. To achieve that, each weight must be non-negative ($w_1, w_2 \geq 0$) and their sum must be unitary ($w_1 + w_2 = 1$). Note that the assumption of two base predictors was made with no loss of generality. Indeed, the same procedure could be applied for a larger number of predictors, i.e. the predictive CDF would be a weighted sum of N_p base predictive CDFs with weights $\boldsymbol{w} = \{w_1, \ldots, w_{N_p}\}$ and $\sum_{i=1}^{N_p} w_i = 1$.

The estimation of the weight(s) in the linear pooling MEM should be aimed to produce and ensemble forecast that performs better than any base predictors, maximizing the sharpness subject to calibration. In the relevant literature, weights were estimated by minimizing the CRPS in the forecasting training period [36, 37]. Also, as LPE predictions may be over-dispersed,[4] if single predictors are neutrally dispersed, some techniques shown in Ref. [22, 39] (e.g. Beta-transformation or multi-objective procedures) may be applied to overcome this problem.

In this chapter, we use a further proper score, i.e. the PLF, which penalizes for observations lying far from a given quantile.

Thus, the estimation of weight w_1 in Eq. (13) is the solution of the following minimization problem:

$$\hat{w}_1 = \arg\min_{w_1} \frac{1}{D} \sum_{d=1}^{D} \sum_{j=1}^{J} PLF(P_d^{(\lambda_j)}, P_d^*) \tag{14}$$

where $PLF(P_d^{(\lambda_j)}, P_d^*)$ is the PLF at the d^{th} hour for the λ_j-quantile, as defined in (A.6), and J is the total number of considered quantiles. The estimation $\hat{w}_2$ of w_2 is then trivially obtained as $\hat{w}_2 = 1 - \hat{w}_2$, for the assigned weight properties.

---

[4] Neutral dispersion is a necessary but not sufficient condition for high-quality forecasts. Definitions of over-dispersion, neutral dispersion, and under-dispersion are provided in Definition 2.6 of Ref. [38].

3. Numerical applications

Values of solar irradiance were measured from 1 January 2012 to 31 December 2013 at the National Renewable Energy Laboratory in USA (39.74° N lat., 105.18° W long.) [40]. Measurements were collected with a 1-min resolution but were then averaged and pre-processed in order to obtain 17544 hourly values with no outliers or bad data. Also measurements of cloud cover and air temperature were selected in order to be used as exogenous variables in the base predictors forecasting procedures. The rated power of the considered PV installation was set to $P_r = 110$ kW.

Probabilistic forecasts were performed through the multi-model ensemble method presented in Section 2.3 in order to validate the usefulness of the procedure. Forecasts were performed for several lead times k, and results for $k = 24$ hours (*next day forecast*) are initially shown with extensive details in this section; then, results for $k = 1$ hour (*next hour forecast*) are also provided, but with less details, for the sake of conciseness. In particular, the PV power output was forecasted from February to December 2013 (11 months of forecasting), and results for May 2013 are shown below. In this case, the interval used to train the base predictor methods was made of eleven months (from May 2012 to March 2013), while the calibration of base predictors and the choice of weights of the multi-model ensemble method were performed in the following month (April 2013).

The proposed multi-model ensemble method is compared to both probabilistic base predictors and also to a benchmark based on the probabilistic persistence method (PPM) [41], in order to verify its usefulness. The comparison is performed numerically in terms of PLF and graphically through the inspection of PIT histograms [42] and reliability diagrams [43]. Also, the maximum deviation from perfect reliability (MDPR; see Appendix) is considered in order to compare different forecasts. In all numerical applications, night-time hours were not considered for forecast, as the total PV power output was set equal to zero, and therefore, they were not considered in indices and diagrams evaluation.

Table 1 shows the results in terms of PLF and MDPR for BM, QM, MEM, and PPM, and **Table 2** shows the corresponding estimated weights obtained in the MEM procedure for the next-day forecast. From the analysis of **Table 1**, the proposed method appears to improve the performances of base predictors. Indeed, the PLF decreases by about 2% and also the MDPR is

Index	BM	QM	MEM	PPM
PLF (kW)	53.65	53.97	52.50	68.14
MDPR (%)	4.15	3.46	2.07	12.44

Table 1. Pinball loss function and maximum deviation from perfect reliability of next-day forecast in May 2013.

	$\hat{W}_1$	$\hat{W}_2$
Estimated weight (–)	0.219	0.781

Table 2. Estimated ensemble weights of next-day forecast in May 2013.

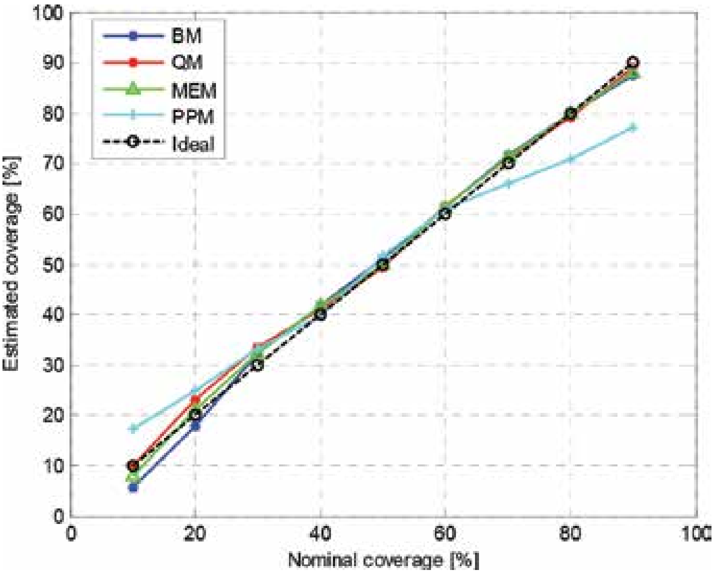

Figure 3. Reliability diagrams of base predictors, multi-model ensemble method, and probabilistic persistence method, compared to ideal reliability in May 2013.

reduced by about 2 and 1.4% with respect to the BM and QM, respectively, with a relative reduction of 50 and 40%, respectively. Base predictors and the proposed MEM outperformed the PPM benchmark in terms of PLF by about 22–23%. Also, even if the performances in terms of PLF are quite similar for BM and QM, they are weighted differently in the MEM, with a prevalence of QM as shown in **Table 2**.

Selected base predictors are acknowledged in the relevant literature as very competitive forecasting tools. Then, also a not impressive reduction in terms of PLF is a valuable contribution toward well-performing methods for PV power forecasting. Further improvements could be obtained by merging more base probabilistic predictors in the MEM.

We outline that MDPR gives a rough evaluation on the performances of probabilistic methods in terms of reliability, but it is important to evaluate also how the probabilistic method performs in each individual quantile. Thus, reliability diagrams for base predictors, MEM and PPM are shown in **Figure 3**, while PIT histograms show the relative frequencies of these methods in **Figure 4**. From the graphical inspection of **Figure 3**, base predictors appear to perform well in terms of reliability, especially for higher quantiles and with only a little deviation in lower quantiles. The MEM also shows good performances, as estimated coverages are very close to the ideal ones on overall. PPM instead appears to provide under-dispersed forecasts.

This trend is also confirmed by the inspection of **Figure 4**, as base predictors and MEM appear to be normally dispersed, i.e. a necessary condition for the overall reliability. The under-dispersion trend seen in the PPM reliability diagram is confirmed in the graphical inspection of PPM PIT histogram.

As a further comment on numerical simulations performed from February to December 2013, we note that the MEM was able to outperform both base predictors in terms of PLF in 9 months on 11; in the other 2 months, the results are only slightly worse. A slight prevalence of QM weight was observed with respect to the BM weight. In 4 months, the resulting ensemble forecast was affected by a slight over-dispersion, due to the normal-dispersion of base predictors; this will need some techniques to be developed in order to overcome this problem.

Finally, also simulations for different lead times were performed. In particular, the results for $k = 1$ hour are particularly significant for comparison. In this case, only in 5 months the weight of BM was different from zero. This was due the different behaviour of BM and QM for next-hour forecasting, as the performances of QM were particularly better than BM in terms of PLF. In three of these five months the proposed MEM led to a better forecast in terms of PLF than both base predictors, and only in one month the problem of over-dispersion of ensemble forecasts was detected.

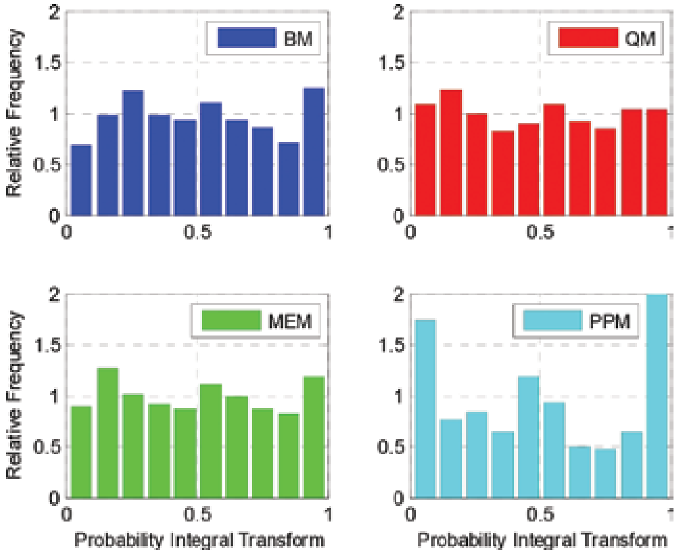

Figure 4. PIT histograms of base predictors (BM and QM), multi-model ensemble method (MEM), and probabilistic persistence method (PPM) in May 2013.

Index	BM	QM	MEM	PPM
PLF (kW)	50.22	28.39	27.49	53.96
MDPR (%)	3.46	3.23	4.84	10.37

Table 3. Pinball loss function and maximum deviation from perfect reliability of next-hour forecast in March 2013.

	$\hat{W}_1$	$\hat{W}_2$
Estimated weight (–)	0.186	0.814

Table 4. Estimated ensemble weights of next-hour forecast in March 2013.

As an example, **Table 3** shows the results in terms of PLF and MDPR for BM, QM, MEM, and PPM, and **Table 4** shows the corresponding estimated weights obtained in the MEM procedure during March 2013 for next-hour forecast. The PLF performance differences are very clear between BM and QM; however, the BM weight is still not negligible and the MEM has better performances than both predictors in terms of PLF, thus leading to a greater value of MDPR.

4. Conclusions

In this chapter, we dealt with the problem of short-term forecasting of PV power in electrical power systems. In the frame of the smart grid paradigm, the needing of accurate, reliable, and sharp probabilistic forecasting is particularly enhanced for industrial operators that are interested in optimally manage their grids and actively participating to liberalized electricity markets. As well-known, probabilistic forecasts can be obtained from single probabilistic predictors or from an ensemble of multiple probabilistic or deterministic predictors. The variability of information available in different predictors would likely contribute to produce forecasts that are better, or at least as good as one of the base predictors.

In this chapter, a proposal of a MEM based on BM and QM predictors was presented, and its effectiveness was evaluated through a large number of numerical applications based on actual irradiance data. The ensemble forecasts were constructed by the application of the linear pooling technique, through a minimization procedure that aims to minimize the PLF, that is a proper score. Results of the numerical applications proved the usefulness of the procedure on actual data, thus sometimes leading to a slight over-dispersion of resulting forecasts. Significantly, better forecasts were obtained for the next day while less significant performances were obtained in case of next hour forecast. The above problems will surely be addressed in new researches.

Appendix

A.1. Probabilistic forecast indices and properties

Two major requirements must be met simultaneously by all probabilistic forecasts, i.e. the forecasts must be sharp and also calibrated (or equivalently reliable) [25, 26], as defined at beginning of Section 2. Note that sharpness and reliability are not distinct one each other, as one property significantly influences the other, and vice versa.

A.1.1. Sharpness

Sharpness is a property of the forecast alone, as the realization of the random variable is not involved in its definition. Sharpness, in the case of forecasts for a real-value variable, can be easily assessed in terms of the associated prediction intervals. The narrower the intervals, the better is the forecast (if the corresponding coverage is, however, coherent, as shown in the following subsection [26]). Usually, 50, 90, 95 and 99% prediction intervals are considered for probabilistic forecasting. Prediction intervals can be easily extracted from a forecasted predictive distribution.

A.1.2. Reliability

Reliability is a property of the probabilistic forecast and of the realization. It involves the correspondence between estimated coverages and actual coverages.

Indeed, let us suppose that a 50% prediction interval is provided for a random variable; the forecast is therefore considered reliable if the observation of the random variable lies in that interval with probability 0.5 for the given time horizon.

The same property can be defined also for predictive quantiles; e.g. if the 0.5-quantile (median) is predicted for a given horizon time, the realizations should be equal or lower than the 0.5-quantile in 50% of cases [20, 21, 32].

Reliability diagrams are very effective tools to evaluate the reliability of a probabilistic method [21, 42, 44]; they show the estimated coverage versus the nominal one, for various nominal coverage values (usually from 0.05 to 0.95, with a 0.05 step, or from 0.1 to 0.9 with a 0.1 step).

The estimated coverages can be found from a predictive distribution in a very intuitive manner. Let $P_h^{(\lambda)}$ be the forecasted λ-quantile extracted from the forecasted distribution of the random variable at the desired time horizon h. The indicator $I_h^{(\lambda)}$ is defined from the comparison between the actual value P_h^* and the forecasted quantile $P_h^{(\lambda)}$, as follows:

$$I_h^{(\lambda)} = \begin{cases} 1, \ if \ P_h^* \le P_h^{(\lambda)} \\ 0, \ if \ P_h^* > P_h^{(\lambda)} \end{cases} \tag{A.1}$$

and, consequently, the estimation $\hat{\lambda}$ of the actual coverage λ based on a set of N_{tot} forecasts is:

$$\hat{\lambda} = \frac{1}{N_{tot}} \sum_{h=1}^{N_{tot}} I_h^{(\lambda)}. \tag{A.2}$$

Obviously, the probabilistic forecasting method is considered reliable if the estimated coverages do not significantly differ from the nominal ones. A necessary condition for the probabilistic calibration is the normal dispersion of forecasts, and this results in a reliability curve that is close to the 45° diagonal line (representing the ideal reliability). Instead, over-dispersed forecasts (usually due to lack of sharpness) result in an inverse S-shaped reliability curve, while under-dispersed forecasts (usually due to too much sharpness) result in a S-shaped reliability curve. Biased forecasts are easily recognized, as the corresponding reliability diagrams strongly differ from perfect curve. **Figure A1** shows examples of reliability diagrams for reliable, over-dispersed, under-dispersed and biased forecasts.

The MDPR is straightforwardly defined as the maximum error between estimated coverages and nominal coverages; i.e.:

---

[5] In a nutshell, the PIT is the value that the predictive CDF attains at the observation, with suitable adaptions at any points of discontinuity [25].

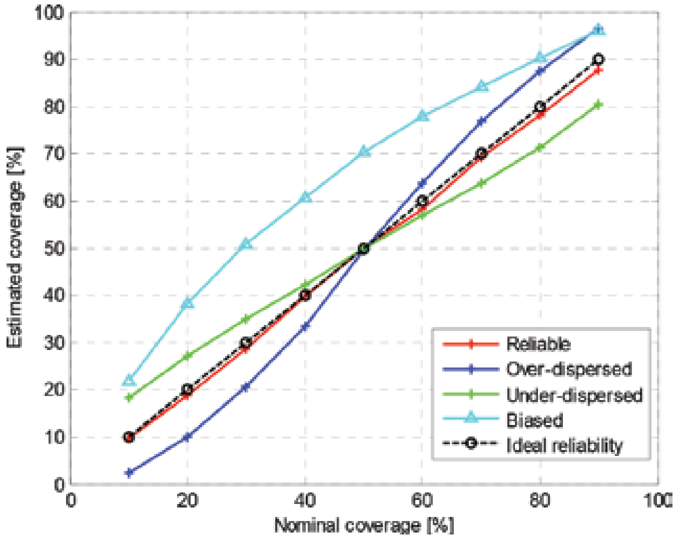

Figure A1. Examples of reliability diagrams for calibrated, over-dispersed, under-dispersed and biased forecasts.

$$MDPR = \max\{|\lambda_1 - \hat{\lambda}_1|, \ldots, |\lambda_J - \hat{\lambda}_J|\} \tag{A.3}$$

Also PIT histograms [25, 42] can be used to empirically check the calibration of forecasts. In these histograms, the PIT values[5] are plotted: for a probabilistically calibrated forecast, the PIT histogram is statistically uniform. Even if the uniformity of PIT histograms is a necessary, but not sufficient condition for the forecast to be perfect [42], from the behaviour of PIT

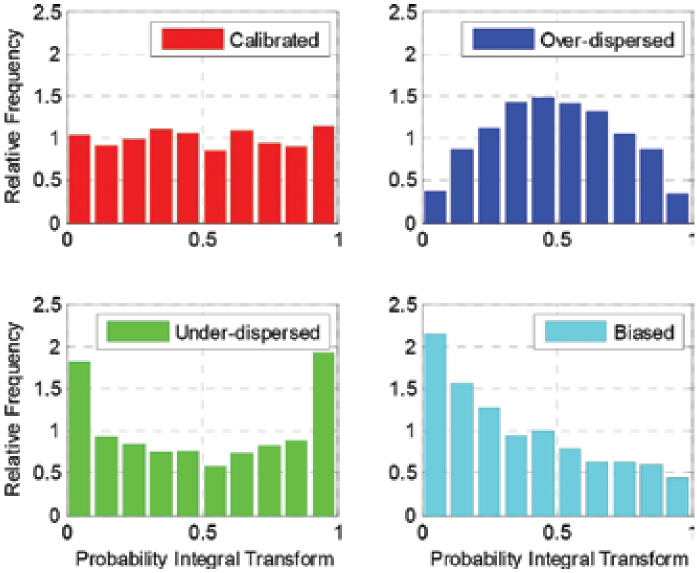

Figure A2. Examples of PIT histograms for calibrated, over-dispersed, under-dispersed and biased forecasts.

histograms, can be derived useful information; in particular, U-shaped histograms indicate under-dispersed predictive distributions as well as inverse U-shaped histograms suggest that the predictive distributions are over-dispersed. Biased predictive distributions have a very irregular PIT histograms. **Figure A2** shows examples of PIT histograms for reliable, over-dispersed, under-dispersed, and biased forecasts.

Anyway, formal tests of the hypothesis that a given forecasting method is probabilistically calibrated are also available, provided that these tests account for complex dependence structures. The reader can refer to the specialized literature to deepen this subject [21, 25].

A.1.3. Proper scores

Probabilistic forecasts can be assessed numerically through the evaluation of proper scores [27]. Two of the most common and versatile proper scores are the PLF and the CRPS, simultaneously addressing both calibration and sharpness [27, 45].

In practice, the CRPS compares the predictive distribution with the observation, both in terms of cumulative distribution functions. In particular, the CDF of the observation is a Heaviside function $\mathrm{H}(\cdot)$ centred in the observation P_h^*, and the CRPS probabilistically accounts for the error area between predictive and actual CDFs (**Figure A3**).

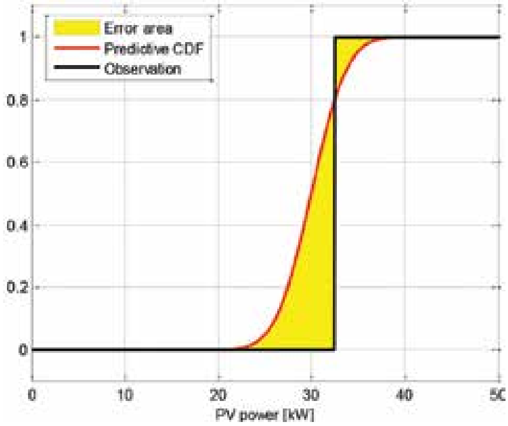

Figure A3. Graphical interpretation of continuous ranked probability score.

Indeed, let $\mathrm{H}(P_h - P_h^*)$ centred in P_h^* be the cumulative distribution function of the actual value of PV power and $\hat{F}_h(P_h)$ be the predictive CDF at the time horizon h; hourly CRPS can be evaluated as follows:

$$CRPS_h = \int_{-\infty}^{+\infty} [\hat{F}_h(P_h) - \mathrm{H}(P_h - P_h^*)]^2 dP_h \tag{A.4}$$

From the analysis of Eq. (A.4), it clearly appears that the CRPS is linked to the total area between the predictive CDF and the Heaviside function. It can be seen that the area (and, consequently, the $CRPS_h$) decreases as the predictive distribution approximates the step function. The calculation of the $CRPS_h$ will result in a value that has the units of the forecast variable. For a total number D of forecasts, the average CRPS is:

$$CRPS = \frac{1}{D}\sum_{d=1}^{D}\int_{-\infty}^{+\infty}[\hat{F}_d(P_d) - \mathrm{H}(P_d - P_d^*)]^2 dP_d \tag{A.5}$$

and it can be interpreted as a probabilistic version of the mean absolute error [25].

The PLF is another widely used proper score [14, 27, 46]. As we defined $P_h^{(\lambda)}$ to be the λ-quantile extracted from the predictive distribution of PV power at the desired time horizon h and P_h^* to be the corresponding actual value of PV power, the PLF is defined as follows:

$$PLF(P_h^{(\lambda)}, P_h^*) = \begin{cases} (1-\lambda)\left(P_h^{(\lambda)} - P_h^*\right), if P_h^* < P_h^{(\lambda)} \\ \lambda\left(P_h^* - P_h^{(\lambda)}\right), if P_h^* \geq P_h^{(\lambda)} \end{cases} \tag{A.6}$$

Summing up the PLFs across all considered quantiles and averaging them throughout the forecast horizon, the PLF of the corresponding probabilistic forecasts is obtained.

A.2. Gamma and beta functions

The Gamma function $\Gamma(x)$ of the complex number x, with $x \in \mathrm{C} - \{0, -1, -2, \ldots\}$, is defined as follows:

$$\Gamma(x) = \int_0^{+\infty} t^{x-1} e^{-t} dt. \tag{A.7}$$

The Beta function $\mathrm{B}(x, y)$ of two complex numbers x, y, with $\mathrm{Re}\{x\}, \mathrm{Re}\{y\} > 0$, is defined as follows:

$$\mathrm{B}(x, y) = \int_0^1 t^{x-1}(1-t)^{y-1} dt \tag{A.8}$$

and its equivalent form in terms of Gamma function is:

$$\mathrm{B}(x, y) = \frac{\Gamma(x)\Gamma(y)}{\Gamma(x+y)}. \tag{A.9}$$

Author details

Antonio Bracale[1], Guido Carpinelli[2]* and Pasquale De Falco[2]

*Address all correspondence to: guido.carpinelli@unina.it

1 University of Napoli Parthenope, Naples, Italy

2 University of Napoli Federico II, Naples, Italy

References

[1] J.P. Chaves-Avila, K. Wurzburg, T. Gomez, P. Linares, The green impact: how renewable sources are changing EU electricity prices, IEEE Power and Energy Magazine, vol. 13, no. 4, pp. 29–40, 2015.

[2] Q. Wang, et al., Review of real-time electricity markets for integrating distributed energy resources and demand response, Applied Energy, vol. 138, pp. 695–706, 2015.

[3] H.A. Rahman, et al., Operation and control strategies of integrated distributed energy resources: a review, Renewable and Sustainable Energy Reviews, vol. 51, pp. 1412–1420, 2015.

[4] P.G. Da Silva, D. Ilić, S. Karnouskos, The impact of smart grid prosumer grouping on forecasting accuracy and its benefits for local electricity market trading, IEEE Transactions on Smart Grids, vol. 5, no. 1, pp. 402–410, 2014.

[5] P. Pinson, C. Chevallier, G.N. Kariniotakis, Trading wind generation from short-term probabilistic forecasts of wind power, IEEE Transactions on Power Systems, vol. 22, no. 3, pp. 1148–1156, 2007.

[6] B. Kraas, M. Schroedter-Homscheidt, R. Madlener, Economic merits of a state-of-the-art concentrating solar power forecasting system for participation in the Spanish electricity market, Solar Energy, vol. 93, pp. 244–255, 2013.

[7] Gestore dei Mercati Energetici website: http://www.mercatoelettrico.org/It/Default.aspx (accessed on 15/09/2016).

[8] A. Muñoz, E.F. Sánchez-Úbeda, A. Cruz, J. Marín, Short-term forecasting in power systems: a guided tour. In S. Rebennack, P.M. Pardalos, M.V.F. Pereira, N.A. Iliadis, Handbook of Power Systems II, Springer, Berlin, Heidelberg, pp. 129–160, 2010.

[9] Gestore dei Servizi Energetici website: http://www.gse.it/it/Pages/default.aspx (accessed on 15/09/2016).

[10] Del. 298/2016/R/eel. Available online: http://www.autorita.energia.it/it/docs/dc/16/298-16.jsp (accessed on 15/09/2016).

[11] A. Costa, A. Crespo, J. Navarro, G. Lizcano, H. Madsen, E. Feitosa, A review on the young history of the wind power short-term prediction, Renewable and Sustainable Energy Reviews, vol. 12, no. 6, pp. 1725–1744, 2008.

[12] J. Widén, et al., Variability assessment and forecasting of renewables: a review for solar, wind, wave and tidal resources, Renewable and Sustainable Energy Reviews, vol. 44, pp. 356–375, 2015.

[13] Y. Ren, P.N. Suganthan, N. Srikanth, Ensemble methods for wind and solar power forecasting—a state-of-the-art review, Renewable and Sustainable Energy Reviews, vol. 50, pp. 82–91, 2015.

[14] T. Hong, P. Pinson, S. Fan, H. Zareipour, A. Troccoli, R.J. Hyndman, Probabilistic energy forecasting: global energy forecasting competition 2014 and beyond, International Journal of Forecasting, vol. 32, no. 3, pp. 896–913, 2016.

[15] R.J. Bessa, A. Trinidade, C.S. Silva, V. Miranda, Probabilistic solar power forecasting in smart grids using distributed information, International Journal of Electric Power & Energy Systems, vol. 72, pp. 16–23, 2015.

[16] K.D. Orwig, et al., Recent trends in variable generation forecasting and its value to the power system, IEEE Transactions on Sustainable Energy, vol. 6, no. 3, pp. 924–933, 2015.

[17] M. Zugno, T. Jónsson, P. Pinson, Trading wind energy on the basis of probabilistic forecasts both of wind generation and of market quantities, Wind Energy, vol. 16, no. 6, pp. 909–926, 2013.

[18] A. Bracale, et al., A Bayesian method for short-term probabilistic forecasting of photovoltaic generation in smart grid operation and control, Energies, vol. 6, no. 2, pp. 733–747, 2013.

[19] A. Bracale, P. De Falco, An advanced Bayesian method for short-term probabilistic forecasting of the generation of wind power, Energies, vol. 8, no. 9, pp. 10293–10314, 2015.

[20] J.K. Møller, H.A. Nielsen, H. Madsen, Time-adaptive quantile regression, Computational Statistics & Data Analysis, vol. 52, no. 3, pp. 1292–1303, 2008.

[21] P. Pinson, et al., Non-parametric probabilistic forecasts of wind power: required properties and evaluation, Wind Energy, vol. 10, no. 6, pp. 497–516, 2007.

[22] R. Ranjan, T. Gneiting, Combining probability forecasts, Journal of the Royal Statistical Society: Series B (Statistical Methodology), vol. 72, no. 1, pp. 71–91, 2010.

[23] A.S. Jore, J. Mitchell, S.P. Vahey, Combining forecast densities from VARs with uncertain instabilities, Journal of Applied Econometrics, vol. 25, no. 4, pp. 621–634, 2010.

[24] S.G. Hall, J. Mitchell, Combining density forecasts, International Journal of Forecasting, vol. 23, no. 1, pp. 1–13, 2007.

[25] T. Gneiting, F. Balabdaoui, A.E. Raftery, Probabilistic forecasts, calibration and sharpness, Journal of the Royal Statistical Society: Series B (Statistical Methodology), vol. 69, no. 2, pp. 243–268, 2007.

[26] A.E. Raftery, T. Gneiting, F. Balabdaoui, M. Polakowski, Using Bayesian model averaging to calibrate forecast ensembles, Monthly Weather Review, vol. 133, no. 5, pp. 1155–1174, 2005.

[27] T. Gneiting, A.E. Raftery, Strictly proper scoring rules, prediction, and estimation, Journal of the American Statistical Association, vol. 102, no. 477, pp. 359–378, 2007.

[28] G. Tina, S. Gagliano, S. Raiti, Hybrid solar/wind power system probabilistic modelling for long-term performance assessment, Solar Energy, vol. 80, no. 5, pp. 578–588, 2006.

[29] Y.M. Atwa, et al., Adequacy evaluation of distribution system including wind/solar DG during different modes of operation, IEEE Transactions on Power Systems, vol. 26, no. 4, pp. 1945–1952, 2011.

[30] A. Gelman, J.B. Carlin, H.S. Stern, D.B. Rubin, Bayesian Data Analysis, Chapman & Hall, London, UK, 1995.

[31] D. Gamerman, Markov Chain Monte Carlo: Stochastic Simulation for Bayesian Inference, Chapman & Hall, London, UK, 1997.

[32] J.B. Bremnes, Probabilistic wind power forecasts using local quantile regression, Wind Energy, vol. 7, no. 1, pp. 47–54, 2004.

[33] T.N. Krishnamurti, et al., A review of multimodel superensemble forecasting for weather, seasonal climate, and hurricanes, Reviews of Geophysics, vol. 54, pp. 336–377, 2016.

[34] M.B. Araújo, M. New, Ensemble forecasting of species distributions, Trends in Ecology & Evolution, vol. 22, no. 1, pp. 42–47, 2007.

[35] R.T. Clemen, R.L. Winkler, Combining probability distributions from experts in risk analysis, Risk Analysis, vol. 19, no. 2, pp. 187–203, 1999.

[36] T.L. Thorarinsdottir, T. Gneiting, Probabilistic forecasts of wind speed: ensemble model output statistics by using heteroscedastic censored regression, Journal of the Royal Statistical Society: Series A (Statistics in Society), vol. 173, no. 2, pp. 371–388, 2010.

[37] M. Scheuerer, Probabilistic quantitative precipitation forecasting using ensemble model output statistics, Quarterly Journal of the Royal Meteorological Society, vol. 140, no. 680, pp. 1086–1096, 2014.

[38] T. Gneiting, R. Ranjan, Combining predictive distributions, Electronic Journal of Statistics, vol. 7, pp. 1747–1782, 2013.

[39] A. Bracale, G. Carpinelli, P. De Falco, A probabilistic competitive ensemble method for short-term photovoltaic power forecasting, IEEE Transactions on Sustainable Energy (accepted for publication). DOI: 10.1109/TSTE.2016.2610523.

[40] NREL Solar Radiation Research Laboratory (SRRL), Baseline Measurement System (BMS), Golden, Colorado, USA. doi: 10.5439/1052221. Available online: https://www.nrel.gov/midc/srrl_bms/ (accessed on 15/09/2016).

[41] P. Pinson, G. Reikard, J.R. Bidlot, Probabilistic forecasting of the wave energy flux, Applied Energy, vol. 93, pp. 364–370, 2012.

[42] T.M. Hamill, Interpretation of rank histograms for verifying ensemble forecasts, Monthly Weather Review, vol. 129, pp. 550–560, 2001.

[43] T.M. Hamill, Reliability diagrams for multicategory probabilistic forecasts, Weather and Forecasting, vol. 12, no. 4, pp. 736–741, 1997.

[44] P. Pinson, J. Juban, G.N. Kariniotakis, On the quality and value of probabilistic forecasts of wind generation, In Proceedings of International Conference on Probabilistic Methods Applied to Power Systems, Stockholm, Sweden, 2006.

[45] H. Hersbach, Decomposition of the continuous ranked probability score for ensemble prediction systems, Weather and Forecasting, vol. 14, pp. 559–569, 2000.

[46] Y. Zhang, J. Wang, GEFCom2014 probabilistic solar power forecasting based on k-nearest neighbor and kernel density estimator, In Proceedings of 2015 IEEE Power & Energy Society General Meeting, Denver, USA, 2015.

Optimizing Hybrid Renewable Energy Systems: A Review

Mahmoud Ghofrani and Negar Niromand Hosseini

Additional information is available at the end of the chapter

http://dx.doi.org/10.5772/65971

Abstract

With the fast progression of renewable energy markets, the importance of combining different sources of power into a hybrid renewable energy system (HRES) has gained more attraction. These hybrid systems can overcome limitations of the individual generating technologies in terms of their fuel efficiency, economics, reliability and flexibility. One of the main concerns is the stochastic nature of photovoltaic (PV) and wind energy resources. Wind is often not correlated with load patterns and may be discarded sometimes when abundantly available. Also, solar energy is only available during the day time. A hybrid energy system consisting of energy storage, renewable and nonrenewable generation can alleviate the issues associated with renewable uncertainties and fluctuations. Large number of random variables and parameters in a hybrid energy system requires an optimization that most efficiently sizes the hybrid system components to realize the economic, technical and designing objectives. This chapter provides an overview of optimal sizing and optimization algorithms for hybrid renewable energy systems as well as different objective functions considered for designing such systems.

Keywords: hybrid energy system, objectives, optimization, renewable energy, sizing

1. Introduction

Use of solar and wind power has become more and more significant, attractive and less expensive, since the oil crises in the early 1970s. Even though there is a need to use renewable energy sources, the main problem with it is the dependency on environmental conditions like solar irradiance and wind speed. The individual energy sources cannot provide continuous power supply to the load because of the uncertainty and on-and-off nature of the environmental conditions [1]. Combining intermittent renewable energy sources with other dispatchable sources of energy such as biogas and fuel cells as well as energy storage systems provides a solution to address this challenge. Hybrid renewable energy system (HRES) is a term to describe the combination of two or more renewable and nonrenewable energy sources. Basic components of such systems are power sources (wind turbine, diesel engine generator and solar arrays), the battery and the power management center, which regulates power production from each of the sources [1]. As an example of such systems, microgrid is an integrated energy system that includes energy resources, loads and storages. Microgrids found popularity over the years due to the needs for distributed generation and with the integration of HRESs including photovoltaic (PV) and wind generators as well as the battery storage devices. The microgrids have many benefits for both utility grids and customers, such as higher power quality, reduction in carbon emission, energy efficiency and reduced costs. Another capability of microgrids is islanding which allows the microgrid to be disconnected from the utility grid in the case of upstream disturbances or voltage fluctuations [2].

Operating an HRES requires optimizing its performance while satisfying its physical and technical constraints. Therefore, optimization tools, techniques and applications have found popularity to achieve these goals [3].

This chapter provides an overview of the optimization techniques, optimization objectives and component sizing for hybrid renewable energy systems. Section 2 summarizes optimal sizing results of hybrid renewable energy systems in different studies. Section 3 describes the three commonly used algorithms to optimize the operation and modelling of hybrid energy systems: classical algorithms, metaheuristic algorithms and hybrid algorithms. Section 4 reviews different objective functions, constraints and indexes in use for the hybrid system optimization.

2. Optimal sizing for hybrid renewable energy systems

HRESs require an optimal design for their component sizing to economically, efficiently and reliably meet the objectives outlined in Section 4. **Table 1** provides examples of studies related

References	Components of the hybrid system	Load specifications	Sizing results
[4]	Wind turbine (WT), photovoltaic (PV) and battery	225 kW peak, 25 kW base	195 kW WT, 85 kW PV, 230 kW microturbine, 2.14 kAh battery
[5]	WT, PV, microturbine and battery	1.5 kW constant	6 kW WT, 12.8 kW PV, 6 kAh battery
[6]	WT, PV, diesel and battery	26 kW peak, 5 kW base	15 kW WT, 24 kW PV50 kW diesel, 151 kWh battery
[7]	WT, PV and battery	1500 W	78 × 100 W PV, 2 × 6 kW WT, 5000 Ah (24 V) battery
[8]	PV, diesel and battery	3.5 kW peak, 0.25 kW base	2.8 kW DG, 4.2 m^2 PV, 2.75 kWh battery
[9]	Wind, PV and energy storage	1 MW peak, 0.4 MW base	2.096 MW wind, 0 MW PV, 6.576 MWh energy storage
[10]	Wind, PV and energy storage		2.42 MW wind, 0 MW PV, 6.7878 MWh energy storage

Table 1. Optimal sizing of HRESs.

to HRES optimal sizing along with details regarding the hybrid system components, their load characteristics and sizing results.

3. Optimization algorithms for hybrid renewable energy systems

Optimization algorithms are ways of computing maximum or minimum of mathematical functions. Different objectives can be considered when optimizing a system's design. Maximizing the efficiency of the system and minimizing the cost of its production are examples of such objectives. Optimization methods and techniques can help to solve complex problems. When designing a HRES, we have to consider its components' performances. The main goal is to have a better performance with reduced costs. These goals can be achieved through optimal modelling of the system [11]. The three commonly used modelling and optimization techniques for hybrid systems are classical algorithms, metaheuristic methods and hybrid of two or more optimization techniques.

3.1. Classical techniques

Classical optimization algorithms use differential calculus to find optimum solutions for differentiable and continuous functions. The classical methods have limited capabilities for applications whose objective functions are not differentiable and/or continuous. Several conventional optimization methods have been used for hybrid energy systems. Linear programming model (LPM), dynamic programming (DP) and nonlinear programming (NLP) are examples of classical algorithms widely in use for optimizing HRESs.

Linear programming model (LPM) studies the cases in which the objective function is linear and the design variable space is specified using only linear equalities and inequalities.

This model has been used in several studies for HRES optimization [12–17]. These studies take advantage of the LPM capabilities to stochastically perform reliability and economic analysis. However, the energy delivery capability of the overall system is adversely affected by failure of any of the renewables to function properly [11].

Nonlinear programming (NLP) model studies the general cases in which the objective functions or the constraints or both contain nonlinear parts. This model has been used in some studies [18, 19]. The model enables solving complex problems with simple operations. However, high number of iterations for numerical methods such as NLP increases the computational burden of the problem [11].

Dynamic programming (DP) studies the cases in which the optimization strategy is based on splitting the problem into smaller subproblems. This method helps solving sequential or multistage problems in which the stages are related together. One advantage of DP is the ability of optimizing each stage. Therefore, it can address the complexity of larger systems. However, high number of recursive functions for DP makes the coding and implementation complex and confusing [11]. Ref. [20] provides an example of studies that uses DP for HRES optimization.

3.2. Metaheuristic techniques

Metaheuristic search techniques have been extensively used for optimizing complex systems such as HRESs due to their capabilities to give efficient, accurate and optimal solutions. These algorithms are nature-inspired as their developments are based on behaviour of nature. Examples of metaheuristic optimization in use for HRESs include genetic algorithm (GA), particle swarm optimization (PSO), simulated annealing (SA) and ant colony (AC) algorithm.

Genetic algorithm (GA) is an evolutionary population-based algorithm that includes several operations such as initialization, mutation, crossover and selection to ensure finding an optimal solution to a given problem. Several studies used GA to optimize the design and operation of HRESs [21–28]. GA may result in local optima if it is not initialized or designed properly.

Particle swarm optimization (PSO) simulates the social behaviour of how a swarm moves to find food in a specific area. It is an iterative algorithm with the goal of finding a solution for a given objective function within a given space. Its application for optimizing HRESs has been investigated in several studies [29–34]. PSO is efficient in solving the scattering and optimization problems. However, it requires several modifications due to its complex and conflicted nature [11].

Simulated annealing (SA) is based on the metal annealing processing. A metal gets melted at a very high temperature and then it gets cooled down and finally gets frozen into a crystalline state with the minimum amount of energy. As a result, the metal develops larger crystal sizes with a minimum amount of defects in its metallic structure. SA has been used for hybrid system sizing in several studies such as [35].

Ant colony (AC) algorithm is based on behaviour of ants to use a specific pheromone to mark the path for other ants. More pheromones are left on the path as more ants follow the same path. On the other hand, if a path is not used, then the smell of the last pheromone will disappear. Ants are more attracted to the paths with the most pheromone smells and it usually leads them to places with most foods. By following this method, ants mark the shortest path towards food. AC simulates this behaviour to find the most optimal solution for a given objective function [36]. This algorithm has been used for size optimization for hybrid systems [37]. AC algorithms have high convergence speed but require long-term memory space [11].

3.3. Hybrid techniques

Combination of two or more optimization techniques can overcome limitations of the individual techniques mentioned above to provide more effective and reliable solutions for HRESs. This combination is referred to as hybrid techniques. Examples of such techniques are SA-Tabu search; Monte Carlo simulation (MCS)-PSO; hybrid iterative/GA; MODO (multiobjective design optimization)/GA; artificial neural fuzzy interface system (ANFIS); artificial neural network/GA/MCS; PSO/DE (differential evolution); evolutionary algorithms and simulation optimization-MCS which have been used in several studies for optimizing HRESs [38–47]. Although hybrid techniques enhance the overall performance of the optimization, they may suffer from some limitations. Examples of such limitations are the partial optimism of the hybrid MCS-PSO method in [40], suboptimal solutions of the hybrid iterative/GA in [41], cost-sizing compromise of the hybrid methods in [42, 43], design complexity of the hybrid ANN/GA/MCS method in [44], random adjusting of the inertia weight of the evolutionary algorithm in [46] and coding complexity of the optimization-MCS in [47].

4. Optimization objectives for HRESs

Various criteria are considered for optimal design and component sizing of HRESs. These criteria can be broadly categorized as economic and technical. Economic criteria are used to minimize costs of HRESs. Technical criteria include reliability, efficiency and environmental objectives to supply the load demand of HRESs at desired reliability levels with maximum efficiency and minimum greenhouse gas emissions.

4.1. Cost optimization

HRESs often times include higher capital costs and lower operation and maintenance (O&M) costs which require an optimization to determine the compromise solution between the costs and benefits. Cost optimization of hybrid renewable energy systems includes minimizing energy cost, net present cost (NPC) and any other costs associated with such systems.

4.1.1. Energy cost minimization

Several studies have investigated minimizing levelized cost of energy (LCE) for HRESs. LCE is the ratio of total cost of the hybrid system to the annual energy supplied by the system. **Table 2** summarizes the related research works, their objective functions, techniques in use for optimization and their main findings.

4.1.2. Net present cost minimization

Net present cost (NPC) of an HRES is defined as the total present value of the system that includes the initial cost of the system components as well as the replacement and maintenance cost within the project lifetime. The objective here is to minimize the NPC of HRESs. **Table 3** summarizes the related research works, their objective functions, techniques in use for optimization and their main findings.

4.1.3. Other cost-related optimization

Other cost-related optimizations include minimizing life cycle cost (LCC), levelized unit electricity cost (LUEC), annualized cost of the system (ACS), capital cost (CC) of the hybrid

References	**Objective function(s)**	**Optimization technique**	**Findings**
[33]	$\min LCE = \dfrac{\left(\left[\dfrac{d(1+d)^n}{(1+d)^n - 1} \times ICC\right]\right) + \left(ANN + \left[O\ \&M \times n\right]\right)}{8760 \times CF_{net}}$ d = interest rate (%); n = operational life (years); ICC: installed capital cost (\$/kW); ANN = the annualized costs (insurance, other expenses); $O\&M$ = operation and maintenance cost (\$/kW); CF_{net} = net capacity factor; 8760 = hours per year.	PSO	Levelized cost of energy is achieved which is based on several factors such as financing, insurance, maintenance and other depreciation factors.
[48]	$\min LCE = \sum_{i=1}^{n} \left(\dfrac{CO_i}{y_i}\right) \Big/ E_{an} = \dfrac{\dfrac{CO_{PV}}{Y_{PV}} + \dfrac{CO_W}{Y_W} + CO_{Bat} / Y_{Bat}}{E_{an}(\gamma, \beta, h)}$ CO_{PV} = the sum of capital cost and maintenance cost in the lifespan of the whole PV system; CO_W = the sum of capital cost and replacement or maintenance cost in the lifespan of the whole wind power generation system; CO_{Bat} = the sum of capital cost and the lifespan maintenance cost of battery bank; Y_{PV} = the lifetime year of PV system; Y_W = the lifetime year of wind system; Y_{Bat} = the lifetime year of battery bank; $E_{an}(\gamma,\beta,h)$ = the annual energy supplied from the hybrid solar-wind system.		An optimal model is developed to ensure capacity sizes are ideal for different hybrid system components including PV system, wind system and battery bank.
[49]	$\min CE = \left[\dfrac{r(1+r)^n}{r(1+r)^n - 1}\right]\left[\dfrac{P}{87.6k}\right] + \left[O\ \&M\right]$ CE = cost of energy in U.S. cents/kWh; k = annual capacity factor in per-unit; n = amortization period, years; $O\&M$ = operation and maintenance cost in U.S. cents/kWh; P = installed (capital) cost in U.S. \$/kW; r = fixed annual interest rate in per-unit.		An optimal sizing model is designed for solar wind systems to meet energy demands.
[50, 51]	$\min LCE = \dfrac{TAC}{E_{tot}} = \dfrac{PVC \times \left[\dfrac{d(1+d)^n}{(1+d)^n - 1}\right]}{E_{tot}}$ PVC = present value of costs; TAC = total annualized cost; E_{tot} = the annual total energy; d = discount rate; n =useful lifetime.		Monthly and daily energy balances are evaluated for optimal configurations of hybrid PV/wind systems.

References	Objective function(s)	Optimization technique	Findings
[52]	$\min LCE = \frac{C_{acap}(x) + C_{amain}(x) + C_{arep}}{E_{annual}}$ E_{annual} = the annual consumed energy (kWh/year); C_{arep} = levelized replacement cost of energy; C_{acap} = levelized capital cost of energy; $C_{amain}(_{x})$ = levelized maintenance and operation cost of energy.	GA	A compromise solution is obtained between the levelized cost of energy and CO_2 emission.
[53]	$\min LCE = \frac{\left(C + L + \sum_{n=1}^{N} \frac{(OM+1) \times C}{(1+r)^n}\right)}{\left(\sum_{n=1}^{N} \frac{S \times TF \times \eta \times (1-d)^n}{(1+r)^n}\right)}$ S = solar resource; TF = tracking factor; d = annual degradation rate; η = performance factor; OM = maintenance cost; C = cost of the system; L = cost of the required land; r = discount rate.		Levelized cost of energy is estimated on the basis of electricity pricing for the entire life cycle of a given hybrid system.
[54]	$\min LCE = \frac{TLCC \times CRF}{E} \cdot \frac{d(1+d)^n}{(1+d)^n - 1}$ $TLCC$ = total life-cycle cost; CRF = capital recovery factor; n = year; E = the annual generated energy (kWh); d = annual degradation rate.		A hybrid wind-PV system is designed for an off-grid electrification project considering several parameters such as number, type and location of generators, controllers, batteries and inverters.
[55]	$\min LCE = \frac{NPC}{\left\{\sum_{n=1}^{N} \left[\frac{Q_n}{(1+d)^n}\right]\right\}}$ Q_n = energy in year n (kWh); d = annual discount rate; NPC =net present cost ($).	GA	PV-diesel hybrid systems are shown to be optimal economic solutions to incorporate renewable energy into pumping for drip irrigation facilities.

Table 2. Optimization of HRESs for minimizing LCE.

system, total cost of the system (TCS) and average generation cost (AGC). **Table 4** summarizes the related research works, their objective functions, techniques in use for optimization and their main findings.

4.2. Technical optimization

Besides the cost optimization explained in Section 4.1, technical objectives can be also optimized when designing an HRES. Technical objectives include, but are not limited to,

References	Objective function	Optimization technique	Findings
[56]	$COE=\frac{TNPC\times CRF}{\sum_{t=1}^{8760}E_{Gen(t)}}$ $CRF(d,n)=\frac{di(1+di)^n}{(1+di)^n}$ COE = cost of energy (%); $TNPC$ = total net present cost; CRF = capital recovery factor; $E_{Gen}({}_t)$ = total generated electricity over a period; di =discount rate (%); d = day of the year (d); n = life of the plant (year).	PSO	A hybrid system of solar, diesel, hydro, biomass and biogas energy is optimally designed to meet the load demand of seven villages in India. CO_2 emissions, renewable fraction, net present cost and cost of energy are included in the model.
[57]	$\min NPC=\frac{TAC}{CRF(i,N)}$ TAC = the total annualized cost (\$/year); CRF = the capital recovery factor; i = annual real interest rate; N = the project lifetime in years.		The PV/diesel/battery HRES configuration is found as the optimum solution among different hybrid system configurations for different study areas within the geopolitical zones of Nigeria.
[58]	$\min NPC=\frac{(ACC+ARC+AMC)}{\left[\frac{i(1+i)^j}{(1+i)^j-1}\right]}$ ACC = the annualized capital cost; ARC = the annualized replacement cost; AMC = the annualized maintenance cost; j = the project lifetime; i = the annual real interest rate.	ANN/GA	A model is developed to evaluate technical and economic impacts of charge controller operation and coulombic efficiency on stand-alone hybrid PV/wind/diesel/battery power systems.
[59]	$\min NPC=\sum_{N=1}^{N=t}f_{d,N}\left(C_{cap}+C_{rep}+C_{main}-C_s\right)$ t = the project life time C_{cap}, C_{rep}, C_{main} and C_s = the nominal capital, the replacement, the O&M cost and the salvage costs, respectively.		Two scenarios are modeled for stand-alone hybrid renewable systems with hydrogen production and storage. The hybrid wind/PV model was found to provide the optimal configuration for the study area.

Table 3. Optimization of HRESs for minimizing NPC.

satisfying desired reliability levels based on loss of power supply probability (LPSP) or loss of load probability (LOL) [64–66], minimizing cost/efficiency ratio [67], minimizing carbon emissions [68] and maximizing power availability [69]. **Table 5** summarizes the related research works, their objective functions, techniques in use for optimization and their main findings.

References	Objective function	Optimization technique	Findings
[42]	$\min LCC = \frac{PW}{Pr} + C_{inst} + C_{maint} x \times x \times \frac{1-x^n}{1-x} + PW_{replace}$ *LCC* = life cycle cost; *Pr* = present worth factor for an item that will be purchased *n* years later; *PW* = power; C_{inst} = installation cost; C_{maint} = maintenance cost; $PW_{replace}$ = present worth of the component considering that it needs to be replaced periodically.	Multiobjective programming (MOP)/GA	A multiobjective optimization is developed to combine life cycle cost, embodied energy and loss of power supply probability as the objectives for designing an autonomous hybrid wind/PV/battery system. An optimal economic and environmental design is obtained among the Pareto solutions based on the designer's preferences.
[60]	$\min LUEC\left(\frac{\$}{kWh}\right) = \frac{LCC \times CRF}{\sum_{t=1}^{8760} E_{Gen}(\mathrm{t})}$ *LUEC* = levelized unit electricity cost; $E_{Gen}(t)$ = total generated electricity over a period; *CRF* = capital recovery factor; *LCC* = the life cycle cost of the hybrid system.		An optimization is developed to incorporate reliability and cost models for a grid-independent hybrid PV/wind system.
[61]	$\min CC = \alpha . N_{PV} + \beta . N_{batt} + C_0$ *CC* = capital cost of the hybrid system; α = cost of a PV module; β = cost of a battery; N_{PV} = number of PV modules; N_{batt} = number of battery storage; C_0 = the total constant costs including the cost of design, installation and a wind turbine.	GA	Optimal component sizes are calculated for a standalone hybrid wind-PV-battery system.
[7]	$\min ACS = C_{cap} . \left[\frac{i(1+i)^{Y_{proj}}}{(1+i)^{Y_{proj}} - 1}\right]$ $(PV + Wind + Bat + Tower)$ $+ C_{rep}\left[\frac{i}{(1+i)^{Y_{rep}} - 1}\right](Bat)$ $+ C_{amain}(PV + Wind + Bat + Tower)$ *ACS* = annualized cost of the system; C_{cap} = the initial capital cost of each component; Y_{proj} = the component lifetime, year; C_{amain} = annualized maintenance cost; Y_{rep} = the component (battery) lifetime, year; C_{rep} = replacement cost of the component (battery); *i* = annual interest rate.	GA	Optimal PV module number and slope angle, wind turbine number and installation height and battery capacity are calculated to design a hybrid system for a telecommunication relay station.
[62]	$\min TCS = \sum_{i=w,S,b} (I_i - S_{P_i} + OM_{P_i})$ *w*, *s*, *b* = the wind power, solar power and battery storage, respectively; I_i, S_{pi}, OM_{pi} = the initial cost, present worth of salvage value and present worth of operation and maintenance (OM) cost for equipment *i*.	PSO	Total cost of a stand-alone hybrid power generation system is reduced while maximizing its reliability.

References	Objective function	Optimization technique	Findings
[63]	$\min C_{av} = \dfrac{\left\{ \dfrac{r(1+r)^n}{(1+r)^n - 1} + m \right\} \sum_i P_i R_i}{(87.6) \sum_i R_i K_i}$ C_{av} = the average generation cost; i = the summation index to include all devices; K_i = the load factor for ith device; m= the operation and maintenance charge rate in per unit; n = the amortization period in years; P_i = the capital cost for the ith device; R_i = the rating in kW of the ith device.		An integrated renewable energy optimization model (IREOM) is developed to size renewable energy systems for desired reliability levels.

Table 4. Optimization of HRESs for minimizing other costs.

References	Objective function	Optimization technique	Findings
[64]	$LPSP = \dfrac{\sum_{t=0}^{T} Power.failure.time\left(P_{supplied}(t) < P_{needed}(t)\right)}{N}$ N = the number of time intervals; t = time, h; T = temperature, K; $P_{supplied}$ = power supplied from the hybrid system; P_{needed} = power needed.	GA	Optimal sizing of HRES is achieved for a custom required loss of power supply probability.
[65]	$LOLP = \dfrac{\sum_{i=1}^{n} hours\left(I_{supplied}(t) < I_{needed}(t)\right)}{n}$ $LOLP$ = loss of load probability; $I_{needed}(t)$ = the current required for the load at hour t; $I_{supplied}(t)$ = the current supplied by HRES at hour t; n = number of samples.		Lower levels of LOLP result in higher costs of the hybrid system and vice versa.
[66]	$LSPS = \Pr\left\{ E_{b,t} \le E_{B\,min}, for\, t \le T \right\}$ $E_{b,t}$ = energy stored in the batteries in hour t; E_{Bmin} = battery minimum allowable energy level.	GA	The total capital cost is minimized while satisfying the constraint of the loss of power supply probability (LPSP).
[67]	$\sum_{j=1}^{6} \sum_{i=1}^{1} \left(\dfrac{C_{ij}}{\eta_{ij}} \right) x_{ij}$ C = unit cost of the system; η = efficiency of the system; i = renewable energy system; j = end use; x = quantum of renewable energy.	Multiobjective programming (MOP)	Analysis was done to find out the reliability factor of solar PV power plant and wind turbine generator.
[68]	$C_{co_2} = CP_{co_2} (\mathrm{E}_i \,\mathrm{x}\, \mathrm{R}_{i,co_2})$ C_{co_2} = the gravimetric cost penalty for carbon emissions; CP_{co_2} = monetary cost of co_2; E_i = the annual system component power consumption/ utilization (kWhr); R_{i,co_2} = specific co_2 emission rate.	PSO	A multiobjective optimization is developed to meet the load and water desalination demand of an HRES.

References	Objective function	Optimization technique	Findings
[69]	$A = 1 - \frac{DNM}{D}$ $DNM = \sum_{t=1}^{T} P_{Batt_{MIN}}(t) - P_{Batt_{SOC}}(t) - (P_{PV}(t) + P_{wind}(t) + P_{Grid}(t) - P_D(t)) \times u(t)$ DNM = demand not met (kWh/year); A = index of availability; D = yearly demand; $P_{Batt_{MIN}}(t)$ = minimum allowable storage level at time t; $P_{Batt_{SOC}}(t)$ = state of charge of battery bank at time t; $P_{Grid}(t)$ = power purchased from utility at time t; $P_{wind}(t)$ = wind power at time t; $P_D(t)$ = demand at time t; $P_{PV}(t)$ = photovoltaic power at time t; T = operational duration under consideration; $U(t)$ = the step function which is zero if the supply power is greater than or equal to demand and one if the demand is not met.	Multiobjective genetic algorithm (MOGA)	A multiobjective optimization is developed that considers the availability of the generated electricity and cost of the equipment for the system design.

Table 5. Optimization of HRESs for technical objectives.

Author details

Mahmoud Ghofrani* and Negar Niromand Hosseini

*Address all correspondence to: mrani@uw.edu

Electrical Engineering, Engineering and Mathematics Division, School of STEM, University of Washington Bothell, Bothell, WA, USA

References

[1] Shivarama Krishna K., Sathish Kumar K. A review on hybrid renewable energy systems. Renewable and Sustainable Energy Reviews 2015; 52: 907–916.

[2] Parhizi S., Lotfi H., Khodaei A., Bahramirad S. State of the art in research on microgrids: a review. IEEE Access 2015; 3: 890–925.

[3] Fathima A., Palanisamy K. Optimization in microgrids with hybrid energy systems – a review. Renewable and Sustainable Energy Reviews 2015; 45: 431–446.

[4] Kalantar M., Mousavi S.M.G. Dynamic behaviour of a stand-alone hybrid power generation system of wind turbine, microturbine, solar array and battery storage. Applied Energy 2010; 87: 3051–3064.

[5] Yang H., Zhou W., Lu L., Fang Z. Optimal sizing method for stand-alone hybrid solar–wind system with LPSP technology by using genetic algorithm. Solar Energy 2003; 82: 354–467.

[6] Boonbumroong U., Pratinthong N., Thepa S., Jivacate C., Pridasawas W. PSO for ac-coupling standalone hybrid power system. Solar Energy 2011; 85: 560–569.

[7] Hongxing Y., Zhou W., Chengzhi L. Optimal design and techno-economic analysis of a hybrid solar–wind power generation system. Applied Energy 2009; 86: 163–169.

[8] Zhang X., Tan S.C., Li G., Li J., Feng Z. Components sizing of hybrid energy systems via the optimization of power dispatch simulations. Energy 2013; 52: 165–172.

[9] Arabali A., Ghofrani M., Etezadi-Amoli M., Fadali M.S., Baghzouz Y. Genetic-algorithm-based optimization approach for energy management. IEEE Transactions on Power Delivery 2013; 28(1): 162–170.

[10] Arabali A., Ghofrani M., Etezadi-Amoli M., Fadali M.S. Stochastic performance assessment and sizing for a hybrid power system of solar/wind/energy storage. IEEE Transactions on Sustainable Energy 2014; 5(2): 363–371.

[11] Siddaiah R., Saini R. A review on planning, configurations, modeling and optimization techniques of hybrid renewable energy systems for off grid applications. Renewable and Sustainable Energy Reviews 2016; 58: 376–396.

[12] Ramakumar R., Abouzahr M., Ashenay K. A knowledge-based approach to the design of integrated renewable energy systems. IEEE Transactions on Energy Conversion 1992; 7(4): 648–659.

[13] Akella A.K., Sharma M.P., Raini R.P. Optimum utilization of renewable energy sources in a remote area. Renewable and Sustainable Energy Reviews 2007; 11(5): 894–908.

[14] Hennet J.C., Samarakou M.T. Optimization of a combined wind and solar power plant. Energy Research 1986; 10(2): 181–188.

[15] Gupta A., Saini R.P., Sharma M.P. Optimized application of hybrid renewable energy system in rural electrification. In: Proceedings of India International Conference on Power Electronics. IEEE, Chennai, India, 2006.

[16] Kanase-Patil A.B., Saini R.P., Sharma M.P. Integrated renewable energy systems for off grid rural electrification of remote area. Renewable Energy 2010; 35(6): 1342–1349.

[17] Nagabhushana A.C., Rohini R., Raju A.B. Economic analysis and comparison of proposed HRES for stand-alone applications at various places in Karnataka state. In: Proceedings of IEEE PES Innovative Smart Grid Technologies. IEEE, Kerala, India; 2011.

[18] Ashok S. Optimized model for community-based hybrid energy system. Renewable Energy 2007; 32: 1155–1164.

[19] El-Zeftawy A.A., Abou El-Ela A.A. Optimal planning of wind-diesel generation units in an isolated area. Electric Power Systems Research 1991; 22(1): 27–33.

[20] Das T.K., Chakraborty D., Swapan S. Energy consumption and prospects for renewable energy technologies in an Indian village. Energy 1990; 15(5): 445–449.

[21] Hochmut G.C.S. A combined optimization concept for the design and operation strategy of hybrid-PV energy systems. Solar Energy 1997; 61(2): 77–87.

[22] Zhao B., Zhang X., Chen J., Wang C. Operation optimization of stand alone micro-grids considering life time characteristics of battery energy storage system. IEEE Transactions on Sustainable Energy 2013; 4(4): 934–943.

[23] Liao G.C. Solve environmental economic dispatch of smart microgrid containing distributed generation system—using chaotic quantum genetic algorithm. International Journal of Electrical Power and Energy Systems 2012; 43(1): 779–787.

[24] Katsigiannis Y.A., Georgilakis P.S., Karapidakis E.S. Multi objective genetic algorithm solution to the optimum economic and environmental performance problem of small autonomous hybrid power systems with renewables. Renewable Power Generation 2010; 4(5): 404–419.

[25] Abbes D., Martinez A., Champenois G. Eco-design optimisation of an autonomous hybrid wind–photovoltaic system with battery storage. IET Renewable Power Generation 2012; 6(5): 358–371.

[26] Koutroulis E., Dionysian K., Antonis P., Kostas K. Methodology for optimal sizing of stand-alone photovoltaic/wind-generator systems using genetic algorithms. Solar Energy 2006; 80(9): 1072–1088.

[27] Koutroulis E., Kolokotsa D. Design optimization of desalination systems power-supplied by PV and wind energy sources. Desalination 2010; 258: 171–181.

[28] Zeng J., Li M., Liu J.F., Wu J., Ngan H.W. Operational optimization of a stand-alone hybrid renewable energy generation system based on an improved genetic algorithm. Proceedings of IEEE Conference, 2010.

[29] Wang L., Singh C. Multi criteria design of hybrid power generation systems based on a modified particle swarm optimization algorithm. IEEE Transactions on Energy Conversion 2009; 24(1): 163–172.

[30] Hakimi S.M., Moghaddas-Tafreshi S.M. Optimal sizing of a stand-alone hybrid power system via particle swarm optimization for Kanauji area in South-East of Iran. Renewable Energy 2009; 34(7): 1855–1862.

[31] Lee T.Y., Chen C.L. Wind-photovoltaic capacity coordination for a time-of-use rate industrial user. IET Renewable Power Generation 2009; 3(2): 152–167.

[32] Ardakani F.J., Gholamhossein R., Mehrdad A. Design of an optimum hybrid renewable energy system considering reliability indices. In: Proceedings of ICEE. IEEE, Isfahan, Iran, 2010.

[33] Amer M., Namaane A., M'Sirdi N.K. Optimization of hybrid renewable energy systems (HRES) using PSO for cost reduction. Energy Procedia 2013; 42: 318–327.

[34] Askarzadesh A., dos Santos Coelho L. A novel frame work for optimization of a grid independent hybrid renewable energy system: a case study of Iran. Solar Energy 2015; 112(1): 383–396.

[35] Fung C.C., Hoand S.C.Y., Nayar C.V. Optimisation of a hybrid energy system using simulated annealing technique. IEEE TENCON 1993; 5: 235–238.

[36] Wu Y., Lee C., Liu L., Tsai S. Study of reconfiguration for the distribution system with distributed generators. IEEE Transactions on Power Delivery 2010; 25(3): 1678–1685.

[37] Fetanat A., Ehsan K. Size optimization for hybrid photovoltaic-wind energy system using ant colony optimization for continuous domains based integer programming. Applied Soft Computing 2015; 31: 196–209.

[38] Sunanda S., Chandel S.S. Review of recent trends in optimization techniques for solar photovoltaic–wind based hybrid energy systems. Renewable and Sustainable Energy Reviews 2015; 50: 775–769.

[39] Katsigiannis Y.A., Georgilakis P.S., Karapidakis E.S. Hybrid simulated annealing Tabu search method for optimal sizing of autonomous power systems with renewable. IEEE Transactions on Sustainable Energy 2012; 3(3): 330–338.

[40] Bashir M., Sadeh J. Optimal sizing of hybrid wind/photovoltaic/battery considering the uncertainty of wind and photovoltaic power using Monte Carlo simulation. In: Proceedings of IEEE International Conference. IEEE, Venice, Italy, 2012.

[41] Khatib T., Mohameda A., Sopian K. Optimization of a PV/wind micro-grid for rural housing electrification using a hybrid iterative/genetic algorithm: case study of Kuala Terengganu, Malaysia. Energy and Buildings 2012; 47: 321–333.

[42] Abbes D., Martinez A., Champions G. Life cycle cost embodied energy and loss of power supply probability for the optimal design of hybrid power systems. Mathematics and Computers in Simulation 2014; 98: 46–62.

[43] Rajkumar R.K., Ramachandaramurthy V.K., Yong B.L., Chia D.B. Techno-economical optimization of hybrid PV/wind/battery system using neuro-fuzzy. Energy 2011; 36(8): 5148–5153.

[44] Lujano-Rojas J.M., Dufo-Lopez R., José L., Agustin B. Probabilistic modelling and analysis of stand-alone hybrid power systems. Energy 2013; 63: 19–27.

[45] Sanchez V.M., Chavez-Ramirez A.U., et al. Techno-economical optimization based on swarm intelligence algorithm for a stand-alone wind-photovoltaic-hydrogen power system at south-east region of Mexico. International Journal of Hydrogen Energy 2014; 39(29): 1646–1655.

[46] Maleki A., Pourfayaz F. Optimal sizing of autonomous hybrids photovoltaic/wind/battery power system with LPSP technology by using evolutionary algorithms. Solar Energy 2015; 115: 471–483.

[47] Chang K., Lin G. Optimal design of hybrid renewable energy systems using simulation optimization. Simulation Modelling Practice and Theory 2015; 52: 40–51.

[48] Yang H., Lu L., Zhou W. A novel optimization sizing model for hybrid solar-wind power generation system. Solar Energy 2007; 81: 76–84.

[49] Ramakumar R., Butler N.G., Rodriguez A.P., Venkata S.S. Economic aspects of advanced energy technologies. In: Proceedings of the IEEE Conference; 1993.

[50] Diaf S., Diaf D., Belhamel M., Haddadi M., Louche A. A methodology for optimal sizing of autonomous hybrid PV/wind system. Energy Policy 2007; 35: 5708–5718.

[51] Diaf S., Notton G., Belhamel M., Haddadi M., Louche A. Design and techno-economical optimization for hybrid PV/wind system under various meteorological conditions. Applied Energy 2008; 85: 968–987.

[52] Bilal B.O., Sambou V., Kebe C.M.F., Ndiaye P.A., Ndongo M. Methodology to size an optimal stand-alone PV/wind/diesel/battery system minimizing the levelized cost of energy and the CO_2 emissions. Energy Procedia 2012; 14: 1636–1647.

[53] Ouedraogo B.I., Kouame S., Azoumah Y., Yamegueu D. Incentives for rural off grid electrification in Burkina Faso using LCOE. Renewable Energy 2015; 78: 573–582.

[54] Ranaboldo M., Domenech B., lberto G.A., Reyes Ferrer-Mart L., Moreno Rafael P., Alberto G. Off-grid community electrification projects based on wind and solar energies: a case study in Nicaragua. Solar Energy 2015; 117: 268–281.

[55] Carroquino J., Rodolfo D., Bernal-Austin Jose L. Sizing of off-grid renewable energy systems for drip irrigation in Mediterranean crops. Renewable Energy 2015; 76: 566–574.

[56] Upadhyay S., Sharma M.P. Development of hybrid energy system with cycle charging strategy using particle swarm optimization for a remote area in India. Renewable Energy 2015; 77: 586–598.

[57] Olatomiwa L., Mekhilef S., ASN H., Ohunakin O.S. Economic evaluation of hybrid energy systems for rural electrification in six geopolitical zones of Nigeria. Renewable Energy 2015; 83: 435–446.

[58] Lujano-Rojas J.M., Rodolfo Dufo-Lopez, Bernal-Agustín J.L. Technical and economic effects of charge controller operation and Columbic efficiency on stand-alone hybrid power system. Energy Conversion and Management 2014; 86: 709–716.

[59] Kalinci Y., Hepbasli A., Dincer I. Techno-economic analysis of a stand-alone hybrid renewable energy system with hydrogen production and storage options. Hydrogen Energy 2015; 40: 7652–7664.

[60] Kaabeche A., Belhamel M., Ibtiouen R. Sizing optimization of grid-independent hybrid photovoltaic/wind power generation system. Energy 2011; 36: 1214–1222.

[61] Borowy B.S., Salameh Z.M. Methodology for optimally sizing the combination of a battery bank and PV array in a wind/PV hybrid system. IEEE Transactions on Energy Conversion 1996; 11(2): 367–375.

[62] Wang L., Singh C. Compromise between cost and reliability in optimum design of an autonomous hybrid power system using mixed-integer PSO algorithm. In: Proceedings of the IEEE Conference. IEEE, Capri, Italy; 2007.

[63] Kanase-Patil A.B., Saini R.P., Sharma M.P. Development of IREOM model based on seasonally varying load profile for hilly remote areas of Uttarakhand State in India. Energy 2011; 36: 5690–5702.

[64] Yang H., Wei Z., Chengzhi L. Optimal design and techno-economic analysis of a hybrid solar-wind power generation system. Applied Energy 2009; 86(2): 163–169.

[65] Deshmukh M., Deshmukh S. Modeling of hybrid renewable energy systems. Renewable and Sustainable Energy Reviews 2008; 12(1): 235–249.

[66] Xu D., Kang L., Chang L., Cao B. Optimal sizing of standalone hybrid wind/PV power systems using genetic algorithms. In: Proceedings of the IEEE on Electrical and Computer Engineering. IEEE, Saskatoon, 2005: 1722–1725.

[67] Iniyan S., Sumathy K. An optimal renewable energy model for various end-uses. Energy 2000; 25(6): 563–575.

[68] Clarke D.P., Al-Abdeli Y.M., Kothapalli G. Multi-objective optimization of renewable hybrid energy systems with desalination. Energy 2015; 88: 457–468.

[69] Shadmand M.B., Balog R.S. Multi-objective optimization and design of photovoltaic-wind hybrid system for community smart DC microgrid. IEEE Transactions on Smart Grid 2014; 5(5): 2635–2643.

Chapter 9

Clean Water from Clean Energy: Decentralised Drinking Water Production Using Wind Energy Powered Electrodialysis

Payam Malek, Helfrid M.A. Schulte-Herbrüggen and
Juan M. Ortiz

Additional information is available at the end of the chapter

http://dx.doi.org/10.5772/65015

Abstract

Supply of potable water requires energy and unfortunately most of the countries with minimal access to safe drinking water are also poor in terms of access to reliable energy grids. However, many of such regions have access to other sources of water (such as brackish and groundwater) that can be treated for producing drinking water if correct treatment systems are put in place. Moreover, many of the electrically remote areas are rich in terms of renewable energy (RE) resources (such as wind and solar) which can be potentially employed as the main source of energy for powering water purification systems. Therefore, development and implementation of off-grid RE powered contaminant removal systems, for producing freshwater from available resources (such as brackish and groundwater), can be considered as an effective and potentially sustainable solution for overcoming the drinking water scarcity issue in remote regions of developing countries. This chapter revises the state of the art related to desalination systems using electrodialysis technology powered by wind energy for decentralised water production.

Keywords: electrodialysis, renewable energy, drinking water, brackish water

"On the one hand, the world needs to provide adequate and sustainable access to more than 1.3 billion people who still lack electricity and to more than 700 million people who lack an improved water supply today […], on the other hand, to keep up with the growing demand for both water and energy associated with population growth, rapid urbanization and economic development in a context of increased scarcity of natural resources, pollution, degraded ecosystems, climate change and regulation of greenhouse gas emissions….. In fact, there is an urgent need to address water and energy challenges in an integrated and

coordinated manner to ensure the sustainability of both water and energy services." (Michel Jarraud, the Chair of UN-Water, January 2014)

1. Introduction

Energy and freshwater are undoubtedly the two inseparable and key resources for sustaining human life on earth. Supply of potable water requires energy and unfortunately most of the countries with minimal access to safe drinking water are also poor in terms of access to reliable energy grids. A worldwide map created by Vörösmarty et al. (**Figure 1A**) suggests high levels of exposure to water security risks for more than 80% of the world's population [1]. The term "incident" used in this map refers to exposure to a complex array of stress factors, sourced from both anthropogenic and natural sources, at a given location. Vörösmarty et al. argued that developing countries, and in particular the inhabitants of remote locations, suffer more severely from exposure to water security risks because they do not have the resources necessary to mitigate pressures on water supplies. However, in contrast, the developed countries often have the investment required to offset high stressor levels experienced by the human population, even though the actual pressure on water resources may be worse in these countries compared to the developing countries. Vörösmarty et al. backed up their arguments by publishing a second map, showing shifts in spatial patterns of threat to drinking water scarcity after accounting for water technology benefits (**Figure 1B**). According to the recent report by World Health Organisation [2, 3], around 768 million people lack access to freshwater sources, 83% of whom live in remote areas of developing countries. The problem of freshwater scarcity in remote regions is exacerbated by the fact that more than 84% of 1.3 billion people who have limited access to electricity, also live in these locations [4].

While the lack access to improved water supply is significantly acute in remote locations, many of such regions have access to other sources of water (such as brackish and groundwater) that can be treated for producing drinking water if correct treatment systems are put in place [5–9]. Moreover, many of the electrically remote areas are rich in terms of renewable energy (RE) resources (such as wind and solar) which can be potentially employed as the main source of energy for powering water purification systems [10–16]. Therefore, development and implementation of off-grid RE powered contaminant removal systems, for producing freshwater from available resources (such as brackish and groundwater), can be considered as an effective and potentially sustainable solution for overcoming the drinking water scarcity issue in remote regions of developing countries.

Trace inorganic ions are among the main sources of contamination in groundwater. The levels at which these contaminants exist in groundwater depends on the geological (e.g. leaching from surrounding rocks) or anthropogenic (e.g. industrial or domestic effluents) sources that these contaminants are discharged from [6, 17, 18]. Consumption of water containing trace inorganic contaminants, such as fluoride (F^-) and nitrate (NO_3^-), at concentrations above their recommended levels by drinking water guidelines may result in severe short and long-term physical and nervous disorders [19–24]. There are some other common inorganic ions in brackish and groundwater which are of no significant health concern, but their excess concentrations in a water resource can make the water resource undrinkable (e.g. due to high salt content, taste issue or colour problem). Chloride (Cl^-) and sulphate (SO_4^{2-}) are in this category, for which only drinking water guideline limits for taste have been proposed [21]. Concerns over the toxicity and chemistry of inorganic contaminants in brackish and groundwater have resulted in increased interest in development of cost-effective desalination techniques in the recent years.

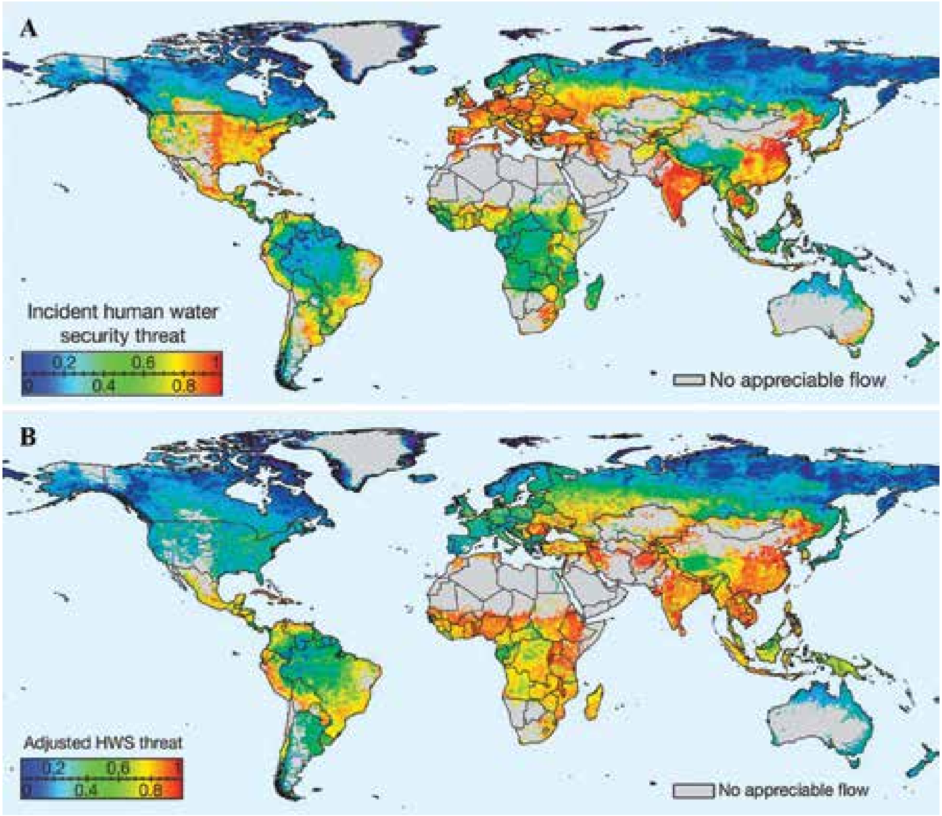

Figure 1. Worldwide incident threat to water security (A) before and (B) after, accounting for water technology benefits (adapted with permission from [1]).

2. Desalination system powered by renewable energy

Renewable energy (RE) powered membrane systems are promising technologies for brackish water desalination in remote regions due to their flexibility to be designed according to the number of inhabitants, available water supply and energy resources [10, 11, 16, 25–27].

Moreover, the application of membrane technologies for brackish water desalination was shown to be energetically less expensive (reverse osmosis (RO): 1.5–3.0 kWh/m^3 and electrodialysis (ED): 0.7–2.5 kWh/m^3) compared to other alternative technologies such as multistage flash distillation (MSF: 19.5–27.3 kWh/m^3), vapour-compression evaporation (VC: 7.0–16.2 kWh/m^3) and multi-effect distillation (MED: 14.5–21.6 kWh/m^3) methods [10, 12, 13]. Among several membrane systems, electrodialysis (ED) has been established as a feasible desalination technique due to its simple ion recuperation, high ion selectivity and efficient ionic separation [28–31]. The high water recovery of 85–94%, the low maintenance required, the long lifetime of ion-exchange membranes due to their strong mechanical and chemical stability plus their tolerance for operation at high temperatures (up to 50°C) and extreme pH levels are features that make ED a particularly suitable desalination system for the use in remote regions with limited water resources. Moreover, the easy start up and shut down of ED makes this system suitable for direct coupling to fluctuating and intermittent sources of energy, such as renewable energies [30, 32, 33].

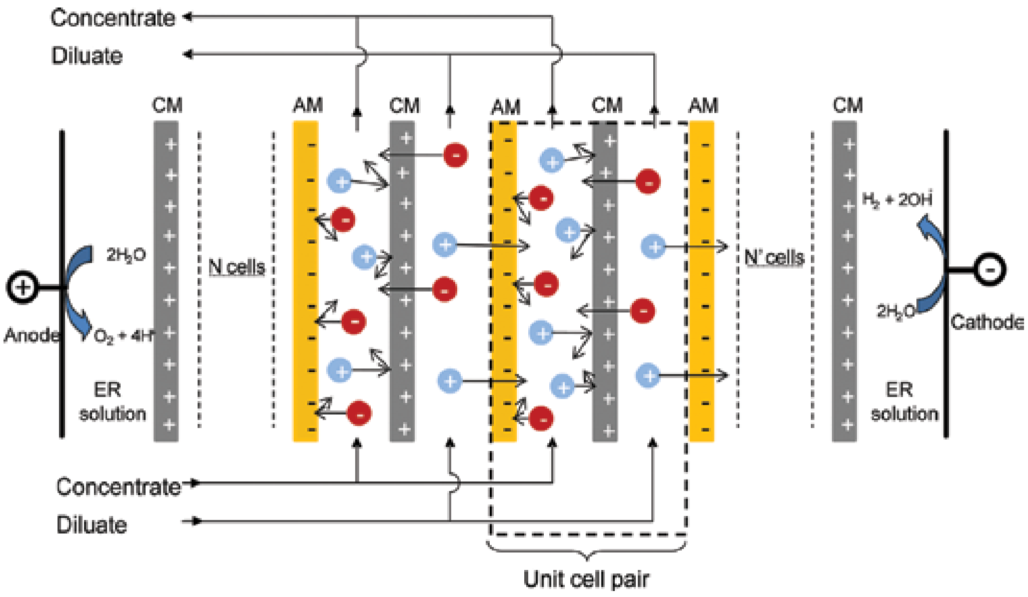

Figure 2. Schematic representation illustrating the ion transport principle across the ion-exchange membranes in an ED system (AM: anion exchange membrane. CM: cation exchange membrane, ER: electrode rinse).

ED is an electrically driven ion separation technique with a well-established use in many industrial applications such as brackish water desalination [34–36], wastewater treatment [28, 37–39], desalting of amino acids and organic solutions [40–43] and salt production [44–46]. An ED system consists of a number of alternatingly positioned cation and anion exchange membranes that are stacked together between two electrodes and are separated from each other by flow spacers [28, 30, 34, 47, 48]. The ion removal principle in an ED system is illustrated in **Figure 2**.

The salt solution is fed into the ED stack in a direction parallel to the ion-exchange membranes. Once a potential difference is applied across the electrodes, each ion in the solution starts to travel toward an oppositely charged electrode. While the passage of the ions is permitted through the oppositely charged ion-exchange membranes, their travel is terminated once they reach a similarly charged ion-exchange membrane. This results in the formation of a series of alternatingly positioned concentrate and diluate channels within the ED stack, through which the ion separation process takes place. This process continues in a batch circulating mode until the target salt concentration, which is often application dependent, is obtained in the diluate stream.

Most of the studies carried out on ED over the last 40 years focused on the conventional mode of operation where a constant voltage or current source is used for operating the membrane system [28, 30, 48–51]. The available studies on renewable energy powered ED technologies are very limited. Lundstrom [52] was the first to present the application of a renewable energy powered ED system for water purification purposes. He demonstrated the use of an off-grid photovoltaic (PV) powered ED system for brackish water desalination in remote regions in the south-western states of the USA where access to reliable electricity grid is minimal but the solar radiation is abundant. Later, Ishimaru [53] presented a study in which a series of PV cells were applied to charge a set of battery banks, which were subsequently used for powering an ED system to desalinate brackish water (TDS ≤ 1500 mg/L). The system showed reliable performance, producing freshwater in the range of 150–400 m^3/day, depending on the season and the solar irradiation, during the two-year period of testing. Although using deep cycle lead-acid batteries governs uninterrupted operation in indirect configuration of RE-membrane system coupling, they result in reduced robustness, lower efficiency, associated with continuous DC-AC-DC conversions and charging-discharging losses, plus increased capital and running costs [54–56]. The impacts of applying pulsed electric fields on minimising concentration polarisation [32, 57–60] and fouling mitigations [33, 61–65] in ED processes were investigated in a number of studies. The satisfactory operation of ED, despite having fluctuations in the energy source in these studies, suggests the possibility of coupling ED directly to fluctuating energy sources such as renewable energies (REs). Direct coupling of ED to an RE source can eliminate the need for having energy storage facilities (e.g. lead-acid batteries and flywheels); hence to minimise the aforementioned adverse behaviours linked with using such systems [54, 66]. More importantly the fact that ED operates with direct current (DC) [28, 30] makes this system particularly favourable for direct coupling to RE sources, as in such configuration no need for DC-AC conversion systems exists. AlMadani [67] was among the first who developed a directly coupled PV-ED system consisting of four hydraulic and two electric stages and demonstrated the impacts of process parameters, i.e. flow rate and temperature on removal of salt from groundwater. Ortiz et al. [68, 69], Uche et al. [70] and Cirez et al. [71] developed mathematical models describing the behaviour of different directly connected PV-ED systems. The models employed to predict the quality of the water product, the rate of desalination and specific energy consumption under given meteorological conditions and PV cell configurations. The results from these models showed very good corroboration with the experimental findings obtained in desalinating of real brackish water using the PV-ED systems.

3. Wind energy as suitable power source for desalination technology

Wind energy is particularly abundant on islands, coastal areas and mountain stations [72–76], and thus it is a favourable source of energy for desalination in such environments. As opposed to solar energy where availability is limited to the availability of sunlight during daytime, wind energy is readily available to be harvested over both day and night, assuming the wind system is well-sited [77]. This makes wind energy a superior alternative, in locations which are rich in terms of wind resources, compared to solar power for continuous powering of different processes, with less need for long-term energy storage. The use of wind energy for powering membrane-based desalination technologies was investigated by a number of researchers [14, 27, 78–84] and was proven to be economically feasible for some technologies including ultrafiltration (UF) and reverse osmosis (RO) [10, 14, 85] (**Figure 3**).

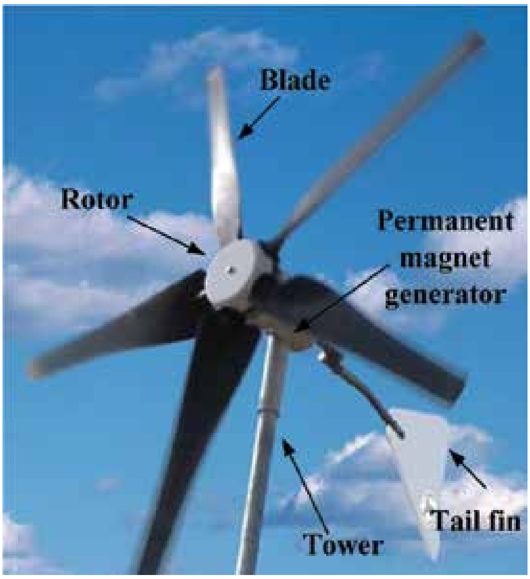

Figure 3. Main components of a small scale 1 kW Future Energy wind turbine (adapted with permission from [86]).

Comparisons made between the solar powered and wind powered membrane techniques show slightly lower specific energy consumption (SEC) for the wind powered membrane systems (e.g. 3.4 kWh/m^3 for a wind-RO system versus 4 kWh/m^3 for a PV-RO system, using the same RO module in both of the setups and desalinating from similar seawater feeds (32,800–34,300 mg/L TDS)) [80, 87–89]. The overall cost of desalination was also suggested to be lower when using wind energy as opposed to solar energy for powering the membrane systems [90]. In a review by El-Ghonemy [91], the cost of water production from brackish water desalination at the rate of 250 m^3/day using PV-RO and wind-RO systems were reported to be 6.7 and 2.7 US$/m^3, respectively. Despite the advantages that wind energy has over solar energy, the number of wind-membrane systems developed and commercialised so far are very limited compared to the solar powered membrane techniques. This can be partially attributed to the extreme fluctuations and intermittencies inherent to wind, making the harvesting of wind energy and coupling the wind turbines to the membrane systems technically very difficult. The latter is expected to be particularly challenging for pressure driven membrane systems (e.g. RO) that require constant power supply to perform satisfactory desalination [92, 93]. However, the extreme variations in the energy supply are expected to be less problematic for electrical driven techniques (e.g. ED) as their desalination performance has shown to be relatively robust despite energy fluctuations [33, 59–62, 65] (**Figure 4**).

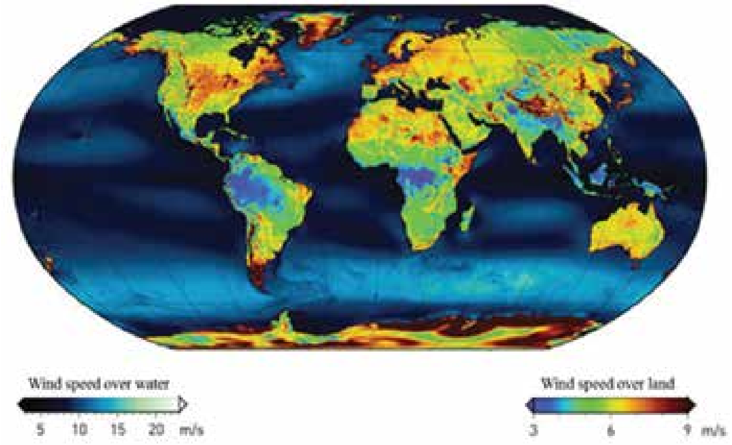

Figure 4. Worldwide average wind speed map, created based on wind speed measurements at the height of 80 m [94].

Up to date, no work on directly coupling ED with wind energy has been done. Veza et al. and Carta et al. [83, 95] studied a large-scale wind energy powered electrodialysis reversal (EDR) system, where a flywheel was employed as an intermediate temporary energy storage/energy buffering device between the wind turbines and the EDR stack (i.e. an indirect coupling of the renewable energy source with the membrane system). The aim was to develop automatic control electronics to allow the system to operate optimally, producing maximum volume of freshwater with minimum energy consumption. Although good quality drinking water was obtained using the wind energy powered membrane system, the field pilot nature of these tests did not allow drawing systematic and comprehensive understanding on how ion transport is influenced by wind speed fluctuations. Moreover, the fact that intermediate devices such as maximum power tracking and energy buffering systems (i.e. flywheel) were involved, it was difficult to specify the direct impacts of actual wind speed fluctuations on the ED performance.

The power produced from a permanent magnet generator-based wind turbine is principally dependent not only on the available wind condition but also on the resistance of the load directly connected to the wind system [96, 97]. Therefore, when connecting a wind turbine directly to an ED system, the power performance of the wind turbine is expected to vary with the change in the resistance of the ED stack during the desalination process. The latter is expected to happen due to the change in the feed concentration or the flow rate of the diluate and concentrate streams. The change in the power performance of the wind turbine can result in further variations in the desalination characteristics of the membrane system and influence the energy expense of the desalination process. The potential behaviours to be seen from the membrane system in direct connection with a wind resource operating at steady wind speed conditions are yet unknown, hence they require systematic studies to be fully understood.

4. Direct desalination using electrodialysis powered by wind energy

As mentioned before, the main challenge in using a wind turbine for direct coupling with the membrane system, with no form of energy storage or energy regulator, is associated with the fluctuations and intermittencies inherent to the wind resource. These fluctuations are a result of movements of large bulks of air over long periods (tens to hundreds of hours) and turbulence and gusts over short periods (seconds to a few minutes) [98–100]. The direct coupling of the wind system to the ED stack can inevitably result in fluctuations in the voltage and the current, ranging from mild fluctuations at low turbulence intensities to cycling on/off incidences occurring at extreme fluctuations. In order to establish solid understandings on how and in what extent the wind fluctuations affect the process of the ED system, it is necessary to carry out desalination studies using the membrane system over a range of wind speed fluctuations and intermittencies.

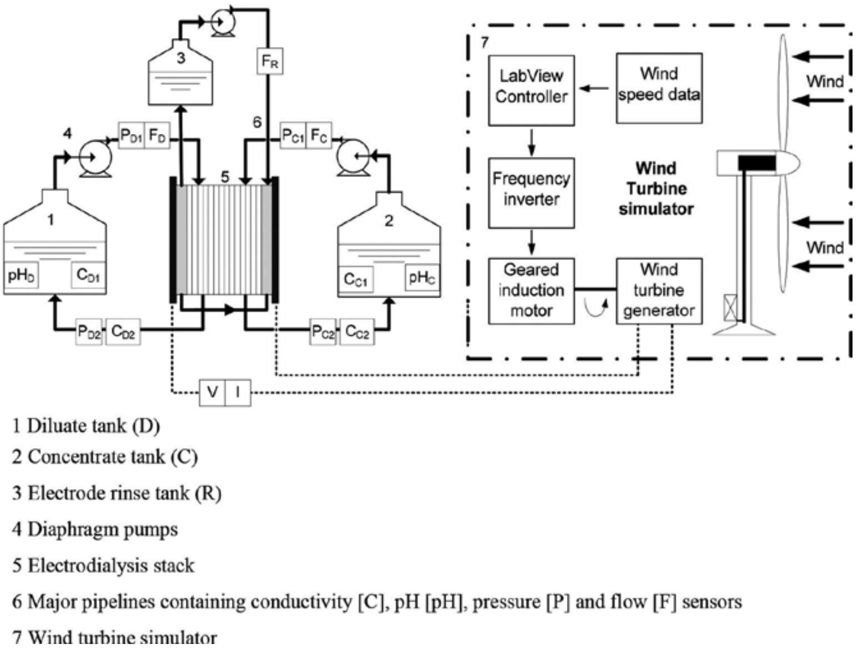

Figure 5. Schematic diagram of the wind-ED experimental setup used in [103].

The extremity and unpredictability of wind speed fluctuations [14, 77, 83, 98], and their significant variations from one location and season to another [73, 75, 76, 101, 102], restrict the choices of desalination technologies (e.g. RO, thermal or ED) that can handle such extreme energy variations, while exhibiting satisfactory desalination performance, when directly connected to wind turbine systems.

The direct connection of the wind turbine to a batch recirculating ED system (see **Figure 5**) was studied by Malek et al. [103] in a novel attempt in terms of coupling a wind turbine to a varying resistance load; since in all previous applications, wind turbines were mainly used to power constant resistance loads, these being either electricity grids or in smaller scales battery banks and supercapacitors [55, 98, 99, 104].

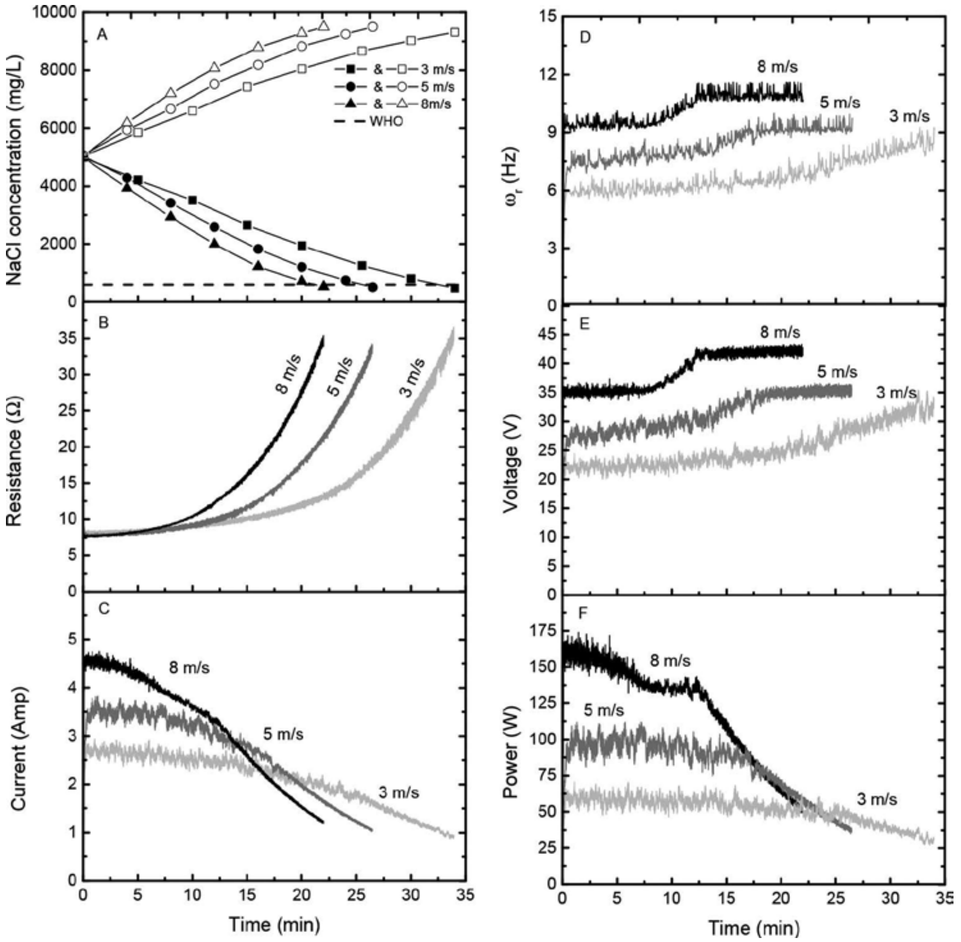

Figure 6. Steady state performance of the wind-ED system in desalinating from a feed of 5000 mg/L NaCl at constant wind speeds of 3, 5, and 8 m/s plotted as (A) NaCl concentration in both the diluate (solid symbols) and concentrate (hollow symbols) streams; (B) ED stack resistance; (C) current driven by the ED stack from the wind turbine; (D) angular velocity of the rotor (ω_r); (E) voltage; (F) wind-ED operating power (mode of operation: batch) [103].

Figure 6 shows the results obtained from systematic investigations of the wind-ED system performance under various wind speed conditions (from 2 to 10 m/s) with the aim of determining the impacts of low and high wind speeds on the desalination performance of ED by measuring clean water production and specific energy consumption (SEC) under constant wind speed conditions.

The results suggest that the desalination performance of the wind-ED system is mainly influenced by the wind speed when operating in the first power region, where no constraints have yet been posed on the voltage increase and, thus, the current transfer across the membranes varies primarily as a result of the wind speed. However, the dependency of the desalination performance on the wind speed diminishes significantly once the torque control system on the frequency inverter is activated to limit the voltage increase, as a result of which the power and correspondingly the desalination performance of the wind-membrane system begin to be principally controlled by the R_{stack} variations [103].

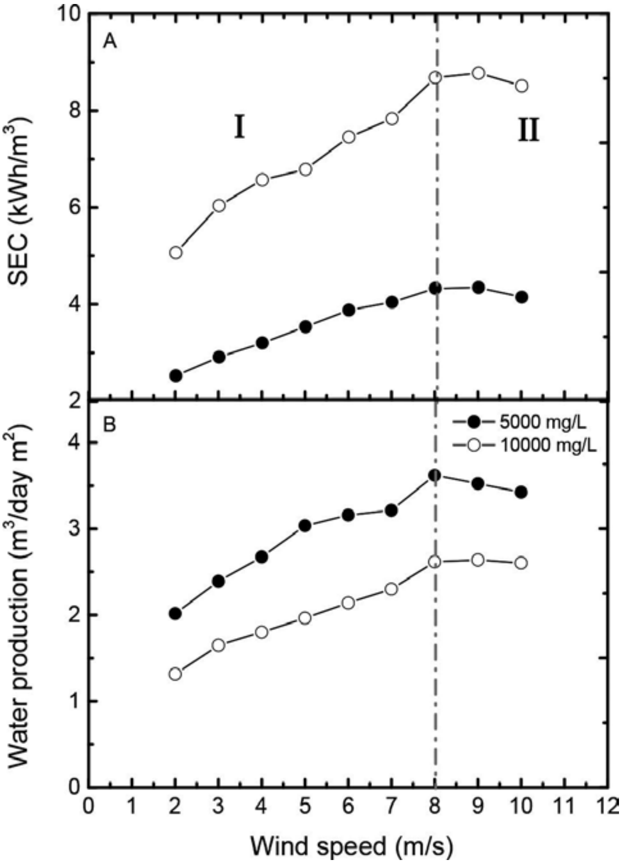

Figure 7. SEC (A) and water production (B) from desalinating feed solutions of 5000 and 10,000 mg/L NaCl over a range of constant wind speeds: 2–10 m/s at the flow rate of 7 L/min. I and II mark the two distinct behavioural regions for operating below and above the rated wind speeds, respectively (mode of operation: batch).

The ED system has been demonstrated to be an energetically robust system, performing effectively in the safe operating window when connected to renewable energy sources (wind power has the most extreme fluctuations among renewable energy alternatives). The main challenge in the direct coupling of the membrane system with a RE resource was seen to be not the size of the fluctuations but the impact of the power cycling off during long oscillation periods, which resulted in reduced water production and increased SECs (**Figure 7**).

5. Conclusions

Renewable energy powered membrane systems are considered as sustainable, energy efficient and reliable solutions for tackling the emerging issue of drinking water scarcity [10, 25, 27, 78]. Development and implementation of such technologies are of particular importance to remote arid areas of developing countries where people suffer the most from the lack of access to safe potable water. In *Malek* et al. [103], the direct coupling of wind energy with membranes was proposed as a solution to reduce the system costs as well as technical drawbacks associated with using intermediate energy storage systems such as acid-lead batteries, supercapacitors and flywheels.

5.1. Advantages of ED over other common desalination technologies for coupling with RE sources

Advantages for ED, in comparison with other common desalination technologies, for direct coupling to renewable energy (RE), can be deduced as specified in points 1–4, below:

1. Flexibility in operation with any amount of available energy

Common desalination technologies (i.e. RO, Thermal Vapour Compression, MED and MSF) [100, 105–107] often require a minimum level of energy to perform satisfactorily; which limits the employment of such technologies in direct coupling with RE systems for desalination in locations where sufficient RE may not be available throughout the year. To address this problem, some studies have proposed the use of energy storage systems [80, 82, 104]. However, energy storage systems increase both the capital and maintenance costs of the operation and also reduce the sustainability of the technology [55, 56]. Therefore, a better approach would be to use an energetically flexible technology, such as ED, that can operate more suitably in direct connection to RE sources with no need for energy storage devices. In terms of a safe operating window, the direct wind-membrane system produced good quality drinking water (<600 mg/L NaCl) over the wide range of wind speeds (2–10 m/s) and regardless of the initial feed concentration or the flow rate.

2. Robustness with respect to fluctuations and intermittencies in the RE source

Extreme fluctuations were shown to lead to reduced permeate quality and increased SEC in RO systems [100, 108, 109]. The use of temporary energy storage systems (e.g. supercapacitors) and energy buffering devices (e.g. flywheels) were proposed in some studies, as useful methods for governing uninterrupted operation of the desalination technologies powered from fluctuating energy sources [66, 83, 95, 104]. However, as mentioned before, the use of energy storage systems is not favourable, as it leads to increased capital and maintenance costs as well as reduced sustainability. Using ED may again be a solution, as the SEC of this technique when directly powered from a wind resource was found to be relatively unaffected by fluctuations of any size (i.e. wind energy exhibits the largest fluctuations among the all REs). Therefore, ED can be introduced as an energetically robust desalination system, suitable for direct coupling with renewable energy sources.

3. Mechanical solidity against energy fluctuations

Energy fluctuations in some studies were suggested to cause reduction in the lifetime and efficiency of the pumps [110, 111] and produce fatigue damage to the membrane polymers [80]. Such problems can be significantly detrimental to the long-term operation of pressure driven technologies such as reverse osmosis. However for ED, since it is not a pressure driven process the ion-exchange membranes are expected to remain relatively unaffected by the fluctuations. Moreover, if the pumps of ED are powered by renewable energies, because they often operate at very low pressures, they are expected to be much less influenced by the fluctuations in the RE resource, compared to the pumps in a RO system.

4. Specific energy consumption (SEC)

SEC of the ED process increased with the wind speed, from 2.52 at 2 m/s to 4.15 kWh/m^3 at 10 m/s, when desalinated a feed solution of 5000 mg/L NaCl. The SEC values obtained were within the range reported in the literature for the ED process (2.64 and 5.5 kWh/m^3) when desalinating brackish waters containing 2500–5000 mg/L total dissolved solids (TDS) [10, 112]. These SEC values were also very close to the minimum SEC reported by Park et al. (2.8 kWh/m^3) for desalinating feeds of 2500–5500 mg/L TDS, using a directly powered wind-reverse osmosis system (wind-RO) [14]. A comparison between the obtained SEC values in direct wind-energy electrodialysis and the ones reported in the literature for other common desalination techniques suggests that ED is energetically competitive with RO (1.5–3.0 kWh/m^3) and significantly more efficient than common distillation-based desalination systems (i.e. MSF: 19.5–27.3 kWh/m^3, MED: 14.5–21.6 kWh/m^3 and VC: 7.0–16.2 kWh/m^3) for treating brackish groundwater containing 5000 mg/L or lower TDS [10, 11, 113, 114].

The overall conclusion is that the wind-ED system is an energetically robust and technically reliable off-grid desalination method for the use in brackish water desalination applications in water stressed remote regions in both developing and developed countries.

Acknowledgements

P. Malek was supported by the University of Edinburgh Diversity in Engineering Scholarship. The University of Edinburgh and Heriot Watt University are acknowledged for providing support and expert facilities. Juan M. Ortiz was supported by the European Union though the MiDes Project. This project has received funding from the European Union's Horizon 2020 research and innovation programme under grant agreement No 685793.

Author details

Payam Malek[1], Helfrid M.A. Schulte-Herbrüggen[1,2] and Juan M. Ortiz[3*]

*Address all correspondence to: juanma.ortiz@imdea.org

1 School of Engineering, The University of Edinburgh, Edinburgh, United Kingdom

2 KTH Royal Institute of Technology, SEED, Stockholm, Sweden

3 IMDEA Water Institute, Madrid, Spain

References

[1] Vörösmarty, C.J., et al., *Global threats to human water security and river biodiversity.* Nature, 2010. 467(7315): p. 555–561.

[2] WHO, *Water Quality and Health Strategy 2013–2020*, 2013, World Health Organisation: Geneva.

[3] WHO/UNICEF, *Progress on Sanitation and Drinking-Water: 2013 Update*, 2013, WHO/UNICEF Joint Monitoring Programme for Water Supply and Sanitation: WHO, Geneva and UNICEF, New York.

[4] IEA, *World Energy Outlook 2011*. 2011, International Energy Agency: Paris, France.

[5] Mahmoudi, H., et al., Assessment of wind energy to power solar brackish water greenhouse desalination units: a case study from Algeria. Renewable and Sustainable Energy Reviews, 2009. 13(8): p. 2149–2155.

[6] Rossiter, H.M.A., et al., *Chemical drinking water quality in Ghana: Water costs and scope for advanced treatment.* Science of the Total Environment, 2010. 408(11): p. 2378–2386.

[7] Schäfer, A.I., et al., Physico-chemical water quality in Ghana: prospects for water supply technology implementation. Desalination, 2009. 248(1–3): p. 193–203.

[8] Ayoub, J. and R. Alward, Water requirements and remote arid areas: the need for small-scale desalination. Desalination, 1996. 107(2): p. 131–147.

[9] Raucher, R., et al., *Guidelines for Implementing Seawater and Brackish Water Desalination Facilities*, 2010, Water Research Foundation and Arsenic Water Technology.

[10] Al-Karaghouli, A. and L.L. Kazmerski, Energy consumption and water production cost of conventional and renewable-energy-powered desalination processes. Renewable and Sustainable Energy Reviews, 2013. 24: p. 343–356.

[11] Al-Karaghouli, A., D. Renne, and L.L. Kazmerski, *Solar and wind opportunities for water desalination in the Arab regions.* Renewable & Sustainable Energy Reviews, 2009. 13(9): p. 2397–2407.

[12] Gude, V.G., N. Nirmalakhandan, and S. Deng, *Renewable and sustainable approaches for desalination.* Renewable and Sustainable Energy Reviews, 2010. 14(9): p. 2641–2654.

[13] Shatat, M., M. Worall, and S. Riffat, *Opportunities for solar water desalination worldwide: review.* Sustainable Cities and Society, 2013. 9: p. 67–80.

[14] Park, G.L., A.I. Schäfer, and B.S. Richards, Renewable energy powered membrane technology: the effect of wind speed fluctuations on the performance of a wind-powered membrane system for brackish water desalination. Journal of Membrane Science, 2011. 370(1–2): p. 34–44.

[15] Richards, L.A., B.S. Richards, and A.I. Schäfer, Renewable energy powered membrane technology: salt and inorganic contaminant removal by nanofiltration/reverse osmosis. Journal of Membrane Science, 2011. 369(1–2): p. 188–195.

[16] Schäfer, A. Broeckmann, and Richards, *Renewable energy powered membrane technology. 1. Development and characterization of a photovoltaic hybrid membrane system*. Environmental Science & Technology, 2006. 41(3): p. 998–1003.

[17] Bassett, R.L., et al., *Identification of groundwater solute sources using boron isotopic composition.* Environmental Science & Technology, 1995. 29(12): p. 2915–2922.

[18] Favre-Réguillon, A., et al., *Selective removal of dissolved uranium in drinking water by nanofiltration.* Water Research, 2008. 42(4–5): p. 1160–1166.

[19] Ergun, E., et al., *Electrodialytic removal of fluoride from water: effects of process parameters and accompanying anions.* Separation and Purification Technology, 2008. 64(2): p. 147–153.

[20] European Union, *Council Directive 98/83/EC of 3 November 1998 on the quality of water intended for human consumption*. Official Journal L 330, 1998: p. 32–54.

[21] WHO, *Guidelines for Drinking-water Quality*. Geneva, Switzerland 2011.

[22] Tamer, M.N., et al., *Osteosclerosis due to endemic fluorosis.* Science of The Total Environment, 2007. 373(1): p. 43–48.

[23] El Midaoui, A., et al., *Optimization of nitrate removal operation from ground water by electrodialysis.* Separation and Purification Technology, 2002. 29(3): p. 235–244.

[24] Amini, M., et al., *Statistical modeling of global geogenic fluoride contamination in groundwaters.* Environmental Science & Technology, 2008. 42(10): p. 3662–3668.

[25] El-Ghonemy, A.M.K., *Water desalination systems powered by renewable energy sources: review.* Renewable and Sustainable Energy Reviews, 2012. 16(3): p. 1537–1556.

[26] Peñate, B., et al., *Design and testing of an isolated commercial EDR plant driven by solar photovoltaic energy*. Desalination and Water Treatment, 2012. 51(4–6): p. 1254–1264.

[27] Subiela, V.J., et al., *Canary Islands Institute of Technology (ITC) experiences in desalination with renewable energies (1996–2008)*. Desalination & Water Treatment, 2009. 7(1–3): p. 220–235.

[28] Xu, T. and C. Huang, *Electrodialysis-based separation technologies: a critical review.* AIChE Journal, 2008. 54(12): p. 3147–3159.

[29] Van der Bruggen, B., et al., *Electrodialysis and nanofiltration of surface water for subsequent use as infiltration water*. Water Research, 2003. 37(16): p. 3867–3874.

[30] Strathmann, H., *Ion-Exchange Membrane Separation Processes*. Membrane Science and Technology. Vol. 9. 2004: Elsevier. 348.

[31] Valero, F., A. Barceló, and R. Arbós, *Electrodialysis technology–theory and applications*, in Desalination, Trends and Technologies, M. Schorr, Editor 2011: Rijeka, Croatia InTech.

[32] Karlin, Y.V. and V.N. Kropotov, *Electrodialysis separation of Na^+ and Ca^+ in a pulsed current mode.* Russian Journal of Electrochemistry, 1995. 31(5): p. 517–521.

[33] Ruiz, B., et al., *Application of relaxation periods during electrodialysis of a casein solution: Impact on anion-exchange membrane fouling*. Journal of Membrane Science, 2007. 287(1): p. 41–50.

[34] Lee, H.-J., et al., *Designing of an electrodialysis desalination plant.* Desalination, 2002. 142(3): p. 267–286.

[35] Demircioglu, M., et al., *Demineralization by electrodialysis (ED)—separation performance and cost comparison for monovalent salts*. Desalination, 2003. 153(1–3): p. 329–333.

[36] Tanaka, Y., *Mass transport and energy consumption in ion-exchange membrane electrodialysis of seawater*. Journal of Membrane Science, 2003. 215(1–2): p. 265–279.

[37] Bernardes, A.M., et al., *Electrochemistry as a clean technology for the treatment of effluents: the application of electrodialysis*. Metal Finishing, 2000. 98(11): p. 52–114.

[38] Goodman, N.B., et al., *A feasibility study of municipal wastewater desalination using electrodialysis reversal to provide recycled water for horticultural irrigation*. Desalination, 2013. 317: p. 77–83.

[39] Korngold, E., K. Kock, and H. Strathmann, *Electrodialysis in advanced waste water treatment.* Desalination, 1977. 24(1–3): p. 129–139.

[40] Boniardi, N., et al., *Lactic acid production by electrodialysis. Part I: experimental tests.* Journal of Applied Electrochemistry, 1997. 27(2): p. 125–133.

[41] Boniardi, N., et al., *Lactic acid production by electrodialysis. Part II: modelling.* Journal of Applied Electrochemistry, 1997. 27(2): p. 135–145.

[42] Montiel, V., et al., *Recovery by means of electrodialysis of an aromatic amino acid from a solution with a high concentration of sulphates and phosphates*. Journal of Membrane Science, 1998. 140(2): p. 243–250.

[43] Poquis, J.A., et al., *Partial electro-neutralisation of d-α-p-hydroxyphenylglycine in sulphuric acid medium*. Journal of Membrane Science, 2000. 170(2): p. 225–233.

[44] Turek, M., *Dual-purpose desalination-salt production electrodialysis*. Desalination, 2003. 153(1–3): p. 377–381.

[45] Yamamoto, M., et al., *A new electrodialyzer technique for the salt production by ion-exchange membrane*, in Eighth World Salt Symposium, May 7–11 2000, The Hague: Netherlands. p. 1647–1652.

[46] Takashima, K., et al., *The seawater pretreatment facilities for electrodialysis at Sanuki Salt Manufacturing Co., Ltd.*, in Eighth World Salt Symposium May 7–11 2000, The Hague: Netherlands. p. 1641–1646.

[47] Eigenberger, G., H. Strathmann, and A. Grabovskiy, *Membrane assembly, electrodialysis device and method for continuous electrodialytic desalination*, 2005, Germany WO 2005/009596 Int. Cl. A1, B01D 61/44.

[48] Strathmann, H., *Electrodialysis, a mature technology with a multitude of new applications*. Desalination, 2010. 264(3): p. 268–288.

[49] Krol, J.J., *Monopolar and bipolar ion-exchange membranes: mass transport limitations*, 1997, University of Twente: Enschede, The Netherlands.

[50] Ben Sik Ali, M., B. Hamrouni, and M. Dhahbi, *Electrodialytic defluoridation of brackish water: effect of process parameters and water characteristics*. CLEAN—Soil, Air, Water, 2010. 38(7): p. 623–629.

[51] Gnusin, N. and O. Demina, *Modeling of transfer in electrodialysis systems*. Theoretical Foundations of Chemical Engineering, 2006. 40(1): p. 27–31.

[52] Lundstrom, J.E., *Water desalting by solar powered electrodialysis*. Desalination, 1979. 31(1–3): p. 469–488.

[53] Ishimaru, N., *Solar photovoltaic desalination of brackish-water in remote areas by electrodialysis*. Desalination, 1994. 98(1–3): p. 485–493.

[54] Hadjipaschalis, I., A. Poullikkas, and V. Efthimiou, *Overview of current and future energy storage technologies for electric power applications*. Renewable and Sustainable Energy Reviews, 2009. 13(6–7): p. 1513–1522.

[55] Beaudin, M., et al., *Energy storage for mitigating the variability of renewable electricity sources: an updated review*. Energy for Sustainable Development, 2010. 14(4): p. 302–314.

[56] Kousksou, T., et al., *Energy storage: applications and challenges*. Solar Energy Materials and Solar Cells, 2014. 120, Part A: p. 59–80.

[57] Dukhin, S.S. and N.A. Mishchuk, *Intensification of electrodialysis based on electroosmosis of the second kind.* Journal of Membrane Science, 1993. 79(2–3): p. 199–210.

[58] Mishchuk, N.A., *Perspectives of the electrodialysis intensification.* Desalination, 1998. 117(1–3): p. 283–295.

[59] Mishchuk, N.A., L.K. Koopal, and F. Gonzalez-Caballero, *Intensification of electrodialysis by applying a non-stationary electric field.* Colloids and Surfaces A: Physicochemical and Engineering Aspects, 2001. 176(2–3): p. 195–212.

[60] Mishchuk, N.A., S.V. Verbich, and F. Gonzales-Caballero, *Concentration polarization and specific selectivity of membranes in pulse mode.* Colloid Journal, 2001. 63(5): p. 586–594.

[61] Lee, H.-J. and S.-H. Moon, *Enhancement of electrodialysis performances using pulsing electric fields during extended period operation*. Journal of Colloid and Interface Science, 2005. 287(2): p. 597–603.

[62] Lee, H.-J., S.-H. Moon, and S.-P. Tsai, *Effects of pulsed electric fields on membrane fouling in electrodialysis of NaCl solution containing humate*. Separation and Purification Technology, 2002. 27(2): p. 89–95.

[63] Casademont, C., et al., *Electrodialysis of model salt solution containing whey proteins: enhancement by pulsed electric field and modified cell configuration*. Journal of Membrane Science, 2009. 328(1–2): p. 238–245.

[64] Cifuentes-Araya, N., G. Pourcelly, and L. Bazinet, *Impact of pulsed electric field on electrodialysis process performance and membrane fouling during consecutive demineralization of a model salt solution containing a high magnesium/calcium ratio*. Journal of Colloid and Interface Science, 2011. 361(1): p. 79–89.

[65] Cifuentes-Araya, N., G. Pourcelly, and L. Bazinet, *Multistep mineral fouling growth on a cation-exchange membrane ruled by gradual sieving effects of magnesium and carbonate ions and its delay by pulsed modes of electrodialysis*. Journal of Colloid and Interface Science, 2012. 372(1): p. 217–230.

[66] Subiela, V.J., J.A. Carta, and J. González, *The SDAWES project: lessons learnt from an innovative project.* Desalination, 2004. 168: p. 39–47.

[67] AlMadani, H.M.N., *Water desalination by solar powered electrodialysis process.* Renewable Energy, 2003. 28(12): p. 1915–1924.

[68] Ortiz, J.M., et al., *Photovoltaic electrodialysis system for brackish water desalination: modeling of global process*. Journal of Membrane Science, 2006. 274(1–2): p. 138–149.

[69] Ortiz, J.M., et al., *Desalination of underground brackish waters using an electrodialysis system powered directly by photovoltaic energy*. Solar Energy Materials and Solar Cells, 2008. 92(12): p. 1677–1688.

[70] Uche, J., et al., *On-grid and off-grid batch-ED (electrodialysis) process: simulation and experimental tests*. Energy, 2013. 57: p. 44–54.

[71] Cirez, F., et al., *Batch ED fed by a PV unit: a reliable, flexible, and sustainable integration.* Desalination and Water Treatment, 2013. 51(4–6): p. 673–685.

[72] Maatallah, T., et al., *Wind power assessment and evaluation of electricity generation in the Gulf of Tunis, Tunisia*. Sustainable Cities and Society, 2013. 6: p. 1–10.

[73] Chang, T.J. and Y.L. Tu, *Evaluation of monthly capacity factor of WECS using chronological and probabilistic wind speed data: a case study of Taiwan*. Renewable Energy, 2007. 32(12): p. 1999–2010.

[74] Jowder, F.A.L., *Wind power analysis and site matching of wind turbine generators in Kingdom of Bahrain*. Applied Energy, 2009. 86(4): p. 538–545.

[75] de Araujo Lima, L. and C.R. Bezerra Filho, *Wind energy assessment and wind farm simulation in Triunfo—Pernambuco, Brazil.* Renewable Energy, 2010. 35(12): p. 2705–2713.

[76] Ahmed Shata, A.S. and R. Hanitsch, *Electricity generation and wind potential assessment at Hurghada, Egypt.* Renewable Energy, 2008. 33(1): p. 141–148.

[77] Peinke, J., et al., *Turbulence, a challenging problem for wind energy.* Physica A: Statistical Mechanics and its Applications, 2004. 338(1–2): p. 187–193.

[78] Charcosset, C., *A review of membrane processes and renewable energies for desalination*. Desalination, 2009. 245(1–3): p. 214–231.

[79] Dehmas, D.A., et al., *On the use of wind energy to power reverse osmosis desalination plant: a case study from Ténès (Algeria)*. Renewable and Sustainable Energy Reviews, 2011. 15(2): p. 956–963.

[80] Infield, D., *Performance analysis of a small wind powered reverse osmosis plant*. Solar Energy, 1997. 61(6): p. 415–421.

[81] Lindemann, J.H., *Wind and solar powered seawater desalination applied solutions for the Mediterranean, the Middle East and the Gulf countries*. Desalination, 2004. 168: p. 73–80.

[82] Peñate, B., et al., *Assessment of a stand-alone gradual capacity reverse osmosis desalination plant to adapt to wind power availability: a case study*. Energy, 2011. 36(7): p. 4372–4384.

[83] Veza, J., B. Peñate, and F. Castellano, *Electrodialysis desalination designed for off-grid wind energy.* Desalination, 2004. 160(3): p. 211–221.

[84] Veza, J.M., B. Peñate, and F. Castellano, *Electrodialysis desalination designed for wind energy (on-grid tests).* Desalination, 2001. 141(1): p. 53–61.

[85] Garcia-Rodriquez, L., *Renewable energy applications in desalination: state of the art.* Solar Energy, 2003. 75(5): p. 381–393.

[86] FutureEnergy. http://www.futurenergy.co.uk/. 2010 [cited 2014 01 May]; Available from: http://www.futurenergy.co.uk/.

[87] Miranda, M.S. and D. Infield, *A wind-powered seawater reverse-osmosis system without batteries.* Desalination, 2003. 153(1–3): p. 9–16.

[88] Thomson, M. and D. Infield, *A photovoltaic-powered seawater reverse-osmosis system without batteries*. Desalination, 2003. 153(1–3): p. 1–8.

[89] Thomson, M. and D. Infield, *Laboratory demonstration of a photovoltaic-powered seawater reverse-osmosis system without batteries*. Desalination, 2005. 183(1–3): p. 105–111.

[90] Gilau, A.M. and M.J. Small, *Designing cost-effective seawater reverse osmosis system under optimal energy options*. Renewable Energy, 2008. 33(4): p. 617–630.

[91] El-Ghonemy, A.M.K., *Future sustainable water desalination technologies for the Saudi Arabia: a review.* Renewable and Sustainable Energy Reviews, 2012. 16(9): p. 6566–6597.

[92] Souari, L. and M. Hassairi, *Sea water desalination by reverse osmosis: the true needs for energy.* Desalination, 2007. 206(1–3): p. 465–473.

[93] Petersen, G., et al., *Wind and solar powered reverse osmosis desalination units—design, start up, operating experience*. Desalination, 1981. 39: p. 125–135.

[94] Farris, A. *Wind*. 2012 [cited 2014 30 April]; Available from: http://www.energybc.ca/profiles/wind.html.

[95] Carta, J., J. González, and V. Subiela, *The SDAWES project: an ambitious R&D prototype for wind-powered desalination.* Desalination, 2004. 161(1): p. 33–48.

[96] Dubois, M.R.J., *Optimized Permanent Magnet Generator Topologies for Direct-drive Wind Turbines*, 2004, Delft University: Les Imprimeries ABC Inc., Lévis, Canada. p. 237.

[97] Stander, J.N., G. Venter, and M.J. Kamper, *Review of direct-drive radial flux wind turbine generator mechanical design.* Wind Energy, 2012. 15(3): p. 459–472.

[98] Burton, T., et al., *Wind Energy Handbook*. West Sussex, England 2001: John Wiley & Sons Ltd.

[99] Manwell, J.F., *Wind Energy Explained: Theory, Design and Application*. West Sussex, England 2002: John Wiley & Sons Ltd.

[100] Park, G.L., *Wind-powered membrane desalination of brackish water*, in School of Engineering and Physical Sciences, 2012, Heriot-Watt University: Edinburgh, UK.

[101] Ackermann, T. and L. Söder, *An overview of wind energy-status 2002.* Renewable and Sustainable Energy Reviews, 2002. 6(1–2): p. 67–127.

[102] Justus, C.G., W.R. Hargraves, and A. Yalcin, *Nationwide assessment of potential output from wind-powered generators.* Journal of Applied Meteorology, 1976. 15(7): p. 673–678.

[103] Malek, P., Ortiz, J.M., Schulte-Herbrüggen, H.M.A., *Decentralized desalination of brackish water using an electrodialysis system directly powered by wind energy*, Desalination, 2016, 377, 54–64.

[104] Park, G.L., A.I. Schäfer, and B.S. Richards, *Renewable energy-powered membrane technology: supercapacitors for buffering resource fluctuations in a wind-powered membrane system for brackish water desalination*. Renewable Energy, 2013. 50: p. 126–135.

[105] Peñate, B. and L. García-Rodríguez, *Current trends and future prospects in the design of seawater reverse osmosis desalination technology*. Desalination, 2012. 284: p. 1–8.

[106] Likhachev, D.S. and F.-C. Li, *Large-scale water desalination methods: a review and new perspectives.* Desalination and Water Treatment, 2013. 51(13–15): p. 2836–2849.

[107] Alkhudhiri, A., N. Darwish, and N. Hilal, *Membrane distillation: a comprehensive review.* Desalination, 2012. 287: p. 2–18.

[108] Tzen, E., et al., *Design and development of a hybrid autonomous system for seawater desalination*. Desalination, 2004. 166: p. 267–274.

[109] Tzen, E., D. Theofilloyianakos, and Z. Kologios, *Autonomous reverse osmosis units driven by RE sources experiences and lessons learned.* Desalination, 2008. 221(1–3): p. 29–36.

[110] Vick, B.D. and R.N. Clark, *Experimental investigation of solar powered diaphragm and helical pumps*. Solar Energy, 2011. 85(5): p. 945–954.

[111] Protogeropoulos, C. and S. Pearce, *Laboratory evaluation and system sizing charts for a 'second generation' direct PV-powered, low cost submersible solar pump*. Solar Energy, 2000. 68(5): p. 453–474.

[112] Adiga, M.R., et al., *Performance analysis of photovoltaic electrodialysis desalination plant at Tanote in Thar desert*. Desalination, 1987. 67: p. 59–66.

[113] Abraham, T. and A. Luthra, *Socio-economic & technical assessment of photovoltaic powered membrane desalination processes for India*. Desalination, 2011. 268(1–3): p. 238–248.

[114] Li, C.N., Y. Goswami, and E. Stefanakos, *Solar assisted sea water desalination: a review.* Renewable & Sustainable Energy Reviews, 2013. 19: p. 136–163.

Edited by Ahmed F. Zobaa,
Sara N. Afifi and Ioana Pisica

The sustainable energy sources are potentially employed to substitute petrol fuels in transport engines such as buses and small vehicles. Hydrogen-enriched compressed natural gas engines are forthcoming energy carriers for the internal combustion engine, with higher thermal efficiency and less pollutant emissions. The different availability of renewables has allowed various countries to adopt the most appropriate type of renewable energy technology according to their energy source adequacy/abundance. In Taiwan, ocean energy is considered as an abundant source of renewables due to its geographical location as an island. The Taiwanese government has approved the investment to construct an MW-scale demonstration electricity plant. In this book, the Taiwanese ocean energy experience is comprehensively presented. The technical and legal analyses of ocean energy implementation are provided. The challenges that they had to overcome to optimize the utilization of the most available ocean energy potential are discussed. The sustainable transition in South Africa would be a good example for implementing rooftop solar, especially in low-income communities. Apart from the environmental benefits, sustainable energy technologies can boost the socioeconomic level of developing countries. Other advantages may be the continuous supply of energy and creation of new job opportunities. Moreover, sustainable renewable energy sources such as the wind could be employed for generating electricity to operate water purification systems in remote areas. This, in turn, would overcome the health problems associated with drinking water scarcity issues. This book is an attempt to cover the sustainable energy issues from a technical perspective. Furthermore, the sustainable energy applications and existing case studies are helpful illustrations for the broad understanding of the importance of sustainable energy.

Photo by Petmal / iStock

IntechOpen

ISBN 978-953-51-6689-4
9 789535 166894